

Optical spectroscopy in biomedicine -
detection of embedded inclusions and
in vivo pharmacokinetics

Jenny Svensson

Doctoral Thesis
Department of Physics
2007



LUND UNIVERSITY

© Jenny Svensson, 2007
All rights reserved.

Doctoral Thesis
Atomic Physics Division
Department of Physics
Faculty of Engineering LTH
Lund University
P.O. Box 118
SE-221 00 Lund
Sweden

Lund Reports on Atomic Physics, LRAP-374
ISSN 0281-2762
ISBN 978-91-628-7128-4

Printed by Media-Tryck, Lund, Sweden, 2007

Till min familj

Abstract

The main theme of this thesis is the use of fluorescence spectroscopy in biomedicine. The work presented in the thesis can be divided into three areas of applications.

The first area involves the use of fluorescence to find the location of a deeply situated fluorophore within turbid media. Fluorescence emitted from the fluorophore will be attenuated when propagating through the medium, due to the optical properties of the surroundings. The fluorescence light will be more attenuated at some wavelengths as the tissue optical properties are wavelength-dependent, and this difference will be more pronounced the longer the light travels. An intensity ratio of fluorescence at two selected wavelengths can therefore provide information about the depth of the inclusion. This has been investigated with both simulations and experiments with tissue phantoms. A further step has been to incorporate this depth-dependent ratio into a reconstruction algorithm used in fluorescence tomography.

Photodynamic therapy (PDT) is a local treatment modality of tumors, requiring light, oxygen and an administered photosensitizer, which preferably accumulates in tumor tissue. The second main area in this thesis has been the study of the pharmacokinetics of a liposomal formulation of the photosensitizer Temoporfin in different animal tumor models. Fluorescence measurements have been performed in order to estimate the quantity of photosensitizer within tumor and normal tissues following either topical or systematical administration of the drug. These quantities were compared to the drug concentrations obtained with chemical extraction. Time intervals of 2–8 hours between administration and measurements were investigated. Absorption spectroscopy was also performed when using topical application of the drug, yielding a good correlation of photosensitizer concentration compared to extraction data. Tumor selectivity of this liposomal Temoporfin formulation was shown at these short time intervals. Fluorescence measurements have also been performed in a first clinical PDT trial using topical application of this new formulation.

The final application utilizing fluorescence was to measure temperature optically. Certain crystals change their fluorescence spectrum when the temperature is altered. By attaching a crystal to a fiber tip, the temperature can be monitored at the position of the fiber. An intensity ratio of detected fluorescence in two wavelength bands can provide an estimate of the temperature. The temperature was monitored during a 10 minutes long light illumination on skin of a volunteer, indicating a temperature increase. The technique was also tested interstitially in meat, showing a temperature increase during the entire illumination as no perfusion was present, which normally stabilizes the temperature.

Sammanfattning

Denna avhandling beskriver hur fluorescens kan användas inom biomedicinområdet. Fluorescens är ett fenomen, som uppstår när molekyler absorberar inkommande ljus och sedan återutsänder ljus som har längre våglängd än det inkommande ljuset, och därför lägre energi, då en del av det absorberade ljuset omvandlats till värme i det omkringliggande mediet. I mänsklig vävnad finns flera olika molekyler, så kallade fluoroforer, som kan absorbera ljus och skapa fluorescens.

Arbetet som denna avhandling bygger på kan delas in i tre delar, där varje del innefattar mätning och analys av fluorescensljus som genererats.

Den första delen behandlar möjligheten att bestämma djupet av ett fluorescerande objekt som befinner sig någonstans under ytan i ett spridande material. Fluorescensljuset, som sänds ut från det fluorescerande objektet, kommer att dämpas medan det färdas från objektet till ytan, där ljuset kan detekteras. Dämpningen uppkommer då vävnaden både sprider och absorberar ljus. Fluorescensen vid olika våglängder kommer att dämpas olika mycket då både spridning och absorption är våglängdsberoende. Denna skillnad kommer att bli mer påtaglig ju längre väg ljuset färdas i vävnaden. En kvot mellan intensiteterna vid två olika detekterade våglängder kan därmed ge information om djupet av det fluorescerande objektet. Detta har studerats både med simuleringar och experiment med så kallade vävnadsfantomer, vilka uppvisar optiska egenskaper liknande mänsklig vävnad. Det senaste arbetet inom detta området beskriver hur denna djupinformation kan utnyttjas för att kunna rekonstruera ett fluorescerande objekt från tomografiska mätningar.

Fotodynamisk tumörterapi är en metod för lokal behandling av tumörer. Ljus, syre och en kemisk substans, som ackumuleras i högre grad i tumör jämfört med frisk vävnad, är de tre komponenter som krävs för själva behandlingen. Inom det andra stora projektet i denna avhandling har farmakokinetiska mätningar av substansen Temoporfin utförts, d.v.s. monitorering av hur mycket det finns av substansen i tumör respektive frisk vävnad vid olika

tidpunkter efter att substansen tillförts. Dessa försök har utförts i djurmodell både då substansen applicerats på huden och också via injicering i blodet. En uppskattning av mängden substans i olika vävnader har utförts med fluorescensspektroskopi och dessa värden har sedan jämförts med den koncentration som uppmätts via kemisk extraktion av substansen i vävnaden. Resultaten visar att det finns en selektivitet av substansen i tumör jämfört med normal vävnad vilket är positivt för att kunna behandla tumörer och spara normal vävnad. Fluorescensmätningar har också utförts under behandling av patienter, då med ytlig applicering av Temoporfin.

Den sista delen av avhandlingen beskriver en optisk metod för att mäta temperatur. Det finns vissa kristaller vars fluorescens ändrar karaktär med temperaturen. Om en liten bit av en sådan kristall limmas fast på en fiberspets, är det sedan möjligt att studera temperaturen i just den punkt där fibern är placerad genom att mäta kristallens fluorescensljus. Under en 10 minuter lång belysning med laserljus via fibern med kristallen placerad på mänsklig hud, kunde en temperaturökning under de första minuterna monitoreras. Tekniken testades också interstitiellt i kött, varvid en temperaturökning under hela belysningen uppmättes eftersom inget blodflöde fanns som kunde kyla ner vävnaden.

Contents

Abstract	i
Sammanfattning	iii
Contents	v
List of papers	vii
1 Introduction	1
2 Light-tissue interaction	3
2.1 Absorption	3
2.2 Scattering	4
2.3 Transport equation	5
2.4 Diffusion approximation	6
2.5 The Monte Carlo method	7
2.5.1 Fluorescence Monte Carlo	8
2.6 Determination of optical properties	9
2.6.1 Inverse adding-doubling	9
2.6.2 Measurement of μ_a	9
3 Fluorescence spectroscopy	11
3.1 Fluorescence	11
3.2 Autofluorescence	12
3.3 Exogenous fluorophores	13
3.4 Laser-induced fluorescence	14
3.5 Fluorescence detection techniques	14
3.5.1 Point monitoring	15
3.5.2 Imaging	15
3.6 Influencing factors on fluorescence spectra	16
3.6.1 Optical properties	16
3.6.2 Illumination-detection geometry	17
3.7 Depth estimation through fluorescence measurements	18
3.8 Clinical applications of fluorescence spectroscopy .	19

4 Photodynamic therapy and pharmacokinetics of photosensitizers	21
4.1 Photodynamic therapy	21
4.1.1 Tissue response to PDT	23
4.1.2 Photosensitizers	24
4.1.3 Selectivity of photosensitizers	25
4.1.4 Clinical results	26
4.2 Improvements of selectivity and delivery of photosensitizers	27
4.2.1 Penetration enhancers	27
4.2.2 ALA derivatives	28
4.2.3 Liposomes	28
4.2.4 Active targeting with lipoproteins and antibodies	29
4.3 Quantification of photosensitizer concentration	30
4.3.1 Fluorescence studies	30
4.3.2 Absorption spectroscopy	31
4.3.3 Chemical extraction	32
4.4 Interstitial photodynamic therapy and temperature monitoring	32
4.4.1 Doped crystals	33
4.4.2 Temperature measurements with doped crystals	33
5 Molecular imaging	37
5.1 Optical activatable probes	38
5.1.1 Non-specific probes	38
5.1.2 Specific probes	39
5.1.3 Activatable probes	39
5.1.4 Fluorescent proteins	39
5.1.5 Quantum dots	40
5.2 Molecular imaging techniques	40
5.3 Optical imaging techniques	41
5.3.1 Bioluminescence imaging	41
5.3.2 Planar fluorescence imaging	42
5.3.3 Fluorescence lifetime imaging	42
5.4 Optical tomography	42
5.4.1 Fluorescence mediated tomography	45
5.5 Improve robustness in optical tomography reconstruction	48
5.6 Multivariate analysis	48
Acknowledgments	51
Summary of papers	53
Bibliography	57

List of papers

- I. **Fluorescence spectra provide information on the depth of fluorescent lesions in tissue**
J. Swartling, J. Svensson, D. Bengtsson, K. Terike and S. Andersson-Engels.
Applied Optics **44**(10):1934–1941, 2005.
- II. **Modeling of spectral changes for depth localization of fluorescent inclusion**
J. Svensson and S. Andersson-Engels.
Optics Express **13**(11):4263–4274, 2005.
- III. **Fluorescence spectroscopy in tissue phantoms for improved depth resolution in tissue imaging**
J. Svensson, A. Garofalakis, H. Meyer, F. Forster, J. Ripoll and S. Andersson-Engels.
in *Photon Migration and Diffuse-Light Imaging II*, eds. K. Licha and R. Cubeddu, Proc. SPIE 5859:1–6, 2005.
- IV. **Multispectral prior knowledge used for data pre-processing in fluorescence molecular tomography**
J. Axelsson, J. Svensson and S. Andersson-Engels.
Manuscript in preparation.
- V. **External Parameter Orthogonalisation - Least Squares Support Vector Machine (EPO-LSSVM) and Partial Least Squares (PLS) for localization of embedded inclusions using detection of fluorescence**
F. Chauchard, J. Svensson, J. Axelsson, S. Andersson-Engels and S. Roussel.
Chemometrics and Intelligent Laboratory Systems: Submitted, 2006.
- VI. **Fluorescence and absorption assessment of a lipid mTHPC formulation following topical application in a non-melanotic skin tumor model**
A. Johansson, J. Svensson, N. Bendsoe, K. Svanberg, E. Alexandratou, M. Kyriazi, D. Yova, S. Gräfe, T. Trebst and

S. Andersson-Engels.

Journal of Biomedical Optics: Accepted, 2007.

VII. Tumor selectivity at short times following systemic administration of a liposomal Temoporfin formulation in a murine tumor model

J. Svensson, A. Johansson, S. Gräfe, B. Gitter, T. Trebst, N. Bendsoe, S. Andersson-Engels and K. Svanberg.

Photochemistry and Photobiology: Accepted, 2007.

VIII. Fluorescence monitoring of a topically applied liposomal Temoporfin formulation and photodynamic therapy of non-pigmented skin malignancies

N. Bendsoe, L. Persson, A. Johansson, J. Axelsson, J. Svensson, S. Gräfe, T. Trebst, S. Andersson-Engels, S. Svanberg and K. Svanberg.

Journal of Environmental Pathology, Toxicology and Oncology: Submitted, 2006.

IX. Tissue temperature monitoring during interstitial photodynamic therapy

J. Svensson, A. Johansson, K. Svanberg and S. Andersson-Engels.

in *Thermal Treatment of Tissue: Energy Delivery and Assessment III*, ed. T.P. Ryan, Proc. SPIE 5698:126–136, 2005.

Introduction

Fluorescence spectroscopy has been used in several decades for medical applications, for example for tumor detection and tissue diagnostics. A great advantage with fluorescence monitoring is that it is a non-invasive method and can be performed in real-time. Fluorescence can be used to help physicians in finding areas with cancer that may not be visible during white-light examination. How is tissue fluorescence induced? To be able to generate fluorescence light, the tissue needs to be illuminated with light of a specific wavelength. Different molecules in the tissue can absorb the excitation light, and after a short time period the molecules will re-emit light, called fluorescence. Fluorescence is characterized with a broad wavelength distribution and the emission consists of longer wavelengths than the exciting light.

Papers I–V involve work in connection to the multidisciplinary field called molecular imaging. My part within this project has been to evaluate a method to determine the depth of a fluorescent object embedded in tissue, or rather in tissue-like phantoms, by studying the emitted fluorescence. The principle is based on the fact that emitted fluorescence light is attenuated as it propagates from the source through the medium to the detection at the tissue surface. This attenuation is due to the optical properties of tissue and that these are wavelength dependent. Distinct fluorescence wavelengths may be differently attenuated, and more so if the light has travelled a longer way. Therefore, a ratio between two such wavelengths can provide information about the depth of the inclusion. However, there are limitations with this intensity ratio and these have also been investigated with simulations in Papers I–II. The next step was to use this multispectral information in the reconstruction algorithm of fluorescence tomography. These preliminary results are presented in Paper IV.

Photodynamic therapy (PDT) is a treatment modality of ma-

lignant tumors, where light together with an administered photosensitizer and oxygen induce cell death. A property of the administered photosensitizer is that it should preferably accumulate in the tumor to be treated and not in non-diseased tissue. An important task is to study the pharmacokinetics of these photosensitizers. In Papers VI–VII the pharmacokinetics of a liposomal formulation of the photosensitizer Temoporfin has been studied in animal tumor models. Different methods have been utilized; optical methods as well as high pressure liquid chromatography, in order to estimate the amount of photosensitizer in tumors and healthy tissue. A first clinical study has also been performed using topical application of Temoporfin, presented in Paper VIII.

The last paper in the thesis, Paper IX, involves work on how to measure temperature with an optical method using certain crystals attached to optical fibers. The special feature with these crystals is that the spectral shape of the emitted fluorescence changes when the temperature in the crystals increases or decreases. By studying the spectral changes, the temperature can be determined within the object where the crystal is located.

This thesis is divided into four main chapters. Chapter 2, which describes the interaction of light with tissue and Chapter 3, which explains fluorescence and different detection techniques of fluorescence light. The field of molecular imaging is introduced in Chapter 4. Chapter 5 describes PDT and different aspects of photosensitizers. A short background of optical temperature measurements is also given in this last chapter. In the final part of the thesis the papers are included.

Light-tissue interaction

Light consists of photons with specific energies. The energy of a photon is directly related to the wavelength of the light. Spectroscopic measurements for tissue diagnostics are usually performed in the wavelength region from the ultraviolet (UV) to the infrared (IR) region. The visible wavelength region, from 400 nm to 700 nm, is located between the UV and IR regions.

When tissue is illuminated, light can be reflected at the surface. This is due to differences in refractive index between air and tissue, and is often referred to as specular reflectance. The light not reflected at the surface is transmitted into the tissue, see Figure 2.1. When light interacts with tissue it can either be scattered or absorbed. Scattering is a phenomenon where light changes direction because of the structure inside the tissue. Cells and their constituents cause scattering as the refractive indices of the structures differ from their surrounding. Absorption means that the photon energy is absorbed by molecules in the tissue, e.g. by the strong absorber hemoglobin. When light is absorbed, several processes can take place. The absorbed energy can excite the molecule and after some time the molecule will decay to its initial state and emit fluorescence light. Fluorescence will be described in more detail in Chapter 3. Another possibility is that the absorbed energy will be converted into heat, increasing the temperature in the tissue.

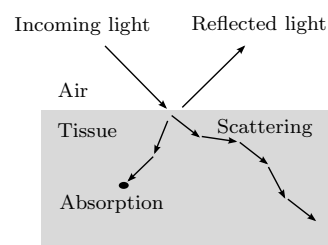


Figure 2.1. When tissue is illuminated light can be reflected at the surface or transmitted into the tissue. Inside the tissue the light can either be absorbed or scattered.

2.1 Absorption

Absorption in tissue is described by the absorption coefficient μ_a [m^{-1}], which gives the probability of absorption per unit length¹. An absorber is a substance which absorbs radiation. The specific part of a molecule in the substance that gives rise to the absorption, through electronic transitions, is called a chromophore. In tissue,

the main absorbers are deoxy- and oxy-hemoglobin, water, lipid and melanin.

The absorption coefficient of an absorber is described by the product of the extinction coefficient, ε [$\text{M}^{-1}\text{cm}^{-1}$], and the concentration, c [M], of the specific absorber. The total absorption coefficient in tissue is a sum of the absorption coefficients of the present absorbers as denoted in Eq. 2.1.

$$\mu_a(\lambda) = \sum_k \varepsilon_k(\lambda)c_k(\lambda) . \quad (2.1)$$

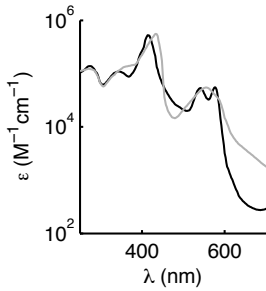


Figure 2.2. Extinction coefficients as a function of wavelength for deoxy-hemoglobin (gray) and oxy-hemoglobin (black)².

The absorption coefficient of tissue is strongly wavelength dependent due to the fact that the chromophores absorb light of different wavelengths. In Figure 2.2 the extinction coefficient as a function of wavelength can be seen for deoxy- and oxy-hemoglobin, respectively. The overall absorption in tissue is relatively low in the wavelength region 650–1300 nm. Therefore, this region is often called the tissue optical window. Light can penetrate deep into the tissue when the absorption is low, and therefore this region is favorable to use for certain types of tissue diagnostics.

Hemoglobin is the pigment that carry oxygen in the red blood cells. Hemoglobin can be found in both an oxygenated and a deoxygenated form. Oxygenated hemoglobin shows a difference in absorption compared to deoxygenated hemoglobin due to differences in the molecular structure. Both forms have two strong absorption bands around 420 and 550 nm in the visible region, but deoxy-hemoglobin shows a stronger absorption around 660 nm compared to the oxygenated form. Melanin is a pigment in skin, hair and in the iris of the eye. It is a dark pigment that is a strong absorber in the UV and blue wavelength regions. Therefore, melanin protects the lower layers of the skin from dangerous UV-rays emitted by the sun. Lipids exist in most tissues, but in different amounts, and they absorb mostly in the near infrared region. Water absorbs mainly in the UV and IR regions.

2.2 Scattering

Light is scattered inside tissue as it interacts with the structural differences present in tissue. Scattering in tissue is described by the scattering coefficient μ_s [m^{-1}], which gives the probability of scattering per unit length¹. The differences in structure are also found on a subcellular level, where cell organelles, e.g. the mitochondria, can scatter light³. Also the scattering coefficient shows a dependence on wavelength, but only as a small decrease as the wavelength is increased. The relationship between scattering coefficient and wavelength is given by Eq. 2.2:

$$\mu_s = A \cdot \lambda^{-b} , \quad (2.2)$$

where A and b are constants and where b is usually in the order of one in tissue.

If light is scattered with the same probability in all directions, the scattering is called isotropic. In tissue the light is mostly scattered in a forward direction. The scattering direction is often described by the scattering anisotropy or g -factor, which is given by Eq. 2.3 as the expectation value of $\cos \theta$:

$$g = \langle \cos \theta \rangle , \quad (2.3)$$

where θ is the angle between the incoming light and the scattered light¹. The g -factor is in the range of 0.7–1.0 for different tissue types⁴.

If light is scattered many times in tissue the light will become diffuse and the g -factor and μ_s cannot be separated. Therefore, a new parameter called the reduced scattering coefficient, μ'_s , is introduced and given by:

$$\mu'_s = \mu_s(1 - g) . \quad (2.4)$$

2.3 Transport equation

One way to model the light propagation in tissue is to use the radiative transport equation (RTE)¹, described by Eq. 2.5.

$$\frac{1}{c} \frac{\partial L(\mathbf{r}, \mathbf{s}, t)}{\partial t} = -\mathbf{s} \cdot \nabla L(\mathbf{r}, \mathbf{s}, t) - (\mu_a + \mu_s)L(\mathbf{r}, \mathbf{s}, t) + \mu_s \int_{4\pi} L(\mathbf{r}, \mathbf{s}', t) p(\mathbf{s}, \mathbf{s}') d\omega + q(\mathbf{r}, \mathbf{s}, t) , \quad (2.5)$$

where c is the velocity of light in tissue, $L(\mathbf{r}, \mathbf{s}, t)$ is the radiance [$\text{W}/\text{m}^2\text{sr}$], meaning the power passing perpendicular to an area element in the direction \mathbf{s} and per angle, $d\omega$, around the vector \mathbf{s} at a certain point in time. The term $p(\mathbf{s}, \mathbf{s}')$ is the probability of scattering of light from the direction \mathbf{s}' into the direction \mathbf{s} . The last term, $q(\mathbf{r}, \mathbf{s}, t)$, corresponds to a light source inside the volume element. RTE is based on energy conservation in a small volume element¹, dV . The meaning of the different terms in the transport equation are illustrated in Figure 2.3.

It is difficult to solve the radiative transport equation analytically. Therefore, different methods to simplify the equation have been developed. One method is to use a diffusion approximation and another approach is to use a statistical method where Monte Carlo simulations are performed. Both methods will be described in the following sections. To solve the RTE a discrete-ordinate finite-difference method can also be used. In this approach the equation is discretized in both the directional- and room variables and the derivatives are approximated numerically.

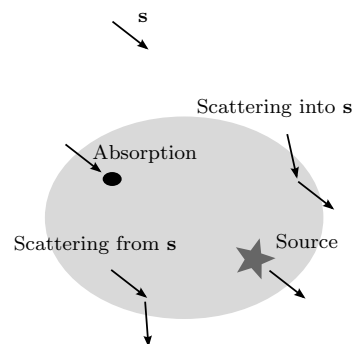


Figure 2.3. The different terms in the radiative transfer equation.

2.4 Diffusion approximation

Light transport through a medium, where scattering is much larger than the absorption, can be described using the diffusion approximation^{5,6}. In order for the diffusion approximation to be valid it is necessary that the light is diffuse. Therefore, the source and detector must be separated sufficiently for this to happen. In tissue the light is assumed to be diffuse after approximately ten scattering events.

The concept of the diffusion approximation is that the radiance, $p(\mathbf{s}, \mathbf{s}')$ and the source term of the RTE are expanded into spherical harmonics, Y_{lm} . The expansion of the radiance is given by Eq. 2.6:

$$L(\mathbf{r}, \mathbf{s}, t) = \sum_{l=0}^{\infty} \sum_{m=-l}^l \sqrt{\frac{2l+1}{4\pi}} L_{lm}(\mathbf{r}, t) Y_{lm}(\mathbf{s}) . \quad (2.6)$$

Two quantities utilized in the derivation of the diffusion approximation are the fluence rate, $\phi(\mathbf{r}, t)$ [W/m²], and the photon flux, $\mathbf{F}(\mathbf{r}, t)$ [W/m²]. Definitions of these two quantities are given in Eqs. 2.7 and 2.8, respectively.

$$\phi(\mathbf{r}, t) = \int_{4\pi} L(\mathbf{r}, \mathbf{s}, t) d\omega , \quad (2.7)$$

$$\mathbf{F}(\mathbf{r}, t) = \int_{4\pi} L(\mathbf{r}, \mathbf{s}, t) \mathbf{s} d\omega . \quad (2.8)$$

The expansion in Eq. 2.6 can be truncated by only including terms with $l \leq N$, giving rise to a so called P_N -approximation. Most often the P_1 -approximation is used, where only terms corresponding to $l = 0, 1$ are incorporated. Using the P_1 -approximation together with Eqs. 2.7 and 2.8 the radiance can be expressed as:

$$L(\mathbf{r}, \mathbf{s}, t) \approx \frac{1}{4\pi} (\phi(\mathbf{r}, t) + 3\mathbf{F}(\mathbf{r}, t) \cdot \mathbf{s}) , \quad (2.9)$$

where the first term, including ϕ , symbolizes an isotropic part of the radiance and the second term, including \mathbf{F} , can be seen as a small directional component in the radiance.

By assuming an isotropic light source and a constant flux vector in time, light transport can now be described by the diffusion equation according to Eq. 2.10:

$$\frac{1}{c} \frac{\partial \phi(\mathbf{r}, t)}{\partial t} - D \nabla^2 \phi(\mathbf{r}, t) + \mu_a \phi(\mathbf{r}, t) = q(\mathbf{r}, t) , \quad (2.10)$$

where c is the velocity of light in tissue and D is the diffusion coefficient, described by:

$$D = \frac{1}{3(\mu_a + \mu'_s)} . \quad (2.11)$$

However, in the visible wavelength region the absorption is no longer much less than the scattering and the diffusion coefficient given by Eq. 2.11 is no longer accurate. A modified diffusion coefficient has been derived⁷, given by Eq. 2.12, where α is both absorption and scattering dependent. Using this modified coefficient, Eq. 2.10 has been shown to be valid in medium with somewhat higher absorption.

$$D = \frac{1}{3(\alpha\mu_a + \mu'_s)} . \quad (2.12)$$

The diffusion equation has the advantage that it can be solved analytically for simple geometries. An analytical solution to the diffusion equation is its corresponding Green's function assuming a homogenous medium and an isotropic point source. A solution for the time-independent case is given by:

$$\phi(\mathbf{r}) = \frac{1}{4\pi D} \cdot \frac{e^{-\mu_{eff}r}}{r} , \quad (2.13)$$

where μ_{eff} is the effective attenuation coefficient given by $\mu_{eff} = \sqrt{3\mu_a(\mu_a + \mu'_s)}$. If the geometry is not an infinite homogenous medium, the source is usually not an isotropic point source but rather a laser beam entering at the tissue surface. Then the source can instead be treated as an isotropic point source located at a distance $1/\mu'_s$ below the surface⁸. It is also important to take into account appropriate boundary conditions when dealing with non-infinite media. When more difficult geometries and inhomogeneous media are considered, numerical methods can be used instead. The finite element method (FEM) is such a numerical approach where the medium is divided into a mesh and the solution to the diffusion equation is approximated by simple functions, e.g. low-order polynomials, in each mesh element. Close to inhomogeneities a finer mesh can be defined in order to approximate the solution more accurately.

2.5 The Monte Carlo method

A statistical method for approximating the solution to the radiative transport equation is to perform Monte Carlo simulations of photons in a turbid medium^{9;10}. The light distribution is simulated with a random walk of photons (or photon packages) inside the medium. By repeating this random walk for a large number of photons, good statistics can be achieved. Different outputs can

be obtained from the simulations: absorption, reflection, transmission and light fluence. The main input parameters to a Monte Carlo simulation software are the optical properties, (μ_s, μ_a, g) , the refractive index and the geometry of the medium. There are several advantages with this method. One being that there is no restriction in the range of optical properties as compared to the diffusion approximation, where scattering dominates over absorption. Another advantage is that any geometry could potentially be used.

The principle of a Monte Carlo simulation is that a photon package is launched onto the medium. At the boundary the photon package can either be transmitted or reflected, if reflection occurs this event is saved and a new photon package is launched. If the photon package enters the medium, the step size of the propagation and the scattering angles are drawn from probability distributions determined by the input parameters, and the photon package is moved to its new coordinates. At each interaction site part of the package can be absorbed, and the absorbed part is saved at that specific location. The random determination of scattering and absorption of the photon package is repeated until the photon package leaves through a boundary of the medium or until the package is totally absorbed.

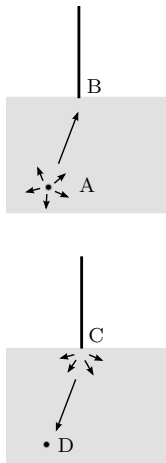


Figure 2.4. The amount of fluorescence created in A and detected in B is proportional to the amount of fluorescence detected in D due to a source in C.

2.5.1 Fluorescence Monte Carlo

It is also of interest to study fluorescence using Monte Carlo simulations. There exist different Monte Carlo codes to simulate fluorescence^{11;12}. A layered accelerated fluorescence Monte Carlo code has been developed by Swartling *et al*¹¹. This code has been used to simulate fluorescence in tissue to determine the depth of a fluorescent layer inside a medium in Papers I–II. To be able to simulate fluorescence light several Monte Carlo simulations need to be performed. First a simulation is performed to achieve the absorption of the excitation light by the fluorophores inside a medium. Then another simulation is performed to obtain the fluorescence propagation from all possible sources within the medium to the surface, assuming optical properties for the wavelength of the fluorescence light in the medium. An efficient way of achieving this is by using a reciprocity theorem, illustrated in Figure 2.4. Only one simulation is required for each specific fluorescence wavelength, assuming the source of fluorescence on the surface instead of inside the tissue¹¹. The two matrices, absorption of excitation light and emission of fluorescence light, are convolved in the radial direction to produce the probability of transmitted or reflected fluorescence light as a function of radius on the surface.

2.6 Determination of optical properties

The optical properties of tissue are often not known beforehand, therefore some measurements need to be performed to obtain these properties. There are at least four different methods to obtain the optical properties: spatially resolved measurements^{13–15}, time-resolved measurements^{8;16;17}, frequency domain measurements^{18;19} and integrating sphere measurements²⁰. All methods, except the last one, give only two of the optical properties (μ_a , μ'_s). To obtain all three parameters, (μ_a , μ_s , g), an integrating sphere set-up can be used. The inner surface of an integrating sphere consists of a highly reflecting material, which makes it possible to collect all light entering the sphere. Measurements of the diffuse reflectance and diffuse transmittance²⁰ of the sample with the sphere, can give estimates of μ_a and μ'_s . An additional measurement with a collimated light beam measures the sum of the absorption and scattering coefficients. After these three measurements have been performed, the optical properties of the tissue can be calculated. The method has one major drawback as the measurements must be conducted on thin slabs and cannot be performed *in vivo*.

2.6.1 Inverse adding-doubling

When using an integrating sphere three different measurements are performed, and the measured values are total reflection and transmission, and unscattered transmission. A way to determine the optical properties of the sample from the measured quantities with the integrating sphere is to use the method inverse adding-doubling (IAD)²¹. It is a numerical solution of the radiative transport equation and has an advantage, compared to e.g. the diffusion approximation, that it requires no limits in the optical properties. IAD is often used to determine the optical properties of biological samples compressed between two glass slides. Using IAD the reflection and the transmission are calculated iteratively from an initial guess of the optical properties. When the calculated and the measured values agree, the optical properties of the sample have been determined.

2.6.2 Measurement of μ_a

It has been shown that there is a specific source-detector separation range, r_s , illustrated in Figure 2.5, where the effective path length of the detected photons is approximately independent of the scattering in tissue^{22;23}. The effective path length is the distance that can replace all the individual path lengths of the detected photons, thus it can be seen as a pseudo-mean path length. By using a probe with this specific source-detector fiber separation,

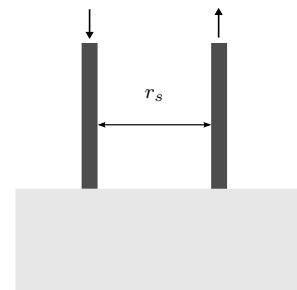


Figure 2.5. Source and detection fibers separated by a distance r_s .

the absorption coefficient can be determined without knowing the scattering coefficient. In tissue with a reduced scattering coefficient of $5\text{--}15\text{ cm}^{-1}$ this fiber separation will be in the range²³ 1.5–2.6 mm. Although the effective path length is insensitive to variations in scattering in this range of source-detector separations, the detected intensity can still be affected.

In Paper VI we wanted to determine the concentration of a drug in tumor tissue. By performing spatially resolved measurements of reflectance the absorption due to the drug could be determined and hence the concentration, see Eq. 2.1. The probe used had a distance of 2.0 mm between the source and detection fibers, thus reducing the effect of scattering in the measurements.

Another specific distance between the source and detection fibers is the so called pivot point, where the detected intensity is invariant with respect to the scattering in tissue. Measurements at the pivot point can also be used to determine an approximate value of the absorption coefficient¹⁵.

Fluorescence spectroscopy

Most of the work presented in the thesis is related to fluorescence spectroscopy. This chapter will give an introduction to fluorescence spectroscopy, including the basic theory of fluorescence and the origin of tissue fluorescence. Fluorescence detection techniques as well as factors influencing acquired fluorescence spectra will also be discussed in this chapter.

3.1 Fluorescence

As for atoms, energy diagrams of molecules consist of electronic energy levels. However, molecules can also rotate and vibrate, introducing a splitting of the electronic energy levels into many sub-levels. If the energy of an incoming photon matches the difference between two energy levels in the molecule, the photon can be absorbed. From here different processes can take place as illustrated in Figure 3.1. All these processes result in the molecule releasing its excess energy gained when absorbing the photon²⁴.

The molecule is most probable to be located in the ground state, S_0 , at energy equilibrium. After absorption the molecule is excited to another singlet state, S_n . From here the molecule will directly relax into the lowest vibrational state within this excited electronic state. This non-radiating process is called vibrational relaxation (VR). The release of the excess energy is converted into heat.

From the excited state, S_n , the molecule will move to a lower electronic state, S_{n-1} , through a process called internal conversion (IC). The molecule will once again relax to the lowest vibrational level within this state through VR. After several IC and VR processes the molecule will end up in the state S_1 . From here the remaining excess energy of the molecule can be released as

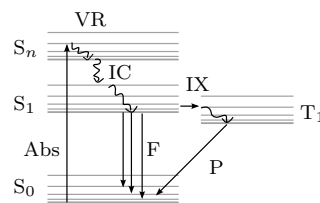


Figure 3.1. An energy level diagram where the different processes that can occur after excitation of the molecule are illustrated. S and T denote a singlet and a triplet state in the molecule, respectively. Abs-absorption, VR-vibrational relaxation, IC-internal conversion, F-fluorescence, IX-intersystem crossing, P-phosphorescence.

a photon when the molecule returns to any vibrational level in the ground state. This process is called fluorescence. The fluorescence photon will have a longer wavelength than the incoming photon, as the molecule loses some energy in the non-radiative relaxation processes. The generated fluorescence contains light of a broad wavelength range and not a sharp peak since the relaxation process can be carried out to any vibrational level in the ground state.

A transition of the molecule into a triplet state from a singlet state is also possible, which is called inter-system crossing (IX). The molecule will then relax to the lowest triplet state, T_1 , through VR and IC processes. From here the molecule can return to its ground state by emitting a photon. This phenomenon is called phosphorescence. During phosphorescence it takes longer time for the molecule to return to the ground state as compared to the fluorescence process. This is due to the fact that the lifetime of the triplet state is long, because the transition from a triplet to a singlet state is forbidden as a pure dipole-transition.

There is yet another relaxation path where the absorbed energy is transferred to and exciting a neighboring molecule. This path is not marked in the figure. If the absorbed photon is re-emitted immediately without losing any energy to the molecule, the process is called scattering.

3.2 Autofluorescence

Tissue autofluorescence is the fluorescence emitted from different natural fluorophores in tissue, usually upon excitation with UV or blue light. Autofluorescence is usually emitted in the blue-green region. Examples of tissue fluorophores contributing to this autofluorescence are; reduced nicotinamide adenine dinucleotide (NADH), flavin adenine dinucleotide (FAD), elastin, collagen, tryptophan and endogenous porphyrins²⁵⁻²⁷. These tissue fluorophores have individual excitation and emission maxima.

The oxidized forms NAD and FAD are electron acceptors in the metabolism of the cell. After accepting an electron the carriers are reduced into the forms NADH and FADH₂, respectively. Later these reduced forms transfer the electrons to oxygen in the mitochondria, and they once again become oxidized²⁷. It is the reduced form NADH and the oxidized form FAD that are fluorescent in the visible region. Depending on the state of the cell the balance between the concentrations of oxidized and reduced forms will change and lead to differences in the fluorescence spectrum, which therefore can give information about the metabolic function of the cell and tissue²⁵.

Collagen and elastin are proteins that are found in supportive tissue, and are important fluorophores in the extracellular matrix.

Tryptophan is an amino acid that fluoresces strongly when excited with light with a wavelength shorter than 300 nm. Endogenous porphyrins exhibit fluorescence in the red wavelength region²⁸.

Autofluorescence acquired from a vocal cord is seen in Figure 3.2. Fluorescence spectra from tissue show a broad emission, corresponding to the sum of the fluorescence emitted from several fluorophores. The shape of the autofluorescence depends also on chromophores reabsorbing emitted fluorescence and varies depending on tissue type.

In precancerous tissue the fluorescence intensity normally decreases when using near UV excitation and the peak of the emission is shifted towards the red²⁹. Emitted fluorescence from abnormal cells can be changed due to the fact that these cells often have changed metabolism and different cell structure. The often increased blood flow in tumors can absorb a large amount of light yielding a lower level of induced fluorescence.

When studying the fluorescence *in vivo* from the uterine cervix it has been shown that the absolute contribution of collagen fluorescence decreases and the relative contribution of NADH fluorescence increases when going from normal to abnormal tissue^{29;30}. A decrease in collagen fluorescence in tumor tissue compared to normal tissue has also been observed in samples of human intestinal tissue *in vitro*³¹ and *in vivo*³², but also in skin *in vivo*³³. This decrease in collagen fluorescence can be due to that the upper epithelium layer of these tissue types gets thicker as it progresses into abnormal tissue, as is illustrated in Figure 3.3. Since most of the collagen is located in the underlying structures of the tissue, less excitation light will penetrate deep enough and hence less collagen fluorescence is induced as the epithelium layer gets thicker. This suggests that the changes in autofluorescence from epithelial tissue are related to the morphological state of the tissue^{29;32}.

3.3 Exogenous fluorophores

Sometimes it can be difficult to diagnose tissue by only studying the tissue autofluorescence. The fluorescence yield of tissue fluorophores is rather low, providing a low signal of tissue fluorescence. It is also necessary to have a thorough knowledge about the correlation between the cell biology and tissue autofluorescence. As mentioned before, the autofluorescence can change in different ways and this makes it difficult to diagnose tissue by only studying this endogenous fluorescence. A way to increase the sensitivity of tumor detection, is to administer a fluorescent tumor marker, which accumulates in tumor tissue to a higher degree than in normal tissue²⁷. These tumor markers usually emit fluorescence light in the red or near-infrared region, making it easy to separate

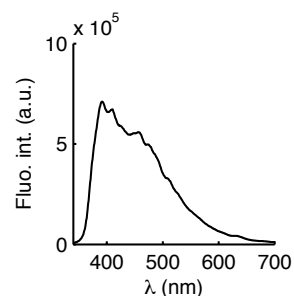


Figure 3.2. The emitted autofluorescence from the vocal cords after excitation with 337 nm light.

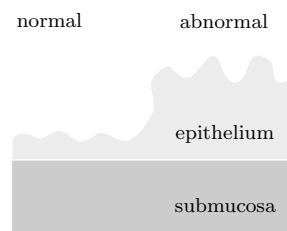


Figure 3.3. Epithelium layer is thicker in abnormal compared to normal tissue.

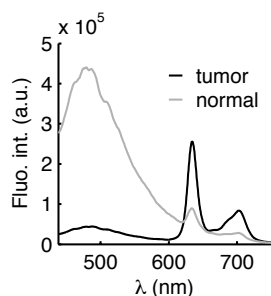


Figure 3.4. The spectra show the red fluorescence from the tumor marker PpIX after excitation at 405 nm for normal and premalignant tissue, respectively.

the fluorescence of the tumor marker from the blue–green tissue autofluorescence.

Porphyrin derivatives and chlorins are groups of different tumor markers used for fluorescence diagnostics²⁷. One example of a tumor marker is the fluorescent molecule Protoporphyrin IX (PpIX), which is converted in the cells from the administered precursor δ -aminolevulinic acid (ALA). The fluorescence from PpIX can be seen in Figure 3.4. The graph shows the measured fluorescence following excitation with 405 nm light from normal and premalignant tissue of the vocal cords. The peak due to the tumor marker is clearly seen in the red part of the spectrum from the non-healthy tissue. Different tumor markers, also used as photosensitizers in Photodynamic therapy (PDT) treatments, are discussed in more detail in Chapter 3.

3.4 Laser-induced fluorescence

Laser-induced fluorescence (LIF) spectroscopy is a method developed for tissue diagnostics³⁴. An important application is to find tumors and delineate its borders. The method is non-invasive and can be performed in real-time. The method makes it possible to investigate inner hollow organs by using optical fibers compatible with endoscopes. The tissue is irradiated with a laser of a specific wavelength that induces fluorescence from the present fluorophores. To study tissue autofluorescence, UV or blue lasers are primarily used as excitation sources. Only superficial lesions can be detected following excitation in the violet to the blue wavelength region, as the penetration depth is very shallow. By using longer wavelengths, the light can penetrate several millimeters inside the tissue and deeper lying lesions can be detected. The fluorescence light will be attenuated as it propagates through tissue, especially for light with long path lengths. It is not only the wavelength though that can influence the recorded fluorescence spectrum, but also the illumination-detection geometries used. The influences due to optical properties as well as illumination-detection geometries will be discussed in more detail later in this chapter.

Using LIF as a guide, more precise biopsies could be taken. The goal when using LIF as a guiding tool is to avoid unnecessary biopsies and only sampling biopsies where LIF finds something suspicious.

3.5 Fluorescence detection techniques

An important factor for fluorescence measurements is what light source to be used for the excitation of the fluorophores. If a continuous wave (CW) source is used superficial measurements need to be performed in a dark room, due to the induced fluorescence light

being much lower in intensity than the background light from the examination lamps. A way to overcome this is to use a pulsed light source, allowing the use of gated detection. This means that the detection system is opened only for a short time period when the induced fluorescence light is assumed to reach the detector. Even though the average fluorescence light intensity is much lower than the scattered background light, it can be much stronger during the short periods after the excitation light pulse³⁵.

The two most common techniques to detect fluorescence, point monitoring and imaging, will be discussed in the following subsections.

3.5.1 Point monitoring

Point monitoring detection of fluorescence is usually based on a fiber-coupled laser system^{32;36;37}. The excitation light is then guided to the tissue through a fiber and the fluorescence is collected and guided back to the instrument through the same or another fiber, see Figure 3.5. The fluorescence light can be directed to a spectrometer making it possible to study the entire fluorescence emission spectrum. This is of great importance when learning how the characteristic fluorescence spectra of different tissues appear, and thereby extracting contributions from various tissue fluorophores of diagnostic value. Other ways to obtain similar information is to scan the excitation wavelength (excitation spectroscopy) or measure the fluorescence decay in time (time-resolved fluorescence). An emission type of point monitoring system may use a pulsed light source and gated detection. There are some disadvantages with the point monitoring technique, one is that the detection is performed only in one spot in the tissue, making it difficult for instance to find or delineate tumors. Another drawback when optical fibers are used is that they can damage the tissue and give rise to bleeding. The blood can then reabsorb the fluorescence light and change the spectral shape in a non-wanted manner.

3.5.2 Imaging

To be able to delineate tumors fluorescence imaging techniques are preferable. Different techniques are employed relying on the number of detected wavelength bands used; single-band, dual-band or multi-color imaging. When working with imaging it is often difficult to detect fluorescence from many wavelengths at the same time in several detection points. Therefore, a selection has to be done to choose a few wavelengths that provide the most interesting information for diagnostics. Point detection of emitted fluorescence is needed to find these interesting features in the fluorescence spectrum. Other imaging modalities are time-gated imaging, where the fluorescence lifetimes for different fluorophores are studied³⁸.

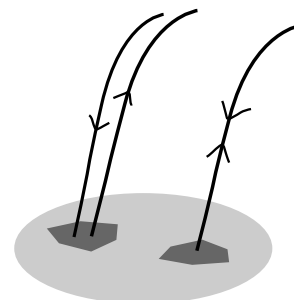


Figure 3.5. Point monitoring detection schemes.

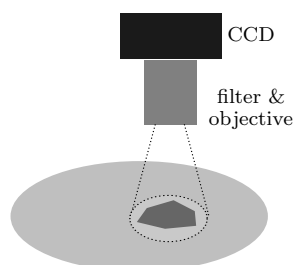


Figure 3.6. Fluorescence imaging detection scheme.

The detection unit in an imaging system usually consists of a filter selecting the appropriate wavelength, an objective that covers the region of interest and a charge-coupled device (CCD) camera detecting the fluorescence intensity of the area, see Figure 3.6. To select the interesting fluorescence wavelengths, different absorption or interference filters can be used. Absorption filters have a high transmission for a specific wavelength range, but not a sharp line between transmission and no transmission. The advantage with interference filters is the possibility of achieving a narrow and sharp bandpass effect. However, if many wavelengths are considered or the system have multiple purposes, it is more convenient to use e.g. a liquid crystal tunable filter (LCTF), where the wavelength can automatically be tuned within a range of several hundred nanometers³⁹. A disadvantage is that the transmission through a LCTF is rather low in the visible wavelength region. An acousto-optic tunable filter (AOTF) is another alternative when detection of fluorescence in many different wavelength bands is of interest⁴⁰.

3.6 Influencing factors on fluorescence spectra

An acquired fluorescence spectrum is influenced by several factors, for instance tissue optical properties and illumination-detection geometry. Optimally these effects are removed in order to obtain the intrinsic fluorescence spectrum of a fluorophore, i.e. the true fluorescence spectrum that has not been altered by any external effects. The intrinsic fluorescence can be used to determine the concentration of a fluorophore since the fluorescence light emitted from the fluorophore is proportional to the concentration.

3.6.1 Optical properties

The intensity and spectral shape of the fluorescence light can be altered due to absorption and scattering in tissue. If a large amount of e.g. hemoglobin is present, hemoglobin can reabsorb the emitted fluorescence light due to its strong absorption lines in the visible region⁴¹.

A common way to evaluate acquired fluorescence spectra is to calculate fluorescence intensity ratios to reduce the influences of experimental factors such as excitation light variations. However, these ratios will still be dependent on the optical properties of the tissue. One way to reduce the influence of, for instance, hemoglobin in a calculated intensity ratio is to use the intensities at wavelengths where hemoglobin has equally strong absorption. This has been demonstrated in the detection of atherosclerotic plaque in vessels⁴².

A double ratio technique can be used to determine the concentration of an exogenous fluorophore from fluorescence mea-

measurements^{43;44}. Two excitation wavelengths are used, and the same two fluorescence wavelengths are detected for each excitation source and a double intensity ratio is calculated. This double ratio has shown to be independent of optical properties.

There exist several different methods to calculate correction factors to retrieve the intrinsic fluorescence spectrum. The influences of optical properties in the fluorescence spectrum can be taken care of by performing combined reflectance and fluorescence measurements. Using a white-light reflectance measurement the optical properties can be determined at both the excitation and the fluorescence emission wavelengths.

Müller *et al.* used a photon migration model to remove the effects of optical properties of the acquired fluorescence spectra⁴⁵. An expression for the intrinsic fluorescence is based on both fluorescence measurement and measured reflectance at the excitation and emission wavelengths. The intrinsic fluorescence spectra of both tissue phantoms and *in vivo* tissue were recovered with good accuracy. Finlay *et al.* demonstrated a method combining reflectance and fluorescence measurements, by which they were able to recover the intrinsic fluorescence⁴⁶. However, they have also shown promising results when estimating the optical properties as well as the intrinsic fluorescence by fitting a number of basis spectra to a single fluorescence measurement⁴⁶. A drawback with this last method, when using the method for *in vivo* measurements, is that the basis spectra of all involved fluorophores have to be known.

3.6.2 Illumination-detection geometry

It is not only tissue optical properties that can affect the spectral shape and intensity of the detected fluorescence, but also the detection geometry, or rather the combination of these two.

A fiber optic probe for fluorescence measurements can be constructed in two different ways. One alternative utilizes one single fiber for both delivering the excitation light and to collect emitted fluorescence light. The second way is to use one fiber for delivering excitation light and another fiber for collection of emitted light, where these two fibers are separated a distance L from each other.

As the fiber diameter increases in the case of a single fiber probe or the distance between the delivery and collection fibers increases in the case of two fibers, fluorescence originating from deeper structures in the tissue can be probed. This is due to that a photon generated deeper in the tissue will in general arrive at a larger lateral distance from the delivering fiber at the surface⁴⁷, as shown in Figure 3.7.

The intensity of the detected fluorescence light will decrease as the distance between the delivery and collection fiber increases.

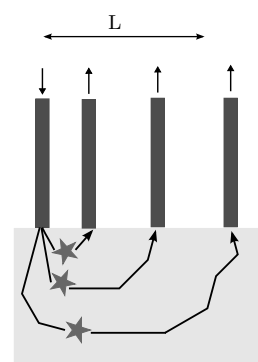


Figure 3.7. Larger separation between the delivery and collection fibers probe fluorescence emitted from deeper structures.

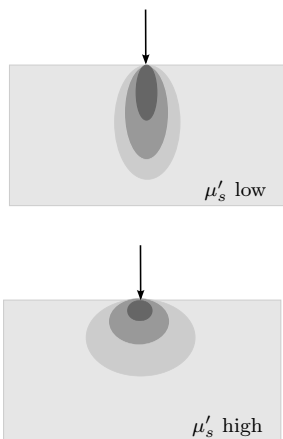


Figure 3.8. Higher scattering widens the distribution of the excitation light, and therefore also the fluorescence light. This provides the possibility to detect the fluorescence light at further distances from the excitation fiber.

The intensity also decreases with increased absorption in tissue. A spectral shift will be introduced if the absorption is wavelength-dependent. This is more pronounced at large source-detector separations due to a longer mean path length of the photons⁴⁸.

Scattering in tissue also affects the intensity of the detected light. When the separation between the delivery and collection fibers is inside the pivot point, mentioned in Section 2.6.2, a higher intensity will be detected with higher scattering compared to lower scattering. This is due to that the distribution of the excitation light is confined closer to the tip of the excitation fiber when the scattering is high. Hence the spatial distribution of the fluorescence light appears to be broadened inside the pivot point⁴⁹, as illustrated in Figure 3.8. At fiber separations outside of the pivot point less fluorescence light will be detected since less light manage to diffuse all the way to the collection fiber when scattering increases. The intermediate distance where the detected intensity is invariant with respect to scattering defines the pivot point¹⁵.

When an imaging approach is used geometrical effects such as non-uniform distribution of the excitation light and incident and emission angles need to be corrected for in the acquired fluorescence images. This has been done by forming a ratio of detected fluorescence and detected diffuse reflectance since both are affected by the same geometrical factors⁵⁰. Different approaches to this correction method have been used, either dividing the fluorescence by the diffuse reflectance at the excitation wavelength⁵¹, i.e. $F(\lambda)/R(\lambda_{exc})$, or by dividing the fluorescence by the diffuse reflectance at the corresponding wavelength⁵⁰, $F(\lambda)/R(\lambda)$.

3.7 Depth estimation through fluorescence measurements

In Papers I–II we investigated the depth-dependence of a ratio between the intensities at two fluorescence wavelengths, selected where tissue shows significant differences in optical properties. The fluorescence light at these two wavelengths will therefore be differently attenuated during the passage from the source of fluorescence to the surface. Other groups have also used fluorescence measurements in order to obtain depth information of an embedded object, Figure 3.9.

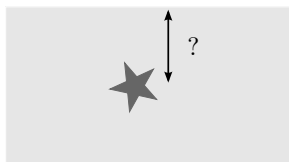


Figure 3.9. Determination of the depth of a fluorescent inclusion.

Stasic *et al.*⁵² performed spatially resolved fluorescence measurements, Figure 3.7, and simulations of a layered structure. The aim was to determine the depth of the boundary between an upper layer containing no fluorophore and a second bottom layer containing a fluorophore. This could for instance represent a skin treatment by light where an administered exogenous fluorophore photobleaches during treatment, i.e. increasing the depth of the

boundary. Accurate results were obtained to depths of the boundary of less than 3 mm, which may be sufficient for skin applications.

Another example of acquiring the depth of a fluorophore is the work presented by Eidsath *et al.*, with the aim to simulate the detection of lymphatic sentinel nodes in cancer patients. In this work experimental results from tissue phantoms were compared to a theoretical photon migration model based on random walk theory⁵³.

3.8 Clinical applications of fluorescence spectroscopy

Fluorescence spectroscopy is applied in several clinical applications for tissue diagnosis. In this section some interesting application areas will be discussed.

Delineation of skin tumors, for example basal cell carcinomas (BCCs), are well suited for fluorescence spectroscopy since the skin is easily reachable for fluorescence detection systems⁵⁴. Sometimes it can be difficult to visualize the borders of tumors with the naked eye, and in those cases fluorescence imaging can provide additional information⁵⁵⁻⁵⁷. Some of the imaging systems developed use fluorescence both from endogenous molecules and exogenously administered compounds to increase the sensitivity and/or specificity of the diagnostics. The fluorescence intensity is studied in two to three different wavelength bands, and the intensities at these wavelengths are compared to provide information on which pixels that correspond to healthy or diseased tissue. In Paper VIII fluorescence spectroscopy was utilized to study the demarcation of tumors with a new photosensitizer formulation in connection to PDT.

Another field where fluorescence imaging is used is in tumor detection in lungs and larynx, often referred to as light-induced fluorescence endoscopy (LIFE)⁵⁸⁻⁶⁰. To visualize these kinds of tissues, the imaging modality needs to be compatible with endoscopes used to reach the organs. There are commercial imaging systems available. Often only autofluorescence from the tissue is studied, but sometimes also a fluorescent tumor marker is used. These systems are important because they can detect and localize tumors in early stages. When working with vocal cords, for example, the delineation of tumors is crucial as the physician does not want to remove too much of the tissue, because that affects the voice of the patient in a negative way.

Fluorescence spectroscopy is also used for detection of cancer and precancers in the uterine cervix^{29;61;62}. An instrument, called Hyper-Spectral Diagnostic Imaging (HSDI®), developed by the company Science and Technology International (USA), has been used to detect early cervical malignancies. The instrument uses

excitation light at 365 nm and detects autofluorescence from the cervix in the range 420–760 nm⁶³.

Photodynamic therapy and pharmacokinetics of photosensitizers

Photodynamic therapy (PDT) is a light-induced modality for local treatment of tumors⁶⁴. This chapter will give an introduction to what parameters are important for PDT, especially factors concerning the administered photosensitizer. The pharmacokinetics of the photosensitizer Temoporfin have been investigated in Papers VI–VII. In Paper VIII the results from a clinical PDT study is presented. At the end of this chapter a possible concept of how to measure temperature during PDT is described, related to the work in Paper IX.

4.1 Photodynamic therapy

Three components are required to induce damage to the tumor cells with PDT: the presence of a photosensitizing drug and oxygen, as well as light of appropriate wavelength, see Figure 4.1. The photosensitizing drug can be administered to the patient in different ways. With systemic administration the drug is injected intravenously or intraperitoneally, but can also be given orally. Another administration route is topical application of the drug.

After the administration, the photosensitizer most often accumulates to a higher degree in tumor compared to normal tissue, leading to a selectivity of the drug in tumor tissue. This accumulation can take hours to days depending on the kind of photosensitizer used and the target tissue location.

The area, consisting of the tumor and its closest surroundings, is then illuminated with light that matches an absorption peak of the photosensitizer. Different light sources can be used, e.g. lasers and light-emitting diodes. Light penetrates through tissue and

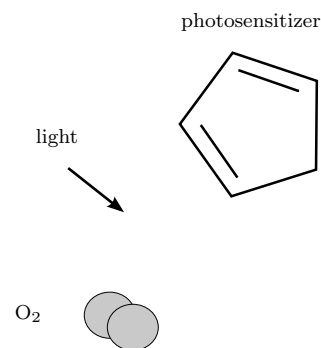


Figure 4.1. Three components are needed in PDT: photosensitizer, light and oxygen.

typically therapeutic light at 635 nm gives an adequate light dose down to 3 mm in skin⁶⁵. The photosensitizer molecules are excited by the light and in turn these molecules can transfer their excess energy to other molecules in their surrounding initiating chemical reactions. These reactions result in tumor cell death. The primary effects leading to cell damage can be divided into two mechanisms called Type I and Type II reactions, respectively, see Figure 4.2.

Type I reactions lead to an interaction between the excited photosensitizer and either a substrate, for instance a cell membrane, or a molecule in the tissue, leading to the formation of free radicals through hydrogen or electron transfer⁶⁶. In turn these radicals can react with oxygen and produce reactive oxygen species⁶⁶.

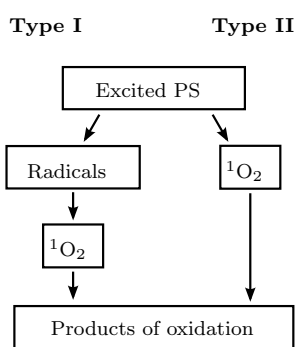


Figure 4.2. Type I and Type II reactions involved in PDT.

In Type II reactions, energy is transferred from the excited photosensitizer to an oxygen molecule, where oxygen is excited into a very reactive singlet state⁶⁷. After this interaction, the photosensitizer molecule returns to its ground state and can again be excited by the therapeutic light. Singlet oxygen can react with cellular components as e.g. proteins, nucleic acids, leading to the damage of function and structure of the cell. As the lifetime of singlet oxygen in tissue is very short⁶⁸, the diffusion path of these molecules becomes very limited. Therefore, the damage to the intracellular targets is close to where the photosensitizer was excited.

Photobleaching is the phenomenon in which the produced singlet oxygen and other reactive oxygen species react and oxidize the photosensitizer molecules. When this occurs, the number of photosensitizer molecules are reduced and the efficacy of PDT is diminished. The effect of photobleaching has been investigated for PDT after topical application of the precursor δ -aminolevulinic acid (ALA) in animal models^{69;70} as well as in patients⁷¹. These studies indicate a higher photobleaching rate when using a lower fluence rate of the treatment light, since it gives less depletion of oxygen. Monitoring of the photobleaching process during PDT has been performed in Paper VIII.

A favorable property of PDT is that the tumor treatment is local. The selectivity of the treatment is due to the irradiation being local, selectivity of drug accumulation and to cancer cells being more easily damaged compared to normal cells.

Other advantages with PDT is that the method is minimally or non-invasive, gives good cosmetic results⁷² and that the treatment can be repeated⁷³. Two treatment modalities, cryosurgery and PDT, were compared in the treatment of basal cell carcinomas (BCCs)⁷². The result showed that PDT had a shorter healing time and showed a better cosmetic result compared to cryosurgery. The treatment outcome were comparable for the two methods.

4.1.1 Tissue response to PDT

There are mainly three pathways for PDT to induce tumor cell death. One is the direct cell kill, the second is damage of the microvascular system supplying the tumor with blood and the third is activation of the anti-tumor immune system⁶⁴. It seems that all these PDT effects are of importance for complete tumor destruction.

The first pathway is the direct cell kill. Here, cell death can occur by either necrosis or apoptosis. Apoptosis is referred to as programmed cell death and can be induced by the PDT procedure. With other words, this means that the cell initiate its own death, where the nuclear DNA is destroyed and the cell shrinks without the involvement of the inflammatory system⁷⁴. However, it has been stated that malignant cells have an impaired ability to undergo apoptosis⁷⁴.

Depending on where in the cell the photosensitizer is localized, PDT will induce different kind of damages to the cell⁶⁴. Lipophilic sensitizers mostly accumulate in the membrane structure of both the cell and the cell organelles e.g. the mitochondria and endoplasmatic reticulum. Damage to the membrane occurs rapidly after the PDT treatment⁶⁴. Hydrophilic and aggregated sensitizers are usually taken up by endocytosis and pinocytosis in the cell, after which they localize within lysosomes and endosomes^{75;76}. During PDT the hydrophilic sensitizers will be released into the cytosol and from there the sensitizer can bind to tubulin. Photodamage of the microtubuli occurs, leading to cell death⁷⁵. Lipophilic sensitizers have a higher probability to induce cell damage, leading to the conclusion that membrane structures are more likely to be damaged by the PDT procedure⁶⁴, and therefore lipophilic sensitizers are considered as more potent photosensitizers.

The second pathway involves destruction of the vasculature system of the tumor. It is not only the tumor tissue that can be enriched by photosensitizer. If the drug is administered systemically, vascular endothelial cells can also accumulate the sensitizer, leading to damage of these cells. In turn, this can lead to cell death in the tissue volume supplied by the vessel as the oxygen delivery is then destroyed⁷⁷. At short time intervals after systemic administration of a drug most of the photosensitizer is located in the vascular endothelial cells and in tumor cells in close vicinity of the vessels. At longer time intervals more of the photosensitizer has been able to diffuse into the cells of the tumor⁷⁸. As mentioned earlier the diffusion path of singlet oxygen is very limited. Therefore, the initial tissue damage is induced where the photosensitizer is located. As the oxygen supply comes from the vasculature system, it would be possible to treat at earlier time points as both the oxygen and drug are located close to each other and in this way induce vascular destruction. By using this mechanism a more pro-

nounced PDT effect was achieved when the PDT procedure was performed at earlier times after drug delivery in an animal tumor model with the photosensitizer mTHPC⁷⁹.

A reduction of the amount of oxygen present in the tissue can affect the PDT outcome in a negative way. This reduction can be a result of both the destruction of the tumor microvasculature system as well as the oxygen consumption during the PDT process⁶⁴. By introducing fractionation of the light delivery, oxygen molecules can diffuse into the treatment area again^{80;81}. This has shown to prolong the delay in tumor growth in animal studies^{80;82}.

Finally, the third pathway that lead to tumor destruction is the immune response initiated by PDT. Often an inflammatory reaction occurs after the PDT procedure and results in an invasion of leukocytes into the irradiated area due to the immune system^{83;84}. Examples of leukocytes are neutrophils and macrophages. It has also been suggested that there is a long-term tumor control due to that a systemic anti-tumor response is induced after the local PDT treatment⁸⁴. This happens as some lymphocytes are activated through the release of tumor antigens after PDT, and these lymphocytes can then destroy remaining parts of the tumor and also prevent the build up of metastases.

4.1.2 Photosensitizers

There exist many different photosensitizers. The early developed sensitizers are usually referred to as first generation sensitizers. Among these, heamatoporphyrin derivative (HPD) and Photofrin can be mentioned. HPD consists of different porphyrins and has an absorption maximum at 630 nm, which is often used as the treatment light for PDT. Photofrin is a purified version of HPD and is one of the most commonly used sensitizers today. However, there are some problems with these first generation of sensitizers^{85;86}. They exhibit low extinction coefficients requiring use of large amounts of the sensitizer and they show a poor selectivity in tumor tissue. Systemic administration of these sensitizers gives also an unwanted photosensitivity in the skin lasting for several weeks.

To improve the photosensitizers a second generation of sensitizers was developed with more favorable properties. These sensitizers have a higher degree of purity, better tumor selectivity, higher extinction coefficients and a faster clearance^{86;87}. Preferable properties of photosensitizers used for PDT are given in Figure 4.3.

Example of groups belonging to this second generation of sensitizers are various porphyrin derivatives, phtalocyanines, naphtalocyanines and chlorins.

A commonly used PDT agent precursor is ALA⁸⁸. This compound exists naturally in the body, where it is a constituent in the first part of the heme synthesis pathway. After a few steps in the

Properties

Physico-chemical

large molar extinction coefficient
low tendency to aggregate

Photo-physical

high yield of 1O_2 generation

Pharmacological

selective targeting
fast clearance

Phototherapeutic

efficient killing of cells

Figure 4.3. Photosensitizer properties adopted from Jori⁸⁷.

heme pathway ALA is converted into the fluorescent compound Protoporphyrin IX (PpIX), which belongs to the porphyrin group. PpIX has been shown to be an efficient photosensitizer. The enzyme ferrochelatase converts PpIX into the final molecule heme. Different steps in the heme cycle takes place either in the mitochondria or in the cytosol of the cell. PpIX is formed in the mitochondria. The fluorescence intensity in normal and non-healthy skin increases with time until it reaches a plateau in the range of 4–14 hours for topical application, whereas maximum PpIX concentrations within skin after systemic administration is approximately after 3–8 h⁸⁹. The time used for topical ALA application is usually 3–8 hours⁸⁹, overlapping the plateau of PpIX concentration.

The sensitizers mTHPC (generic name Temoporfin) and Benzoporphyrin derivative (BPD) are examples of sensitizers within the chlorin family. mTHPC is one of the most potent sensitizers used for clinical PDT. One reason for this enhanced potency is the high extinction coefficient at the treatment wavelength. This enables the use of a lower drug concentration as well as a lower light dose compared to when using Photofrin⁹⁰. When PDT is performed at short drug-light intervals, mostly blood vessels and vascular endothelial cells are targeted with mTHPC. This induces preferably a vascular response to PDT^{79;91}, whereas at longer drug-light intervals a higher tumor-to-normal ratio of the sensitizer concentration is obtained. Pharmacokinetics studies of Temoporfin in a liposomal delivery system has been evaluated in Papers VI–VII. This Temoporfin formulation has also been used in a first clinical PDT study (Paper VIII).

4.1.3 Selectivity of photosensitizers

The reason for the tumor selectivity is not fully understood for all photosensitizers. The selectivity depends probably most on the difference in physiology between tumor and normal tissue. Factors that could influence the selectivity are for instance tumors having a leaky microvasculature system, poor lymphatic drainage, low pH, elevated amount of macrophages and an increased number of low-density protein receptors⁹².

There are a few additional factors that may lead to tumor selectivity of PpIX. One example is that the conversion of ALA into PpIX in the cells is dependent on the enzymatic activity. In all cells producing heme, there is a negative feedback control on ALA synthesis. When exogenous ALA is administered to the tissue this control is bypassed and the porphyrins are allowed to accumulate as the enzyme is not able to immediately convert all PpIX molecules into heme. Accumulation of PpIX in the tumor cells is also partly due to a decreased amount of the enzyme ferrochelatase, leading to lower conversion rate of PpIX into heme⁸⁸. Another reason for the build-up of PpIX in superficial skin tumors follow-

ing topical application of ALA is an increased penetration of ALA through the damaged epidermis above the tumor, compared to the non-damaged epidermis above normal tissue⁸⁸.

The intracellular localization of the sensitizers also affects the selective treatment response following PDT irradiation, as has been described in the Section 4.1.1. Lipophilic sensitizers mainly target membranes, whereas hydrophilic sensitizers rather localize in lysosomes and endosomes.

Liver, spleen, kidney and skin are tissue types that are rich in cells from the reticuloendothelial system, e.g. macrophages. Although these tissues are healthy, they tend to accumulate some sensitizers. This effect is contributed to the macrophages, as it has been shown that some photosensitizers accumulate to high levels in these macrophages. This has for instance been verified in a mouse model after injection of Photofrin⁹³.

The distribution of the sensitizer within tissue and also the effect of direct cell kill depends on the proximity of blood vessels to the tumor cells. The closer the cells are located to a blood vessel, the larger effect of direct cell kill⁹⁴. During prolonged topical application of ALA in a mouse model it has been demonstrated that ALA enters the circulation and a production of PpIX can be measured in remote untreated areas of the skin⁶⁹.

4.1.4 Clinical results

Commonly used photosensitizers in clinical practice are PpIX (with its precursor ALA or the methylated derivative of ALA, mALA) and mTHPC. The first PDT treatments of superficial BCCs and squamous cell carcinomas (SCCs) using topical application of ALA were performed in 1990⁹⁵. A complete response of 79% at a 3 months follow-up were reported when treating 300 patients with superficial BCCs with one single treatment⁹⁶. An extensive review on ALA-PDT in clinical applications has been published by Peng *et al.*⁸⁹.

Topical administration of mTHPC was first used in a clinical PDT study on Bowen's disease and BCCs in 1999⁹⁷. The application time was 24 hours and the complete response was only 32%, where an explanation to the low response could be the method of application. Not only superficial areas have been investigated with mTHPC. When using systemic administration of mTHPC the drug-light interval is approximately 2–4 days, where patients are restricted to limited light exposure. Lou *et al.* showed that mTHPC-PDT could be used as a salvage method for patients with recurrent head and neck cancers⁹⁸. A phase I clinical trial on pancreas using mTHPC has been reported⁹⁹, indicating that PDT could be an alternative for patients that cannot undergo surgery. In both these studies, optical fibers delivering the light had to be inserted into the volume to be treated.

4.2 Improvements of selectivity and delivery of photosensitizers

To create an efficient photosensitizer for PDT one alternative is to separate the photo-physical properties of the photosensitizer from the properties determining its distribution in tissue. This can be achieved by incorporating the photosensitizer into a vehicle, creating a photosensitizer drug delivery system. This provides the possibility to optimize the photo-physical properties of the drug and its biodistribution separately.

There are several reasons for creating these delivery systems. One is to enhance the penetration of the sensitizer following topical application, and another is to increase tumor selectivity. By increasing the penetration higher concentrations of the sensitizer is possible at positions far from the application site, while an increased tumor selectivity will result in better treatment discrimination. Many of the developed second generation photosensitizers are also lipophilic⁸⁶, with a high risk of aggregation in aqueous media. Therefore, it is necessary to incorporate these sensitizers within a delivery system, to be able to administer these drugs as efficiently as possible. An important aspect when creating a delivery system though is that the properties of the sensitizer should not be negatively altered as it is incorporated into the system.

The challenges to overcome with a delivery system are manifested by for instance a poor outcome of topical PDT of nodular BCCs. A limiting factor for topical PDT is mainly the penetration of the drug into the deeper regions of the lesion, rather than limitations in the light penetration.

Different methods for improving the biodistribution of the photosensitizer are the use of penetration enhancers, ALA derivatives, photosensitizers incorporated with liposomes, lipoproteins and antibodies. These are presented in more detail in the following subsections. Especially the case of incorporation the photosensitizer with liposomes is of interest as the Temoporfin formulation used in Papers VI–VIII consisted of a delivery system based on liposomes.

4.2.1 Penetration enhancers

Different alternatives to improve the penetration of the photosensitizers exist today. An example is the use of Dimethylsulphoxide (DMSO) together in a cream with ALA for topical application on skin with underlying tumors in mice¹⁰⁰. With the use of DMSO, the main result is to enhance ALA penetration through skin but also to increase the endogenous PpIX production. The PpIX production increased both in tumor and the overlying skin when using DMSO, with a slightly larger increase in skin.

In a study performed by Casas *et al.*¹⁰¹, different vehicles such as saline, cream, vaseline and liposomes were used for the delivery

of ALA into a murine subcutaneous adenocarcinoma model. When using saline as the vehicle, the best PpIX accumulation within the tumor was accomplished together with higher tumor selectivity. The addition of DMSO to the saline solution gave similar results in the penetration of ALA as a saline solution without DMSO. However, an improved PpIX production in the skin overlying the tumor and the upper part of the tumor was achieved when DMSO was added to the saline solution.

4.2.2 ALA derivatives

To enhance tissue penetration it has been suggested to use ALA derivatives instead of ALA. These derivatives are more lipophilic compared to ALA, which is a hydrophilic molecule. ALA has difficulties to penetrate through cell membranes, whereas for the derivatives it is easier due to their lipophilic nature. An example is the comparison of topically applied ALA and 5-aminolevulinic acid hexylester (h-ALA) for detection of PpIX fluorescence in bladder cancer patients¹⁰². The study showed a 2-fold increase in PpIX fluorescence using h-ALA compared to ALA even though a significantly lower concentration of h-ALA was used.

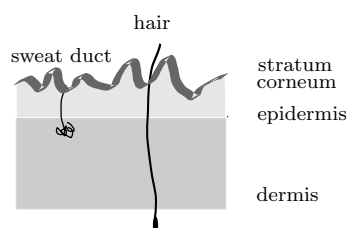


Figure 4.4. The structure of human skin.

Similar experiments have been performed in mouse skin models using topical administration of different ALA-esters. These results did not show, in contradiction to the case with the bladder, higher PpIX levels using the esters compared to free ALA^{103;104}. In these studies a possible explanation was the slower penetration of the esters through the stratum corneum as compared to the pure ALA compound. Stratum corneum is the top layer of the skin, see Figure 4.4, and consists mainly of fatty acids and cholesterol. If an ester is too lipophilic the molecules will be accumulated in this layer¹⁰⁵. This would prevent deeper drug penetration. Removing the stratum corneum by tape-stripping of the skin has been listed as an option.

It has been noted that ALA is more likely to enter the circulation compared to its esters following topical application. This could lead to a photosensitization in remote areas of the tissue¹⁰⁶. This in turn leads to a slower clearance of ALA than for its esters. Another issue to mention is that the esters need to be cleaved by specific enzymes, esterases, into ALA to be able to enter the heme cycle. The enhanced penetration of the ALA-esters does not automatically mean that there will be more PpIX, as these esterases act differently in different areas¹⁰⁵.

4.2.3 Liposomes

A liposome is a sphere with a lipid bilayer surrounding an aqueous interior, see Figure 4.5. An advantage with the liposomes is

that they can transport both lipophilic and hydrophilic sensitizers. Lipophilic sensitizers are incorporated in the lipid bilayer, whereas hydrophilic compounds are kept in the center of the liposome. Conventional liposomes usually consists of phospholipids like phosphatidylcholine¹⁰⁷. Cholesterol can also be a constituent to improve the rigidity of the membrane. This provides good biocompatibility as these substances naturally occur in the body⁸⁶.

Especially hydrophobic sensitizers tend to aggregate in aqueous media. Therefore, incorporation of the sensitizer within liposomes can have the positive effect to keep the sensitizer in its monomeric form, which has been shown for cell cultures *in vitro*¹⁰⁸. This has the advantage of improving the PDT effect as sensitizers are more efficient in a monomeric than in an aggregated form. Damoiseau *et al.* showed an increased oxygen consumption and decrease in cell survival with the use of the photosensitizer bacteriochlorin *a* incorporated into conventional liposomes¹⁰⁸.

Conventional liposomes have a rather short circulation lifetime, in the order of minutes, leading to low tumor uptake¹⁰⁷. Two main factors are responsible for this. First a lipid exchange between the liposomes and the lipoproteins leads to the release of the sensitizer in the blood, whereafter the sensitizer quickly attaches to the lipoproteins. The second factor is that conventional liposomes are easily recognized by the mononuclear phagocyte system, for instance by the macrophages, after opsonization of plasma proteins. Macrophages transport the liposomes to tissues with a rich mononuclear phagocyte system e.g. liver, spleen and lungs. To prolong the circulation lifetime of the liposomes and therefore potentially increasing the localization at the target site, an alternative is to add a specific compound to the liposome as illustrated in Figure 4.6. A hydrophilic polymer as for instance polyethylene glycol (PEG) can be used to prevent recognition by the macrophages¹⁰⁹.

Incorporation of photosensitizers within liposomes have been demonstrated in several studies. The use of a liposomal formulation of benzoporphyrin monoacid ring A (BPD-MA) showed a slight increase in delivery of the drug to the tumor site, and a more efficient PDT result was achieved compared to an aqueous solution of BPD¹¹⁰. Higher tumor-to-muscle and tumor-to-skin ratios were obtained with a liposomal delivery of the photosensitizer hypocrellin A¹¹¹. Liposomes have also been used to incorporate ALA, which has shown to give a better synthesis of porphyrin compared to free ALA¹¹². A tumor-to-skin ratio of porphyrin of 30 was obtained after 10 hours in the referred study.

4.2.4 Active targeting with lipoproteins and antibodies

Active targeting of substances to photosensitizer molecules is a way to increase tumor selectivity, where these substances can be

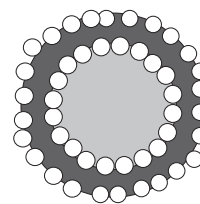


Figure 4.5. Liposome consisting of a lipid bilayer surrounding an aqueous core.

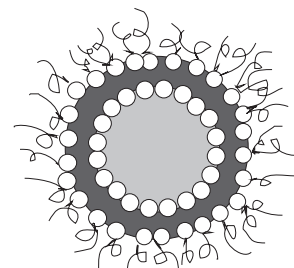


Figure 4.6. Liposome with PEG coating.

for instance a lipoprotein or an antibody. A molecule that has some kind of specificity or affinity to a marker on the tumor cells can be attached to the sensitizer. Sometimes in tumor cells there is an increased expression of specific antigens compared to normal cells. Antibodies against these antigens can be linked to the photosensitizer molecule and a targeted delivery system is created⁸⁶. Active targeting of liposome delivery systems has also been used in order to enhance the selectivity of the sensitizer to tumor tissue¹⁰⁷.

Low-density lipoproteins (LDL) transport and deposit lipophilic photosensitizers to cells with a high expression of LDL receptors¹¹³. Rapidly proliferating cells, as e.g. tumor cells, need a lot of cholesterol to build membranes. Cholesterol can be obtained via uptake of LDL via receptor pathway activity. This leads to that proliferating cells exhibit a large amount of LDL receptors⁸⁶. The use of lipoproteins as drug delivery vehicles leads to a selectivity of the photosensitizer in tumor cells. Lipophilic drugs can be incorporated in the lipophilic core of the lipoprotein without changing the sensitizers physical and biological properties. Another advantage with lipoprotein incorporation is that lipoproteins naturally exists in the blood. The macrophages will therefore not recognize the sensitizer-lipoprotein complex, leading to a longer circulation time. Confirming this, it has been reported of an increased selectivity and cell kill after PDT with BPD-MA incorporated with LDL as compared to the free formulation¹¹⁴.

4.3 Quantification of photosensitizer concentration

Several techniques are available to study the pharmacokinetics of photosensitizers. Optical spectroscopy directly on the tissue of interest is one of the interesting techniques as it can allow *in vivo* assessment of the concentration. As most photosensitizers exhibit fluorescence properties, fluorescence spectroscopy is a promising alternative. This method usually monitors the superficial quantity of the sensitizer. Absorption spectroscopy is another option to determine the concentration of a sensitizer. Today, chemical extraction of excised tissue is considered as gold standard for concentration measurements. These three methods were used in Papers VI–VII for pharmacokinetic studies and will be described in the following subsections.

4.3.1 Fluorescence studies

Fluorescence spectroscopy is a useful tool in the study of photosensitizer accumulation. The technique as well as different instruments for fluorescence diagnostics have been described in Chapter 3, and will therefore not be repeated in this section.

Fluorescence spectroscopy is a more sensitive method for determining the amount of photosensitizer within a sample compared to absorption spectroscopy. This is due to the fact that in fluorescence the signal is detected on a relatively weak background signal. The background signal is weak as the detected fluorescence signal is spectrally separated from the strong excitation light. This is not the case in absorption measurements. A disadvantage with fluorescence spectroscopy is that the emitted fluorescence signal may be sensitive to the chemical environment of the photosensitizer e.g. resulting in changes in intensity and spectral shifts.

Photosensitizers that are in an aggregated form usually are non-fluorescent and are also less likely to be involved in the PDT procedure. Absorption spectroscopy may wrongly include these aggregated forms⁶⁸.

4.3.2 Absorption spectroscopy

Absorption spectroscopy has the potential to measure the concentration of a photosensitizer by studying the absorption after white-light illumination of tissue. If there is a photosensitizer in the tissue, there will be an imprint in the acquired absorption spectrum at the wavelengths where the sensitizer exhibits absorption peaks. In Figure 4.7 differences in transmission spectra from normal and tumor tissue can be seen. The dip at 650 nm corresponds to absorption due to mTHPC, reflecting a higher sensitizer concentration within tumor tissue as compared to normal tissue.

Absorption spectroscopy has been used to determine sensitizer concentration in prostate tissue using the sensitizer Motexafin lutetium (MLu)¹¹⁵. With absorption spectroscopy it is not only the sensitizer concentration that can be determined, but also the concentration of other compounds in the tissue, e.g. hemoglobin. Absorption spectroscopy of chemotherapy drugs has been performed in an *in vivo* animal model²³. An instrument similar to the one in the mentioned study, was used in Paper VI for determination of mTHPC concentration in tissue.

To be able to determine the sensitizer concentration correctly it is preferable that the sensitizer does not absorb in the same wavelength bands as hemoglobin and water. The evaluation becomes much more difficult in such cases.

As has been noted in Paper VI, where absorption spectroscopy was performed in an animal tumor model to study the pharmacokinetics of a novel liposomal formulation of Temoporfin, it is necessary to take into account the effect of fluorescence in the evaluation of the absorption spectrum. If the sensitizer is a strongly fluorescing compound this is of importance in the evaluation of the absorption.

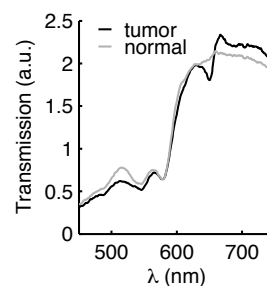


Figure 4.7. Transmission spectra of a sensitizer acquired from normal and tumor tissue.

4.3.3 Chemical extraction

In assessment of the concentration of a substance in tissue by chemical extraction, the sample needs to be minced and dissolved in some liquid. High performance liquid chromatography (HPLC) can then be used to separate the compounds that exist in the solution. The separation of compounds can be achieved by different means, e.g. they can be separated due to their size or charge. Determination of the concentration can be accomplished with fluorescence or absorption measurements.

4.4 Interstitial photodynamic therapy and temperature monitoring

One limitation with superficial PDT illumination is that it provides good results only for superficial and thin tumors, due to both the limited light penetration and the limited drug penetration when applied topically. A way to treat deeper-lying and thicker tumors is to insert optical fibers into the tumor mass and deliver the treatment light through these fibers. This extension of PDT is called interstitial photodynamic therapy (IPDT). The concept is illustrated in Figure 4.8. The IPDT system described by Soto Thompson *et al.*¹¹⁶ has been used for the temperature measurements in Paper IX.

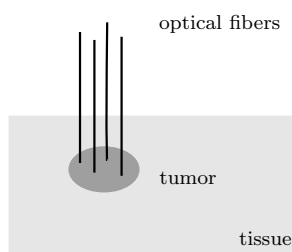


Figure 4.8. The concept of IPDT, where optical fibers are inserted into the tumor.

During PDT with high light flux the tissue temperature may rise due to absorption of light. Tissue temperature during photoradiation depends on several factors such as the tissue optical properties, thermal conductivity and the blood vasculature system¹¹⁷. It is also known that the scattering coefficient is increased for temperatures high enough to cause protein coagulation^{118;119}. The absorption coefficient behaves more ambivalently, where both an increase and decrease with temperature have been reported^{118;119}. These alterations result in a decrease in optical penetration depth when higher temperatures are reached. This change in optical properties and penetration depth occurs mainly between 50–65°C. Above 65°C no significant changes are seen¹¹⁸.

When delivering light during a photodynamic treatment session tissue may be heated to such a degree as to cause thermal damage. It may thus be of importance to monitor the temperature during the treatment to understand whether the damage is of photodynamic or thermal character. An abrupt temperature increase during an IPDT session could for instance be an indication of a bleeding in the proximity of the tip of the fiber used in the treatment, resulting in a decreased light penetration and treatment efficiency. By monitoring the temperature a bleeding can be detected providing a possibility to rearrange the fiber.

Another application where temperature control could be of interest is when PDT of tumors is performed in combination with

hyperthermia. Temperatures in the range of about 41–47°C defines hyperthermia¹²⁰. Tumor tissue seems to be slightly more sensitive to heat compared to healthy tissue in the range 42–44°C. The combination of PDT and hyperthermia has shown to improve the treatment outcome^{121;122}. During the treatment the temperature in the tumor is raised to 43–44°C. Hyperthermia can be applied simultaneously or directly after the PDT treatment. The temperature needs to be monitored during the entire treatment to ensure that and to what extent hyperthermia is present.

There are different techniques to measure the temperature in tissue. Small temperature devices that can be inserted into tissue during treatments are e.g. thermistors¹²⁰ and thermocouples. If a larger area is to be monitored an infrared camera is a better alternative. The use of an infrared camera has been used to study the temperature during superficial PDT on skin¹²³. Alternatively, crystals, doped with some specific ions that emit temperature dependent fluorescence, can be used to measure the temperature optically. Crystals doped with rare-earth ions are commonly used for temperature measurements¹²⁴.

4.4.1 Doped crystals

The optical technique to measure temperature, used in Paper IX, is based on the method where the fluorescence from crystals doped with Cr³⁺-ions shows a temperature behavior. Examples of such crystals are Alexandrite, Cr:YAG, Ruby and Cr:LiSAF. All these crystals have different temperature sensitivity in different temperature regions, and therefore it is important to choose the right crystal for each application¹²⁵.

Cr³⁺-doped crystals are a good choice in the case of monitoring temperature during IPDT, because the Cr³⁺-doped crystals can be excited at 635 nm. This particular wavelength is used for the treatment light during IPDT treatments when PpIX is used as a photosensitizer. The temperature can be measured in a spot where the fluence is high if a small piece of the crystal is attached to the fiber tip where the treatment light is delivered, see Figure 4.9. No other objects than the IPDT treatment fibers have to be inserted into the tissue. Another benefit is that the temperature is measured directly at the fiber tip, compared to a thermistor that would measure the temperature at a small distance from the region with the highest light fluence.

4.4.2 Temperature measurements with doped crystals

A way to determine the temperature of the crystal is to measure the intensity of the emitted fluorescence after excitation¹²⁵. According to the Boltzmann's distribution, the number of atoms in a

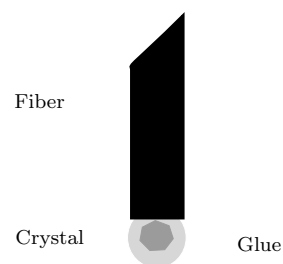


Figure 4.9. A fiber with a small piece of crystal glued to the tip of the fiber.

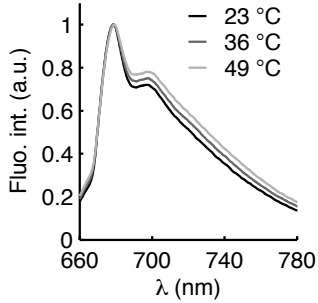


Figure 4.10. The fluorescence spectrum changes when the temperature increases.

specific electronic state is dependent on the temperature and the energy difference between two electronic states. At room temperature most atoms are in the ground state, but as the temperature increases more atoms will populate higher states.

As the temperature in the tissue changes, the shape of the fluorescence emitted from the crystal is affected, see Figure 4.10. Fluorescence spectra are shown for three different temperatures measured through a fiber with a Cr^{3+} -doped Alexandrite crystal attached to the tip. The fiber was placed in Intralipid that was slowly heated. The temperature in the Intralipid was determined by a thermistor in close contact to the fiber with the attached crystal.

A ratio can be calculated by dividing the intensities measured in two different wavelength regions, where the temperature has influenced the emitted fluorescence. The ratio, γ , is then calculated for several temperatures using Eq. 4.1 to build a calibration curve.

$$\gamma(\text{temperature}) = \frac{I(\lambda_1)}{I(\lambda_2)} , \quad (4.1)$$

where $I(\lambda_1)$ and $I(\lambda_2)$ are the fluorescence intensities in the two wavelength bands, respectively. In the data presented in Paper IX these wavelength intervals were 675–683 and 698–706 nm, respectively.

Each fiber with an attached crystal needs to be treated individually and is required to be calibrated once. An advantage of using fluorescence intensity measurements is that the instrumentation is relatively simple, in principle only consisting of a light source and a spectrometer. One disadvantage is that background fluorescence from other fluorophores in the tissue, such as the sensitizer itself, can influence the temperature measurements, if it is emitted in the same wavelength region as the fluorescence from the crystal.

Another alternative is to measure the fluorescence lifetime of the crystal¹²⁶, in this case the light source used to induce fluorescence needs to be modulated. One option is to use a sinusoidally modulated light source as illustrated in Figure 4.11. The emitted fluorescence light will also be modulated, but lagging the excitation light, and thereby introducing a phase-shift. The fluorescence lifetime is calculated with Eq. 4.2.

$$\tan \varphi = \tau \omega , \quad (4.2)$$

where φ is the measured phase difference between the laser source and the induced fluorescence light, ω is the angular frequency of the modulated signal and τ is the fluorescence lifetime¹²⁵. The fluorescence lifetime is calculated for several temperatures and a calibration curve can be constructed. The limitation when measuring the fluorescence lifetime is the need for more complicated

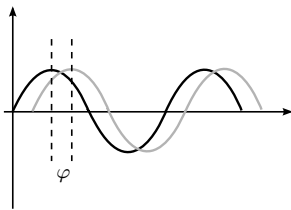


Figure 4.11. Modulated light source for lifetime measurements of the induced fluorescence. A phase shift, φ , appears between the incoming light (black) and the fluorescence light (gray).

instrumentation, but has the advantage that the temperature dependence is more robust due to a decreased sensitivity to background signals, for example room light, that interfere with the measurements. The lifetime of the autofluorescence is in the order of ns, while the fluorescence lifetime of the doped crystals are in the range of μs –ms. The difference in lifetime will prevent autofluorescence from disturbing the measurements of the fluorescence lifetimes of the crystal.

Molecular imaging

Molecular imaging is a multidisciplinary field that visualizes and quantifies biological processes at cellular and subcellular levels *in vivo*¹²⁷. The goal with molecular imaging is to be able to monitor specific molecules and cellular processes *in vivo* that provide information about biological phenomena in the cells. The idea with molecular imaging is not primarily to resolve the molecules or cells of interest. The aim is instead often to detect the signals from the marked molecules *in vivo* in the scope of cells to whole animals with the techniques used in molecular imaging together with probes acting as contrast agents, see Figure 5.1.

There exist various applications where molecular imaging provides important tools in the research of diseases. In the case of cancer diagnostics molecular imaging can be used for detection and treatment of malignant tumors in an early stage. The spreading of metastatic lesions can also be monitored. Molecular imaging can furthermore be applied in the study of neurodegenerative¹²⁸ and auto-immune diseases¹²⁹. Nuclear and optical imaging techniques have been used in the case of rheumatoid arthritis diagnosis by monitoring inflammatory cells¹²⁹. Visualization of the treatment response in the joints affected by rheumatoid arthritis has also been demonstrated.

Molecular imaging provides the possibility to perform long-term studies of animals *in vivo* without the need to sacrifice the animals. This could e.g. be utilized when studying treatment responses and in drug development, where the effect the drug has on the cells could be monitored¹³⁰.

Specific probes that only emit signals when attached to the molecules of interest in the cells, are highly desirable when monitoring cellular processes. An important task in the development of powerful molecular imaging techniques is the development of such probes. Probes used in fluorescence measurements can be more

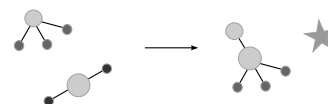


Figure 5.1. Molecular interaction resulting in a detectable signal.

or less complicated, ranging from common fluorophores, that fluoresce wherever and whenever excitation light is present, to fluorescent proteins that can be produced by gene-manipulated cells and to the newest developed probes based on quantum dots. Probes emitting fluorescence in the red or NIR region are favorable. The signal originating from the fluorophore is easier to detect because the tissue autofluorescence is rather weak in this wavelength region and light with longer wavelengths penetrate deeper into the tissue. Techniques to detect the emitted signal from the probes in combination with evaluation algorithms can be used in order to find the spatial location, i.e. the concentration distribution, of fluorescence-marked lesions inside tissue. A long term goal is to adopt molecular imaging techniques into a clinical environment to image human diseases.

This chapter is mainly devoted to the use of optical techniques in molecular imaging, but other techniques as well as the description of molecular probes are also presented in this chapter as an introduction to the field of molecular imaging. The fluorescence intensity ratio, showing a depth dependence due to differences in tissue optical properties, evaluated in Papers I–III, has been suggested to be used as additional information in fluorescence tomography reconstruction in Paper IV. This could in future studies be used within molecular imaging for detection of signals from e.g. fluorescent proteins in order to study diseases.

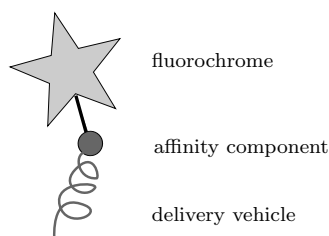


Figure 5.2. Parts of a fluorescent molecular probe.

5.1 Optical activatable probes

As mentioned in the introduction, a molecular probe is necessary in the cell or animal that is about to be imaged. Desirable properties of these molecular probes are that the probe is very specific in its uptake and has a preferentially high biodistribution to the target. These probes often consist of three different parts, see Figure 5.2. First there is an affinity component that interacts with the target, which can be a cell, protein or some other molecule. The second component is often a fluorochrome that emits a detectable signal. A delivery vehicle can also be used to get a more favorable biodistribution. The different molecular probes can be divided into three categories: non-specific, specific and activatable probes^{127;131;132}. However, the toxicity of molecular probes needs to be studied in more detail before they could possibly be used for human applications.

5.1.1 Non-specific probes

Non-specific probes do not have a specific target and can therefore not be used to study molecular or cellular processes¹²⁷. These non-specific probes are instead used in the study of physiological processes, like changes in blood flow and blood perfusion as

illustrated in Figure 5.3. Fluorochromes that are good to use in fluorescence studies are Fluorescein and Cyanine dyes, because they have a high extinction coefficient and absorb and fluoresce in the range from visible to the NIR region. One example of a non-specific probe approved for clinical use is the fluorochrome indocyanine green, which emits in the NIR region.

5.1.2 Specific probes

The Cyanine dyes can be made more specific to attach to certain targets in the cells. A specific probe consists of an affinity ligand, which can be an antibody or another substrate that can interact with specific parts inside the cell or attach to specific cells, see Figure 5.4. This interaction allows specific biological structures to be imaged¹³¹. One disadvantage with the specific probes is that the probes fluoresce even though they have not reached their target. This makes it more difficult to detect the probes that are actually attached to their targets, due to a low signal-to-background ratio. With a high binding affinity one can, however, wait until most of the non-bound fluorescing molecules have been cleared from the circulation¹³².

5.1.3 Activatable probes

The activatable probes are also called smart probes or beacons. The great advantage with these smart probes is that a signal is not emitted until the probe finds and is attached to its target, see Figure 5.5. The smart probe often consists of one fluorophore and one quencher at each end of a single DNA strand. As the probe has not found its target, the DNA strand is formed like a hairpin, which means that the fluorophore and the quencher are very close to each other. The quencher prohibits the fluorophore to fluoresce. When the probe reaches its target, e.g. a specific enzyme will unfold the DNA strand. The quencher and the fluorophore are then separated, and the fluorophore emits light that can be detected^{127;131}. Smart probes have been developed to fluoresce in the NIR region, which is favorable¹³³.

5.1.4 Fluorescent proteins

Fluorescent proteins is a special class of fluorescent probes. They are produced by gene-manipulated cells. The gene coding for a fluorescent protein can be linked to the genes of the proteins of interest. When the proteins of interest are expressed they are automatically fluorescent.

A commonly used fluorescent protein is the green fluorescent protein (GFP)^{131;134}. GFP has been found naturally in different species, for example the jelly fish *Aequorea victoria*. The name



Figure 5.3. The concept of a non-specific probe that can be used to study changes in blood flow. The probe fluoresces inside a blood vessel.

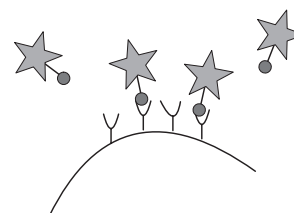


Figure 5.4. Specific molecular probes that target special cells.

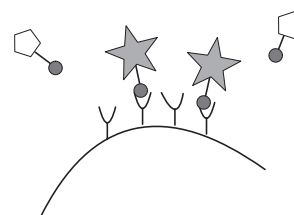


Figure 5.5. A smart molecular probe only emits fluorescence when it finds and is attached to its target.

Protein	Emission (nm)
mCitrine	529
mOrange	562
mStrawberry	596
mCherry	610
mPlum	649

Figure 5.6. List of red-shifted fluorescent proteins, where “m” stands for monomer.

GFP comes from the fluorescence emitted by the fluorescent protein being green. Whole-body imaging of mice has been performed to study GFP-expressing tumor cells, both how the tumor is growing and how the metastases are spread in several organs¹³⁵.

Other varieties of fluorescent proteins have been found or modified from GFP to change the spectral region of the fluorescent proteins. There are many different varieties, where cyan-shifted proteins (CFPs) and yellow-shifted proteins (YFPs) could be mentioned. A red-shifted fluorescent protein called DsRed has been isolated from corals. Most of the fluorescent proteins emit in the visible wavelength region, providing a low penetration depth of light and a strong influence of tissue autofluorescence. A list of available modified fluorescent proteins¹³⁶ emitting in the red are given in Figure 5.6. It is also possible to use multiple fluorescent proteins for labelling and imaging of different targets.

5.1.5 Quantum dots

Another interesting group of fluorescent probes used for molecular imaging is quantum dots^{137;138}. Quantum dots are semiconductor crystals with sizes of a few nanometers. The size of the quantum dots can be varied as the size affects the absorption and emission properties. Today the existing dots fluoresce from the visible region to the NIR region. There are some advantages with the quantum dots compared to other fluorescent probes. They often have a broad absorption spectrum, but the emission is in a narrow wavelength region. This is a very attractive feature when studying multiple quantum dots with separated emission bands, as the same excitation source can be used throughout the measurements¹³⁹. Another advantage is that the dot is rather photostable, making it possible to use it to study processes during a longer time period. They are also very bright and can be tagged to target molecules.

5.2 Molecular imaging techniques

Today there are several different imaging techniques used within the field of molecular imaging. A number of utilized techniques are positron emission tomography (PET), single photon emission computed tomography (SPECT), computed tomography (CT), magnetic resonance imaging (MRI) and different optical imaging techniques^{127;140}. Optical imaging methods will be discussed in Section 5.3.

PET is a technique where biological molecules have been marked with isotopes, e.g. ¹⁵O and ¹⁸F, that emit positrons as they decay. Subsequently a positron and an electron collide and two γ -rays at 511 keV are emitted in opposite directions and can then be detected at the same time. By studying the intersection of

the lines produced by the γ -rays in a detector utilizing specific algorithms, the location of the γ -ray emission can be reconstructed. SPECT is also a technique where γ -rays are detected with a rotating gamma camera in multiple directions. The radionuclides used are for example ^{123}I and ^{99m}Tc , each emitting one γ -ray.

In CT detection of transmitted X-rays from a narrow beam can be used to image a thin cross-section of a body. The X-ray source and detector are rotated around the specimen to detect X-rays in several projections to reconstruct the 3D internal structure of the tissue. An imaging contrast agent can be administered to be able to detect tumors, as soft tissue can be difficult to study with CT.

MRI is an imaging technique that provides images with different contrast for various tissue types, due to different environments of protons in the tissue. Protons, which are the nuclei in hydrogen atoms, normally have random nuclear spin orientations. In the presence of a strong magnetic field, the protons become aligned to the magnetic field. A radio signal flips the nuclear spins and they emit signals when they reorient parallel to the field. These signals are picked up by sensitive detectors. The difference in magnetic shielding of protons in various molecules permits reconstruction of an image of the tissue types present. It is also possible to image the relaxation time instead of imaging the amount of protons in the tissue, as the relaxation time can be different in tumors and normal tissue.

Advantages and disadvantages with these mentioned techniques as well as optical methods are given in Figure 5.7.

5.3 Optical imaging techniques

Optical imaging techniques are based on the detection of light and are more related to the work presented in this thesis. Examples of optical techniques are: bioluminescence imaging, planar fluorescence imaging, optical tomography, fluorescence mediated tomography and fluorescence lifetime imaging. Tomography will be discussed in Section 5.4.

5.3.1 Bioluminescence imaging

Bioluminescence is a phenomenon where light is emitted from certain species, for example fire-flies and certain bacteria^{140;141}. The light can be emitted as a communication or as an attraction to other species. Luciferin is the name of light emitting pigments that are found in the above mentioned species. When luciferin is oxidized by a certain enzyme, a luciferase, photons are emitted. The emission of light occurs when the reaction takes place and no external excitation light source is needed. The components in the process is illustrated in Figure 5.8. The terms luciferin and

Imaging techniques

PET/SPECT

- + high sensitivity for probe detection
- low resolution
- radioactivity

CT

- + high resolution
- ionizing radiation

MRI

- + high resolution
- + functional and anatomical imaging
- slow, high cost

Optical/Fluorescence

- + high sensitivity for probe detection
- + fast, low cost
- low resolution

Figure 5.7. Table of pros and cons with molecular imaging techniques.

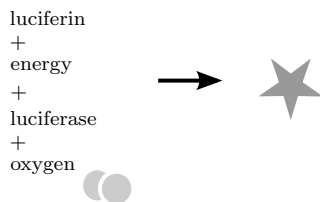


Figure 5.8. Bioluminescence process.

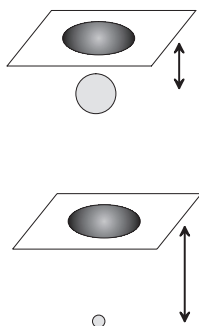


Figure 5.9. The detected fluorescence signal is similar for a larger object placed more shallow and a small deep-lying object.

luciferase are not the names of specific molecules, instead they refer to a substrate and its associated enzyme, which catalyzes the bioluminescence process. Genes that express a luciferase can be inserted into tumor cells in organisms. When a luciferin is present light will be emitted if luciferase has been expressed and the chemical reaction has taken place. Bioluminescence has been used to study tumor cell growth. The emitted light is often blue-green, allowing imaging of only superficial tissue. The advantage with bioluminescence is that there is no background tissue fluorescence that can disturb the studied weak signal.

5.3.2 Planar fluorescence imaging

With a planar fluorescence imaging technique the emitted fluorescence from an object is usually detected with a sensitive CCD camera¹⁴². Both reflection and transmission geometries can be employed, but the reflection geometry is most commonly used because the thickness and the optical properties of the sample influence the amount of transmitted light. However, in a reflection geometry the measurements are more sensitive to tissue autofluorescence¹⁴³. This technique usually becomes rather limited when fluorescence from deeper structures are to be measured as the fluorescence is non-linearly dependent on e.g. depth and optical properties. Therefore, these measurements are often restricted to superficially located structures. The measured signal is more difficult to interpret as the emitted fluorescence from a small deep-lying object and a larger more shallow object will appear similar on the tissue surface, see Figure 5.9. This is due to the scattering properties in tissue.

5.3.3 Fluorescence lifetime imaging

Another fluorescence technique is to image the fluorescence lifetime of a fluorophore inside an object¹⁴⁴. The fluorescence lifetime of a fluorophore is dependent on the micro-environment and changes in lifetime can be due to differences in chemical interactions due to the binding site of the fluorophore, fluorescence resonance energy transfer (FRET) or pH¹⁴⁵. Also blood flow and temperature can influence the lifetime. Therefore, it may be possible to study the functional status of for example a tumor. Fluorescence lifetime imaging has been performed *in vivo* in mice and the results showed a small difference in lifetime of NIR-fluorochromes located in tumor and liver, separating the two tissue environments¹⁴⁶.

5.4 Optical tomography

Optical tomography is a non-linear reconstruction method to image objects inside tissue from optical measurements in several pro-

jections. The goal is to reconstruct the distribution of absorption and scattering properties in tissue. The light intensity detected in the different projections depends non-linearly on the optical properties of the tissue and the distance travelled by the light to the detection site.

Reconstruction of objects, obtained with optical tomography, is a more difficult problem compared to X-ray methods like CT. X-rays follow a straight line through the sample, and the attenuation due to absorption is measured in several projections. Light of optical frequencies is not only absorbed but also scattered in the tissue, meaning that each projection probes almost the entire volume.

When studying diffuse light the term diffuse optical tomography (DOT) is often used. DOT has been used to reconstruct images of the oxygenation and blood volume in neonatal brains¹⁴⁷ and in optical mammography to find lesions inside breast tissue¹⁴⁸.

Figure 5.10 shows a schematic diagram of how a reconstruction algorithm in optical tomography can be implemented. The reconstruction is started with an initial guess of the sought optical properties inside the tissue. With the use of a forward model the light distribution is modelled inside the tissue and the detector readings for the projections are predicted. These predicted values and the values obtained from the real measurements are compared. If there is no match, the optical properties of tissue are updated with some optimization algorithm, which often involves trying to calculate the derivative of the simulated values when small changes in the optical properties are applied. The inverse problem is to find the optimal choice of the changes in optical properties. The procedure is repeated until the difference between the predicted and measured values is sufficiently small, then the reconstruction of the tissue has been accomplished¹⁴⁹. A more detailed description about the forward problem and the reconstruction is given below.

Forward problem

The diffusion approximation is often used to model light transport in tissue in the forward problem. This approximation is valid for most tissues where $\mu'_s \gg \mu_a$. To solve the diffusion approximation mainly two techniques are utilized^{150;151}. Green's functions are analytical solutions to the diffusion approximation in an infinite medium. This strategy is straight forward for very simple geometries. However, if more complex geometries with inhomogeneous distribution of optical properties are to be modelled, the finite element method (FEM) can be used.

In highly absorbing tissue, e.g. in liver, and when the source-detector separation is small the diffusion approximation breaks down and another forward model is required. This is also the case when there are non-diffusive regions, for example the cerebrospinal

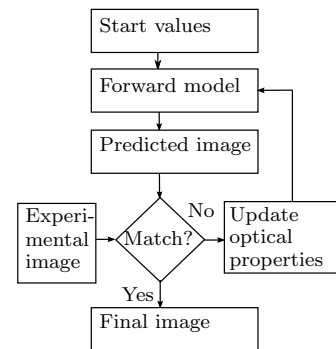


Figure 5.10. Flow-chart showing the algorithm used to solve the non-linear inverse problem in optical tomography.

fluid, inside the medium to be reconstructed. Then the radiative transport equation (RTE) can be used to model the light propagation¹⁵².

Parameter reconstruction

The forward problem gives $y = f(x)$, where x is a vector of the parameters to be reconstructed for instance the optical properties at all voxels in the studied volume, f represents the forward model and y is a vector containing the output from the forward model representing the measurements. To reconstruct the parameters it is necessary to solve the inverse problem, $x = f^{-1}(y)$. If $f(x)$ is a linear function with respect to x , the forward problem can be rewritten as the vector equation $y = \mathbf{F} \cdot x$. Usually the number of unknowns far exceeds the number of measurements, which makes the equation system highly underdetermined. To obtain the parameter x the matrix \mathbf{F} is inverted using some sort of matrix pseudo-inversion technique.

If the forward model is non-linear with respect to the parameters, then other approaches are considered in the reconstruction. Sometimes it is possible to perform a linearization^{150;151}, if the actual parameters x are close to the initial guess x_0 and the measurements y are close to the measurements given by the forward model y_0 . If $y = f(x)$ is expanded in a Taylor series and only the two first terms are kept, a linear relation given by Eq. 5.1 is obtained, where \mathbf{J} is the Jacobian. This kind of linearization is called the Born approximation. An example of the Born approximation in the one-dimensional case is illustrated in Figure 5.11.

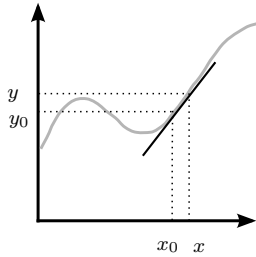


Figure 5.11. Example of a Born approximation in 1D.

$$y - y_0 = \mathbf{J} \cdot (x - x_0) . \quad (5.1)$$

To obtain the change in the parameters, $x - x_0$, \mathbf{J} needs to be inverted. Inversion of the often underdetermined system matrices \mathbf{F} and \mathbf{J} can be performed with standard inversion methods like algebraic reconstruction techniques (ART) and singular value decomposition (SVD)^{150;151}.

If a linearization of the forward problem is not a good enough approximation, then a full non-linear problem must be solved. This is achieved by forming an objective function χ , which captures the errors of the forward model¹⁵¹:

$$\chi = (y_{measured} - f(x))^2 . \quad (5.2)$$

The x that minimizes the objective function is the wanted solution. The minimization can be performed with standard least-squares methods, e.g. Newton-like methods as the Levenberg-Marquardt algorithm.

Since the problem is ill-conditioned and there always will be noise in the measurements the inverse often needs to be stabilized.

This is called regularization¹⁵¹, and the objective function can then be written in the form:

$$\chi = (y_{measured} - f(x))^2 - \alpha B^2, \quad (5.3)$$

where α is a regularization weight and B represents the difference between the intermediate solution x and some prior information. When the term $(y_{measured} - f(x))^2$ is close to zero the additional penalty term, αB^2 , may become significant, forcing the optimization towards a solution more like the prior information and thus reducing the penalty term. How this prior information can be determined is discussed later on in Section 5.5.

Optical tomography techniques

Optical tomography imaging can be performed with three different concepts¹⁴⁹. In the first concept, measurements can be performed in the time-domain using the idea of time-of-flight measurements following the launch of a short pulse (ps) into the tissue. The pulse is broadened as it propagates through tissue because of multiple scattering, yielding different paths of the photons. The form of the recorded time-of-flight curve will reflect the optical properties of the medium. The second method to be mentioned is based on the frequency domain, where sinusoidally amplitude-modulated light is used. The detected light has been phase-shifted and demodulated, which can provide corresponding information about the optical properties. The third method involves a continuous wave light source and measurements of the attenuated light at several source-detector distances.

A light source at a specific wavelength is used to illuminate the object in several projections as illustrated in Figure 5.12. The propagated diffusive light is detected around the boundary of the specimen. The choice of wavelength is determined due to what parameters are to be reconstructed. Usually only one wavelength is used to provide a spatial map of the estimated optical properties within the volume examined. When using two or more wavelengths, the properties can be reconstructed at all the measured wavelengths. The concentration of the two hemoglobin constituents in tissue can be estimated with the use of two wavelengths as the reconstructed absorption is proportional to the concentration. This can also provide an estimate of the blood saturation in tissue.

5.4.1 Fluorescence mediated tomography

It is not only differences in optical properties that are utilized in the reconstruction in optical tomography, also the distribution of fluorophores, used as contrast agents inside tissue, can be reconstructed. In fluorescence mediated tomography (FMT) usually

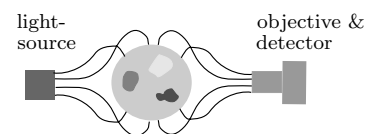


Figure 5.12. Optical tomography set-up.

two measurements are performed, one with the detection of the transmitted excitation light, and one measurement where the fluorescence light is detected. For the reconstruction there is a need to model both the transport of the excitation light from the light source to the fluorophore inside tissue, as well as the transport of the induced fluorescence light from the fluorophore to the detector.

Both the diffusion approximation^{153;154} and the RTE¹⁵⁵ has been used as forward models in FMT. By using the diffusion approximation, and assuming a simple geometry and a homogeneous medium, the light transport can be analytically modelled by Green's functions. The fluence rate at the excitation wavelength, $U_x(\bar{\mathbf{r}}_s, \bar{\mathbf{r}})$, reaching an arbitrary point $\bar{\mathbf{r}}$ within the volume from a point light source positioned at $\bar{\mathbf{r}}_s$ is given by

$$U_x(\bar{\mathbf{r}}_s, \bar{\mathbf{r}}) \sim \frac{1}{D_x} \cdot G_x(\bar{\mathbf{r}}_s, \bar{\mathbf{r}}) , \quad (5.4)$$

where D_x is the diffusion coefficient in the medium for the excitation wavelength and $G_x(\bar{\mathbf{r}}_s, \bar{\mathbf{r}})$ is the Green's function of the diffusion equation. The created fluorescence fluence rate is given by $U_x n(\bar{\mathbf{r}})$, where $n(\bar{\mathbf{r}})$ is the product of the quantum yield of the fluorophore, γ , and the absorption due to the fluorophore, μ_a^{flu} .

The fluorescence irradiance at the detector located at $\bar{\mathbf{r}}_d$, created in a point $\bar{\mathbf{r}}$ due to an excitation light source in $\bar{\mathbf{r}}_s$ is given by Eq. 5.5:

$$U_m(\bar{\mathbf{r}}_s, \bar{\mathbf{r}}_d, \bar{\mathbf{r}}) \sim U_x(\bar{\mathbf{r}}_s, \bar{\mathbf{r}}) \cdot n(\bar{\mathbf{r}}) \cdot \frac{1}{D_m} \cdot G_m(\bar{\mathbf{r}}, \bar{\mathbf{r}}_d) , \quad (5.5)$$

where D_m and $G_m(\bar{\mathbf{r}}, \bar{\mathbf{r}}_d)$ are the diffusion coefficient in tissue and Green's function at the emission wavelength, respectively. It should be noted that these approximations are only valid for low fluorophore concentrations.

Not only the distribution of the fluorophore is of interest, the reconstruction also provides a map of the fluorophore concentration within the medium. However, then the quantum yield and the extinction coefficients of the fluorophore need to be known. Accurate information about how much excitation light entering the tissue is also required. To prevent the problem from being too complex the intrinsic optical properties of tissue are often assumed to be known. The techniques used for parameter reconstruction in optical tomography is also applied to fluorescence tomography.

Normalized Born approximation

A way to improve the robustness of the reconstruction is to use a normalized Born approach¹⁵³, which makes the measurements independent of some experimental difficulties as e.g. fiber couplings and excitation fluctuations. It has also been shown to improve the

reconstruction in heterogenous medium¹⁵⁶. The normalized Born quantity, U^{NB} , is given by Eq. 5.6:

$$U^{NB} = \frac{U_{fluo}(\bar{\mathbf{r}}_s, \bar{\mathbf{r}}_d)}{U_x(\bar{\mathbf{r}}_s, \bar{\mathbf{r}}_d)}, \quad (5.6)$$

where $U_{fluo}(\bar{\mathbf{r}}_s, \bar{\mathbf{r}}_d) = \int_V U_m(\bar{\mathbf{r}}_s, \bar{\mathbf{r}}_d, \bar{\mathbf{r}}) dr$.

The use of the normalized Born approximation gives rise to a linear problem where the parameters of interest can be obtained with an inversion of the system matrix.

FMT set-ups

There are mainly three different set-ups used in FMT for continuous wave measurements. A fiber-based set-up involves fibers both for object illumination in several projections as well as for the detection of propagated light, see Figure 5.13. Appropriate filters are needed in front of the detection system to ensure selection of only the wanted fluorescence component.

A second alternative is to use fibers for illumination and a CCD camera with appropriate filter for detection, as illustrated in Figure 5.14. This kind of set-up has been used in the experiments presented in Paper IV. The use of a CCD instead of fibers at the detection site increases the spatial resolution as more source-detector pairs can be provided due to all pixels on the CCD chip. In the two mentioned set-ups, the object is often placed in a fluid inside a chamber with a slab or cylinder geometry. This provides known boundary conditions, which can simplify the reconstruction algorithm.

A third alternative is a non-contact system, shown in Figure 5.15, where only one laser spot is used for illumination and a CCD with filters is used for detection. In this case the object is not placed inside a chamber, therefore, measurements to reconstruct the surface of the object are first performed. The object can be rotated to obtain data from several projections.

FMT applications

With FMT, *in vivo* molecular processes in tissue can be studied, resolving and quantifying very low concentrations of fluorophores in animals¹⁵⁴. FMT further provides the possibility to investigate several targets simultaneously by quickly changing a wavelength selecting filter in the detection unit as different targets can be labelled with probes emitting fluorescence at separate wavelengths. This approach has been demonstrated in animals *in vivo*¹⁵⁷. FMT has also been used to study tumor progression *in vivo* by detecting the fluorescence from cells expressing fluorescence proteins¹⁴³. A great advantage with FMT compared to the planar fluorescence imaging technique is the ability to study deeper-lying targets.

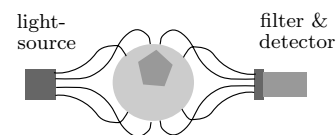


Figure 5.13. FMT set-up using fibers as both sources and detectors.

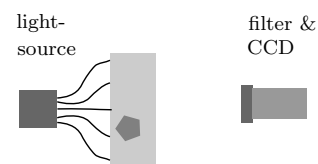


Figure 5.14. FMT set-up using fibers as sources and a CCD for detection.

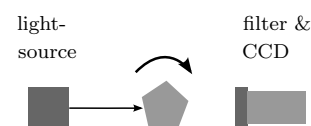


Figure 5.15. A non-contact FMT system.

5.5 Improve robustness in optical tomography reconstruction

In optical tomography the parameter reconstruction is an ill-conditioned problem, because different combinations of optical properties can yield very similar values in the measurements. Therefore, some kind of *a priori* information is desirable to find the best solution. A prior can e.g. include spatial and/or spectral information. Spatial information can be obtained from high-resolution techniques, for example images from MRI have been used^{158;159}. There is an increasing interest in developing instruments capable of multimodality imaging, where two or more of the different techniques used in molecular imaging are combined.

With multispectral measurements the concentration of tissue absorbers may be reconstructed directly without the need of first reconstructing the optical properties at each wavelength measured, as absorption is proportional to the concentration. Spectral priors can then include e.g. the extinction coefficients, $\varepsilon(\lambda)$, of the various absorbers^{159–161}. Multispectral data can also reduce the ill-posedness in optical tomography. This is due to the increase in the number of measurements while the number of unknowns are kept constant.

Multispectral prior information has in Paper IV been used in fluorescence tomography to create a spatial probability map of a fluorescent inclusion. This prior information was created by utilizing the intensity ratio, discussed in Paper I–II.

5.6 Multivariate analysis

In Paper V multivariate analysis was used to estimate the radius and depth of a fluorescent inclusion inside a medium using simulated fluorescence spectra as input variables. A very brief introduction to principal component analysis (PCA), partial least squares (PLS) and support vector machines (SVM), which are different multivariate analysis methods, is given in this section.

The goal with multivariate analysis¹⁶² is in general to build a model, F , from a calibration data set, given the relation $Y_{cal} = F(X_{cal})$. In this type of problems X is often referred to as an independent variable and Y is thus referred to the dependent variable. The purpose of the model is to predict wanted variables Y from a new data set, $Y = F(X)$. The methods are based on the idea of reducing the dimensionality of the measured data into a simpler form, as illustrated with a simple case in Figure 5.16.

In PCA new orthogonal coordinate axes, called principal components, are found capturing the variations in the data set. The first principal component, PC_1 , is a new coordinate axis oriented in such a way that it captures the largest variations in the data set.

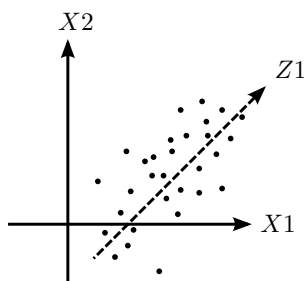


Figure 5.16. Data dimensionality reduction. The important variations of a two-dimensional data set is here captured along a new single dimension, $Z1$.

PC_2 is then chosen as the direction with the next largest variation orthogonal to PC_1 and so on. A disadvantage of PCA is that the found PCs are only based on the independent variables, X_{cal} , and not the variables that are to be predicted. To remedy this a PLS model can be used instead since it tries to find the variations in X_{cal} that correlates the most with Y_{cal} . In this way the effect of large but not important features in X_{cal} is reduced. The direction in X_{cal} that correlates best with Y_{cal} is defined as the first PLS component. The second PLS component is found in the same way but only after the effects from the first component has been removed from the data set.

PCA and PLS are linear methods, where the dependent variables are linear combinations of the independent variables. Some problems are inherently non-linear, as e.g. the depth dependence of fluorescence intensity in measured fluorescence spectra. In these cases the linear methods can not be used and non-linear methods as SVM are introduced in order to improve the prediction of the dependent variables¹⁶³.

Acknowledgments

Det finns många personer som har varit involverade i och bidragit till mitt arbete under tiden jag varit doktorand i medicingruppen. Jag är mycket tacksam för all er hjälp. Speciellt skulle jag vilja tacka:

Min handledare Stefan Andersson-Engels för ditt stöd och den vägledning jag fått under de fem år som jag varit en del av medicingruppen. Jag har framförallt uppskattat våra konferensresor tillsammans, där du alltid tagit dig tid att förklara kryptiska föredrag för mig. Sedan skulle jag vilja tacka mina två biträdande handledare Katarina Svanberg och Sune Svanberg för ert engagemang och uppmuntran i min forskning. Katarina vill jag speciellt tacka för gott samarbete vid flertalet mätkampanjer runt om i Europa.

Ann, Tomas, Johan, Christoffer, Marcelo, Sara, Johannes och Thomas. Tack för att ni varit så trevliga kollegor och för de intressanta diskussioner vi haft om forskning och annat. Jag vill även tacka er för alla roliga aktiviteter vi gjort utanför jobbet. Speciellt vill jag tacka: Ann, för att du är en riktig kompis och för alla roliga resor vi gjort ihop. Turerna längs autobahn kommer jag alltid att komma ihåg med glädje. Christoffer, tack för allt ditt ovärderliga stöd och för att du är en så bra vän. Johan, min molecular imaging-kompanjon, tack för all kul tid nere i labbet. Tomas, för att du alltid livar upp stämningen och att du gett "12" en helt ny innebörd.

I would also like to thank Florian, Nazila and Bastiaan for the nice company during your visits in our group here in Lund.

Jag vill tacka Niels Bendsøe och Linda Persson för det arbete vi utfört tillsammans inom den kliniska studien på hudmottagningen. Niels, för att du spritt "dansk hygge" i gruppen. Jag vill tacka Roland Rydell för trevligt samarbete och för att jag fått

utföra mätningar på klinik.

Jag vill passa på att tacka övriga personer på avdelningen för hjälp med både det ena och det andra, och för de trevliga tisdagsfikorna ihop. Speciellt vill jag tacka Minna för all hjälp med administrativa saker inför avhandlingen och Bertil för all datorsupport. Jag vill även tacka alla examensarbetare som har vistats i gruppen, däribland speciellt Daniel Bengtsson, Khaled Terike, Mikael Karlsson, Edward Birch-Jensen och Johan Stensson.

I would like to express my appreciation to all the people I have gotten the opportunity to work with during the measurement campaigns within the BRIGHT project; Susanna Gräfe, Tilmann Trebst, Burkhard Gitter, Eleni Alexandratou, Maria Kyriazi and Dido Yova. Especially, I would like to thank Susanna for such a nice collaboration, both during our visits in Jena and in the evaluation after the measurement campaigns.

I would like to show my gratitude towards my collaborators Fabien Chauchard and Sylvie Roussel at Ondalys in Montpellier, for teaching me more about chemometrics, and towards Anikitos Garofalakis, Heiko Meyer and Jorge Ripoll for letting me stay at FORTH in Crete for a few weeks to perform measurements within the Molecular Imaging project.

Till sist vill jag tacka släkt och vänner för att ni ser till att mitt liv inte bara handlar om jobb. Jag vill speciellt tacka mina föräldrar, Karin och Gunnar, min syster Malin och min sväger Peter för att ni alltid trott på mig och för att ni alltid stöttat mig. Framförallt vill jag tacka min käre Markus för att du finns. Utan ditt stöd hade den här avhandlingen inte blivit till.



Part of this work was funded by the EC integrated projects BRIGHT.EU FP6-IST-2003-511722 and Molecular Imaging LSHG-CT-2003-503259.

Summary of papers

I. Fluorescence spectra provide information on the depth of fluorescent lesions in tissue

J. Swartling, J. Svensson, D. Bengtsson, K. Terike and S. Andersson-Engels.

Spectral changes of the fluorescence caused by tissue optical properties can be used to determine the depth of a fluorescent layer inside tissue. A ratio can be calculated from the fluorescence intensities at two NIR wavelengths. This ratio is dependent on the depth of the layer. Both experimental work and simulations were performed to investigate the depth-dependent ratio. An accuracy of 0.6 mm was achieved when determining the position of a fluorescent layer down to a depth of 10 mm. The effect of the detection geometry on the measured fluorescence was also studied with Monte Carlo simulations and experiments on a resin phantom.

Contribution:

I performed the work concerning the effect of the detection geometry on the measured fluorescence spectra. I also supervised parts of the remaining work and took part in writing the manuscript.

II. Modeling of spectral changes for depth localization of fluorescent inclusion

J. Svensson and S. Andersson-Engels.

Fluorescence Monte Carlo simulations of a layered geometry were performed to study the ratio of two fluorescence wavelengths in the visible wavelength region to find the depth of a fluorescent layer. The study was focused on the fluorescence contrast influences on the determination of the layer depth. Simulations were also performed to investigate the depth determination when there are uncertainties in tissue optical properties. The results indicated a strong dependence on fluorescence contrast in the intensity ratio.

Contribution:

I performed the simulations, the evaluation and wrote the manuscript.

III. Fluorescence spectroscopy in tissue phantoms for improved depth resolution in tissue imaging

J. Svensson, A. Garofalakis, H. Meyer, F. Forster, J. Ripoll and S. Andersson-Engels.

Experiments were performed to study the fluorescence emitted from an embedded object inside excised tissue. Fluorescence was detected in two wavelength bands in the visible region, where the ratio of the intensities gave information about the depth of the object.

Contribution:

I performed the experimental work and the evaluation. I also wrote the manuscript.

IV. Multispectral prior knowledge used for data pre-processing in fluorescence molecular tomography

J. Axelsson, J. Svensson and S. Andersson-Engels.

In this paper fluorescence tomography measurements were performed in order to reconstruct a fluorescent tube inside a tissue phantom. The intensity ratio at two wavelengths was used as a prior to the location of the fluorescent object. Including this prior information the location of the object was more accurately reconstructed.

Contribution:

My contribution to this paper was in the experimental part and the following discussions about the evaluation.

V. External Parameter Orthogonalisation - Least Squares Support Vector Machine (EPO-LSSVM) and Partial Least Squares (PLS) for localization of embedded inclusions using detection of fluorescence

F. Chauchard, J. Svensson, J. Axelsson, S. Andersson-Engels and S. Roussel.

In this study we analyzed the emitted fluorescence from a deep-lying spherical inclusion with the use of multivariate techniques, to determine the depth and radius of the object. The fluorescence spectra were obtained from simulations and a large data set was used as input to the multivariate methods. The effects of uncertainties in optical properties as well as fluorescence contrast could be removed with a pre-processing technique. In order to predict the depth

of the inclusion with a non-linear multivariate method, this pre-processing was required.

Contribution:

I performed the fluorescence simulations and took part in writing the manuscript.

VI. Fluorescence and absorption assessment of a lipid mTHPC formulation following topical application in a non-melanotic skin tumor model

A. Johansson, J. Svensson, N. Bendsoe, K. Svanberg, E. Alexandratou, M. Kyriazi, D. Yova, S. Gräfe, T. Trebst and S. Andersson-Engels.

Fluorescence and absorption measurements were performed *in vivo* in an animal tumor model to study the pharmacokinetics of a topically applied liposomal formulation of the photosensitizer mTHPC. The optical results were compared to mTHPC concentrations obtained with chemical extraction. The three methods showed a tumor selectivity of mTHPC at 4 hours after application of the drug. The concentration obtained with absorption spectroscopy correlated significantly with the extraction data.

Contribution:

I took part in the experimental and evaluation work.

VII. Tumor selectivity at short times following systemic administration of a liposomal Temoporfin formulation in a murine tumor model

J. Svensson, A. Johansson, S. Gräfe, B. Gitter, T. Trebst, N. Bendsoe, S. Andersson-Engels and K. Svanberg.

In this study the pharmacokinetics of a systemically administered liposomal formulation of Temoporfin was studied in an animal model with subcutaneously implanted tumors. Fluorescence measurements, both in an imaging and a point-monitoring mode, were conducted on tumors and other internal organs *ex vivo*. The estimated Temoporfin levels by the two spectroscopic methods were correlated to the concentrations obtained by means of chemical extraction. The results indicated tumor selectivity of Temoporfin 2–8 hours following drug administration.

Contribution:

I took part in the experiments, data evaluation and writing the manuscript.

VIII. Fluorescence monitoring of a topically applied liposomal Temoporfin formulation and photodynamic

therapy of non-pigmented skin malignancies

N. Bendsoe, L. Persson, A. Johansson, J. Axelsson, J. Svensson, S. Gräfe, T. Trebst, S. Andersson-Engels, S. Svanberg and K. Svanberg.

A first clinical PDT study was performed on 10 patients with skin lesions using a topically applied liposomal Temoporfin formulation. Fluorescence spectroscopy measurements were performed prior, during and post PDT to study the photobleaching of the sensitizer, which indicated a 30-35% bleaching. The distribution of the sensitizer was also investigated with the fluorescence measurements, showing a tumor selectivity of the drug.

Contribution:

I took part in the planning of this study as well as the experimental work and data evaluation.

IX. Tissue temperature monitoring during interstitial photodynamic therapy

J. Svensson, A. Johansson, K. Svanberg and S. Andersson-Engels.

An Alexandrite crystal was used to measure the temperature during light irradiation on skin. The crystal was attached to the tip of an optical fiber used in an interstitial photodynamic therapy system. The temperature was determined by studying the spectral changes in the fluorescence of the crystal. Light irradiations were performed both superficially on skin and interstitially in meat, showing a slight increase in temperature.

Contribution:

I took part in the experimental work and the evaluation. I also wrote the manuscript.

Bibliography

1. A.J. Welch and M.J.C. van Gemert. *Optical-Thermal Response of Laser-Irradiated Tissue*. Plenum Press, New York, USA, 1995.
2. S.A. Prahl. Tabulated molar extinction coefficient for hemoglobin in water, <http://omlc.ogi.edu/spectra/hemoglobin/summary.html>.
3. B. Beauvoit, S.M. Evans, T.W. Jenkins, E.E. Miller, and B. Chance. Correlation between the light scattering and the mitochondrial content of normal tissues and transplantable rodent tumors. *Analytical Biochemistry*, **226**(1):167–174, 1995.
4. W.-F. Cheong, S.A. Prahl, and A.J. Welch. A review of the optical properties of biological tissues. *IEEE Journal of Quantum Electronics*, **26**(12):2166–2185, 1990.
5. W.M. Star. *Diffusion theory of light transport. Optical-Thermal Response of Laser-Irradiated Tissue*, pages 131–206. Plenum Press, New York, USA, 1995.
6. S.R. Arridge. Optical tomography in medical imaging. *Inverse Problems*, **15**:R41–R93, 1999.
7. J. Ripoll, D. Yessayan, G. Zacharakis, and V. Ntziachristos. Experimental determination of photon propagation in highly absorbing and scattering media. *Journal of the Optical Society of America A*, **22**(3):546–551, 2005.
8. M.S. Patterson, B. Chance, and B.C. Wilson. Time resolved reflectance and transmittance for the non-invasive measurement of tissue optical properties. *Applied Optics*, **28**:2331–2336, 1989.
9. S.A. Prahl, M. Keijzer, S.L. Jacques, and A.J. Welch. A Monte Carlo model of light propagation in tissue. Dosimetry of laser radiation in medicine and biology. volume IS 5, pages 102–111. Proceedings of Society of Photo-optical Instrumentation Engineers, 1989.
10. L. Wang, S.L. Jacques, and L. Zheng. MCML - Monte Carlo modeling of light transport in multi-layered tissues. *Computer Methods and Programs in Biomedicine*, **47**:131–146, 1995.
11. J. Swartling, A. Pifferi, A.M.K. Enejder, and S. Andersson-Engels. Accelerated Monte Carlo model to simulate fluorescence spectra from layered tissues. *Journal of the Optical Society of America A*, **20**(4):714–727, 2003.
12. A.J. Welch, C.M. Gardner, R. Richards-Kortum, E. Chan, G. Criswell, J. Pfefer, and S. Warren. Propagation of fluorescence light. *Lasers in Surgery and Medicine*, **21**:166–178, 1997.
13. T.J. Farrell, M.S. Patterson, and B. Wilson. A diffusion theory model of spatially resolved, steady-state diffuse reflectance for noninvasive determination of tissue optical properties in vivo. *Medical Physics*, **19**(4):879–888, 1992.
14. R.M.P. Doornbos, R. Lang, M.C. Aalders, F.W. Cross, and H.J.C.M. Sterenborg. The determination of in vivo human tissue optical properties and absolute chromophore concentrations using spatially resolved steady-

- state diffuse reflectance spectroscopy. *Physics in Medicine and Biology*, **44**:967–981, 1999.
15. J.S. Dam, C.B. Pedersen, T. Dalgaard, P.E. Fabricius, P. Aruna, and S. Andersson-Engels. Fiber optic probe for non-invasive real-time determination of tissue optical properties at multiple wavelengths. *Applied Optics*, **40**(7):1155–1164, 2001.
 16. T. Svensson, M. Einarsdóttir, K. Svanberg, and S. Andersson-Engels. In vivo optical characterization of human prostate tissue using near-infrared time-resolved spectroscopy. *Journal of Biomedical Optics*, **12**(1):014022–1–014022–10, 2006.
 17. L. Spinelli, A. Torricelli, A. Pifferi, P. Taroni, G.M. Danesini, and R. Cubeddu. Bulk optical properties and tissue components in the female breast from multiwavelength time-resolved optical mammography. *Journal of Biomedical Optics*, **9**(6):1137–1142, 2004.
 18. B.J. Tromberg, O. Coquoz, J.B. Fishkin, T. Pham, E.R. Anderson, J. Butler, M. Cahn, J.D. Gross, V. Venugopalan, and D. Pham. Non-invasive measurements of breast tissue optical properties using frequency-domain photon migration. *Philosophical Transactions of the Royal Society of London Series B: Biological Sciences*, **352**:661–668, 1997.
 19. M. Gurfinkel, T. Pan, and E. Sevick-Muraca. Determination of optical properties in semi-infinite turbid media using imaging measurements of frequency-domain photon migration obtained with an intensified charge-coupled device. *Journal of Biomedical Optics*, **9**(6):1336–1346, 2004.
 20. J.S. Dam, T. Dalgaard, P.E. Fabricius, and S. Andersson-Engels. Multiple polynomial regression method for determination of biomedical optical properties from integrating sphere measurements. *Applied Optics*, **39**(7):1202–1209, 2000.
 21. S.A. Prahl, M.J.C. van Gemert, and A.J. Welch. Determining the optical properties of turbid media by using the adding-doubling method. *Applied Optics*, **32**(4):559–568, 1993.
 22. J.R. Mourant, I.J. Bigio, D.A. Jack, T.M. Johnson, and H.D. Miller. Measuring absorption coefficients in small volumes of highly scattering media: source-detector separations for which path lengths do not depend on scattering properties. *Applied Optics*, **36**(22):5655–5661, 1997.
 23. J.R. Mourant, T.M. Johnson, G. Los, and I.J. Bigio. Non-invasive measurement of chemotherapy drug concentrations in tissue: preliminary demonstrations of in vivo measurements. *Physics in Medicine and Biology*, **44**(5):1397–1417, 1999.
 24. T. Vo-Dinh and B.M. Cullum. *Fluorescence spectroscopy for biomedical diagnosis Biomedical Photonics Handbook*, pages 28–1–28–50. Number 28. CRC Press, Boca Raton, USA, 2005.
 25. M. Monici. Cell and tissue autofluorescence research and diagnostic applications. *Biotechnology Annual Review*, **11**:227–256, 2005.
 26. R. Richards-Kortum and E. Sevick-Muraca. Quantitative optical spectroscopy for tissue diagnosis. *Annual Review of Physical Chemistry*, **47**:555–606, 1996.
 27. N. Ramanujam. *Fluorescence spectroscopy in vivo. Encyclopedia of analytical chemistry*, pages 20–56. John Wiley & Sons Ltd, Chichester, 2000.
 28. Y. Yang, Y. Ye, F. Li, Y. Li, and P. Ma. Characteristic autofluorescence for cancer diagnosis and its origin. *Lasers in Surgery and Medicine*, **7**:528–532, 1987.
 29. N. Ramanujam, M.F. Mitchell, A. Mahadevan, S. Warren, S. Thomsen, E. Silva, and R. Richards-Kortum. In vivo diagnosis of cervical intraepithelial neoplasia using 337-nm-excited laser-induced fluorescence. *Proceedings of the National Academy of Sciences of the United States of America*, **91**:10193–10197, 1994.
 30. I. Georgakoudi, B.C. Jacobson, M.G. Müller, E.E. Sheets, K. Badizadegan, D.L. Carr-Locke, C.P. Crum, C.W. Boone, R.R. Dasari, J. van Dam, and M.S. Feld. NAD(P)H and collagen as in vivo quantitative fluores-

- cent biomarkers of epithelial precancerous changes. *Cancer Research*, **62**:682–687, 2002.
31. K. Izuishi, H. Tajiri, T. Fujii, N. Boku, T. Ohtsu, T. Ohnishi, M. Ryu, T. Kinoshita, and S. Yoshida. The histological basis of detection of adenoma and cancer in the colon by autofluorescence endoscopic imaging. *Endoscopy*, **31**(7):511–516, 1999.
 32. K.T. Schomacker, J.K. Frisoli, C.C. Compton, T.J. Flotte, J.M. Richter, N.S. Nishioka, and T.F. Deutsch. Ultraviolet laser-induced fluorescence of colonic tissue: Basic biology and diagnostic potential. *Lasers in Surgery and Medicine*, **12**:63–78, 1992.
 33. L. Brancalion, A.J. Durkin, J.H. Tu, G. Menaker, J.D. Fallon, and N. Kollias. In vivo fluorescence spectroscopy of nonmelanoma skin cancer. *Photochemistry and Photobiology*, **73**(2):178–183, 2001.
 34. S. Andersson-Engels, J. Johansson, K. Svanberg, and S. Svanberg. Fluorescence imaging and point measurements of tissue: Applications to the demarcation of malignant tumors and atherosclerotic lesions from normal tissue. *Photochemistry and Photobiology*, **53**(6):807–814, 1991.
 35. S. Svanberg. *Atomic and Molecular Spectroscopy - Basic Aspects and Practical Applications*. 4th ed. Springer Verlag, Heidelberg, Germany, 2004.
 36. C. af Klinteberg, M. Andreasson, O. Sandström, S. Andersson-Engels, and S. Svanberg. Compact medical fluorosensor for minimally invasive tissue characterisation. *Review of Scientific Instruments*, **76**(3):034303–034306, 2005.
 37. U. Gustafsson, S. Pålsson, and S. Svanberg. Compact fibre-optic fluorosensor using a continuous wave violet diode laser and an integrated spectrometer. *Review of Scientific Instruments*, **71**(8):3004–3006, 2000.
 38. R. Cubeddu, P. Taroni, and G. Valentini. Time-gated imaging system for tumor diagnosis. *Optical Engineering*, **32**(2):320–325, 1993.
 39. H. Brettel, J.Y. Hardeberg, and F. Schmitt. Multispectral image capture across the web. IS&T/SID seventh color imaging conference: Color science, systems and applications. volume 7, pages 314–316, 1999.
 40. T. Vo-Dinh, B. Cullum, and P. Kasili. Development of a multi-spectral imaging system for medical applications. *Journal of Physics D*, **36**(14):1663–1668, 2003.
 41. S. Andersson-Engels, A. Gustafson, J. Johansson, U. Stenram, K. Svanberg, and S. Svanberg. Laser-induced fluorescence used in localizing atherosclerotic lesions. *Lasers in Medical Science*, **4**:171–181, 1989.
 42. S. Andersson-Engels, J. Johansson, U. Stenram, K. Svanberg, and S. Svanberg. Malignant tumor and atherosclerotic plaque diagnosis using laser-induced fluorescence. *IEEE Journal of Quantum Electronics*, **26**(12):2207–2217, 1990.
 43. M. Sinaasappel and H.J.C.M. Sterenberg. Quantification of the hematoporphyrin derivative by fluorescence measurement using dual-wavelength excitation and dual-wavelength detection. *Applied Optics*, **32**(4):541–548, 1993.
 44. H.J.C.M. Sterenberg, A.E. Saarnak, R. Frank, and M. Motamedi. Evaluation of spectral correction techniques for fluorescence measurements on pigmented lesions in vivo. *Journal of Photochemistry and Photobiology B: Biology*, **35**:159–165, 1996.
 45. M.G. Müller, I. Georgakoudi, Q. Zhang, J. Wu, and M.S. Feld. Intrinsic fluorescence spectroscopy in turbid media: disentangling effects of scattering and absorption. *Applied Optics*, **40**(25):4633–4646, 2001.
 46. J.C. Finlay and T.H. Foster. Recovery of hemoglobin oxygen saturation and intrinsic fluorescence with a forward-adjoint model. *Applied Optics*, **44**(10):1917–1933, 2005.
 47. T.J. Pfefer, L.S. Matchette, A.M. Ross, and M.N. Ediger. Selective detection of fluorophore layers in turbid media: the role of fiber-optic probe design. *Optics Letters*, **28**(2):120–122, 2003.
 48. M. Keijzer, R.R. Richards-Kortum, S.L. Jacques, and M.S. Feld. Fluoro-

- rescence spectroscopy of turbid media: Autofluorescence of the human aorta. *Applied Optics*, **28**(20):4286–4292, 1989.
49. Q. Liu, C. Zhu, and N. Ramanujam. Experimental validation of Monte Carlo modeling of fluorescence in tissues in the UV-visible spectrum. *Journal of Biomedical Optics*, **8**(2):223–236, 2003.
 50. J. Wu, M.S. Feld, and R.P. Rava. Analytical model for extracting intrinsic fluorescence in turbid media. *Applied Optics*, **32**(19):3585–3595, 1993.
 51. J.Y. Qu, Z. Huang, and J. Hua. Excitation-and-collection geometry insensitive fluorescence imaging of tissue-simulating turbid media. *Applied Optics*, **39**(19):3344–3356, 2000.
 52. D. Stasic, T.J. Farrell, and M.S. Patterson. The use of spatially-resolved fluorescence and reflectance to determine interface depth in layered fluorophore distributions. *Physics in Medicine and Biology*, **48**:3459–3474, 2003.
 53. A. Eidsath, V. Chernomordik, A. Gandjbakhche, P. Smith, and A. Russo. Three-dimensional localization of fluorescent masses deeply embedded in tissue. *Physics in Medicine and Biology*, **47**:4079–4092, 2002.
 54. C. af Klinteberg, A.M.K. Enejder, I. Wang, S. Andersson-Engels, S. Svanberg, and K. Svanberg. Kinetic fluorescence studies of 5-aminolaevulinic acid-induced protoporphyrin IX accumulation in basal cell carcinomas. *Journal of Photochemistry and Photobiology B: Biology*, **49**(2-3):120–128, 1999.
 55. F. Fischer, E.F. Dickson, J.C. Kennedy, and R.H. Pottier. An affordable, portable fluorescence imaging device for skin lesion detection using a dual wavelength approach for image contrast enhancement and aminolaevulinic acid-induced protoporphyrin IX. Part II. In vivo testing. *Lasers in Medical Science*, **16**(3):207–212, 2001.
 56. J. Hewett, V. Nadeau, J. Ferguson, H. Moseley, S. Ibbotson, J.W. Allen, W. Sibbett, and M. Padgett. The application of a compact multispectral imaging system with integrated excitation source to in vivo monitoring of fluorescence during topical photodynamic therapy of superficial skin cancers. *Photochemistry and Photobiology*, **73**(3):278–282, 2001.
 57. S. Andersson-Engels, J. Johansson, and S. Svanberg. Medical diagnostic system based on simultaneous multispectral fluorescence imaging. *Applied Optics*, **33**(34):8022–8029, 1994.
 58. Y. Kusunoki, F. Imamura, H. Uda, M. Mano, and T. Horai. Early detection of lung cancer with laser-induced fluorescence endoscopy and spectrofluorometry. *Chest*, **118**(6):1776–1782, 2000.
 59. M. Zargi, I. Fajdiga, and L. Smid. Autofluorescence imaging in the diagnosis of laryngeal cancer. *European Archives of Oto-Rhino-Laryngology*, **257**(1):17–23, 2000.
 60. C. Arens, T. Dreyer, H. Glanz, and K. Malzahn. Indirect autofluorescence laryngoscopy in the diagnosis of laryngeal cancer and its precursor lesions. *European Archives of Oto-Rhino-Laryngology*, **261**:71–76, 2004.
 61. P. Hillemanns, H. Weingandt, R. Baumgartner, J. Diebold, W. Xiang, and H. Stepp. Photodetection of cervical intraepithelial neoplasia using 5-aminolevulinic acid-induced porphyrin fluorescence. *Cancer*, **88**(10):2275–2282, 2000.
 62. R.A. Drezek, R. Richards-Kortum, M.A. Brewer, M.S. Feld, C. Pitris, A. Ferenczy, M.L. Faupel, and M. Follen. Optical imaging of the cervix. *Cancer (Suppl.)*, **98**(9):2015–2027, 2003.
 63. U. Gustafsson, E. McLaughlin, E. Jacobson, J. Håkansson, P. Troy, M.J. DeWeert, S. Pålsson, M. Soto Thompson, S. Svanberg, A. Vaitkuviene, and K. Svanberg. Fluorescence and reflectance monitoring of human cervical tissue in vivo - a case study. Spectral imaging: instrumentation, applications, and analysis II Proc. SPIE. volume 4959, pages 100–110, San Jose, CA, 2003. SPIE.
 64. T.J. Dougherty, C.J. Gomer, B.W. Henderson, G. Jori, D. Kessel, M. Korbelik, J. Moan, and Q. Peng. Photodynamic therapy. *Journal of the*

- National Cancer Institute*, **90**(12):889–905, 1998.
65. L.O. Svaasand, B.J. Tromberg, P. Wyss, M.-T. Wyss-Desserich, Y. Tadir, and M.W. Berns. Light and drug distribution with topically administered photosensitizers. *Lasers in Medical Science*, **11**:261–265, 1996.
 66. D.E.J.G. Dolmans, D. Fukumura, and R.K. Jain. Photodynamic therapy for cancer. *Nature Reviews Cancer*, **3**(5):380–387, 2003.
 67. K.R. Weishaupt, C.J. Gomer, and T.J. Dougherty. Identification of singlet oxygen as the cytotoxic agent in photo-inactivation of a murine tumor. *Cancer Research*, **36**(7):2326–2329, 1976.
 68. J. Moan and K. Berg. The photodegradation of porphyrins in cells can be used to estimate the lifetime of singlet oxygen. *Photochemistry and Photobiology*, **53**(4):549–553, 1991.
 69. P. Juzenas, V. Iani, S. Bagdonas, R. Rotomskis, and J. Moan. Fluorescence spectroscopy of normal mouse skin exposed to 5-aminolaevulinic acid and red light. *Journal of Photochemistry and Photobiology B: Biology*, **61**(1-2):78–86, 2001.
 70. D.J. Robinson, H.S. de Bruijn, N. van der Veen, M.R. Stringer, S.B. Brown, and W.M. Star. Protoporphyrin IX fluorescence photobleaching during ALA-mediated photodynamic therapy of UVB-induced tumors in hairless mouse skin. *Photochemistry and Photobiology*, **69**(1):61–70, 1999.
 71. M.B. Ericson, C. Sandberg, B. Stenquist, F. Gudmundson, M. Karlsson, A.M. Ros, A. Rosén, O. Larko, A.M. Wennberg, and I. Rosdahl. Photodynamic therapy of actinic keratosis at varying fluence rates: assessment of photobleaching, pain and primary clinical outcome. *British Journal of Dermatology*, **151**(6):1204–1212, 2004.
 72. I. Wang, N. Bendsoe, C. af Klinteberg, A.M.K. Enejder, S. Andersson-Engels, S. Svanberg, and K. Svanberg. Photodynamic therapy vs. cryosurgery of basal cell carcinomas: results of a phase III clinical trial. *British Journal of Dermatology*, **144**(4):832–840, 2001.
 73. K. Svanberg, T. Andersson, D. Killander, I. Wang, U. Stenram, S. Andersson-Engels, R. Berg, J. Johansson, and S. Svanberg. Photodynamic therapy of non-melanoma malignant tumours of the skin using topical δ -aminolevulinic acid sensitization and laser irradiation. *British Journal of Dermatology*, **130**:743–751, 1994.
 74. N.L. Oleinick, R.L. Morris, and T. Belichenko. The role of apoptosis in response to photodynamic therapy: what, where, why, and how. *Photochemical & Photobiological Sciences*, **1**(1):1–21, 2002.
 75. K. Berg and J. Moan. Lysosomes and microtubules as targets for photochemotherapy of cancer. *Photochemistry and Photobiology*, **65**(3):403–409, 1997.
 76. K.W. Woodburn, Q. Fan, D.R. Miles, D. Kessel, Y. Luo, and S.W. Young. Localisation and efficacy analysis of the phototherapeutic lutetium texaphyrin (PCI-0123) in the murine EMT6 sarcoma model. *Photochemistry and Photobiology*, **65**(3):410–415, 1997.
 77. V.H. Fingar, T.J. Wieman, S.A. Wiehle, and P.B. Cerrito. The role of microvascular damage in photodynamic therapy: The effect of treatment on vessel constriction, permeability and leukocyte adhesion. *Cancer Research*, **52**:4914–4921, 1992.
 78. S. Mitra, E. Maugain, L. Bolotine, F. Guillemin, and T.H. Foster. Temporally and spatially heterogeneous distribution of mTHPC in a murine tumor observed by two-color confocal fluorescence imaging and spectroscopy in a whole-mount model. *Photochemistry and Photobiology*, **81**(5):1123–1130, 2005.
 79. P. Cramers, M. Ruevekamp, H. Oppelaar, O. Dalesio, P. Baas, and F.A. Stewart. Foscan[®] uptake and tissue distribution in relation to photodynamic efficacy. *British Journal of Cancer*, **88**(2):283–290, 2003.
 80. T.H. Foster, R.S. Murant, R.G. Bryant, R.S. Knox, S.L. Gibson, and R. Hilf. Oxygen consumption and diffusion effects in photodynamic therapy. *Radiation Research*, **126**:296–303, 1991.

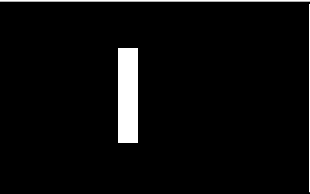
81. A. Curnow, J.C. Haller, and S.G. Bown. Oxygen monitoring during 5-aminolaevulinic acid induced photodynamic therapy in normal rat colon. Comparison of continuous and fractionated light regimes. *Journal of Photochemistry and Photobiology B: Biology*, **58**(2-3):149–155, 2000.
82. S. Iinuma, K.T. Schomacker, G. Wagnieres, M. Rajadhyaksha, M. Bamberg, T. Momma, and T. Hasan. In vivo fluence rate and fractionation effects on tumor response and photobleaching: photodynamic therapy with two photosensitizers in an orthotopic rat tumor model. *Cancer Research*, **59**(24):6164–6170, 1999.
83. A.P. Castano, P. Mroz, and M.R. Hamblin. Photodynamic therapy and anti-tumour immunity. *Nature Reviews*, **6**:535–545, 2006.
84. F.H. van Duijnhoven, R.I.J.M. Aalbers, J.P. Rovers, O.T. Terpstra, and P.J.K. Kuppen. The immunological consequences of photodynamic treatment of cancer, a literature review. *Immunobiology*, **207**(2):105–113, 2003.
85. G. Jori. Factors controlling the selectivity and efficiency of tumor damage in photodynamic therapy. *Lasers in Medical Science*, **5**(2):115–120, 1990.
86. Y.N. Konan, R. Gurny, and E. Allemann. State of the art in the delivery of photosensitizers for photodynamic therapy. *Journal of Photochemistry and Photobiology B: Biology*, **66**:89–106, 2002.
87. G. Jori. Tumour photosensitizers: approach to enhance the selectivity and efficiency of photodynamic therapy. *Journal of Photochemistry and Photobiology B: Biology*, **36**:87–93, 1996.
88. Q. Peng, K. Berg, J. Moan, M. Kongshaug, and J.M. Nesland. 5-aminolevulinic acid-based photodynamic therapy: Principles and experimental research. *Photochemistry and Photobiology*, **65**(2):235–251, 1997.
89. Q. Peng, T. Warloe, K. Berg, J. Moan, M. Kongshaug, K.-E. Giercksky, and J.M. Nesland. 5-aminolevulinic acid-based photodynamic therapy: Clinical research and future challenges. *Cancer*, **79**:2282–2308, 1997.
90. S. Mitra and T.H. Foster. Photophysical parameters, photosensitizer retention and tissue optical properties completely account for the higher photodynamic efficacy of meso-tetra-hydroxyphenyl-chlorin vs photofrin. *Photochemistry and Photobiology*, **81**(4):849–859, 2005.
91. M. Triesscheijn, M. Ruevekamp, M. Aalders, P. Baas, and F.A. Stewart. Outcome of mTHPC mediated photodynamic therapy is primarily determined by the vascular response. *Photochemistry and Photobiology*, **81**(5):1161–1167, 2005.
92. J. Moan and Q. Peng. An outline of the hundred-year history of PDT. *Anticancer Research*, **23**(5A):3591–3600, 2003.
93. M. Korbelik, G. Kros, P.L. Olive, and D.J. Chaplin. Distribution of photofrin between tumour cells and tumour associated macrophages. *British Journal of Cancer*, **64**:508–512, 1991.
94. M. Korbelik and G. Kros. Cellular levels of photosensitisers in tumours: the role of proximity to the blood supply. *British Journal of Cancer*, **70**:604–610, 1994.
95. J.C. Kennedy, R.H. Pottier, and D.C. Pross. Photodynamic therapy with endogenous protoporphyrin IX: Basic principles and present clinical experience. *Journal of Photochemistry and Photobiology B: Biology*, **6**:143–148, 1990.
96. J.C. Kennedy and R.H. Pottier. Endogenous protoporphyrin IX, a clinically useful photosensitizer for photodynamic therapy. *Journal of Photochemistry and Photobiology B: Biology*, **14**:275–292, 1992.
97. G. Gupta, C.A. Morton, C. Whitehurst, J.V. Moore, and R.M. Mackie. Photodynamic therapy with meso-tetra(hydroxyphenyl) chlorin in the topical treatment of Bowen's disease and basal cell carcinoma. *British Journal of Dermatology*, **141**(2):385–386, 1999.
98. P.J. Lou, H.R. Jager, L. Jones, T. Theodossy, S.G. Bown, and C. Hopper. Interstitial photodynamic therapy as salvage treatment for recurrent head and neck cancer. *British Journal of Cancer*, **91**(3):441–446, 2004.
99. S.G. Bown, A.Z. Rogowska, D.E. Whitelaw, W.R. Lees, L.B. Lovat,

- P. Ripley, L. Jones, P. Wyld, A. Gillams, and A.W. Hatfield. Photodynamic therapy for cancer of the pancreas. *Gut*, **50**(4):549–557, 2002.
100. Z. Malik, G. Kostenich, L. Roitman, B. Ehrenberg, and A. Orenstein. Topical application of 5-aminolevulinic acid, DMSO and EDTA: protoporphyrin IX accumulation in the skin and tumours of mice. *Journal of Photochemistry and Photobiology B: Biology*, **28**(3):213–218, 1995.
101. A. Casas, H. Fukuda, G. Di Venosa, and A.M.D. Batlle. The influence of the vehicle on the synthesis of porphyrins after topical application of 5-aminolaevulinic acid. Implications in cutaneous photodynamic sensitization. *British Journal of Dermatology*, **143**(3):564–572, 2000.
102. N. Lange, P. Jichlinski, M. Zellweger, M. Forrer, A. Marti, L. Guilou, G. Wagnières, and H. van den Bergh. Photodetection of early human bladder cancer based on the fluorescence of 5-aminolaevulinic acid hexylester-induced protoporphyrin IX: a pilot study. *British Journal of Cancer*, **80**(1/2):185–193, 1999.
103. J.T.H.M. van den Akker, V. Iani, W.M. Star, H.J.C.M. Sterenberg, and J. Moan. Topical application of 5-aminolevulinic acid hexyl ester and 5-aminolevulinic acid to normal nude mouse skin: Differences in protoporphyrin IX fluorescence kinetics and the role of the stratum corneum. *Photochemistry and Photobiology*, **72**(5):681–689, 2000.
104. A. Juzeniene, P. Juzenas, V. Iani, and J. Moan. Topical application of 5-aminolevulinic acid and its methylester, hexylester and octylester derivatives: Considerations for dosimetry in mouse skin model. *Photochemistry and Photobiology*, **76**(3):329–334, 2002.
105. P. Uehlinger, M. Zellweger, G. Wagnières, L. Juillerat-Jeanneret, H. van den Bergh, and N. Lange. 5-aminolevulinic acid and its derivatives: physical chemical properties and protoporphyrin IX formation in cultured cells. *Journal of Photochemistry and Photobiology B: Biology*, **54**(1):72–80, 2000.
106. J. Moan, L.W. Ma, and V. Iani. On the pharmacokinetics of topically applied 5-aminolevulinic acid and two of its esters. *International Journal of Cancer*, **92**(1):139–143, 2001.
107. A.S.L. Derycke and P.A.M. de Witte. Liposomes for photodynamic therapy. *Advanced Drug Delivery Reviews*, **56**(1):17–30, 2004.
108. X. Damoiseau, H.J. Schuitmaker, J.W.M. Lagerberg, and M. Hoebeke. Increase of the photosensitizing efficiency of the bacteriochlorin a by liposome-incorporation. *Journal of Photochemistry and Photobiology B: Biology*, **60**(1):50–60, 2001.
109. C.R. Lewanski and S. Stewart. Pegylated liposomal adriamycin: a review of current and future applications. *Pharmaceutical Science & Technology Today*, **2**(12):473–477, 1999.
110. A.M. Richter, E. Waterfield, A.K. Jain, A.J. Canaan, B.A. Allison, and J.G. Levy. Liposomal delivery of a photosensitizer, benzoporphyrin derivative monoacid ring A (BPD), to tumor tissue in a mouse tumor model. *Photochemistry and Photobiology*, **57**:1000–1006, 1993.
111. Z.J. Wang, Y.Y. He, C.G. Huang, J.S. Huang, Y.C. Huang, J.Y. An, Y. Gu, and L.J. Jiang. Pharmacokinetics, tissue distribution and photodynamic therapy efficacy of liposomal-delivered hypocrellin A, a potential photosensitizer for tumor therapy. *Photochemistry and Photobiology*, **70**(5):773–780, 1999.
112. H. Fukuda, S. Paredes, and A.M. del C Batlle. Tumour-localizing properties of porphyrins. in vivo studies using free and liposome encapsulated aminolevulinic acid. *Comparative Biochemistry and Physiology*, **102B**(2):433–436, 1992.
113. G. Jori and E. Reddi. The role of lipoproteins in the delivery of tumour-targeting photosensitisers. *International Journal of Biochemistry*, **25**(10):1369–1375, 1993.
114. B.A. Allison, E. Waterfield, A.M. Richter, and J.G. Levy. The effects of plasma lipoproteins on in vitro tumor cell killing and in vivo tumor photosensitization with benzoporphyrin derivative. *Photochemistry and*

- Photobiology*, **54**:709–715, 1991.
115. T.C. Zhu, J.C. Finlay, and S.M. Hahn. Determination of the distribution of light, optical properties, drug concentration, and tissue oxygenation in-vivo in human prostate during motexafin lutetium-mediated photodynamic therapy. *Journal of Photochemistry and Photobiology B: Biology*, **79**(3):231–241, 2005.
 116. M. Soto Thompson, A. Johansson, T. Johansson, S. Andersson-Engels, S. Svanberg, N. Bendsoe, and K. Svanberg. Clinical system for interstitial photodynamic therapy with combined on-line dosimetry measurements. *Applied Optics*, **44**(19):4023–4031, 2005.
 117. A. Orenstein, G. Kostenich, H. Tsur, L. Kogan, and Z. Malik. Temperature monitoring during photodynamic therapy of skin tumors with topical 5-aminolevulinic acid application. *Cancer Letters*, **93**(2):227–232, 1995.
 118. J.P. Ritz, A. Roggan, C.T. Germer, C. Isbert, G. Müller, and H.J. Buhr. Continuous changes in the optical properties of liver tissue during laser-induced interstitial thermotherapy. *Lasers in Surgery and Medicine*, **28**(4):307–312, 2001.
 119. A.M.K. Nilsson, C. Stureson, D.L. Liu, and S. Andersson-Engels. Changes in spectral shape of tissue optical properties in conjunction with laser-induced thermotherapy. *Applied Optics*, **37**(7):1256–1267, 1998.
 120. C. Stureson. *Medical laser-induced thermotherapy - models and applications*. PhD thesis, Lund, Sweden, 1998.
 121. D.K. Kelleher, J. Bastian, O. Thews, and P. Vaupel. Enhanced effects of aminolaevulinic acid-based photodynamic therapy through local hyperthermia in rat tumors. *British Journal of Cancer*, **89**:405–411, 2003.
 122. T.S. Mang. Combination studies of hyperthermia induced by the Neodymium: Yttrium- Aluminum- Garnet (Nd:YAG) laser as an adjuvant to photodynamic therapy. *Lasers in Surgery and Medicine*, **10**:173–178, 1990.
 123. S. Pålsson, L. Gustafsson, N. Bendsoe, M. Soto Thompson, S. Andersson-Engels, and K. Svanberg. Kinetics of the superficial perfusion and temperature in connection with photodynamic therapy of basal cell carcinomas using esterified and non-esterified 5-aminolevulinic acid. *British Journal of Dermatology*, **148**(6):1179–1188, 2003.
 124. B.G. Potter Jr and M.B. Sinclair. Photosensitive and rare-earth doped ceramics for optical sensing: a review. *Journal of Electroceramics*, **2**(4):295–308, 1998.
 125. K.T.V. Grattan and Z.Y. Zhang. *Fiber optic fluorescence thermometry. Sensor physics and technology series*, volume 1. Chapman & Hall, London, UK, 1995.
 126. Z.Y. Zhang, K.T.V. Grattan, A.W. Palmer, V. Fericola, and L. Crovini. Temperature dependence of the YAG:Cr³⁺ fluorescence lifetime over the range 77 to 900 K. *Physical Review B*, **51**(5):2656–2660, 1995.
 127. T.F. Massoud and S.S. Gambhir. Molecular imaging in living subjects: seeing fundamental biological processes in a new light. *Genes & Development*, **17**:545–580, 2003.
 128. D. Kirik, N. Breyse, T. Björklund, L. Besret, and P. Hantraye. Imaging in cell-based therapy for neurodegenerative diseases. *European Journal of Nuclear Medicine and Molecular Imaging*, **32**(14):S417–S434, 2005.
 129. A. Wunder, R.H. Straub, S. Gay, J. Funk, and U. Müller-Ladner. Molecular imaging: novel tools in visualizing rheumatoid arthritis. *Rheumatology*, **44**(11):1341–1349, 2005.
 130. M. Rudin and R. Weissleder. Molecular imaging in drug discovery and development. *Nature Reviews*, **2**:123–131, 2003.
 131. C. Bremer, V. Ntziachristos, and R. Weissleder. Optical-based molecular imaging: contrast agents and potential medical applications. *European Radiology*, **13**:231–243, 2003.
 132. V. Ntziachristos. Fluorescence molecular imaging. *Annual Review of Biomedical Engineering*, **8**:1–33, 2006.

133. R. Weissleder, C.-H. Tung, U. Mahmood, and A. Bogdanov. In vivo imaging of tumors with protease-activated near-infrared fluorescent probes. *Nature Biotechnology*, **17**(4):375–378, 1999.
134. R.M. Hoffman. The multiple uses of fluorescent proteins to visualize cancer in vivo. *Nature Reviews Cancer*, **5**(10):796–806, 2005.
135. M. Yang, E. Baranov, P. Jiang, F.X. Sun, X.M. Li, L. Li, S. Hasegawa, M. Bouvet, M. Al-Tuwaijri, T. Chishima, H. Shimada, A.R. Moossa, S. Penman, and R.M. Hoffman. Whole-body optical imaging of green fluorescent protein-expressing tumors and metastases. *Proceedings of the National Academy of Sciences of the United States of America*, **97**(3):1206–1211, 2000.
136. N.C. Shaner, P.A. Steinbach, and R.Y. Tsien. A guide to choosing fluorescent proteins. *Nature Methods*, **2**(12):905–909, 2005.
137. X. Michalet, F.F. Pinaud, L.A. Bentolila, J.M. Tsay, S. Doose, J.J. Li, G. Sundaresan, A.M. Wu, S.S. Gambhir, and S. Weiss. Quantum dots for live cells, in vivo imaging and diagnostics. *Science*, **307**:538–544, 2005.
138. X. Gao, L. Yang, J.A. Petros, F.F. Marshall, J.W. Simons, and S. Nie. In vivo molecular and cellular imaging with quantum dots. *Current Opinion in Biotechnology*, **16**:63–72, 2005.
139. X. Gao, Y. Cui, R.M. Levenson, L.W.K. Chung, and S. Nie. In vivo cancer targeting and imaging with semiconductor quantum dots. *Nature Biotechnology*, **22**(8):969–976, 2004.
140. K. Shah, A. Jacobs, X.O. Breakefield, and R. Weissleder. Molecular imaging of gene therapy for cancer. *Gene Therapy*, **11**:1175–1187, 2004.
141. H. Deghani, S.C. Davis, S. Jiang, B.W. Pogue, K.D. Paulsen, and M.S. Patterson. Spectrally resolved bioluminescence optical tomography. *Optics Letters*, **31**(3):365–367, 2006.
142. V. Ntziachristos, C. Bremer, and R. Weissleder. Fluorescence imaging with near-infrared light: new technological advances that enable in vivo molecular imaging. *European Radiology*, **13**(1):195–208, 2003.
143. G. Zacharakis, H. Kambara, H. Shih, J. Ripoll, J. Grimm, Y. Saeki, R. Weissleder, and V. Ntziachristos. Volumetric tomography of fluorescent proteins through small animals in vivo. *Proceedings of the National Academy of Sciences of the United States of America*, **102**(51):18252–18257, 2005.
144. M.A. O’Leary, D.A. Boas, X.D. Li, B. Chance, and A.G. Yodh. Fluorescence lifetime imaging in turbid media. *Optics Letters*, **21**(2):158–160, 1996.
145. W. Becker, A. Bergmann, M.A. Hink, K. König, K. Benndorf, and C. Biskup. Fluorescence lifetime imaging by time-correlated single-photon counting. *Microscopy Research and Technique*, **63**(1):58–66, 2004.
146. S. Bloch, F. Lesage, L. McIntosh, A. Gandjbakhche, K. Liang, and S. Achilefu. Whole-body fluorescence lifetime imaging of a tumor-targeted near-infrared molecular probe in mice. *Journal of Biomedical Optics*, **10**(5):054003–1–054003–8, 2005.
147. T. Austin, A.P. Gibson, G. Branco, R.Md. Yusof, S.R. Arridge, J.H. Meek, J.S. Wyatt, D.T. Delpy, and J.C. Hebden. Three dimensional optical imaging of blood volume and oxygenation in the neonatal brain. *Neuroimage*, **31**(4):1426–1433, 2006.
148. P. Taroni, A. Torricelli, L. Spinelli, A. Pifferi, F. Arpaia, G. Danesini, and R. Cubeddu. Time-resolved optical mammography between 637 and 985 nm: clinical study on the detection and identification of breast lesions. *Physics in Medicine and Biology*, **50**(11):2469–2488, 2005.
149. A.H. Hielscher. Optical tomographic imaging of small animals. *Current Opinion in Biotechnology*, **16**:79–88, 2005.
150. D.A. Boas, D.H. Brooks, E.L. Miller, C.A. DiMarzio, M. Kilmer, R.J. Gaudette, and Q. Zhang. Imaging the body with diffuse optical tomography. *IEEE Signal processing magazine*, **18**(6):57–75, 2001.
151. A.P. Gibson, J.C. Hebden, and S.R. Arridge. Recent advances in diffuse

- optical imaging. *Physics in Medicine and Biology*, **50**(4):R1–43, 2005.
152. A.D. Klöse and A.H. Hielscher. Iterative reconstruction scheme for optical tomography based on the equation of radiative transfer. *Medical Physics*, **26**(8):1698–1707, 1999.
 153. V. Ntziachristos and R. Weissleder. Experimental three-dimensional fluorescence reconstruction of diffuse media by use of a normalized born approximation. *Optics Letters*, **26**(12):893–895, 2001.
 154. V. Ntziachristos, C.-H. Tung, C. Bremer, and R. Weissleder. Fluorescence molecular tomography resolves protease activity in vivo. *Nature Medicine*, **8**(7):757–760, 2002.
 155. A.D. Klöse, V. Ntziachristos, and A.H. Hielscher. The inverse source problem based on the radiative transfer equation in optical molecular imaging. *Journal of Computational Physics*, **202**(1):323–345, 2005.
 156. A. Soubret, J. Ripoll, and V. Ntziachristos. Accuracy of fluorescence tomography in the presence of heterogeneities: study of the normalized born ratio. *IEEE Transactions on Medical Imaging*, **24**(10):1377–1386, 2005.
 157. X. Montet, V. Ntziachristos, J. Grimm, and R. Weissleder. Tomographic fluorescence mapping of tumor targets. *Cancer Research*, **65**(14):6330–6336, 2005.
 158. H. Xu, R. Springett, H. Dehghani, B.W. Pogue, K.D. Paulsen, and J.F. Dunn. Magnetic-resonance-imaging-coupled broadband near-infrared tomography system for small animal brain studies. *Applied Optics*, **44**(11):2177–2188, 2005.
 159. B. Brooksby, S. Srinivasan, S. Jiang, H. Dehghani, B.W. Pogue, K.D. Paulsen, J. Weaver, C. Kogel, and S.P. Poplack. Spectral priors improve near-infrared diffuse tomography more than spatial priors. *Optics Letters*, **30**(15):1968–1970, 2005.
 160. A. Corlu, T. Durduran, R. Choe, M. Schweiger, E.M.C. Hillman, S.R. Arridge, and A.G. Yodh. Uniqueness and wavelength optimization in continuous-wave multispectral diffuse optical tomography. *Optics Letters*, **28**(23):2339–2341, 2003.
 161. A. Li, Q. Zhang, J.P. Culver, E.L. Miller, and D.A. Boas. Reconstructing chromosphere concentration images directly by continuous-wave diffuse optical tomography. *Optics Letters*, **29**(3):256–259, 2004.
 162. C. Eker. *Optical characterization of tissue for medical diagnostics*. PhD thesis, Lund, Sweden, 1999.
 163. F. Chauchard, R. Cogdill, S. Roussel, J.M. Roger, and V. Bellon-Maurel. Application of LS-SVM to non-linear phenomena in NIR spectroscopy: Development of a robust and portable sensor for acidity prediction in grapes. *Chemometrics and Intelligent Laboratory Systems*, **71**(2):141–150, 2004.



Fluorescence spectra provide information on the depth of fluorescent lesions in tissue

Johannes Swartling, Jenny Svensson, Daniel Bengtsson, Khaled Terike, and Stefan Andersson-Engels

The fluorescence spectrum measured from a fluorophore in tissue is affected by the absorption and scattering properties of the tissue, as well as by the measurement geometry. We analyze this effect with Monte Carlo simulations and by measurements on phantoms. The spectral changes can be used to estimate the depth of a fluorescent lesion embedded in the tissue by measurement of the fluorescence signal in different wavelength bands. By taking the ratio between the signals at two wavelengths, we show that it is possible to determine the depth of the lesion. Simulations were performed and validated by measurements on a phantom in the wavelength range 815–930 nm. The depth of a fluorescing layer could be determined with 0.6-mm accuracy down to at least a depth of 10 mm. Monte Carlo simulations were also performed for different tissue types of various composition. The results indicate that depth estimation of a lesion should be possible with 2–3-mm accuracy, with no assumptions made about the optical properties, for a wide range of tissues. © 2005 Optical Society of America

OCIS codes: 170.3660, 170.3880, 170.6280, 170.7050.

1. Introduction

There is a rapidly growing interest in fluorescence measurements of embedded structures for tissue diagnostics. The principle is based on noninvasive or low-invasive techniques in which the tissue is irradiated with light and the remitted fluorescence signal is detected on the surface. The measured signal contains information about the concentration and distribution of the fluorophore. This type of measurement has the potential to discriminate diseased regions inside the tissue (e.g., tumors), provided that there is some mechanism for selective uptake of the fluorophore.

By use of long excitation wavelengths, approximately within the 600–900-nm range, it is possible to reach deep into the tissue, partly because of lower scattering, but mainly owing to the lower absorption in this region. A field of intense research is cancer diagnostics that uses fluorophores, which have long excitation wavelengths in the red or near-infrared

(NIR) region. This would enable fluorescence emission from deep structures, of the order of several centimeters.^{1,2} A specific application that has been suggested is detection of sentinel nodes in cancer patients.^{3,4} Tumor spreading is routinely investigated by lymphoscintigraphy of the lymph nodes to which the lymphatic channels drain the tumor bed. A radioisotope is injected into the tumor volume, and the clinician searches for gamma decay in the nearby lymph nodes. Fluorescence-based detection could be a simpler and safer alternative to this procedure. Another application that has attracted interest is measurement of the fluorescence from photosensitizers for photodynamic therapy, with the aim of optimizing treatment parameters and monitoring photobleaching of the drug.^{5,6}

Several reconstruction algorithms have been developed that attempt to recover the distribution of a fluorophore in a tissue volume given a set of measurements on the tissue surface. Fully three-dimensional reconstruction methods are being developed by some groups. They are commonly based on use of diffusion theory as the forward model,^{7–11} but an algorithm based on the discrete-ordinates solution of the transport equation has also been proposed.¹² Many combinations of light source and detection points are needed for full reconstruction, which implies a high complexity of both the instrumentation and the reconstruction algorithm. A sim-

The authors are with the Department of Physics, Lund Institute of Technology, P.O. Box 118, SE-22100 Lund, Sweden. J. Swartling's e-mail address is js604@cam.ac.uk.

Received 20 July 2004; revised manuscript received 3 December 2004; accepted 5 December 2004.

0003-6935/05/101934-08\$15.00/0

© 2005 Optical Society of America

pler approach has been suggested by some authors, based on the approximation that the tissue can be regarded as a semi-infinite volume with fluorescing lesions at some depth beneath the surface. Stasic *et al.* presented a method based on the diffusion equation for a two-layer medium and spatially resolved measurements of both diffuse reflectance and fluorescence.¹³ This method was successful in recovering the absorption and reduced scattering coefficients (μ_a and μ_s' , respectively) of both layers, as well as the fluorophore concentration and layer depth. However, recovery of all parameters was limited to a depth of ~ 3 mm, and determination of the depth itself proved to be difficult for larger depths owing to model coupling among depth, fluorophore concentration, and tissue absorption. Eidsath *et al.* have described a method based on image fluorometry.⁴ Using a random-walk model, they demonstrated good accuracy of the determined depth for pointlike fluorescing lesions.

None of the methods described in the literature seem to make specific use of the spectral properties of the fluorescence signal. The measured emission spectrum following irradiation by excitation light at the surface is a function of several parameters, because the fluorescence light has to pass through tissue with characteristic scattering and absorption properties. Thus the intrinsic fluorescence emission spectrum will be altered in a way determined by the tissue optical properties, by the depth of the fluorophore, and also by the geometry of the light irradiation and the detection system. These effects have been noted by several authors in conjunction with fluorescence from shallow layers (less than ~ 1 mm) and with ultraviolet or blue excitation light.^{14–20}

In the first part of this paper we investigate the effects of the optical properties of the tissue and the measurement geometry on the recorded fluorescence spectra. We use Monte Carlo simulations to compute fluorescence spectra from a turbid medium. The Monte Carlo code was developed earlier and utilizes several techniques to reduce the number of photons necessary in the simulation to make the computation time reasonable even for entire fluorescence spectra and for large depths.²¹ The computed spectra are compared with experimental results from a tissue phantom for different irradiation-detection geometries. The optical properties of the phantom, which are necessary for the simulations, are measured independently with an integrating sphere. The results serve as a validation of this method and demonstrate the effects on the measured fluorescence spectra.

Next we turn to the problem of determining the depth of fluorescent lesions in tissue. We recognize that the shape of the fluorescence spectrum from an embedded lesion is influenced by the depth of the lesion, owing to the fact that the fluorescence light is filtered when it migrates through the tissue to the surface. Thus we investigate the potential of using changes in the fluorescence spectra to estimate the depth, d , of a fluorescing lesion in a semi-infinite volume.

Our method relies on the fact that the absorption coefficient of the tissue is nonuniform over the spectral region of fluorescence emission. This means that relative spectral intensities change for different wavelength bands as the fluorescence light migrates to the surface. These changes can serve as a measure of the depth of the fluorophore. A simple approach is to form the ratio between the measured fluorescence signals at two wavelengths, λ_1 and λ_2 ,

$$\gamma = \frac{\Gamma(\lambda_1)}{\Gamma(\lambda_2)}, \quad (1)$$

where Γ represents the probability of detecting a fluorescence photon and then evaluating the dependence of γ on d . An advantage of this approach is that by forming a ratio there is no need for absolute measurements of the fluorescence light, and some uncontrolled parameters cancel out. To prove the principle of this approach, we performed Monte Carlo simulations of excitation and fluorescence light. The simulation results were directly compared with the results from measurements performed on a tissue phantom to provide experimental verification of the method. We also performed a series of Monte Carlo simulations with realistic tissue optical properties, for various tissue types, to assess the robustness of the method with respect to biological variability.

2. Materials and Methods

A. Monte Carlo Simulations

The Monte Carlo method for simulating fluorescence from layered tissues has been described in depth in a previous study.²¹ Briefly, our method takes advantage of the symmetry aspects to reduce the computation time. We also split the simulation of the excitation light and the emission light into two separate problems. The resulting data sets are convolved to provide the final answer. To increase the efficiency further, we apply a reciprocity theorem for the calculation of the emission light. This effectively reverses the photon paths of the fluorescence light so that only one simulation is needed, with the source of photons placed at the surface. It was shown that for certain applications, the computation time could be reduced by 2 orders of magnitude or more by use of these techniques, compared with the conventional method for simulating fluorescence.²¹ The code is time resolved, which permits studies of the effects of fluorophore lifetimes and photon migration time dispersion.

For experimental validation, we performed Monte Carlo simulations with optical properties similar to those of phantoms, which were measured independently with an integrating-sphere method (Subsections 2.B–2.D below).

We also performed simulations with optical properties similar to those in real tissue. The absorption spectra for tissue were modeled based on data from previous measurements of breast tissue, in which the dominant absorbers in the red and NIR regions

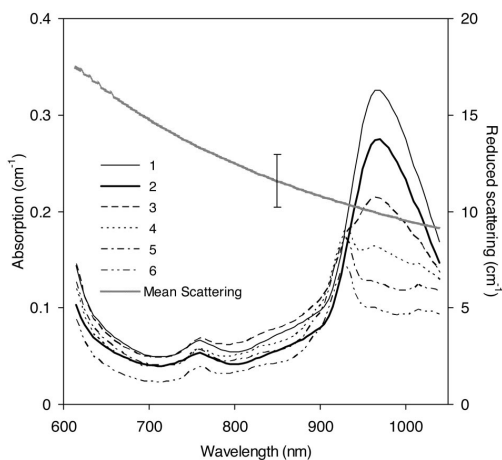


Fig. 1. Optical properties of six different types of breast tissue (from Pifferi *et al.*²²). The absorption spectra represent fitted curves rather than actual measurement data. The reduced scattering spectra represent fits to a power law. Only the mean spectrum is shown for scattering to avoid cluttering in the graph. The error bar indicates the standard deviation.

are water, fat, and deoxygenated and oxygenated hemoglobin.²² The spectra of absorption and the reduced scattering that were used in the simulations are shown in Fig. 1. The tissue types ranged from water rich (62% water, 16% lipid for type 1) to lipid rich (12% water, 68% lipid for type 6) and thus represent a very wide span in terms of different tissue types.

B. Resin Phantom

We constructed a homogeneous solid phantom made of epoxy resin, following the guidelines in Ref. 23. We used TiO₂ particles at a concentration of 1 mg/g (T-8141; Sigma-Aldrich, St. Louis, Missouri) as a scatterer, and we used Amaranth dye at a concentration of 0.8 mg/g (12,056-1; Aldrich Chemical Company, St. Louis, Missouri) as an absorber. Small amounts of the Coumarin 30 dye were used to provide a fluorescence peak in the green region, 450–500 nm, and Sulforhodamin provided a peak in the red region, 550–650 nm, of the spectrum. The fluorescence spectrum of the phantom, following excitation at 407 nm, mimicked that of real tissue. It exhibited a broad peak in the green region that corresponded to tissue autofluorescence, and a red peak similar to the fluorescence from a fluorescent tumor marker.

C. Intralipid Phantom

To show the differences in the fluorescence spectrum for a lesion at different depths, we needed a phantom with an embedded inclusion at a variable depth d . To this end, a phantom was prepared from 1 part Intralipid-20% (Fresenius Kabi, Sweden) and 21 parts water. The phantom consisted of three layers, as depicted in Fig. 2. The upper and lower layers had

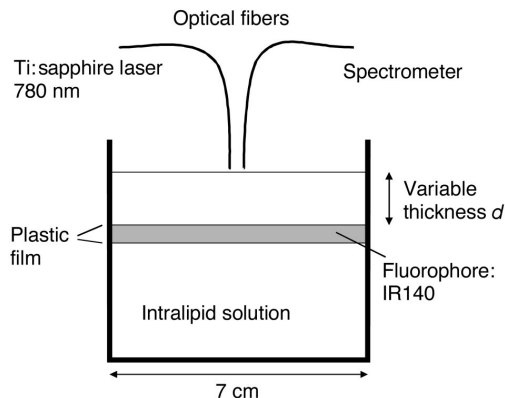


Fig. 2. Schematic picture of the Intralipid phantom. The thickness of the fluorescing layer was 1 mm.

the same optical properties, and black ink was added to provide background absorption (2.3 $\mu\text{l/l}$). The middle layer, 1-mm thick, was separated by thin plastic foil, and to this layer a fluorescent dye (IR-140; Exciton, Dayton, Ohio) was added. The depth of the upper layer, d , could easily be varied by the addition or removal of the liquid.

D. Integrating Sphere Measurements

The optical properties of the phantoms were determined by use of an integrating sphere.²³ In the case of the solid phantom, a small amount of the resin was sandwiched between two glass slides while still not hardened. To measure the optical properties of the Intralipid phantom, we used a cuvette made of glass slides. In both cases the thickness of the samples was 1.00 mm and the lateral dimensions were 3 cm \times 3 cm. The integrating-sphere setup was used to measure the total transmission, total reflectance, and collimated transmittance. In the case of the Intralipid phantom, the optical properties— μ_a , μ_s , and the scattering anisotropy factor g —were evaluated with Monte Carlo look-up tables.²³ For the solid phantom, the collimated measurement could not be performed because of high attenuation; instead, data for the g factor were taken from previous measurements on resin phantoms.²³ The data for the resin phantom were evaluated by use of the inverse adding–doubling method,²⁴ which was more convenient than the Monte Carlo look-up tables owing to the large differences in the optical properties at different wavelengths for this phantom.

E. Fluorescence Measurements

For the measurements on the resin phantom, we used a compact fluorescence point monitoring system to record the fluorescence spectra.²⁵ The fluorescence light from the sample was guided through a 600- μm -core-diameter step-index fiber (N.A. = 0.22) to a spectrometer and a cooled CCD camera (DH501-25U-01, Andor Technology, North-

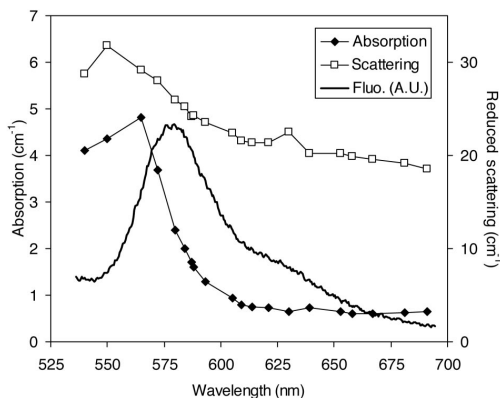


Fig. 3. Optical properties of the resin phantom measured with the integrating-sphere setup. Also shown is the intrinsic fluorescence spectrum (Fluo.) following excitation at 407 nm (arbitrary units).

ern Ireland). The tip of the fiber was in contact with the sample. For the excitation light source, we used a krypton-ion laser emitting at 407 nm with an output

power of 20 mW. Light from the laser was focused on a 400- μm fiber, and the distal end of the fiber was imaged with a lens on the surface of the phantom. This 1:1 imaging arrangement gave a 400- μm top-hat excitation distribution on the surface. Fluorescence spectra were acquired for distances of 0.5–7 mm, in steps of 0.5 mm, from the excitation laser spot, over the spectral range 540–700 nm. The acquired fluorescence spectra were white-light calibrated and deconvolved from the spectral system response function.

We used a Ti:sapphire laser at 780 nm as the excitation source for the Intralipid phantom with a fluorescent layer. The power was limited to ~ 10 mW. The light was guided to the phantom surface by a 400- μm -core-diameter step-index fiber (N.A. = 0.22), and a similar fiber collected the fluorescence light and guided it to a spectrometer (HoloSpec *f/1.8i*; Kaiser Optical Systems, Ann Arbor, Michigan). The laser wavelength was removed with a long-pass filter. A cooled CCD camera (LN/CCD-1024-EERB/1; Princeton Instruments, Trenton, New Jersey) was used for detection. Spectra were acquired over the spectral range 815–930 nm.

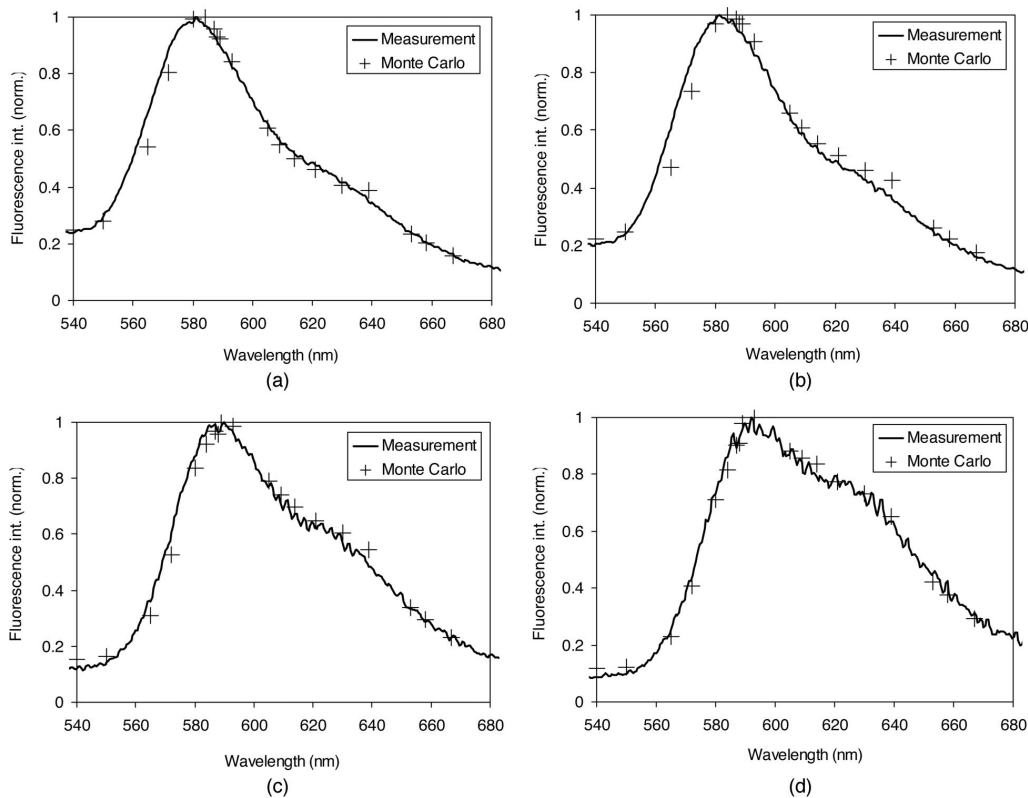


Fig. 4. Experimentally measured and calculated fluorescence spectra for the resin phantom. Results from different distances between the excitation spot and the detection fiber are shown: (a) 0.5 mm, (b) 1 mm, (c) 3 mm, and (d) 5 mm. Int., intensity; norm., normalized.

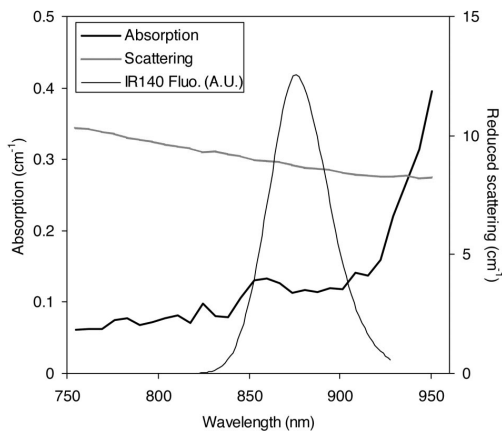


Fig. 5. Optical properties of the Intralipid phantom, as determined by the integrating-sphere setup. Also shown is the intrinsic fluorescence spectrum (Fluo.) of IR140 following excitation at 780 nm (arbitrary units).

3. Results

A. Resin Phantom and Monte Carlo Simulations

The optical properties of the resin phantom, as determined with the integrating-sphere system, are presented in Fig. 3, together with the intrinsic fluorescence spectra of the fluorophores. These data were subsequently used in the Monte Carlo simulations. The scattering anisotropy factor g was around 0.7 over the wavelength range.²³ The results of the simulations are presented in Fig. 4, together with the measurement results for the excitation wavelength of 407 nm. Four different fiber distances are shown: 0.5, 1, 3, and 5 mm. We observed a significant spectral shift as the fiber distance increased. Clearly, a good agreement between simulation and measurement was achieved.

B. Intralipid Phantom and Monte Carlo Simulations

The optical properties of the Intralipid phantom, as determined by the integrating-sphere method (shown in Fig. 5), were used as input for the Monte Carlo simulations. In this case g was around 0.65 over the wavelength range (data not shown). The measured fluorescence spectra at different depths are presented in Fig. 6, which shows the shift of the spectrum as the depth increases. In the Monte Carlo simulations the highest value of the ratio γ was obtained with $\lambda_1 = 815$ nm and $\lambda_2 = 960$ nm. However, owing to the low fluorescence signal at long wavelengths, we had to use a lower λ_2 to obtain a good signal-to-noise ratio from the measurements. Owing to the influence of autofluorescence when the excitation and detection fibers were close together, we used a fiber distance of 5 mm. Therefore the measurement was limited to depths larger than ~ 1 mm. In Fig. 7 we present γ (normalized to the value at $d = 2$ mm) as a function of d for $\lambda_1 = 886$ nm and $\lambda_2 = 922$ nm.

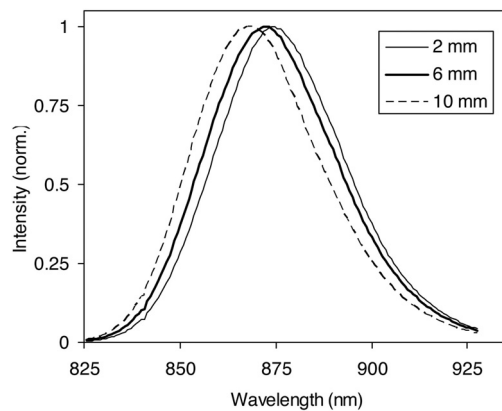


Fig. 6. Measured (normalized) fluorescence spectra for different layer depths (2, 6, and 10 mm) with fluorescing IR140.

By using the simulation results as a calibration curve, we also attempted to predict the depth of the fluorophore from the experimental values of γ . We then calculated the differences between the predicted and the true values of d , which resulted in a standard deviation in the predicted values of 0.6 mm.

C. Tissue Monte Carlo Simulations

For the simulations of realistic tissue, we assumed an excitation wavelength of 615 nm and simulated the fluorescence in the region 625–1005 nm in steps of 10 nm. For each individual simulation (i.e., one wavelength and one set of tissue optical properties), 5×10^5 photon histories were traced. The fluorescing lesion was simulated as a 1-mm-thick layer. The depth of the upper layer to the lesion was varied from 0 to 10 mm.

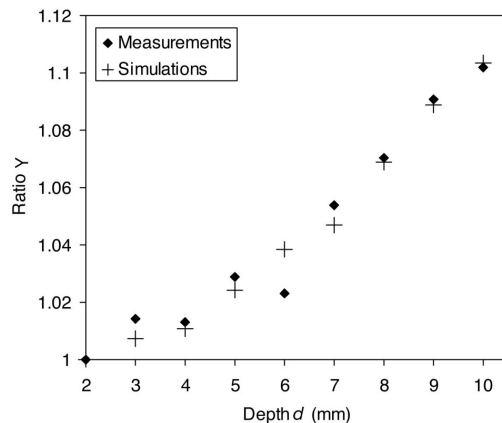


Fig. 7. Ratio γ shown for $\lambda_1 = 886$ nm and $\lambda_2 = 922$ nm as a function of the depth d , normalized to the value for $d = 2$. Results from both the Intralipid phantom measurements and the Monte Carlo simulations are shown.

The simulations were repeated for six different sets of tissue optical properties to account for typical biological variability of the tissue composition, as presented in Fig. 1. First, we wanted to investigate which ratios are the largest and thus best suited for evaluating the depth of the fluorophore. To determine the optimal choice of wavelengths for the method, we plotted $d\gamma/dd$ for $625 \text{ nm} < \lambda_1 < 1025 \text{ nm}$, $625 \text{ nm} < \lambda_2 < 1025 \text{ nm}$. Since the initial results showed that $\gamma(d)$ was approximately linear, we chose to plot $d\gamma/dd$ as determined by the slope of a regression line, rather than plotting $\gamma(d)$ for various depths. The results are presented in Figs. 8(a) and 8(b) for tissue types 1 and 6, respectively. The average of $d\gamma/dd$ for all six tissue types is shown in Fig. 8(c). The points with the largest values in these plots may be interpreted as corresponding to the best wavelength choices in terms of obtaining a high ratio.

By looking at $d\gamma/dd$, it is also possible to assess how robustly the ratios correspond to a given depth for different tissue types. We accomplished this by searching for the λ_1 - λ_2 pair that gives the least variation in $d\gamma/dd$ among the six tissue types. With the requirement that we want $d\gamma/dd$ to be relatively high, the best combinations turned out to be $\lambda_2 = 935 \text{ nm}$, with $\lambda_1 = 695 \text{ nm}$, $\lambda_1 = 745$ - 755 nm , or $\lambda_1 = 875 \text{ nm}$. At $(\lambda_1, \lambda_2) = (695, 935 \text{ nm})$, the mean value was $d\gamma/dd = 0.063 \text{ mm}^{-1}$, with a standard deviation of 0.005 mm^{-1} . At $(\lambda_1, \lambda_2) = (875, 935 \text{ nm})$, the mean value was $d\gamma/dd = 0.043 \text{ mm}^{-1}$, with a standard deviation of 0.005 mm^{-1} . We then applied these values to predict d from the simulation of each of the six tissue types. The result is shown in Fig. 9(a) for $(\lambda_1, \lambda_2) = (695, 935 \text{ nm})$, and in Fig. 9(b) for $(\lambda_1, \lambda_2) = (875, 935 \text{ nm})$. In the first case, most of the predicted values of d are within 1.5 mm of the true value, except for the most water-rich tissue type (1), which consistently overestimates the depth by approximately 2 - 2.5 mm . In the second case, the largest errors occur for tissue types 2 and 6, which are underestimated by as much as 2 mm .

4. Discussion

The results from the resin phantom (Fig. 4) clearly reveal that the shape of the recorded emission spectrum changes according to the detection geometry. As the distance between the source and the detector increases, more spectral intensity shifts to longer wavelengths where the absorption is lower. Similar findings have been reported by other authors.^{16,18-20} The other important conclusion from the results of the resin phantom is that there is very good agreement between the Monte Carlo simulations and the measurements. Thus we are confident in the method of measuring the optical properties of the phantom independently by using the integrating sphere and then applying these values in the Monte Carlo simulations.

The results from the Monte Carlo simulations for a fluorescing layer show that the ratio $\gamma(\lambda_1, \lambda_2)$ is indeed a useful indicator of the depth of a fluorescing

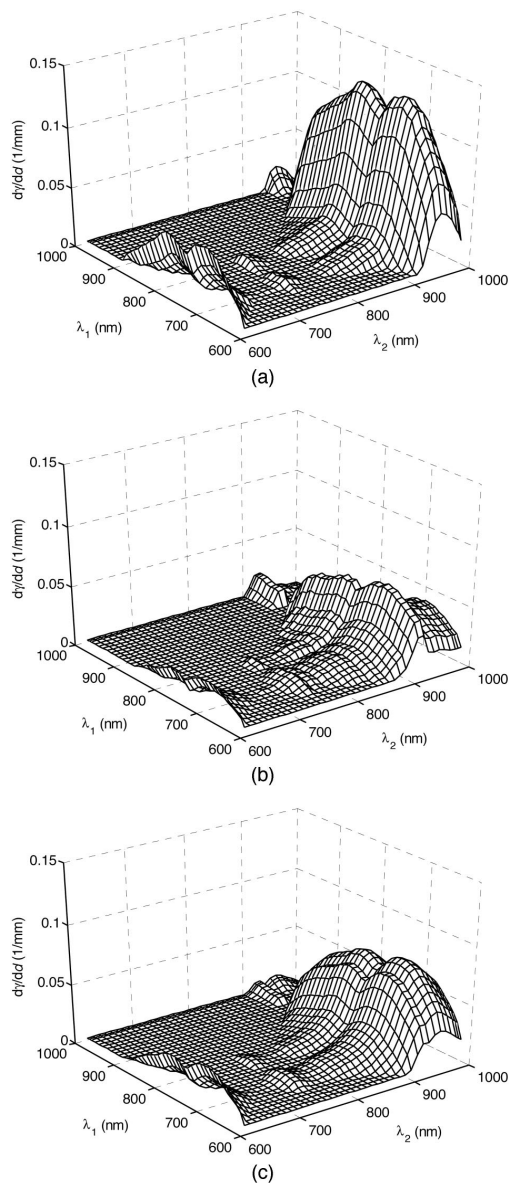


Fig. 8. Plots showing $d\gamma/dd$ as a function of λ_1 and λ_2 . Only the values where $\gamma > 1$ are plotted. (a) Tissue type 1, water rich; (b) tissue type 6, lipid rich; (c) average of all six tissue types.

lesion for the right combinations of wavelengths λ_1 and λ_2 . The results from the phantom measurements corroborate the simulations and show that the method is practically feasible with a relatively simple experimental setup. In the case of the Intralipid phantom, we utilize the difference in water absorption at the slope of the vibrational overtone band that

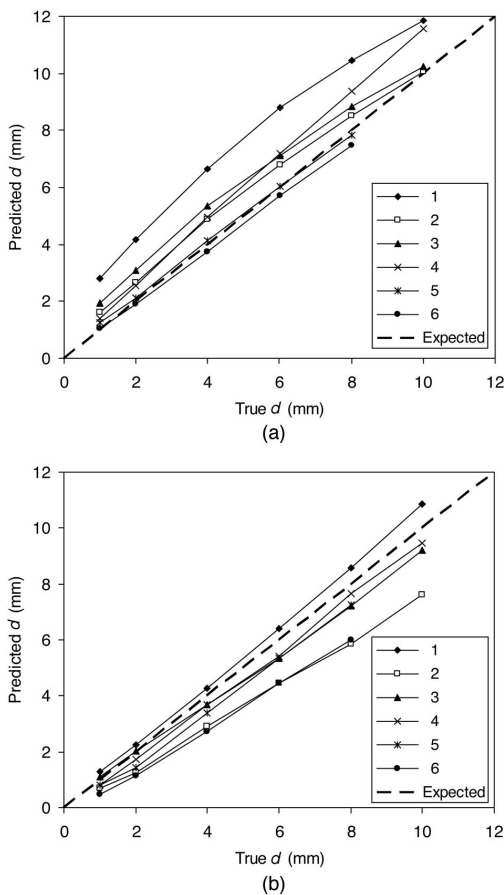


Fig. 9. Values of the depth d predicted from the Monte Carlo simulations for each of the six different tissue types. In all six cases the same calibration was used. (a) Calibration based on the mean value $d\gamma/dd = 0.063 \text{ mm}^{-1}$ at $(\lambda_1, \lambda_2) = (695, 935 \text{ nm})$. (b) Calibration based on the mean value $d\gamma/dd = 0.043 \text{ mm}^{-1}$ at $(\lambda_1, \lambda_2) = (875, 935 \text{ nm})$.

has a maximum absorption at 970 nm. Here we used $\lambda_2 = 922 \text{ nm}$. Although a longer wavelength would have given a higher ratio γ , we were limited to $\sim 930 \text{ nm}$ by the spectrometer and the fact that the fluorescence spectrum for IR140 drops to a low intensity for longer wavelengths (see Fig. 5). We were able to recover the depth of the fluorescing layer from the experimental data with an accuracy of 0.6 mm.

In real tissue there are two regions that may be of interest for choosing the wavelengths λ_1 and λ_2 . One can either use the same slope of the water absorption band above 900 nm, as discussed above, or the slope of the hemoglobin absorption in the 600–650-nm region. The plot in Fig. 8(c) indicates that choosing $\lambda_1 = 695 \text{ nm}$ and $\lambda_2 = 975 \text{ nm}$ would be optimal. However, to get a robust estimate of the depth in a tissue in which the optical properties are unknown *a priori*,

the best choice is also governed by the requirement that γ be insensitive to biological variability. At $\sim 970 \text{ nm}$ the water absorption band yields large differences between water-rich and lipid-rich tissue types, which means that there will be a large variation in $d\gamma/dd$ if $\lambda_2 = 975 \text{ nm}$ is chosen. Instead, using $\lambda_2 \approx 930$ is useful because this is a quasi-isobestic point at which the variation between various soft tissues is minimal, owing to the fact that the absorption spectra of lipid and water cross at this wavelength.²² Considering this, we found that the most robust combination of wavelengths was $\lambda_1 = 695 \text{ nm}$ and $\lambda_2 = 935 \text{ nm}$. With this combination we could recover the depth of the layer with an error of less than 1.5 mm for all tissue types except the most water rich (type 1). Considering the very large differences in tissue composition and thus optical properties between the six tissue types, such a good prediction accuracy is quite encouraging. The use of the wavelength pair $(\lambda_1, \lambda_2) = (695, 935 \text{ nm})$ may be problematic in practice, owing to difficulties in finding a suitable fluorophore with such a wide emission spectrum. Using the wavelengths $(\lambda_1, \lambda_2) = (875, 935 \text{ nm})$ is a more realistic alternative, and the results in Fig. 9(b) show that the depth prediction accuracy for these wavelengths is similar.

It should also be noted that we found the relation between γ and d to be close to linear in all the cases we investigated, meaning that a single value of $d\gamma/dd$ is all that is needed to estimate the depth of a lesion for any measurement. However, the linear dependence of γ on d was only true when small distances between the excitation and the detection fibers were used. For distances above $\sim 5 \text{ mm}$, the relation deviated from linear when the depth was smaller than 1 or 2 mm. This could be of practical concern in some instances, since it may not be possible to place the excitation source and the detector close to each other because of the influence of autofluorescence in the tissue close to the excitation light source. In such cases it may be necessary to have a longer distance and to use nonlinear calibration curves.

It may be possible to improve the accuracy of the depth evaluation by incorporating methods to estimate the optical properties of the tissue, e.g., by measuring the diffuse white-light reflectance of the tissue. This would give some *a priori* information about the absorption and scattering properties in a manner related to the methods described by Stasic *et al.*¹³ and Muller *et al.*¹⁷

We have also considered using temporal information to estimate the depth. The Monte Carlo simulations show that this may be possible, but there are several difficulties. Apart from the increased complexity in the instrumentation, decoupling the fluorophore lifetime and the photon migration time of flight is a nontrivial problem, especially since fluorophore lifetimes are typically an order of magnitude longer than the time of flight. The intrinsic fluorophore lifetime may change depending on the chemical environment, making this procedure increasingly difficult. For our method, we are analogously dependent on the

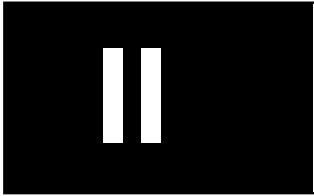
assumption that the intrinsic emission spectrum of the fluorophore does not change according to the chemical environment in the lesion. However, in our case such variations are likely to be small, whereas in the case of the lifetime it will be the dominating effect.

With the present method, we envision a potential application based on a probe that delivers excitation light and at the same time detects the fluorescence light by means of relatively simple photodetectors and wavelength-selecting filters. The operator would manually scan the probe across the tissue, and the information would be presented in the form of an indicator of fluorescence intensity and the estimated depth of the fluorophore. We also consider our method to be quite promising in terms of providing the depth information for image fluorometry and molecular imaging as a means for resolving the fluorophore distribution in three dimensions.²⁶

The authors want to thank Gabriel Somesfalean, Ann Johansson, and Christoffer Abrahamsson. This study was supported by the European Commission grant LSHG-CT-2003-503259 "Molecular Imaging." The authors also acknowledge financial support by the Swedish Research Council. J. Swartling acknowledges support from the Swedish Foundation for International Cooperation in Research and Higher Education and from the Swedish Research Council.

References

1. V. Ntziachristos, J. Ripoll, and R. Weissleder, "Would near-infrared fluorescence signals propagate through large human organs for clinical studies?" *Opt. Lett.* **27**, 333–335 (2002).
2. V. Ntziachristos, C.-H. Tung, C. Bremer, and R. Weissleder, "Fluorescence molecular tomography resolves protease activity *in vivo*," *Nat. Med.* **8**, 757–760 (2002).
3. J. S. Reynolds, T. L. Troy, R. H. Mayer, A. B. Thompson, D. J. Waters, K. K. Cornell, P. W. Snyder, and E. M. Sevick-Muraca, "Imaging of spontaneous canine mammary tumors using fluorescent contrast agents," *Photochem. Photobiol.* **70**, 87–94 (1999).
4. A. Eidsath, V. Chernomordik, A. H. Gandjbakhche, P. Smith, and A. Russo, "Three-dimensional localization of fluorescent masses deeply embedded in tissue," *Phys. Med. Biol.* **47**, 4079–4092 (2002).
5. T. J. Farrell, R. P. Hawkes, M. S. Patterson, and B. C. Wilson, "Modeling of photosensitizer fluorescence emission and photobleaching for photodynamic therapy dosimetry," *Appl. Opt.* **37**, 7168–7183 (1998).
6. T. Johansson, M. S. Thompson, M. Stenberg, C. af Klinteberg, S. Andersson-Engels, S. Svanberg, and K. Svanberg, "Feasibility study of a novel system for combined light dosimetry and interstitial photodynamic treatment of massive tumors," *Appl. Opt.* **41**, 1462–1468 (2002).
7. M. A. O'Leary, D. A. Boas, X. D. Li, B. Chance, and A. G. Yodh, "Fluorescence lifetime imaging in turbid media," *Opt. Lett.* **21**, 158–160 (1996).
8. D. Y. Paithankar, A. U. Chen, B. W. Pogue, M. S. Patterson, and E. M. Sevick-Muraca, "Imaging of fluorescent yield and lifetime from multiply scattered light reemitted from random media," *Appl. Opt.* **36**, 2260–2272 (1997).
9. J. Chang, H. L. Graber, and R. L. Barbour, "Imaging of fluorescence in highly scattering media," *IEEE Trans. Biomed. Eng.* **44**, 810–822 (1997).
10. M. J. Eppstein, D. J. Hawrysz, A. Godavarty, and E. M. Sevick-Muraca, "Three-dimensional, Bayesian image reconstruction from sparse and noisy data sets: near-infrared fluorescence tomography," *Proc. Natl. Acad. Sci. USA* **99**, 9619–9624 (2002).
11. A. B. Milstein, S. Oh, K. J. Webb, C. A. Bouman, Q. Zhang, D. A. Boas, and R. P. Millane, "Fluorescence optical diffusion tomography," *Appl. Opt.* **42**, 3081–3094 (2004).
12. A. D. Klose and A. H. Hielscher, "Fluorescence tomography with simulated data based on the equation of radiative transfer," *Opt. Lett.* **28**, 1019–1021 (2003).
13. D. Stasic, T. J. Farrell, and M. S. Patterson, "The use of spatially-resolved fluorescence and reflectance to determine interface depth in layered fluorophore distributions," *Phys. Med. Biol.* **48**, 3459–3474 (2003).
14. M. Keijzer, R. R. Richards-Kortum, S. L. Jacques, and M. S. Feld, "Fluorescence spectroscopy of turbid media: autofluorescence of the human aorta," *Appl. Opt.* **28**, 4286–4292 (1989).
15. S. Avrillier, E. Tinet, D. Etori, J. M. Tualle, and B. Gélébart, "Influence of the emission-reception geometry in laser-induced fluorescence spectra from turbid media," *Appl. Opt.* **37**, 2781–2787 (1998).
16. C. Eker, "Optical characterization of tissue for medical diagnostics," Ph.D. dissertation (Lund Institute of Technology, Lund, Sweden, 1999).
17. M. G. Muller, I. Georgakoudi, Q. Zhang, J. Wu, and M. S. Feld, "Intrinsic fluorescence spectroscopy in turbid media: disentangling effects of scattering and absorption," *Appl. Opt.* **40**, 4633–4646 (2001).
18. Q. Liu, C. Zhu, and N. Ramanujam, "Experimental validation of Monte Carlo modeling of fluorescence in tissues in the UV-visible spectrum," *J. Biomed. Opt.* **8**, 223–236 (2003).
19. T. J. Pfeifer, L. S. Matchette, A. M. Ross, and M. N. Ediger, "Selective detection of fluorophore layers in turbid media: the role of fiber-optic probe design," *Opt. Lett.* **28**, 120–122 (2003).
20. U. Utzinger and R. R. Richards-Kortum, "Fiber optic probes for biomedical optical spectroscopy," *J. Biomed. Opt.* **8**, 121–147 (2003).
21. J. Swartling, A. Pifferi, A. M. K. Enejder, and S. Andersson-Engels, "Accelerated Monte Carlo model to simulate fluorescence spectra from layered tissues," *J. Opt. Soc. Am. A* **20**, 714–727 (2003).
22. A. Pifferi, J. Swartling, E. Chikoidze, A. Torricelli, P. Taroni, A. Bassi, S. Andersson-Engels, and R. Cubeddu, "Spectroscopic time-resolved diffuse reflectance and transmittance measurements of the female breast at different interfiber distances," *J. Biomed. Opt.* **9**, 1143–1151 (2004).
23. J. Swartling, J. S. Dam, and S. Andersson-Engels, "Comparison of spatially and temporally resolved diffuse-reflectance measurement systems for determination of biomedical optical properties," *Appl. Opt.* **42**, 4612–4620 (2003).
24. S. A. Prahl, M. J. C. van Gemert, and A. J. Welch, "Determining the optical properties of turbid media by using the adding-doubling method," *Appl. Opt.* **32**, 559–568 (1993).
25. C. af Klinteberg, M. Andreasson, O. Sandström, S. Andersson-Engels, and S. Svanberg, "Compact medical fluorosensor for minimally invasive tissue characterisation," *Rev. Sci. Instrum.*, submitted for publication.
26. C. Bremer, V. Ntziachristos, and R. Weissleder, "Optical-based molecular imaging: contrast agents and potential medical applications," *Eur. J. Radiol.* **13**, 231–243 (2003).



Modeling of spectral changes for depth localization of fluorescent inclusion

Jenny Svensson and Stefan Andersson-Engels

Lund University Medical Laser Centre, Department of Physics, Lund Institute of Technology,
P.O. Box 118, SE-221 00 Lund, Sweden
jenny.svensson@fysik.lth.se

Abstract: We have performed modeling of fluorescence signals from inclusions inside turbid media to investigate the influence of a limited fluorescence contrast and how accurately the depth can be determined by using the spectral information. The depth was determined by forming a ratio of simulated fluorescence intensities at two wavelengths. The results show that it is important to consider the background autofluorescence in determining the depth of a fluorescent inclusion. It is also necessary to know the optical properties of the tissue to obtain the depth. A 20% error in absorption or scattering coefficients yields an error in the determined depth of approximately 2-3 mm (relative error of 10-15%) in a 20 mm thick tissue slab.

©2005 Optical Society of America

OCIS codes: (170.5280) Photon migration; (170.3660) Light propagation in tissues; (170.6510) Spectroscopy, tissue diagnostics

References and links

1. S. Gross and D Piwnica-Worms, "Spying on cancer: Molecular imaging in vivo with genetically encoded reporters," *Cancer Cells*, **7**, 5-15 (2005).
2. T. F. Massoud and S. S. Gambhir, "Molecular imaging in living subjects: seeing fundamental biological processes in a new light," *Genes & Development*, **17**, 545-580 (2003).
3. K Shah, A. Jacobs, X. O. Breakefield, and R. Weissleder, "Molecular imaging of gene therapy for cancer," *Gene Therapy*, **11**, 1175-1187 (2004).
4. V. Ntziachristos, C. Bremer, and R. Weissleder, "Fluorescence imaging with near-infrared light: new technological advances that enable in vivo molecular imaging," *Eur. Radiol.* **13**, 195-208 (2002).
5. C. Bremer, V. Ntziachristos, and R. Weissleder, "Optical-based molecular imaging: contrast agents and potential medical applications," *Eur. Radiol.* **13**, 231-243 (2003).
6. V. Ntziachristos, C.-H. Tung, C. Bremer, and R. Weissleder, "Fluorescence molecular tomography resolves protease activity *in vivo*," *Nature Medicine*, **8**, 757-760 (2002).
7. V. Ntziachristos, C. Bremer, E. Graves, J. Ripoll, and R. Weissleder, "In vivo tomographic imaging of near-infrared fluorescent probes," *Molecular Imaging*, **1**, 82-88 (2002).
8. V. Ntziachristos, E. A. Schellenberger, J. Ripoll, D. Yessayan, E. Graves, A. Bogdanov, L. Josephson, and R. Weissleder, "Visualization of antitumor treatment by means of fluorescence molecular tomography with an annexin V-Cy5.5 conjugate," *Proc. Natl. Acad. Sci. USA*, **101**, 12294-12299 (2004).
9. X Gao, L Yang, J. A. Petros, F. F. Marshall, J. W Simons, and S. Nie, "In vivo molecular and cellular imaging with quantum dots," *Current Opinion in Biotechnology*, **16**, 63-72 (2005).
10. X. Michalet, F. F. Pinaud, L. A. Bentolila, J. M. Tsay, S. Doose, J. J. Li, G. Sundaresan, A. M. Wu, S. S. Gambhir, and S. Weiss, "Quantum dots for live cells, in vivo imaging and diagnostics," *Science*, **307**, 538-544 (2005).
11. J. Swartling, J. Svensson, D Bengtsson, K Terike, and S. Andersson-Engels, "Fluorescence spectra provide information on the depth of fluorescent lesions in tissue," *Appl. Opt.* **44**, 1934-1941 (2005).
12. S. Avriillier, E. Tinet, D. Ettore, J.-M. Tualle, and B. Gélébart, "Influence of the emission-reception geometry in laser-induced fluorescence spectra from turbid media," *Appl. Opt.* **37**, 2781-2787 (1998).
13. M. Keijzer, R. R. Richards-Kortum, S. L. Jacques, and M. S. Feld, "Fluorescence spectroscopy of turbid media: Autofluorescence of the human aorta," *Appl. Opt.* **28**, 4286-4292 (1989).
14. Q. Liu and N. Ramanujam, "Experimental proof of the feasibility of using fiber-optic probe for depth-sensitive fluorescence spectroscopy of turbid media," *Opt Lett.* **29**, 2034-2036 (2004).
15. Q. Liu, C. Zhu, and N. Ramanujam, "Experimental validation of Monte Carlo modeling of fluorescence in tissues in the UV-visible spectrum," *J. Biomed. Opt.* **8**, 223-236 (2003).

16. M. G. Muller, I. Georgakoudi, Q. Zhang, J. Wu, and M. S. Feld, "Intrinsic fluorescence spectroscopy in turbid media: disentangling effects of scattering and absorption," *Appl. Opt.* **40**, 4633-4646 (2001).
17. T. J. Pfeifer, L. S. Matchette, A. M. Ross, and M. N. Ediger, "Selective detection of fluorophore layers in turbid media: the role of fiber-optic probe design," *Opt Lett.* **28**, 120-122 (2003).
18. S. Andersson-Engels, A. Gustafson, J. Johansson, U. Stenram, K. Svanberg, and S. Svanberg, "Laser-induced fluorescence used in localizing atherosclerotic lesions," *Lasers Med. Sci.* **4**, 171-181 (1989).
19. T. H. Foster, E. L. Hull, M. G. Nichols, D. S. Rifkin, and N. Schwartz, "Two-steady-state methods for localizing a fluorescent inhomogeneity in a turbid medium" in *Optical Tomography and Spectroscopy of Tissue: Theory, Instrumentation, Model, and Human Studies II*, B. Chance and R. R. Alfano, eds., Proc. SPIE **2979**, 741-749 (1997).
20. E. L. Hull, M. G. Nichols, and T. H. Foster, "Localization of luminescent inhomogeneities in turbid media with spatially resolved measurements of cw diffuse luminescence emittance," *Appl. Opt.* **37**, 2755-2765 (1998).
21. M. S. Patterson, S. Andersson-Engels, B. C. Wilson, and E. K. Osei, "Absorption spectroscopy in tissue-simulating materials: a theoretical and experimental study of photon paths," *Appl. Opt.* **34**, 22-30 (1995).
22. M. S. Patterson and B. W. Pogue, "Mathematical model for time-resolved and frequency-domain fluorescence spectroscopy in biological tissues," *Appl. Opt.* **33**, 1963-1974 (1994).
23. J. Swartling, A. Pifferi, A. M. K. Enejder, and S. Andersson-Engels, "Accelerated Monte Carlo model to simulate fluorescence spectra from layered tissues," *J. Opt. Soc. Am. A.* **20**, 714-727 (2003).
24. A. Torricelli, A. Pifferi, P. Taroni, E. Giambattistelli, and R. Cubeddu, "In vivo optical characterization of human tissues from 610 to 1010 nm by time-resolved reflectance spectroscopy," *Phys. Med. Biol.* **46**, 2227-2237 (2001).
25. S. A. Prah., "Optical Absorption of Hemoglobin." (Oregon Medical Laser Center, 2004), <http://omlc.ogi.edu/spectra/hemoglobin/index.html>
26. S. Montán, K. Svanberg, and S. Svanberg, "Multi-color imaging and contrast enhancement in cancer tumor localization using laser-induced fluorescence in hematoporphyrin derivative (HpD)-bearing tissue," *Opt. Lett.* **10**, 56-58 (1985).
27. K. M. Yoo, F. Liu, and R. R. Alfano, "Imaging through a scattering wall using absorption," *Opt. Lett.* **16**, 1068-1070 (1991).
28. T. Svensson, J. Swartling, P. Taroni, A. Torricelli, P. Lindblom, C. Ingvar, and S. Andersson-Engels. "Characterization of normal breast tissue heterogeneity using time-resolved near-infrared spectroscopy." *Phys. Med. Biol.* (to be published).
29. C. Eker, S. Montán, E. Jaramillo, K. Koizumi, C. Rubio, S. Andersson-Engels, K. Svanberg, S. Svanberg, and P. Slezak, "Clinical spectral characterisation of colonic mucosal lesions using autofluorescence and δ aminolevulinic acid sensitisation," *Gut.* **44**, 511-518 (1999).
30. N. Ramanujam, M. F. Mitchell, A. Mahadevan-Jensen, S. L. Thomsen, G. Staerke, A. Malpica, T. Wright, N. Atkinson, and R. Richards-Kortum, "Cervical precancer detection using a multivariate statistical algorithm based on laser-induced fluorescence spectra at multiple excitation wavelengths," *Photochem. Photobiol.* **64**, 720-735 (1996).
31. V. V. Verkhusha and K. A. Lukyanov, "The molecular properties and applications of Anthozoa fluorescent proteins and chromoproteins," *Nature Biotechnology.* **22**, 289-296 (2004).
32. S. R. Arridge, "Optical tomography in medical imaging," *Inverse Problems.* **15**, R41-R93 (1999)

1. Introduction

One biomedical field where fluorescent inclusions are to be found is molecular imaging, where biological processes can be studied at cellular and molecular levels [1-3]. Biological processes can be monitored by using specific molecular probes, which seek out target molecules. These probes are frequently designed to provide characteristic fluorescence. To collect the induced fluorescence light, an optical imaging technique is employed.

Detection of fluorescence light emitted from the molecular probes can be used to determine the spatial location of specific cells inside the tissue and the concentration of the probe. Several optical imaging techniques can be used to detect tissue luminescence: fluorescence reflectance imaging (FRI), bioluminescence imaging (BLI) and fluorescence-mediated molecular tomography (FMT) [2-4].

One aspect of molecular imaging is the development of molecular probes emitting in the NIR region, where tissue exhibits low absorption, allowing deep penetration of light into the tissue. In the NIR region, deeply located inclusions could then also be monitored in highly vascularized tissue [5]. Molecular probes emitting fluorescence in the NIR region are desirable and under development [5-10]. Presently most fluorescence detection is conducted

with probes fluorescing in the visible, mainly by fluorescent proteins. Tissue autofluorescence is relatively high in this wavelength region, leading to a relatively low fluorescence contrast between the fluorescence from the probe at low concentrations and tissue autofluorescence [5]. Fluorescence contrast is defined as the ratio of the induced fluorescence in the fluorescent probe and the background fluorescence. Visible light also has low penetration in tissue, and deeply located inclusions, especially in tissue with a high hemoglobin concentration, are difficult to detect.

In a previous study, we demonstrated a method to determine the depth of an embedded inclusion marked with a fluorescent probe [11]. As the depth, size of inclusion, and concentration are parameters that can be difficult to evaluate independently with fluorescence imaging [4], independent information on any of these parameters will make the determination and localization of the object more accurate. The demonstrated method relies on spectral changes in the fluorescence as it propagates through the tissue. The characteristics of the detected fluorescence light depend on many different factors, for example, the optical properties of the tissue, the depth of the fluorescent inclusion, and the detection geometry [12–18]. Studies to determine the depth of a luminescent source embedded in a liquid phantom have been performed previously [19,20]. The concept of forming a ratio of acquired data to determine the depth of a fluorescent inclusion has been reported using two different excitation beam diameters [19]. An expression of diffusion theory for the emittance from a luminescent source has been fitted to spatially resolved measurements of the diffuse reflectance, providing an accuracy of the depth of an isotropic point source of 1 mm [20]. Also Patterson *et al.* used fluorescence to study the depth of light transport in tissue [21,22].

The absorption coefficient in tissue is strongly wavelength-dependent in the region from the visible to the NIR region. The dependence of tissue absorption and scattering on wavelength leads to a spectral change in the fluorescence light as it propagates through the tissue, especially the dependence of tissue absorption has been discussed in [18]. The deeper a fluorescent lesion is located in the tissue, the greater the change in intensity between different fluorescence wavelengths. In our previous study [11], the depth of a fluorescent layer was determined with both Monte Carlo simulations and experiments on a liquid phantom, by studying the fluorescence emitted in the 800–900 nm range in reflection geometry. The depth of a fluorescent layer could be determined with an accuracy of 0.6 mm down to a depth of 10 mm.

The aim of this study was to further investigate the usefulness of a depth-resolving technique based on spectral information in the visible wavelength region. Two fluorescence wavelengths (540 nm and 615 nm) were chosen where difference in tissue absorption is large. The wavelengths could in principle be chosen according to a difference in tissue scattering, but as the differences in scattering in general are smaller, the wavelengths were selected based on absorption changes. Limited fluorescence contrast and uncertainties in the optical properties are two important issues in the technique investigated here, especially of importance for detection in the visible region. The effect on a calculated ratio between the fluorescence intensities at two wavelengths as a function of depth was investigated when the optical properties were changed. Low fluorescence contrast is also a realistic problem when working in the visible wavelength region, because of the tissue autofluorescence emitted upon illumination with blue-green light. When working in the NIR region the problem with low fluorescence contrast is much smaller, because tissue autofluorescence is very weak in this wavelength region. The fluorescence contrast will be low when working with fluorescent proteins, because most of them fluoresce in the visible region.

2. Material and methods

2.1 Geometry of the modeled tissue

In Fig. 1, a schematic of the simulation geometry is shown. A layered structure is assumed. The model of tissue is divided into 60 elements in the radial direction, each element being 0.05 cm wide. The z -direction is divided into 80 or 120 elements depending on the thickness of the model, each element being 0.025 cm long. A fluorescent layer with a thickness of 1 mm can be inserted at any depth in the model.

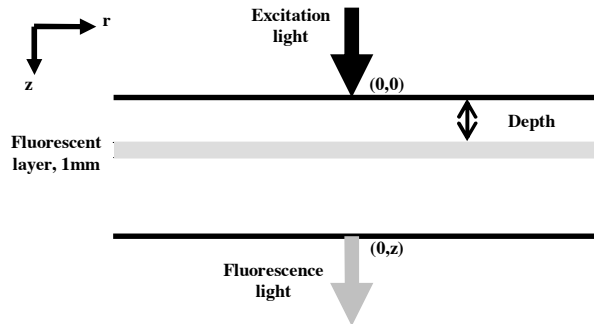


Fig. 1. Schematic of the geometry used to simulate fluorescence with Monte Carlo calculations. It assumes a layered structure, where z denotes the thickness of the sample.

A pencil beam is assumed to enter the phantom at the point $(r,z) = (0,0)$, as illustrated in Fig. 1. The transmitted fluorescence light is detected as a function of the radius, r . This corresponds to illumination with a thin laser beam and imaging detection of the transmitted fluorescence.

2.2 Fluorescence Monte Carlo simulations

An accelerated fluorescence Monte Carlo method, described in detail previously [23], was used to simulate the fluorescence generated inside an object and its transport to the back surface, where it could be detected. In this code, a Monte Carlo simulation is first performed using optical properties specified for the modeled tissue at the excitation wavelength. This simulation provides an absorption map of the fluorophore. Another simulation is then performed at the fluorescence emission wavelength, yielding a probability distribution of the generated fluorescence inside the volume to be detected at position $(0,z)$. The matrices for the excitation and emission wavelengths are then convolved to yield the probability of detecting a transmitted fluorescent photon (Γ) as a function of radial distance. Additional inputs to the Monte Carlo simulations, apart from the optical properties of the different layers and the geometry, are the fluorescence contrast and the absorption coefficient of the fluorophores in the fluorescent layer and surrounding tissue. The simulations are accelerated by using a reciprocity theorem. With this concept only one simulation is required for each emission wavelength, rather than one per wavelength for each volume element in the model [23].

2.3 Evaluation of the data

For each wavelength a vector with the probability of detecting a transmitted fluorescence photon as a function of radial distance was calculated. The ratio of the vectors obtained from simulations at two different emission wavelengths was calculated according to Eq. (1):

$$\gamma = \frac{\Gamma(540)}{\Gamma(615)} \quad (1)$$

Data from a point (0,z) was selected for the illustrations, in order to easily compare the results of the ratio as a function of depth for different parameters in the same graph.

2.4 Optical properties of the tissue model

The optical properties used in the simulations were extracted from the results presented in Ref. [24]. In that study, the measurements were performed on *in vivo* muscle tissue with relatively low blood content. The relations in Eqs (2) and (3) were employed to obtain optical properties at the wavelengths used, where hemoglobin and oxyhemoglobin are assumed to be the dominant absorbers in the visible wavelength region [24]. The absorption is given by

$$\mu_a(\lambda) = \sum_i c_i \varepsilon_i(\lambda) \quad (2)$$

where c_i is the concentration and ε_i is the extinction coefficient of the absorbing molecule, while the reduced scattering can be expressed as

$$\mu_s'(\lambda) = a\lambda^b \quad (3)$$

The extinction coefficients for hemoglobin and oxyhemoglobin at 488 and 540 nm were obtained from Ref [25] and the concentrations of hemoglobin and oxyhemoglobin were obtained from Ref [24]. The optical properties obtained for the phantom at the three wavelengths are given in Table 1. The fluorescence yields were assumed to be the same at both wavelengths.

Table 1. Optical properties of the tissue model

Wavelength / nm	μ_a / cm^{-1}	μ_s' / cm^{-1}
488	0.89	18
540	2.13	16
615	0.14	14

2.5 Simulation of a 3 cm thick tissue model

The number of photons used in each simulation was 70 million, with a total thickness of the phantom of 3 cm. The optical properties used are given in Table 1. One simulation was performed for the excitation wavelength and for each of the two fluorescence emission wavelengths. The matrix obtained for the excitation light was multiplied, pixel-by-pixel, by the matrix giving the fluorescence yield. One such multiplication was performed for each depth of the fluorescence layer, yielding an excitation matrix for each depth of the layer. Finally, a convolution was performed between the excitation matrix and each of the two fluorescence matrices. The convolution was performed for each depth of the fluorescent layer. The depths of the layer in the model were: 1, 4, 7, 10, 13, 16, 19, 22, 25 and 28 mm from the excitation surface.

2.6 Changes in optical properties

The optical properties of the tissue model were altered slightly to evaluate the sensitivity of the fluorescence emission ratio, γ , to such variations. Five different simulations were performed, changing the absorption or reduced scattering coefficient at all wavelengths by $\pm 20\%$. When not altered, the optical properties given in Table 1 were used. The properties

changed are listed in Table 2. The total thickness of the model was 20 mm, and the number of photons for each simulation was 10 million. In all other aspects, the simulations were identical to these described in Section 2.5.

Table 2. The optical properties used to simulate the effects of changes in optical properties on the fluorescence ratio.

λ / nm	$\mu_a -20 \%$		$\mu_a +20 \%$		$\mu'_s -20 \%$		$\mu'_s +20 \%$	
	μ_a / cm^{-1}	μ'_s / cm^{-1}						
488	0.71	18	1.07	18	0.89	14.4	0.89	21.6
540	1.7	16	2.56	16	2.13	12.8	2.13	19.2
615	0.11	14	0.17	14	0.14	11.2	0.14	16.8

Simulations were also performed to model how the ratio is affected when the relative attenuation of the two fluorescence wavelengths is changed. The absorption coefficient was varied for the fluorescence wavelength at 540 nm according to Table 3. The depths of the layer in the model were: 3, 7, 10, 13 and 19 mm from the excitation surface.

Table 3. Absorption coefficient of the tissue model with different attenuation at the fluorescence wavelengths

$\mu_a (540 \text{ nm}) / \text{cm}^{-1}$	$\mu_a (615 \text{ nm}) / \text{cm}^{-1}$	Factor
0.28	0.14	2
0.7	0.14	5
1.4	0.14	10
2.13	0.14	15

2.7 Contrast in fluorescent phantoms

In the last part of this study, the influence of fluorescence contrast in the tissue model was studied. Here we simulated the case where the bulk tissue surrounding the layer also exhibited fluorescence, and the contrast between the bulk tissue and the fluorescent layer was varied. The fluorescence contrast of the tissue model was assumed to be 1, 10, 25, 50, 100 and infinity. Fluorescence contrast of 1 corresponds to the situation of having only autofluorescence in the entire model and a contrast of infinity corresponds to fluorescence induced in the fluorescent layer only. The different values of the fluorescence contrast were chosen to study the trend of the intensity ratio as a function of depth when changing the contrast value. The investigated depths of the layer were 4, 10, 16, 19, 25 and 28 mm. Otherwise the input data in Section 2.5 were used.

3. Results

Figure 2 shows the simulated radial profiles in a logarithmic scale of fluorescence emitted from the surface of a tissue model containing a fluorescent layer at three different depths 13, 16 and 19 mm. The graph to the left shows the radial profiles for the transmitted fluorescence at 540 nm, while the graph in the middle shows the corresponding fluorescence at 615 nm. The graph to the right shows the radial profile of the ratio between 540 and 615 nm. These results are given for an ideal case with infinite fluorescence contrast where fluorescence is induced only in the thin fluorescent layer.

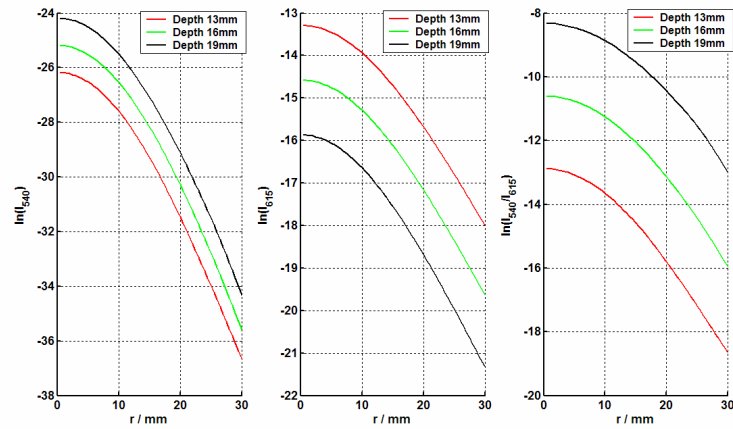


Fig. 2. Left: the radial profile for the yellow fluorescent wavelength for depths of 13, 16 and 19 mm. Middle: the radial profile for the red fluorescence at the same depths, and right: the ratio between the yellow and the red fluorescence at the same depths.

The image in the upper left corner of Fig. 3 shows the simulated distribution of the excitation light on a logarithmic scale in a tissue model, assuming the optical properties listed in Table 1 in the entire volume. The image to the lower left describes the fluorescence emitted in a layer at $z = 4$ mm. The images in the center show the probability of detecting fluorescence at $r = 0$ in the model, emitted from various positions in the model at two fluorescence wavelengths (upper row 540 nm and lower row 615 nm). These maps were modeled using a reverse Monte Carlo simulation from the backside of the model.

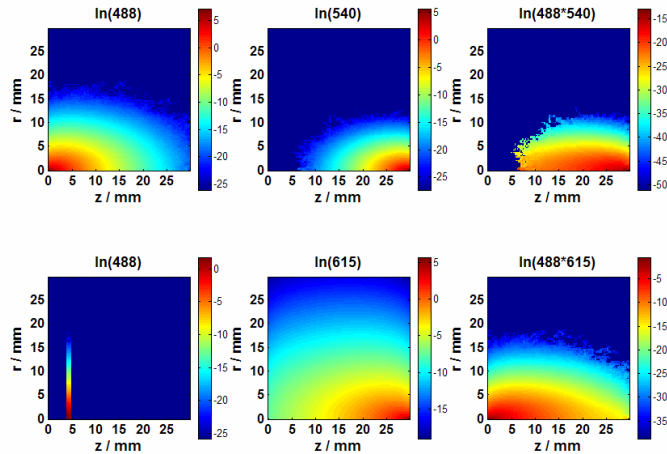


Fig. 3. Upper row: left, the distribution of the excitation light where the light can be absorbed; middle, the probability of fluorescence emitted at 540 nm to be detected at position $r = 0$ and $z = 30$; and right, the result of multiplying the excitation and emission images. Lower row: corresponding images for fluorescence emission light at 615 nm. The image in the lower left corner shows the distribution of the fluorescence emission inside the model with a fluorescence layer at $z = 4$ mm and an infinite fluorescence contrast.

To the right in Fig. 3, the results of a multiplication of the excitation by the fluorescence light is shown, assuming that the entire model has a uniform fluorescence efficiency of unity, i.e. using the map in the upper left corner for the excitation. This multiplication provides maps of the areas contributing to the fluorescence emitted at $r = 0$, and are calculated as an overlap between the excitation and the fluorescence light. Such a map is of interest when evaluating fluorescence at different wavelengths escaping the model versus the position of the fluorescent layer.

In Fig. 4 the calculated yellow/red ratio as a function of depth of the fluorescent layer is presented in logarithmic scale for various optical properties (see Table 2). The absorption or scattering coefficients for the three wavelengths were changed by $\pm 20\%$ at the same time. Figure 5 shows the logarithmic value of the ratio as a function of depth when the relative attenuation of the two wavelengths is changed. The absorption coefficient at 540 nm was changed to achieve a relative difference of the two wavelengths by the factors 2, 5, 10 and 15.

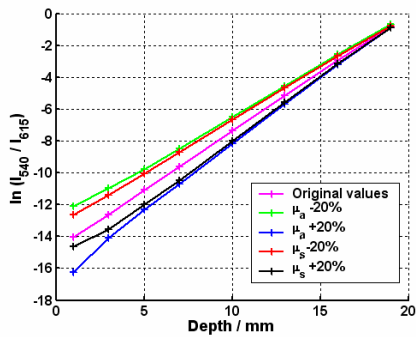


Fig. 4. Logarithmic value of the yellow/red ratio as a function of depth for optical properties according to Table 2.

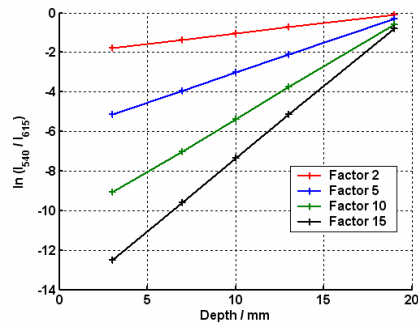


Fig. 5. Ratio of the two intensities in a logarithmic scale as a function of depth, when the relative attenuation of the two wavelengths is changed.

The results below show how the detected fluorescence is altered by autofluorescence from the surrounding bulk tissue. Figure 6 shows the detected yellow and red intensities as a function of depth of the fluorescent layer for different contrast between the layer and the rest of the tissue model and also the yellow/red ratio. As can be seen the slope of the curve decreases as the contrast is reduced, leading to a less sensitive determination of the depth of the object. For a low contrast it becomes difficult to determine the depth, especially in the center of the model.

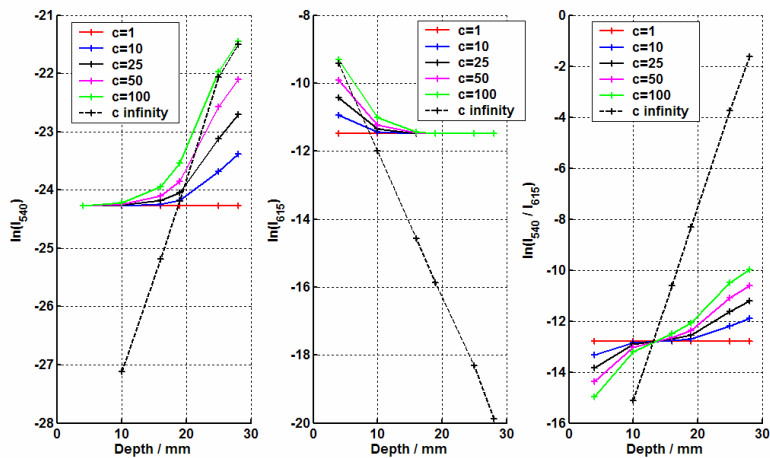


Fig. 6. Left: the detected yellow intensity as a function of the depth of the layer, middle: the corresponding for the red intensity and right: the yellow/red ratio. The legend corresponds to the contrast between the layer and the rest of the tissue model. c denotes the fluorescence contrast.

4. Discussion

Monte Carlo simulations were performed to determine the depth of a fluorescent layer inside a homogeneous tissue-like medium, assuming excitation with blue light and detection of yellow and red fluorescence wavelengths in transmission geometry. A calculated yellow/red ratio is depth-dependent when the tissue model exhibits difference in absorption at the two detection wavelengths, as the spectral shape changes as the light propagates through the medium [18].

To determine the depth, we utilized the concept of a dimensionless ratio. In real measurements there are always advantages in using a dimensionless ratio, because some of the experimental parameters will be canceled out. Examples of these parameters are fluctuations in the illumination source and object distance [26]. By forming a ratio, we limit the evaluation to two wavelengths. This automatically leads to the question of which wavelengths should be used to yield the best depth resolution and robustness. The choice of wavelengths depends on both the availability of a suitable fluorophore as well as the optical properties of the tissue and the presence of tissue autofluorescence. Below we discuss the choice of wavelength range in terms of light penetration, uncertainties in optical properties, and the presence of tissue autofluorescence.

Light obviously penetrates better, the lower the attenuation coefficient. This means that it is easier to detect fluorescence embedded in tissue in the NIR region between 600 and 900 nm, as at these wavelengths the absorption by hemoglobin, lipids and water is low. This is especially important for thick tissues containing large amounts of hemoglobin. Higher absorption will, however, preferentially attenuate light with a long path length in the tissue, yielding a less diffuse image. Increased absorption thus means a lower signal, but higher spatial resolution. This has previously been explored by Yoo *et al.* [27].

One should also choose a pair of wavelengths for which the relative attenuation is more or less independent of the exact composition of the tissue. This is of great importance when the tissue composition varies in the volume studied, or is unknown because of large interindividual variations, for example, due to lipid and water content. If two wavelengths are identified, for which different tissue types exhibit almost the same optical properties, the depth of a fluorescent inclusion can be determined much more robustly. In a previous simulation

study [11], the depth resolution for NIR fluorescence was investigated for six tissue types, ranging from water-rich to lipid-rich. Using the data obtained from those simulations, the depth of a lesion could be determined with an accuracy of 2 mm, without knowing the tissue composition. It thus seems to be possible to find such a wavelength pair around 930 nm, where water and lipids are the major absorbers, and absorb to similar degree. Variations in tissue composition are, from the absorption point of view, due to the relative amounts of lipids and water. In the visible region, where hemoglobin is the major absorber, it is not possible to find such wavelength regions, where the absorption is equal for tissue with various amount of hemoglobin. As the absorption of both wavelengths used scale linearly with the hemoglobin concentration, the relative absorption will, however, remain the same and a proper wavelength pair can thus be selected. Alterations of $\pm 20\%$ correspond to the variation in hemoglobin content that we found to be realistic for intersubject variation [28]. As hemoglobin is the main absorber for the excitation wavelength, as well as for both detection wavelengths in the visible region, all absorption coefficients were varied simultaneously in the simulations. The results show that a change of 20% in either the absorption or scattering coefficient still causes a considerable difference in the ratio at positions far from the detector (small depths), yielding a depth variation determined from the ratio of approximately 2–3 mm, see Fig. 4. This corresponds to a relative error in the determination of the depth of 10–15%. For layers closer to the detector the ratio is more or less independent of the optical properties, and the depth variation is only 0.5–1 mm. It is interesting to note in Fig. 4 that a change in μ_a of +20% and a change in μ'_s of +20% cause almost the same effect on the ratio. If diffusion of light can be assumed in the medium, scattering effects are described with the reduced scattering coefficient μ'_s , and the remaining light fluence rate as a function of distance from a source is described by the exponential law $\exp(-\mu_{\text{eff}} \cdot d)$, where μ_{eff} is the effective attenuation coefficient, see Eq. (4), and d is the distance.

$$\mu_{\text{eff}} = \sqrt{3\mu_a(\mu_a + \mu'_s)} \quad (4)$$

This explains why the change in μ_a and μ'_s provides similar results. A $\pm 20\%$ change in the absorption or scattering coefficient results in an approximately $\pm 10\%$ difference in μ_{eff} . If diffusion is assumed, the logarithmic ratio between the fluorescence intensities at two wavelengths as a function of depth will thus be linear with a slope determined by the differences in μ_{eff} . Figures 4 and 5 show linear relations of the logarithmic ratio as a function of depth, which suggests diffusion being valid. It should, however, be noted that diffusion is not always valid and non-linear shapes of the logarithmic ratio may occur.

This leads to the question of how great a difference in absorption between the two detection wavelengths is needed to achieve sufficient depth resolution. It is not always ideal to have as large difference as possible. A larger difference in absorption provides better depth resolution, but too high absorption prevents the light from penetrating deeply into the tissue. This is clearly illustrated in Fig. 3. Only inclusions close to the detector would be detected with a high absorption. Here the overlap of excitation light and emitted fluorescence light can be seen for the two fluorescence wavelengths involved. If there is no overlap, no fluorescence will be observed at the detector surface. As can be seen, no value can be obtained for the ratio for layers located at depths less than 0.5 cm when using the optical properties given in Table 1. This would be the case for the layer at the depth of 4 mm where the fluorescence would only be induced in this layer, which is indicated in the lower left image in Fig. 3. The absorption at 540 nm is so large that the light cannot reach the detector side. This can be compared to the situation when measuring in reflection geometry, then the method would be more sensitive to fluorescence from depths closer to the excitation side. These images show how important it is to select the fluorescence wavelengths carefully. If a wavelength with too high an absorption is chosen then the detectable depths will be limited to a smaller region. Another interesting remark is that the trend of the yellow fluorescence curve differs from that

of the red fluorescence curve, as can be seen in Figs. 2 and 6. The trend of the yellow fluorescence curve indicates an increase in fluorescence; this is because of the higher absorption of the yellow light compared to the absorption of the excitation light. This can also be seen in the images in the upper row in Fig. 3. For the red wavelength it is the opposite relation providing a decrease in fluorescence instead, as can also be seen in the images in the lower row in Fig. 3. In Fig. 5 it is also illustrated how important it is to know the relative attenuation of the two wavelengths used in order to determine the depth of an inclusion, as the slope of the ratio as a function of depth alters significantly with changes in the relative attenuation.

The concept of using a ratio to evaluate the spectral changes may be improved by using the statistical approach of multivariate analysis. These techniques have been used to analyze tissue in order to distinguish between malignant and non-malignant tissue and to delineate tumors in various types of tissue [29,30]. Utilizing this concept, information obtained from many wavelengths could be used to increase the depth-resolution. More spectral information should make the analysis more robust when the optical properties of the medium are not fully known. It would also reduce some of the work involved in finding the wavelength pair that provides the best depth resolution. This is something we plan to investigate in the near future.

When illuminating tissue with blue or green light, it will always emit autofluorescence. This autofluorescence is often strong compared to the weak signals from the fluorescence probe, as the volume of the surrounding tissue is so much larger than that of the embedded inclusion. Many fluorescent probes used today, for example the fluorescent proteins, emit in the visible wavelength region, where tissue autofluorescence is much stronger than in the NIR range. It is thus of importance to investigate the more realistic case when the rest of the phantom also fluoresces and not only the embedded object. The results of our Monte Carlo simulations show that a low fluorescence contrast makes it difficult to investigate the fluorescent inclusion, including determining its depth. When the fluorescence contrast is 10, the fluorescence detected from the inclusion is strongly influenced by the autofluorescence, making it difficult to determine the depth of the inclusion as illustrated in Fig. 6. It can also be seen in Fig. 6 that a tissue model containing autofluorescence only, meaning that the contrast is 1, gives a constant value of the ratio. This is a rather trivial result, as the fluorescence should be independent of the position of the layer, in this case when the layer has identical fluorescence properties as the rest of the model. The autofluorescence will contribute to a background fluorescence level. If the detectable fluorescence from the layer is not stronger than this background fluorescence, it will fall into the background noise. This is clearly shown for both wavelengths in Fig. 6. Only in the case with infinite fluorescence contrast, when the surrounding tissue has zero autofluorescence, no such effect is seen. It is interesting to note that it is in the central part of the model where it is difficult to evaluate the depth. This is due to that the 540 nm light is more absorbed than light at the excitation wavelength, yielding a positive slope of the detected fluorescence as a function of depth, while the corresponding curves for 615 nm exhibit a negative slope, as fluorescence emission at this wavelength is less attenuated than the excitation light. This yields a flat region in the central part of the model for the ratio curves. If other wavelengths with a different relation of the optical properties had been chosen, the flat region could have been at either end of the tissue model. The contribution from the autofluorescence thus clearly needs to be considered when the depth is determined by the ratio. The ongoing development of probes in the NIR region is therefore of great importance, so that imaging can be performed in the region where the tissue autofluorescence is minimized and also greater depths can be investigated. Both quantum dots and fluorescent proteins are under development in the NIR region [10,31].

In this study we focused on a homogeneous layered structure, but of course it needs to be investigated what happens for other geometries. There is also a need to study the ratio as a function of depth for a fluorescent object with a different shape. It should be noted that a large object close to the detector has the same radial profile as a small object far from the detector

[4]. It is also important to investigate how this method would work in tissues with other optical properties.

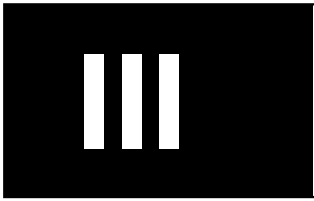
The spectral information to provide depth information of an inclusion may be shown to be useful as independent *a priori* information in tomographic evaluation algorithms. In the NIR region where scattering dominates over absorption the reconstruction of the medium becomes ill conditioned, as discussed for absorption tomography by e.g. Arridge [32]. It can thus become difficult to determine the spatial location of the object and also its size. Additional information may help to refine the reconstruction algorithm.

5. Conclusions

In this study, we have shown that the depth of a fluorescent inclusion can be determined by calculating the ratio of the intensities of two fluorescent wavelengths (yellow and red). We have especially investigated the effect on the ratio when the optical properties are changed, and with different fluorescence contrast.

Acknowledgments

The authors would like to thank Johannes Swartling and Christoffer Abrahamsson. This research was supported by the EU Integrated Project "Molecular Imaging" LSHG-CT-2003-503259.



Fluorescence spectroscopy in tissue phantoms for improved depth resolution in tissue imaging

Jenny Svensson^{*a}, Anikitos Garofalakis^b, Heiko Meyer^b, Florian Forster^a, Jorge Ripoll^b,
Stefan Andersson-Engels^a

^aLund University Medical Laser Centre, Department of Physics, Lund Institute of Technology,
P.O. Box 118, SE-221 00 Lund, Sweden

^bInst. of Electronic Structure & Laser - FORTH, P.O. Box 1527, Vassilika Vouton,
71110 Heraklion, Greece

ABSTRACT

A way to determine the depth of an embedded fluorescent object, for example deep-lying tumors marked with a fluorescent probe, is to detect fluorescent light that has propagated through the medium at two different wavelength bands. A ratio can then be calculated between the corresponding intensities. The wavelength regions should be chosen such that there is a difference in the absorption in the medium. This spectral information could be used as a complement in other methods, for example in tomography, due to its straightforward implementation. In this study we have performed phantom measurements to determine the depth of a fluorescent object, filled with fluorophores. The transmission of yellow and red fluorescence was measured and a ratio of yellow to red fluorescence was calculated for several depths in tissue with a thickness of 2 cm. The ratio showed a clear dependence on the depth of the object.

Keywords: fluorescence spectroscopy, molecular imaging, light propagation

1. INTRODUCTION

Optical tomography is a method to extract the position of small fluorescing volumes embedded in highly scattering media. Several different tomographic techniques have been evaluated to reconstruct the spatial distribution of fluorescent objects in tissue-like media, where the diffusion approximation is often used in this context to describe the light propagation.¹⁻⁵ Also within molecular imaging it is of interest to visualize fluorescent volumes. Molecular imaging is a field in which molecular pathways and events occurring at the molecular level can be monitored by means of fluorescent reporters.^{6,7} To monitor molecular interactions *in vivo*, specific molecular probes are needed that seek specific target molecules. These probes may be designed to emit fluorescent light upon excitation and to be activated only in the presence of specific enzymes,⁸ yielding information on processes occurring at the molecular level. Different optical techniques have been developed for light emission-based molecular imaging: fluorescence reflectance imaging (FRI),^{7,9} bioluminescence imaging (BLI)⁷ and fluorescence-mediated molecular tomography (FMT).^{8,10-12} FMT is a technique that reconstructs three-dimensional images of the distribution of a fluorescent molecular probe in tissue. In FMT, tissue is illuminated with excitation light at several projections. Fluorescence light that has propagated through the tissue is then detected.¹¹ The tomographic algorithm is often relatively ill conditioned in turbid media, making it difficult to accurately and independently predict the depth, size and concentration of the fluorescent inclusion. In the NIR wavelength region where light penetrates well and is highly scattered, due to the relatively low absorption, it is of interest to use as much *a priori* knowledge as possible. Spectral information could be used to improve the robustness in the tomographic evaluation.

The spectral changes in the fluorescence as it propagates through the tissue can be used to determine the depth of an embedded inclusion labeled with a fluorescent probe.^{13,14} Different factors, for example the optical properties in tissue, the depth of the fluorescent inclusion and the detection geometry can influence the spectral shape of the fluorescence.¹⁵⁻¹⁸ The absorption coefficient of tissue is wavelength-dependent in the region from the visible to the NIR region. Different wavelength components of the fluorescent light will be attenuated differently by the absorption as it propagates through

* jenny.svensson@fysik.lth.se; phone +46 46 2223119

the tissue. There will be a greater change in intensity between different fluorescent wavelengths that originates from a deeper-lying lesion in the tissue. The ratio of the fluorescence signals at two wavelengths can provide additional information about the depth of the fluorescent inclusion. In a previous study,¹⁴ the concept of forming a dimensionless ratio between two fluorescence wavelengths was demonstrated with both Monte Carlo simulations and experiments on a liquid phantom using a fluorophore in the 800-900 nm range. The results showed that the depth of a fluorescent layer could be determined with an accuracy of 0.6 mm down to a depth of 10 mm.

In the NIR region, light can penetrate deep into tissue, providing the possibility to study deep-lying inclusions in tissue.¹⁹ Therefore the development of specific molecular probes in the NIR region is of importance.^{8,11,12,20,21} A group of molecular probes are based on the specific genes that can control the production of fluorescent proteins in cells.^{7,22} There exists a variety of fluorescent proteins that fluoresce in different parts of the visible spectrum.^{7,23} Investigations utilizing fluorescent proteins as molecular probes are of great importance, since they can be used, for example to identify tumors in experimental studies.^{7,19} Studies with these fluorescent proteins however, have to deal with the limitation that they emit light in the visible wavelength region. In this region high absorption yields a low penetration of light and the tissue autofluorescence is strong. These effects have so far limited their use to small animals or to tissues with absorption. A benefit of the high absorption is that the tomographic algorithm is less ill conditioned, as light in a more narrow path between excitation and detection positions is favored.²⁴

The aim of this study was to investigate whether the fluorescence ratio concept could provide useful information in tissue in the visible region where low fluorescence contrast between the inclusion and the bulk tissue can influence the measurements. Fluorescence measurements were performed in tissue with an inserted glass tube containing a fluorescent liquid. The glass tube was placed at different depths in a tissue phantom. For each depth fluorescence images were acquired, one yellow and one red fluorescence image. The two fluorescence images were then used to calculate a depth-dependent ratio.

2. MATERIAL AND METHODS

2.1 Experimental equipment

The experimental setup used in the study is illustrated in Figure 1. A multiline argon-ion laser (Coherent, Innova400, Santa Clara, CA 95054 USA) emitting at several wavelengths (488 and 514 nm) was used as an excitation source. A laser beam, with a diameter of 6 mm, illuminates one side of the phantom. The tissue phantom used was an excised tissue sample consisting of porcine muscle *in vitro*. A thin glass tube containing two fluorophores is placed at different depths in the tissue. The light excites the fluorophores in the sample and the induced fluorescence propagates through the phantom. A cooled ICCD camera (ANDOR Corp., DH734-18F-73, Belfast, Northern Ireland) equipped with a 50 mm f/4 macro standard objective camera lens is used to detect the transmitted fluorescence from a specific area of the phantom. A 3 mm thick cut-off filter OG550 (Schott, Bromma, Sweden) was placed in front of the objective. By sequentially using two different band pass filters (ESCO, Oak Ridge, New Jersey, USA) in front of the ICCD, yellow (550 ± 10 nm) and red (630 ± 10 nm) fluorescence images can be acquired.

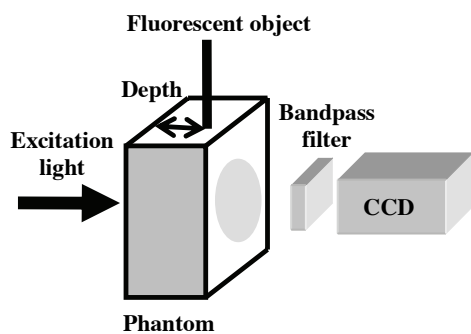


Figure 1: Schematic illustration of the experimental setup.

2.2 Preparation of the phantom

For the experiments, a piece of porcine muscle was placed in a 20 mm thick, 100 mm wide and 100 mm high glass vessel. A thickness of 20 mm is relevant for small animal imaging studies. The fluorophores used in the tissue experiments was a 50/50 mixture of Rhodamine 110 (Lambda Physik, LC5700, Goettingen, Germany) (2mg/ml) and Rhodamine 101 (Lambda Physik, LC6400, Goettingen, Germany) (1mg/ml) solved in 95% ethanol. A glass tube with an inner diameter of 1.50 mm and an outer diameter of 2.3 mm was filled with the fluorophore mixture and placed at different positions inside the meat.

2.3 Measurement procedure

The total power for the excitation light for the tissue measurements was approximately 0.5 W. Different exposure times were used for the yellow and the red filters, as can be seen in Table 1. The depths of the glass tube were 1, 3, 6, 8, 11, 13, 17 and 19 mm. An image was acquired with each of the filters.

Table 1: Exposure times used with the tube in the tissue phantom.

Depth / mm	Exp. time / s (yellow)	Exp. time / s (red)
1	5	0.003
3	5	0.005
6	5	0.020
8	1	0.030
11	0.9	0.008
13	5	0.100
17	3	0.300
19	1.5	0.300

2.4 Evaluation of the data

The intensities in the acquired images were normalized with respect to the exposure time. A region of interest of 33x33 mm in all images was selected. A depth-dependent ratio was calculated in two different ways. First, a ratio was calculated for each pixel in the selected region of interest by dividing the value in the yellow image by the corresponding value in the red image. A new image was then formed as a pixel-by-pixel ratio. The second method involved calculating a mean value over the entire region of interest for the yellow and red images separately. The mean value for the yellow image was then divided by the mean value for the red image, resulting in a value corresponding to a certain depth.

3. RESULTS

The method used to determine the depth by calculating a ratio between the intensities at two fluorescence wavelengths was applied to tissue in this study. The images were acquired on porcine muscle *in vitro* with an inserted glass tube containing the fluorophores. Figure 2 shows the normalized images acquired for two depths of the glass tube in tissue, 6 mm (right column) and 13 mm (left column). The image area is 25x25 mm. The first row shows the images acquired with the yellow filter in front of the ICCD camera and the second row shows the images acquired with the red filter. The images in the last row show the pixel-by-pixel ratio. Figure 3 shows the yellow/red ratio based on the mean values of the images as a function of depth for the glass tube inserted into meat. The results indicate that the method of determining the depth of a fluorescent object works in tissue.

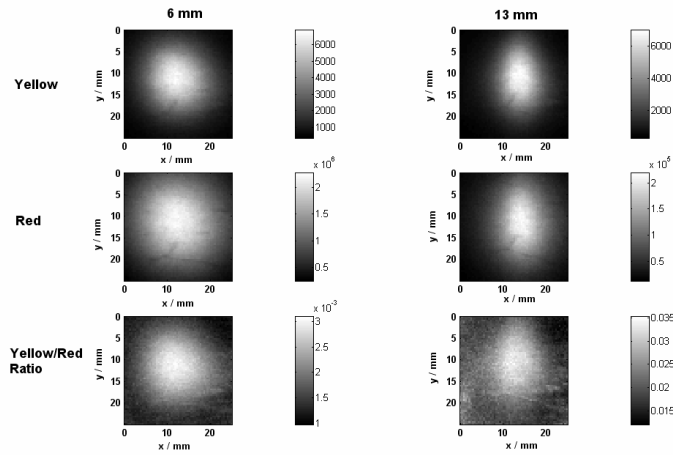


Figure 2: The first row shows the images acquired with the yellow filter, for a tube located at the depths 6 and 13 mm in tissue. The second row shows the corresponding red images. The images in the lower row show the yellow/red ratio for the two depths.

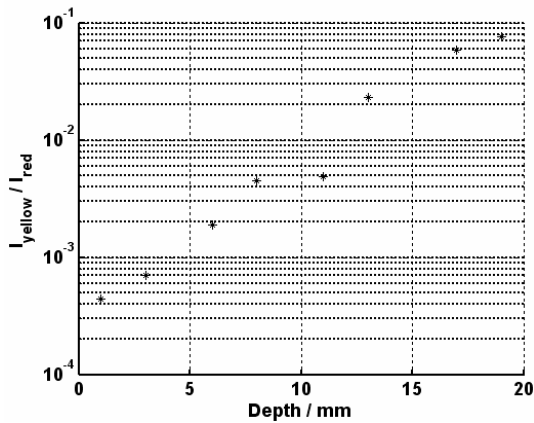


Figure 3: The yellow/red ratio for a fluorescent tube located at different depths in a tissue phantom.

4. DISCUSSION

The fluorescence from a tumor seeking fluorescent compound can be detected in several projections to reconstruct the location of the tumor with optical tomography. The reconstruction problem becomes, however, ill conditioned when scattering in the medium is high compared to the absorption. In those cases it would be of great aid to utilize available *a priori* information to be able to perform the reconstruction in a robust manner. Spectral information obtained by measuring the fluorescence intensity at several wavelengths could yield such *a priori* information. In this study, the fluorescence intensities in two wavelength bands were measured from fluorophores located at different depths in tissue. A difference in the absorption coefficient in tissue for the two fluorescence wavelengths affects the spectral shape of the recorded fluorescence. By forming a ratio of the intensities in the two wavelength regions, a value was obtained that

provides information on the depth of the fluorescent object. By evaluating a ratio of two intensities, no absolute measurements are necessary. This yields certain benefits, because unknown parameters can be canceled out, for example instrument-dependent factors that may not be known in detail.²⁵

Most of the fluorescent probes used today emit in the visible region,¹⁹ where tissue autofluorescence is strong. This provides a low fluorescence contrast, where it is difficult to detect the weak fluorescence signal from the probe. When measuring visible fluorescence from a small inclusion in tissue, there will thus always be background fluorescence from the tissue itself. This was studied in a tissue specimen. Figure 4 shows the yellow/red ratio for a tube in tissue with a relatively large fluorescence contrast. To be able to detect the fluorescence from the fluorophore, a relatively high concentration is needed so that it is not overwhelmed by tissue autofluorescence. This becomes increasingly important for smaller inclusions, since the relative volume becomes small compared to the bulk tissue. The relative signal of the fluorophore needs thus to be much higher in the visible region compared to the NIR region. The depth-dependent ratio, with different degrees of fluorescence contrast has been investigated with Monte Carlo simulations in a recent study.¹³ The results show that the depth-resolving technique works, even though the tissue fluoresces, but tissue autofluorescence will lead to poorer depth resolution due to a reduction in contrast. This problem is expected to be reduced if a tomographic algorithm is employed, as the fluorescence contribution from much smaller volumes can be evaluated.

5. CONCLUSION

The presented results showed that the ratio of the fluorescence intensity in two wavelength regions can provide information on the depth of an embedded fluorescent object in tissue. The concept used in this study is to utilize differences in the absorption in tissue in the two wavelength regions. The experiments were performed in tissue *in vitro* where autofluorescence is present, which decreases the fluorescence contrast.

ACKNOWLEDGEMENTS

The authors would like to thank Lotta Gustafsson. This research was supported by the EU Integrated Project "Molecular Imaging" LSHG-CT-2003-503259. H. Meyer acknowledges support from the EU MOLEC-IMAG Early Stage Training site MEST-CT-2004-007643. F. Forster acknowledges the support by a fellowship within the Postdoc-Program of the German Academic Exchange Service (DAAD).

REFERENCES

1. A. Eidsath, V. Chernomordik, A. Gandjbakhche, P. Smith, and A. Russo, "Three-dimensional localization of fluorescent masses deeply embedded in tissue," *Phys. Med. Biol.* **47**, 4079-4092 (2002)
2. A. B. Milstein, O. Seungseok, K. J. Webb, C. A. Bouman, Q. Zhang, D. A. Boas, and R. P. Millane, "Fluorescence optical diffusion tomography," *Appl Opt* **42**(16), 3081-3094 (2003)
3. M. A. O'Leary, D. A. Boas, X. D. Li, B. Chance, and A. G. Yodh, "Fluorescence lifetime imaging in turbid media," *Opt. Lett.* **21**(2), 158-160 (1996)
4. D. Stasic, T. J. Farrell, and M. S. Patterson, "The use of spatially-resolved fluorescence and reflectance to determine interface depth in layered fluorophore distributions," *Phys. Med. Biol.* **48**, 3459-3474 (2003)
5. D. Hall, G. Ma, F. Lesage, and Y. Wang, "Simple time-domain optical method for estimating the depth and concentration of a fluorescent inclusion in a turbid medium," *Opt Lett* **29**(19), 2258-2260 (2004)
6. T. F. Massoud and S. S. Gambhir, "Molecular imaging in living subjects: seeing fundamental biological processes in a new light," *Genes & Development* **17**, 545-580 (2003)
7. K. Shah, A. Jacobs, X. O. Breakefield, and R. Weissleder, "Molecular imaging of gene therapy for cancer," *Gene Therapy* **11**, 1175-1187 (2004)
8. V. Ntziachristos, C.-H. Tung, C. Bremer, and R. Weissleder, "Fluorescence molecular tomography resolves protease activity in vivo," *Nature Medicine* **8**(7), 757-760 (2002)
9. V. Ntziachristos, C. Bremer, and R. Weissleder, "Fluorescence imaging with near-infrared light: new technological advances that enable in vivo molecular imaging," *Eur. Radiol.* **13**(1), 195-208 (2002)
10. E. Graves, J. Ripoll, R. Weissleder, and V. Ntziachristos, "A submillimeter resolution fluorescence molecular imaging system for small animal imaging," *Med. Phys.* **30**(5), 901-911 (2003)
11. V. Ntziachristos, C. Bremer, E. Graves, J. Ripoll, and R. Weissleder, "In vivo tomographic imaging of near-infrared

- fluorescent probes," *Molecular Imaging* **1**(2), 82-88 (2002)
12. V. Ntziachristos, E. A. Schellenberger, J. Ripoll, D. Yessayan, E. Graves, A. Bogdanov, L. Josephson, and R. Weissleder, "Visualization of antitumor treatment by means of fluorescence molecular tomography with an annexin V-Cy5.5 conjugate," *Proc. Natl. Acad. Sci. USA* **101**(33), 12294-12299 (2004)
13. J. Svensson and S. Andersson-Engels, "Modeling of spectral changes for depth localization of fluorescent inclusion", Submitted *Optics Express*, (2005)
14. J. Swartling, J. Svensson, D. Bengtsson, K. Terike, and S. Andersson-Engels, "Fluorescence spectra provide information on the depth of fluorescent lesions in tissue," *Appl. Opt.* **44**(10), 1934-1941 (2005)
15. Q. Liu and N. Ramanujam, "Experimental proof of the feasibility of using fiber-optic probe for depth-sensitive fluorescence spectroscopy of turbid media," *Opt Lett* **29**(17), 2034-2036 (2004)
16. Q. Liu, C. Zhu, and N. Ramanujam, "Experimental validation of Monte Carlo modeling of fluorescence in tissues in the UV-visible spectrum," *J. Biomedical Optics* **8**(2), 223-236 (2003)
17. M. G. Muller, I. Georgakoudi, Q. Zhang, J. Wu, and M. S. Feld, "Intrinsic fluorescence spectroscopy in turbid media: disentangling effects of scattering and absorption," *Appl. Opt.* **40**(25), 4633-4646 (2001)
18. T. J. Pfefer, L. S. Matchette, A. M. Ross, and M. N. Ediger, "Selective detection of fluorophore layers in turbid media: the role of fiber-optic probe design," *Opt Lett* **28**(2), 120-122 (2003)
19. C. Bremer, V. Ntziachristos, and R. Weissleder, "Optical-based molecular imaging: contrast agents and potential medical applications," *Eur. Radiol.* **13**, 231-243 (2003)
20. V. Ntziachristos, J. Ripoll, L. V. Wang, and R. Weissleder, "Looking and listening to light: the evolution of whole-body photonic imaging," *Nature Biotechnology* **23**(3), 313-320 (2005)
21. R. Weissleder, C.-H. Tung, U. Mahmood, and A. Bogdanov, "In vivo imaging of tumors with protease-activated near-infrared fluorescent probes," *Nature Biotechnology* **17**(4), 375-378 (1999)
22. R. M. Hoffman, "Green fluorescent protein imaging of tumour growth, metastasis, and angiogenesis in mouse model," *The Lancet Oncology* **3**, 546-556 (2002)
23. V. V. Verkhusha and K. A. Lukyanov, "The molecular properties and applications of Anthozoa fluorescent proteins and chromoproteins," *Nature Biotechnology* **22**(3), 289-296 (2004)
24. K. M. Yoo, F. Liu, and R. R. Alfano, "Imaging through a scattering wall using absorption," *Opt. Lett.* **16**(14), 1068-1070 (1991)
25. S. Montan, K. Svanberg, and S. Svanberg, "Multi-color imaging and contrast enhancement in cancer tumor localization using laser-induced fluorescence in hematoporphyrin derivative (HpD)-bearing tissue," *Opt. Lett.* **10**, 56-58 (1985)

IV

Multispectral prior knowledge used for data preprocessing in fluorescence molecular tomography

Johan Axelsson, Jenny Svensson and Stefan Andersson-Engels

Department of Physics, Lund University, P.O. Box 118, SE-221 00 Lund, Sweden.

Abstract

Fluorescence molecular tomography (FMT) suffers from being mathematically ill-conditioned resulting in non-unique solutions to the reconstruction problem. In an attempt to reduce the number of possible solutions in the underdetermined system of equations in the reconstruction, we present a method to preprocess the recorded data using information from a few multispectral recordings. This simple preprocessing provides regularization of the reconstruction. The method is verified in a tissue phantom setup. The results imply that initial reconstructions with preprocessing show faster and more accurate convergence compared to non-preprocessed reconstructions.

1. Introduction

Fluorescence molecular tomography (FMT) has evolved during the last decade to become an important modality for studying fluorescent markers inside small animal models. Disease and treatment progression can be monitored, within longitudinal small animal studies *in vivo*. For this imaging the fluorescence emitted from fluorophores, attached to specific molecules, is performed.¹ One major challenge in FMT is to obtain a feasible tomographic reconstruction resembling the correct result as well as possible. The reconstruction is mathematically ill-conditioned yielding multiple non-unique solutions satisfying the recorded signals. Hence there is a need for methods to increase the robustness of the mathematical problem. This can be achieved by employing *a priori* information.² Anatomical images retrieved from MR has for instance been used to select a feasible reconstruction region together with diffuse optical tomography.³ Governed by the recent development of non-contact detection schemes for FMT,^{4,5} providing possibilities for high resolution reconstructions, the computational cost is greatly increased. Thus, it is important to optimally define the reconstruction parameters balancing computational expense and resolution in the reconstruction.⁵ In this study we report on a simple approach to preprocess the recorded data to achieve a better reconstruction performance. The method is based on the multispectral fluorescent emission information, as a fluorophore is typically characterized by a broad band fluorescence spectrum.

In an FMT setup laser light is radiating several small spots on the tissue surface sequentially, either through a fiber or by a free laser beam. The excitation light propagates through the tissue and undergoes multiple scattering and absorption events. Upon absorption in a fluorophore, fluorescent light will be emitted, which then propagates through the tissue and is collected by a detector at the rear boundary. Application of multiple detectors will yield information about the spatial intensity distribution of the light escaping from the tissue surface.

The diffusion approximation to the radiative transport equation is here utilized to mathematically describe the light propagation in tissue. The light delivered as a small spot onto the tissue surface is then approximated by a point source positioned one scattering length $1/\mu'_s$ inside the medium. The extrapolated boundary condition is applied using mirrored sources to account for the refractive index mismatch at the boundaries.⁶ The source position is denoted \mathbf{r}_s . The excitation light reaching an arbitrary point \mathbf{r} inside the medium will

induce fluorescence. The fluorescence propagating to the detector at position \mathbf{r}_d is $u_m(\mathbf{r}_s, \mathbf{r}_d, \mathbf{r})$ [W/m^2], defined by:⁷

$$u_m(\mathbf{r}_s, \mathbf{r}_d, \mathbf{r}) = \frac{P_0 G_x(\mathbf{r}_s, \mathbf{r})}{4\pi D_x} \eta_m(\mathbf{r}) \frac{v G_m(\mathbf{r}, \mathbf{r}_d)}{4\pi D_m}. \quad (1)$$

$G_x(\mathbf{r}_s, \mathbf{r}) = |\mathbf{r} - \mathbf{r}_s|^{-1} \exp(ik_x |\mathbf{r} - \mathbf{r}_s|)$ [m^{-1}] is the Green's function to the homogeneous diffusion equation for the excitation light distribution with a point source placed at \mathbf{r}_s . $G_m(\mathbf{r}, \mathbf{r}_d) = |\mathbf{r}_d - \mathbf{r}|^{-1} \exp(ik_m |\mathbf{r}_d - \mathbf{r}|)$ [m^{-1}] is the corresponding Green's function for the emission light detected at \mathbf{r}_d . P_0 [W] is the laser source strength. η_m [m^{-1}] is the product of fluorescence quantum yield (γ_m) for emission wavelength (λ_m) and the fluorophore absorption coefficient (μ_{a_f}), $D_{x,m} = v/(3(\mu_s'^{x,m} + \alpha\mu_a^{x,m}))$ [$m^2 s^{-1}$] is the diffusion coefficient for the emission (m) and excitation (x) light, respectively, while $k_{x,m} = (-v\mu_a^{x,m}/D_{x,m})^{1/2}$ [m^{-1}] is the wave number for the excitation and emission wavelength and v is the speed of light in the medium. The dimensionless constant α (here $\alpha \approx 0.55$) is adopted from Ripoll *et. al.*⁸ to form a modified absorption dependent diffusion coefficient.

Consider an arbitrary fluorescent point inclusion at position \mathbf{r} inside the medium. It has previously been reported that the intensity ratio of the fluorescence emission at two wavelengths from such an inclusion detected at the boundary of the tissue is dependent on the depth of the inclusion.¹⁰ This effect is due to the difference in bulk tissue attenuation, mainly absorption i.e. $\mu_a^{m1} \neq \mu_a^{m2}$. Following the formalism above, the ratio of the two fluorescence signals induced at a location \mathbf{r} is thus given by:

$$u_{mR}(\mathbf{r}, \mathbf{r}_d) = \frac{u_{m1}(\mathbf{r}_s, \mathbf{r}_d, \mathbf{r})}{u_{m2}(\mathbf{r}_s, \mathbf{r}_d, \mathbf{r})} = \frac{D_{m2}\gamma_{m1} G_{m1}(\mathbf{r}, \mathbf{r}_d)}{D_{m1}\gamma_{m2} G_{m2}(\mathbf{r}, \mathbf{r}_d)}. \quad (2)$$

Eq. (2) can be calculated to yield the ratio of the escape probabilities for the two wavelengths emitted from any voxel to each detector. This is performed by utilizing the reciprocity theorem,^{11,12} i.e. $G_m(\mathbf{r}, \mathbf{r}_d) = G_m(\mathbf{r}_d, \mathbf{r})$. We will here use this simple relation to estimate the position of a fluorescence inclusion and use this estimate to make a subsequent FMT reconstruction more robust and accurate.

2. Experiments

The setup used was comprised of a 2.0 cm thick slab shaped glass cuvette. The slab was filled with a 1.1% Intralipid-water solution and 0.4% bovine blood to mimic the optical properties of biological media.¹³ The optical properties were measured using an integrating sphere setup¹⁴ in connection to the experiments. μ_a was 0.78, 0.59 and 0.29 cm^{-1} , while μ_s' was 14, 13 and 12 cm^{-1} for $\lambda_x = 532$ nm, $\lambda_{m1} = 560$ nm and $\lambda_{m2} = 600$ nm, respectively. A thin-walled glass cylinder with an inner radius $R = 2.8$ mm filled with the phantom solution and 1.0 μM Rhodamine 6G was positioned at the depth $z_f = 1.1$ cm. Excitation light of 80 mW at 532 nm (Millennia Vs, Spectra Physics Laser) was delivered through an optical fiber (400 μm) with the distal end in close contact with the sample wall to form a small spot at the surface of the glass cuvette. The position of the source was changed by translating the distal end in incremental steps of 0.5 cm using a grid made of black delrin plastic placed just outside the cuvette wall. The fluorescence originating from the cylinder was detected at the opposite boundary using a CCD-camera (Hamamatsu, C4742-80-12AG) equipped with an objective lens (Nikon, f/1.8, focal length 50 mm) and a Liquid Crystal Tunable Filter (Varispec, LCTF VIS 20-35). The emission centered at $\lambda_{m1} = 560$ nm and $\lambda_{m2} = 600$ nm was collected and normalized for the filter transmission. A total of 10 source positions were used and 31 detector positions were extracted from the acquired images. The relative intrinsic emission spectrum of the fluorophore was measured with a spectrometer (OceanOptics, USB4000) for an aqueous solution of Rhodamine 6G of low concentration. Relative fluorescence quantum yields of $\gamma'_{m1} = 1.0$ and $\gamma'_{m2} = 0.43$ were obtained from this spectrum.

3. Results

The aim is to produce a probability map over the position of a fluorophore that can be used for data-preprocessing. This can be obtained by comparing the value of the measured ratio with the value of the corresponding ratio using the forward model for a small fluorophore positioned at a specific location \mathbf{r}_i . The comparison is conducted for all possible modelled fluorophore positions \mathbf{r}_i within the geometry. The difference between the values given by the forward model (Eq. (2)) calculated in all voxels and the detected intensity ratio should yield a minimum for the positions in the media containing a fluorophore. This difference can be expressed as:

$$\Delta U_{mR}^d(\mathbf{r}_i) = |\ln(u_{mR}(\mathbf{r}_d, \mathbf{r}_i)) - \ln(U_{mR}(\mathbf{r}_d))|, \quad (3)$$

for a voxel at \mathbf{r}_i in a discretized geometry and a detector at \mathbf{r}_d . $U_{mR}(r_d)$ represents the ratio of the measured fluorescence intensity at the two wavelengths. In the evaluation of the difference between modelled and measured values, we have here chosen to use the logarithmic values in order to decrease the dynamic of the resulting difference. Evaluation of Eq. (3) for one detector and all voxels in a plane through the volume yields an arc with minimum values inside the geometry, as seen in Fig. 1. The resulting arc is centered around the specific detector, since the minimum is obtained for all voxels positioned at the same distance from the detector. The minimum value for the three detectors shown in the figure are placed at different distances from the detectors due to the fact that the measured ratios U_{mR} are different, requiring a matching value of $|\mathbf{r}_i - \mathbf{r}_d|$ in the forward model u_{mR} to compensate. A longer propagation distance yields a smaller intensity ratio, hence the arc is placed further away from the detector. Summation of the images shown in Fig. 1 retrieved for all detectors yields a minimum where the arcs overlap, i.e. where the fluorophore is positioned. This is done by calculating the sum, i.e. $S = \frac{1}{31} \sum_{d=1}^{31} \Delta U_{mR}^d(r_i)$.

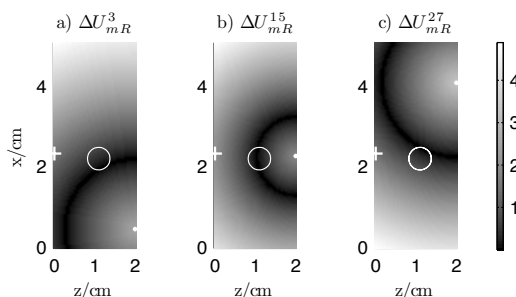


Fig. 1. ΔU_{mR} for detector a) 3, b) 15 and c) 27 extracted for the same excitation source position. The white cross (+) indicates the source position and the white dot (•) represents each detector position. The true position of the cylinder is marked by the circular ring for reference.

The summation of all detectors yields the image shown in Fig. 2 a). This image can be interpreted as some type of map correlated with the probability for the fluorophore position.

The normalized Born approach⁹ was implemented to investigate whether preprocessing data using multi-spectral information improved the reconstruction performance of the fluorophore position. In the normalized Born approach a system of linear equations, based on Eq. (1), can be formed using several source and detector positions. The set of linear equations is then subject to inversion where η_m is sought. Utilizing the normalized Born approach,⁹ the set of linear equations is written as $U_{nB} = \mathbf{W}\mathbf{X}$, where U_{nB} is a vector

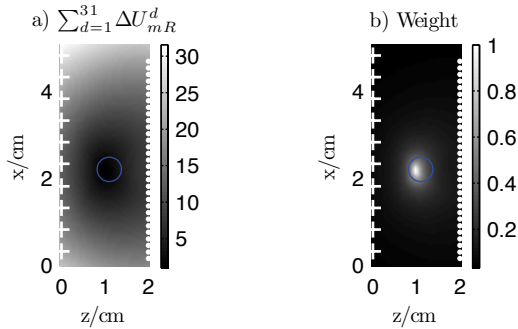


Fig. 2. a) Confinement of a cylinder shaped fluorophore. b) Weight matrix retrieved from confinement.

comprised of the ratio between detected intensities at one emission wavelength and the excitation wavelength for all combinations of sources and detectors. \mathbf{W} is a weight matrix where each element is formed by the forward model,⁹ i.e.

$$W_{h,i} = \frac{P_0(4\pi D_x |\mathbf{r} - \mathbf{r}_{s_h}|)^{-1} \exp(ik_x |\mathbf{r} - \mathbf{r}_{s_h}|) \cdot v(4\pi D_m |\mathbf{r}_{d_h} - \mathbf{r}|)^{-1} \exp(ik_m |\mathbf{r}_{d_h} - \mathbf{r}|)}{P_0(4\pi D_x |\mathbf{r}_{d_h} - \mathbf{r}_{s_h}|)^{-1} \exp(ik_x |\mathbf{r}_{d_h} - \mathbf{r}_{s_h}|)}. \quad (4)$$

In Eq. (4), h is the source-detector pair index and i is the voxel index. The X-vector is constructed of the unknowns $\eta_m(\mathbf{r}_i)$.⁹

To incorporate the preprocessing information in the reconstruction, Fig. 2 a) is scaled so that the minimum value is assigned 1 and all other voxels lower values, see Fig. 2 b). The scaled probability map can then be used as an additional diagonal weight matrix \mathbf{P} where $\mathbf{P}_{i,i}$ is assigned the value for voxel i in Fig. 2 b). The preprocessing is performed by multiplying the matrices, i.e. $\mathbf{W}_{\text{proc}} = \mathbf{W} \times \mathbf{P}$. The algebraic reconstruction technique (ART) was utilized to invert the matrix equation.⁹ The reconstruction with and without multiplication of the additional weight matrix is shown in Fig. 3 a-b).

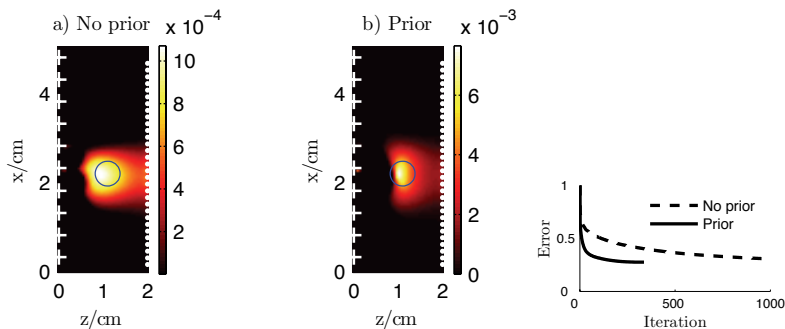


Fig. 3. Reconstructions a) without prior information, b) with preprocessing. c) reconstruction error without prior information (dashed) and with preprocessing (solid).

It is seen that with prior information the fluorophore position is more accurately determined. Since ART is an iterative algorithm, the error between the measured and the forward modelled data can be calculated in each iteration, i.e. $\sum |U_{nB} - WX|/N_{\text{voxels}}$, seen in Fig. 3 c). Iterations were performed until the error

increased again. The faster decrease of the reconstruction error when using the confinement is caused by the change of the weight for each voxel.

4. Conclusions

We have presented a simple and objective procedure to confine the reconstruction region around a fluorescent inclusion in turbid media based solely on the multispectral feature of the fluorescence. The method is based on the difference of the forward model and the detected intensities. This poses no additional computational cost for a reconstruction algorithm, except the forward matrix calculation of the additional emission wavelength. The method yields a prior weight map outlining the most probable fluorophore region. In the results presented the spatial prior is used as an additional weight map. Spatial priors can be applied in numerous ways. In present work we are now extending the spatial prior in a generalized Tikhonov regularization scheme. The spatial prior is then used as a penalizing term in the matrix regularization.

The demonstration presented herein is performed in a homogeneous tissue phantom with autofluorescence subtracted from the measurements. The influence of autofluorescence and inhomogeneities is within current work in our group.

5. Acknowledgement

We acknowledge the discussions with Oliver Dorn. This research was supported by the EU Integrated Project Molecular Imaging LSHG-CT-2003-503259.

References

1. V. Ntziachristos, J. Ripoll, L. V. Wang, and R. Weissleder, *Nat Biotechnol* **23**(3), 313–320 (2005).
2. A. Cong and G. Wang, *Opt. Express* **13**(24), 9847–9857 (2005).
3. H. Xu, R. Springett, H. Dehghani, B. W. Pogue, K. D. Paulsen, and J. F. Dunn, *Appl Opt* **44**(11), 2177–2188 (2005).
4. R. B. Schulz, J. Ripoll, and V. Ntziachristos, *IEEE Trans Med Imaging* **23**(4), 492–500 (2004).
5. E. E. Graves, J. P. Culver, J. Ripoll, R. Weissleder, and V. Ntziachristos, *J Opt Soc Am A Opt Image Sci Vis* **21**(2), 231–241 (2004).
6. D. Contini, F. Martelli, and G. Zaccanti, *Appl Opt* **36**(19), 4587–4599 (1997).
7. M. A. O’Leary, D. A. Boas, X. D. Li, B. Chance, and A. G. Yodh, *Opt. Letters* **21**(2), 158–160 (1996).
8. J. Ripoll, D. Yessayan, G. Zacharakis, and V. Ntziachristos, *J Opt Soc Am A Opt Image Sci Vis* **22**(3), 546–551 (2005).
9. V. Ntziachristos and R. Weissleder, *Opt. Letters* **26**(12), 893–895 (2001).
10. J. Swartling, J. Svensson, D. Bengtsson, K. Terike, and S. Andersson-Engels, *Appl Opt* **44**(10), 1934–1941 (2005).
11. S. R. Arridge, *Inverse Problems* **15**, R41–R93 (1999).
12. J. Swartling, A. Pifferi, A. M. K. Enejder, and S. Andersson-Engels, *J Opt Soc Am A Opt Image Sci Vis* **20**(4), 714–727 (2003).
13. G. Alexandrakis, F. R. Rannou, and A. F. Chatziioannou, *Phys Med Biol* **50**(17), 4225–4241 (2005).
14. J. S. Dam, T. Dalgaard, P. E. Fabricius, and S. Andersson-Engels, *Appl Opt* **39**(7), 1202–1209 (2000).

V

External Parameter Orthogonalisation - Least Squares Support Vector Machine (EPO-LSSVM) and Partial Least Squares (PLS) for localization of embedded inclusions using detection of fluorescence

Fabien Chauchard^{1*}, Jenny Svensson², Johan Axelsson², Stefan Andersson-Engels² and Sylvie Roussel¹

¹ Ondalys, Minéa-Cemagref, 361 rue jean francois Breton, 34196 Montpellier Cedex 5, France

² Department of Physics, Lund University, P.O. Box 118, 221 00 Lund, Sweden

*Corresponding author: Fabien Chauchard, ONDALYS, Minéa-Cemagref, 361 rue j f Breton, 34196 Montpellier Cedex 5, France, Phone: +33 (0)467 04 63 42, Fax: +33 (0)467 4 63 06, E-mail: fchauchard@ondalys.com

Abstract

Fluorescence spectroscopy is a useful technique for tissue diagnostics and is also a promising tool in the characterization of embedded structures in tissue. The emitted fluorescence from an embedded inclusion, marked with a fluorescent compound, is affected by several factors as the light propagates through the medium to the tissue boundary, where the fluorescence light is detected. Tissue absorption, scattering and autofluorescence, as well as the size and depth of the inclusion, affect the detected fluorescence light. The aim of this study is to investigate if the size and location of a fluorescent inclusion could be determined using models based on both Partial Least Squares (PLS) and a combination of External Parameter Orthogonalisation (EPO) and Least Squares Support Vector Machine (LS-SVM) (EPO-LSSVM). The data set consisted of simulated multispectral fluorescence, where depth and radius of a spherical fluorescent inclusion were varied as well as the fluorescence contrast and optical properties of the surrounding tissue. The results showed that it was possible to build a PLS model to predict the radius of the inclusion, but the depth could not be determined uniquely when using PLS. Also, the results demonstrated that both depth and radius affect the fluorescence signal in a non-linear way; therefore the non-linear models based on LS-SVM predict both radius and depth more accurately. It was observed that EPO acts as a useful pre-processing tool on spectra for non-linear models and that it was necessary to perform EPO to be able to predict the depth with the LS-SVM model.

Keywords: multispectral, fluorescence spectroscopy, multivariate analysis, external parameter orthogonalisation, LS-SVM, non-linearity

1. Introduction

Fluorescence spectroscopy can be used as a diagnostic tool in the detection of cancer. Fluorescence is induced by illuminating the tissue at a certain excitation wavelength. The fluorescence will be emitted from the tissue in a broadband spectrum. The emitted fluorescence light is dependent on the concentrations of fluorophores and chromophores as well as on the biochemical properties of the tissue and can be used to distinguish between normal and diseased tissue. One goal with developing fluorescence as a diagnostic tool is to be able to detect precancerous differences in epithelial tissue at such an early stage, that it cannot be seen by the eye of an experienced physician [1]. Benefits with fluorescence spectroscopy are e.g. that it is a non-invasive technique and can be performed in real time. It is, however, not only superficial tissue that can be studied with fluorescence spectroscopy. Also fluorescence imaging of deep-lying inclusions in tissue is of importance. Today this is mostly performed in studies with small animal models [2,3]. To be able to detect these deep-lying objects in tissue, the inclusion needs to be marked with some kind of fluorescent probe and the emitted fluorescence in addition to the transmitted excitation light is detected and analyzed in order to determine the location and size of the inclusion [4]. Commonly used probes are fluorescent proteins, that today are limited to emit fluorescence in the visible wavelength region [5]. Detected fluorescence signal levels depend on several factors including fluorophore concentration, size of inclusion, tissue optical properties [6,7] and detection geometry [7,8]. Tissue absorption in the visible wavelength region is mainly due to the presence of hemoglobin molecules in the tissue. Both oxygenated and deoxygenated blood absorb in this wavelength region with strong absorption peaks at 540 and 569 nm for oxygenated blood and at 557 nm for deoxygenated blood [7]. In previous studies it has been demonstrated that an intensity ratio of two fluorescence wavelengths is dependent on the depth of a fluorescent inclusion [9,10]. The intensity ratio shows such depth dependence, only if the tissue has differences in optical properties at the two wavelengths, affecting the fluorescence light at the two wavelength bands differently. Fluorescence contrast is defined as the ratio of emitted fluorescence light from the inclusion compared to fluorescence emitted from the surrounding medium, e.g. tissue autofluorescence. It has been shown that the above mentioned intensity ratio depends not only on the depth of a fluorescent inclusion, but also on the fluorescence contrast [9]. This

affects the evaluation of depth from this ratio negatively. Especially in the visible wavelength region, a strong tissue autofluorescence decreases the fluorescence contrast. One way to improve the estimation of the location of the fluorescent inclusion could be to increase the spectral resolution and add information from several fluorescence wavelengths.

Chemometrics provide many different and interesting tools and methods for dealing with spectra. Most often these spectra are obtained using spectroscopy methods and aims at predicting chemical constituents. The relationship between chemical constituents and spectra most commonly follow the Beer-Lambert's law. When a diffusion process occurs different preprocessing techniques as e.g. Standard Normal Variate [11], Multiplicative scatter correction [12] and Derivatives [13] can partly correct the non-linearities introduced by photon scattering and enhances the prediction power. Fluorescence signals from highly scattering media are more difficult to use because of important non-linearities with respect to depth and optical properties in the tissue [14], especially when the aim is to predict physical parameters such as depth and size of an inclusion. The accuracy of the predictions will also be more sensitive to external factors as for example fluorescence contrast. Prediction of depth and size of inclusions using fluorescence will therefore involve techniques for correction of external influences and deal with non-linearities. Chemometrics provide interesting tools for dealing with these problems:

(i) External influence can be corrected using projection techniques such as Orthogonal Signal Correction (OSC) [15], External Parameter Orthogonalisation (EPO) [16] and more specifically Dynamic Orthogonal Projection (DOP) [17] for online processes.

(ii) Least Squares Support Vector Machine (LS-SVM) is a non-linear modeling technique that has successfully been used in several spectroscopy [18,19] and imaging applications [20]. SVM has also successfully been used for classification of non-malignant and malignant tumors in breast tissue [21].

In this study the possibility of localizing a fluorescent inclusion inside tissue using Partial Least Squares (PLS) and a combination of EPO and LS-SVM (EPO-LSSVM) is investigated. For this purpose the fluorescence at several wavelengths is evaluated. The fluorescence data is based on finite-element method (FEM) simulations of fluorescence light in turbid media. Both radii and depths of fluorescent volumes are predicted.

2. Theory

Capital bold characters will be used for matrices, e.g. \mathbf{X} ; small bold characters for column vectors, e.g. \mathbf{x}_i will denote the i th column of \mathbf{X} ; row vectors will be denoted by the transpose notation, e.g. \mathbf{x}_j^T will denote the j th row of \mathbf{X} ; non-bold characters will be used for scalars, e.g. matrix elements x_{ij} or indices i . Underlined bold letter, $\underline{\mathbf{C}}$, will denote space and subspace.

2.1. Relation of fluorescence spectrum and physical parameters

Two physical parameters, size and depth of an inclusion, were of interest in this study. It is well known that a physical parameter can have a non-linear relation to the measured signal because of phenomena such as scattering, absorption and emitted fluorescence of different surrounding tissues. Firstly, an oversimplified model was defined by considering only absorption of tissue and fluorescence of the inclusion, while totally neglecting scattering and tissue autofluorescence. This model was constructed for one reason only - to identify adequate preprocessing of the data to obtain a good multivariate model. A schematic illustration of this simplified problem is shown in Fig.1.. Monochromatic light at 514 nm irradiates the tissue surrounding a fluorescent inclusion. After excitation the inclusion will generate broadband fluorescence light observed at the distal boundary. From this model several conclusions can be drawn:

(i) The monochromatic laser light source (i_l) will be attenuated and light penetration through the tissue thus modifies the fluorescence emission from the inclusion at depth d_i . According to the Beer-Lambertian law, the intensity received by the inclusion (i) will be given by:

$$i = i_l \times e^{(-c \times k_{h514} \times d_i)}$$

where c is the concentration of the absorbers and k_{h514} corresponds to the tissue absorption at 514 nm, which is dominated by hemoglobin absorption. The emitted fluorescence intensity i_0 will be directly proportional to the intensity i received by the inclusion.

(ii) The larger the inclusion is, the higher the resulting fluorescence intensity will be. The signal intensity is related to the total volume, which, if we consider a sphere, depends on the radius to the power of three (r^3). The emitted fluorescence spectrum is therefore more correlated to r^3 than r .

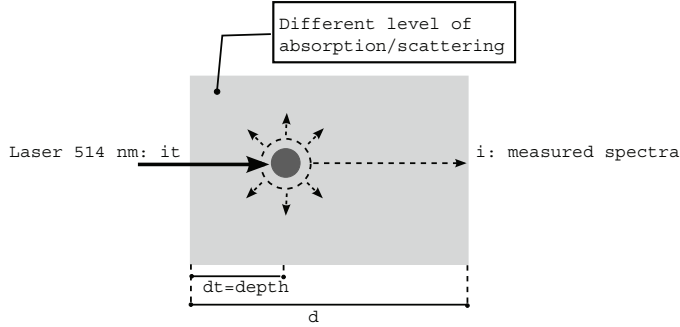


Fig. 1. Simple scheme of the fluorescence problem.

From the above considerations the intensity i_0 of the emitted fluorescence light will be a function of inclusion depth (d_i) and radius (r_i), incoming laser intensity (i_i) and the fluorescence yield of the fluorophores in the inclusion ($\mathbf{k}_t(\lambda)$):

$$\mathbf{i}_0 = \frac{4r_i^3}{3} \pi \times i_i \times \exp(-c \times k_{h514} \times d_i) \times \mathbf{k}_t \quad (1)$$

By applying Beer-Lambert's law from the inclusion to the detector and by taking into account that the solid angle for the detector will be $S/4\pi(d-d_i)^2$, the intensity, the value of the measured spectra, \mathbf{i} , will be given by Eq. (2):

$$\begin{aligned} \mathbf{i} &= \mathbf{i}_0 \times \frac{S}{4 \times \pi \times (d - d_i)^2} \times \exp(-c \times (d - d_i) \times \mathbf{k}_h) \\ &= \frac{1}{3} \mathbf{k}_t \times \frac{r_i^3}{(d - d_i)^2} \times S \times \exp(-c \times (d - d_i) \times \mathbf{k}_h - c \times k_{h514} \times d_i) \end{aligned} \quad (2)$$

where $\mathbf{k}_h(\lambda)$ is the wavelength dependent tissue absorption of the emitted fluorescence light and d is the sample width. Eq. (2) is not aiming at giving a precise physical description of the phenomenon, which is clearly more complex, as surrounding tissue also fluoresces and light scatters. The equation aims at giving an idea about the relation between signal and physical parameters. Hence the signal appears proportional to the radius raised to the power of 3. Depth is more complex and will probably be more difficult to predict because depth dependence is in the exponential part as well as in front of the exponential function in Eq. (2).

2.2. External Parameter Orthogonalisation (EPO)

Projection techniques aim at removing interfering subspace from the space used for model calibration. Several projection methods have recently been proposed for improving the PLS performance. In reference [15], the method OSC is described as a filtering method. Recently another method External Parameter Orthogonalisation (EPO) [16] has been proposed for removing interfering subspace from a dataset. This method has successfully been used for removing temperature influence on near-infrared spectra used to predict sugar contents in fruits. The method assumes that the spectral space $\underline{\mathbf{S}}$ can be split into three subspaces:

- $\underline{\mathbf{C}}$ is defined by the spectral responses, which are independent of the external parameter influence
- $\underline{\mathbf{G}}$ is generated by the perturbations on the spectral response caused by external parameters, e.g. fluorescence contrast or temperature, and is independent of $\underline{\mathbf{C}}$
- $\underline{\mathbf{R}}$ contains the rest of the spectral information.

The interfering subspace, $\underline{\mathbf{G}}$, is estimated by taking into account the effects of the major external parameters. \mathbf{X} is a measured fluorescence spectrum in $\underline{\mathbf{S}}$. If \mathbf{Q} is the projection operator onto $\underline{\mathbf{G}}$, \mathbf{X} is split as follows:

$$\mathbf{X} = \mathbf{X} \mathbf{Q} + \mathbf{X}^+$$

where \mathbf{X}^+ is the remaining spectrum containing as little information as possible on external parameters. \mathbf{Q} is estimated by a Principal Component Analysis (PCA) on a small set of spectra measured containing only the external parameter variations. EPO cleaning does not need the reference value of the calibration model we want to build as is needed with OSC. Therefore no relation is assumed between the 'interesting' reference

value and the spectra. The influence subspace is removed and any kind of modeling can then be performed in the remaining subspace. More precisely, non-linear modeling can be performed in the subspace. With OSC the remaining subspace is optimized for a linear modeling, which may limit the performance of a non-linear model.

2.3. Partial Least Squares (PLS) and Least Squares Support Vector Machine (LS-SVM)

A PLS model [22] uses projection of the vector \mathbf{x} on a regression coefficient \mathbf{b} in order to predict the target parameter y . The matrix equation is:

$$\mathbf{y} = \mathbf{X} \cdot \mathbf{b} + \mathbf{e}$$

The regression coefficient is obtained using the SIMPLS algorithm and \mathbf{e} is the residual part. Cross validation is used in order to avoid over fitting. Prediction of a new sample, \mathbf{x}_{new} , is then performed using \mathbf{b} :

$$\hat{y} = \mathbf{x}_{\text{new}}^T \mathbf{b}$$

With LS-SVM [23], a model is based on a kernel matrix \mathbf{K} [n×n]. This matrix is obtained by using the calibration database \mathbf{X} [n×p] (n samples, p variables).

$$\mathbf{K} = \begin{bmatrix} k_{1,1} & \cdots & k_{1,n} \\ \vdots & \ddots & \vdots \\ k_{n,1} & \cdots & k_{n,n} \end{bmatrix}$$

Where:

$$k_{i,j} = e^{-\frac{\|\mathbf{x}_i - \mathbf{x}_j\|^2}{\sigma^2}}$$

is defined by the Radial Basis Function (RBF). \mathbf{K} can be thought of as a sort of sample-sample correlation matrix. The kernel width parameter, σ , is related to the confidence in the data, or signal-to-noise ratio (SNR). Adjusting σ also influences the non-linear nature of the regression. As σ^2 increases, the kernel becomes wider forcing the model towards a less complex solution. The model equation is then given by:

$$\mathbf{y} = \mathbf{K} \cdot \boldsymbol{\beta} + \mathbf{f},$$

where y is the predicted value and \mathbf{K} is the kernel matrix. $\boldsymbol{\beta}$ is the regression coefficient and \mathbf{f} the residuals. The LS-SVM objective function takes into account the norm of the regression vector in order to increase the model robustness. The classical squared loss function is thus replaced by the following objective function:

$$\min(e) = \min \left[\frac{\sum_{i=1}^n (y_i - \hat{y}_i)^2}{2} + \frac{1}{2\gamma} (\boldsymbol{\beta}^T \boldsymbol{\beta}) \right],$$

where γ is a regularization parameter analogous to the regularization parameter of regularized artificial neural networks, and is used as a weight on the norm. Put simply, γ indicates the level of model complexity. The regression coefficient is calculated using a Karush-Kuhn-Tucker (KKT) system [23].

3. Experimental

3.1. Fluorescence data

3.1.1. Modeling geometry

The geometry used for the simulations in this study can be seen in Fig. 2. The geometry model consisted of a 2.0 cm thick slab with optical properties of those of adipose tissue [24]. Inside the tissue a fluorescent inclusion with the shape of a sphere was placed at a specific depth, measured from the side where the excitation light source was located. The excitation light was a point source at 514 nm and emitted fluorescence from the inclusion was detected on the opposite side of the slab symbolizing an experimental imaging set up. Emission of fluorescence light was assumed to be in the wavelength interval 540-650 nm.

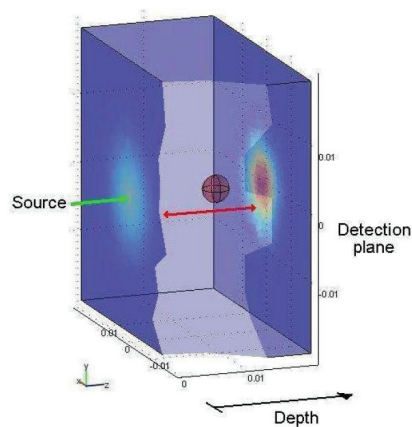


Fig. 2. The geometry used for simulation of fluorescence light.

3.1.2. Modeling of fluorescence light

The distribution of excitation light and emitted fluorescence light was modeled with the diffusion approximation using the finite element method. The software package COMSOL Multiphysics was used for the modeling. Fluorescence light was modeled for 12 wavelengths in the specified fluorescence interval in Section 3.1.1.

3.1.3. Data set

Several simulations, with different input parameters such as radius and depth of the sphere, optical properties in tissue and fluorescence contrast, were performed to build a data set. Eight different values of the sphere radius were used in the simulation, ($r = 0.5, 0.75, 1, 1.25, 1.5, 1.75, 2, 3$ mm). For each radius of the sphere, the depth of the sphere was changed in the range of 6 to 20 mm. Varying optical properties in tissue were studied by changing the level of blood oxygenation in tissue. The same optical properties were assumed in the surrounding tissue as well as in the inclusion. Three blood oxygenation levels were used in this study; 50, 70 and 90%. Only absorption properties were changed when oxygenation was varied. Optical parameters were modeled for adipose tissue according to Refs [24,25]. The last parameter to be changed for each simulation was the fluorescence contrast, meaning that also the surrounding medium can emit fluorescence at the same wavelengths as the inclusion but with different yield. A contrast of 10 means that the inclusion has a fluorophore concentration 10 times higher than the surrounding medium. When changing the contrast, the fluorescence from the inclusion was kept fixed. Three contrasts were evaluated: 5, 10 and 50. In total 783 fluorescence spectra were simulated and these were separated in a calibration set (391 samples) and a test set (392 samples).

3.2. Chemometrics

3.2.1. Correction of influential factors

EPO was used to eliminate oxygenation and fluorescence contrast effects. Three levels of oxygenations and three levels of contrasts were available in our database, which resulted in 9 possible combinations of oxygenation and fluorescence contrast. Nine mean spectra were calculated in order to obtain only variation of oxygenation and contrast, for all radii and depths. This subset was used for calculating a PCA model. The loading, \mathbf{L} , of the principal component was used for characterizing the oxygenation and contrast subspace. Five loading were calculated. Using the loading matrix the projector was calculated as follows:

$$\mathbf{P}_{o2/c} = \mathbf{L} \cdot \mathbf{L}'$$

Five projectors were calculated based on one to five loadings. The number of loadings used for the projector was chosen regarding the modeling performance in cross validation. The spectra were corrected using an orthogonal projection:

$$\mathbf{X}^+ = \mathbf{X} - \mathbf{X} \cdot \mathbf{P}_{o2/c}$$

\mathbf{X}^+ was then used for radius and depth modeling using PLS and LS-SVM. As explained in [16], it is not necessary to pre-process the test set when using a multivariate linear model as the regression coefficient has been calculated orthogonal to the interfering subspace.

3.2.2. Modeling

The first PLS model, PLS_r , was obtained using PLS and pre-processing of taking the radius to power of 3, to predict r^3 . The numbers of latent variables were chosen using full cross validation.

In order to facilitate the depth prediction, spectra from the EPO corrected database were corrected for sphere

radius, either the predicted from PLS, or for the actual radius: $\mathbf{x}^{++} = \frac{\mathbf{x}^+}{\hat{r}^3}$. Then a depth PLS model, PLS_d ,

was calibrated for prediction of depth d_i with no pre-processing of the depth reference value. The number of latent variables was chosen using cross validation.

The non-linear models were obtained using the semi-parametric method LS-SVM. Radius prediction model, $LS-SVM_r$, was calibrated using the EPO processed spectra. The reference values were not pre-processed since LS-SVM is a non-linear technique. The test set was also processed using EPO, because LS-SVM is not a projection method. Kernel width and regularization parameter tuning were done using the Venetian blind technique.

Several models ($LS-SVM_d$) were built for the depth prediction. The first one was based on raw spectra. The second one was based using EPO correction with 3 principal components. The other models were based on

EPO correction with 1 to 5 components combined with the radius pre-processing approach $\mathbf{x}^{++} = \frac{\mathbf{x}^+}{\hat{r}^3}$,

where the estimated radius is the radius predicted by the best $LS-SVM_r$ model.

4. Results and Discussion

4.1. EPO

Oxygenation and contrast mean spectra are plotted in Fig.3. A decrease in fluorescence contrast, i.e. the bulk tissue is more fluorescing, results in an increase of signal intensity mainly in the wavelength region of 590-650 nm. Oxygenation also affects the light intensity, but can also introduce change in peak curvature in the region 600-650 nm.

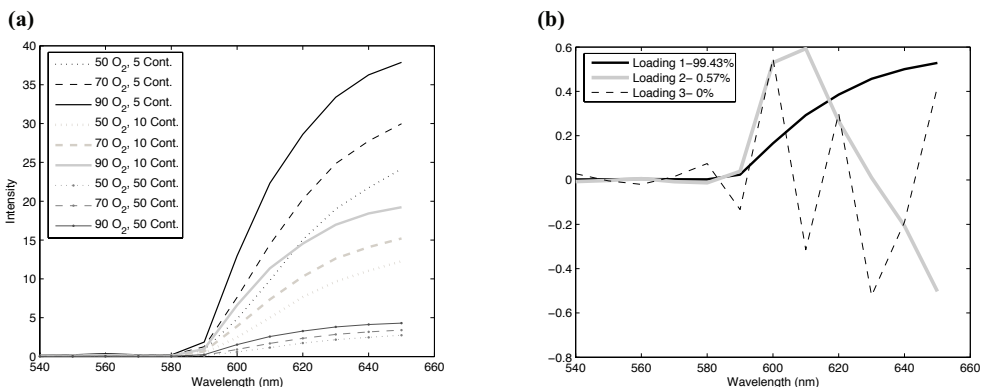


Fig. 3. (a) The nine spectra used for oxygenation and contrast subspace characterization. (b) The first three loadings obtained by PCA and percentage of variance captured.

The loadings obtained from the PCA are also shown in Fig.3.. The first loading captures 99.43% of the variance. This first loading catches the variation in intensity due to contrast but also partly from oxygenation. The shape of this loading, which looks like a mean spectrum, confirms this observation. This kind of result is frequently obtained when scattering can affect the spectrum. The second loading catches 0.57% of variance, and is more related to the oxygenation change. The effect of blood oxygenation on spectra is well known [6]. The first effect of an increase of oxygenation is a slight rise in intensity at 560 nm and 600-650 nm, due to a decrease of absorption. This information holds by the first component. The second effect is a change in curvature at 620 nm. This is the information caught by the second loading, which has a positive value below 620 nm and negative above. This kind of shape typically indicates correction of slope/curvature or peak shift which is consistent with theory. The third loading captures a very small part of the information, relatively to the information captured by the first loading. This loading alternates between positive and negative values. At first glance it could be interpreted as noise. However, this shape can also

introduce peak or spectral shifts. The resulting spectra after three component orthogonalisation are shown in Fig.4.

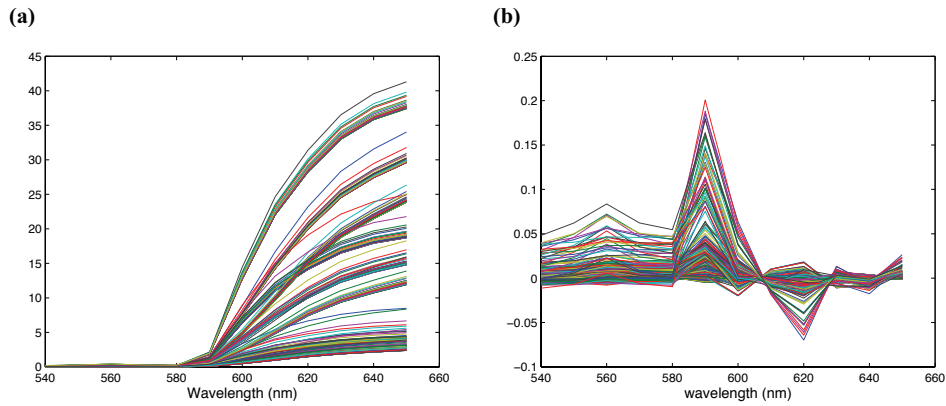


Fig. 4. Raw spectra (a) and pre-processed spectra using EPO with 3 components (b).

As can be seen, the remaining spectra for a three component projection exhibit amplified amplitude in the 540-600 nm region, as compared to the 600-660 nm region. A peak also appears at 590 nm. Since the three component processed spectra still seem to contain information, the third component does not introduce noise but rather a shifting effect. It is interesting to see how the information contained in the wavelength region 540-600 nm is amplified, whereas the high variance in the 600-650 nm is progressively decreased.

4.2. Linear modeling

The effect of EPO on the PLS model for radius prediction with reference value processing is shown in Fig.5, where SECV stands for Standard Error of leave-one-out Cross Validation. EPO does not provide an improvement of model performance compared to the exhaustive calibration.

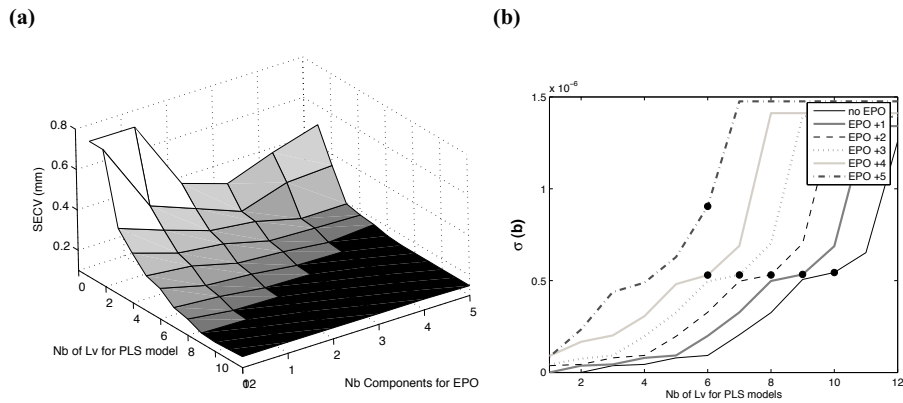


Fig. 5. (a) Effect of EPO on the SECV of the PLS model compared to exhaustive calibration. (b) Standard deviation of the regression coefficient as a function of number of latent variables. A black dot indicates where the lowest SECV is reached.

The 2-D graphics show that the optimum is reached more rapidly when using EPO. The number of latent variables for building the model is therefore decreased. When using EPO the standard deviation of the regression coefficient increases more rapidly. However, since the best SECV is reached faster, the retained regression coefficients have the same standard deviation, see (Fig. 5b). Actually the regression coefficient for EPO-processing PLS or for unprocess EPO PLS are very similar (not shown here). Usually EPO is used for improving robustness rather than using exhaustive robust calibration. In our case we have used EPO only

as a pre-processing tool aiming at simplifying the model - that is probably why there is no improvement in performance. For PLS it is not possible to say that the model has been simplified using EPO because even if the number of latent variables is decreased, the standard deviation of the regression coefficient, i.e. regression complexity, is kept constant. Since EPO does not provide improvement for radius prediction, the selected prediction model was without EPO pre-processing. The prediction plot of this model is shown in Fig.6.

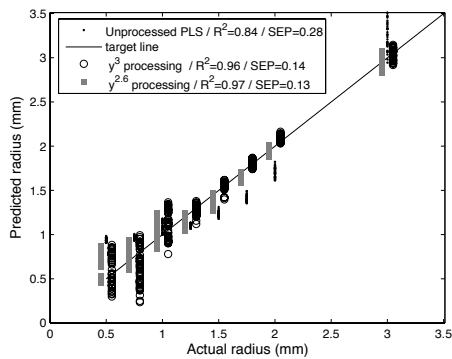


Fig. 6. Model without any reference value processing (black dots) and the selected model without EPO but with r^3 pre-processing (circles). The model using pre-processing with radius to the power 2.6 (gray squares). Note that the three prediction plots have been shifted (+ - 0.05) for clarity.

The model not using reference value processing exhibits a non-linear effect. This is well corrected by using power of 3 pre-processing. This result shows that non-linearities may be corrected using a convenient pre-processing of the reference values as explained in [22]. Even though the determination coefficient, R^2 , is satisfactory, the prediction error is high for small radii. Diagnostically it is of importance to detect inclusions when their radius is small, therefore we can voluntarily keep a small non-linearity to get an overestimated value of the inclusion radius when the radius is small. To meet this objective, rather than predicting r^3 , $r^{2.6}$ can be used. When using $r^{2.6}$ small inclusions are predicted a bit larger, which may be better than predicting a too small radius (≈ 0), if the sensor is used for diagnostics. The determination coefficient is also increased and Standard Error of Prediction (SEP) is slightly decreased.

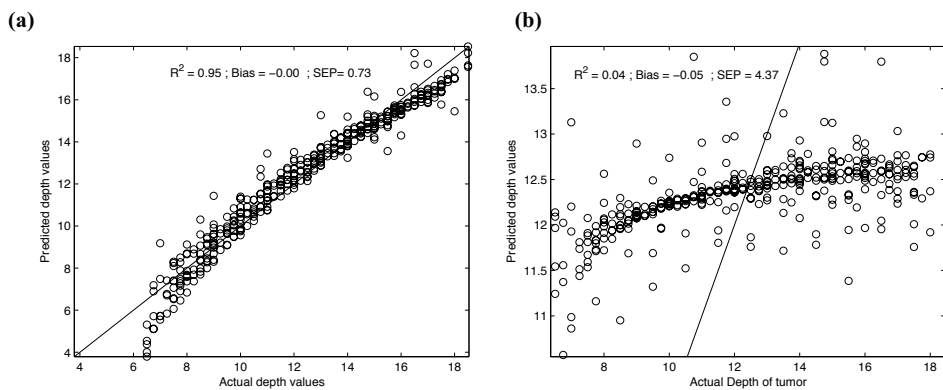


Fig. 7. Depth prediction using PLS. In (a) the predictions seems theoretically possible if using actual value of radius for spectra correction. In (b) it is shown that radius prediction is not accurate enough for correcting the spectra and reaching a good SEP.

The linear depth model investigated involved radius correction of the spectra. Fig.7 shows cross validation model performance when using real values and predicted values of radius, respectively, for spectra correction. The results show that it could be possible to reach a good prediction of depth using very accurate prediction of radius. Unfortunately, the predicted radius values do not sufficiently well reach the theoretical

performance and cannot be used to remove this dependence for subsequent analysis. Thus, the model cannot be used for accurate depth prediction due to too low performances.

4.3. LS-SVM modeling

As for the PLS model, several EPO preprocessing models with varying numbers of components have been tried for improving performance and stability of the LS-SVM models. Fig. 8 gives the SECV depending on the number of components used for the orthogonal correction.

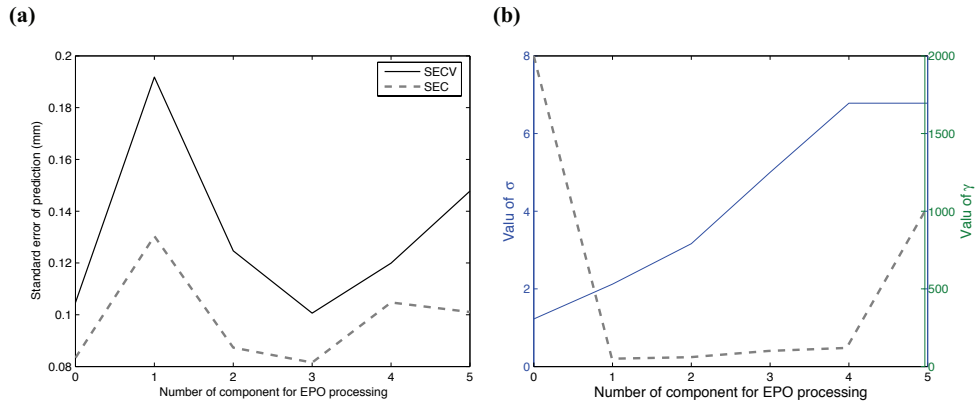


Fig. 8. Performance of the LS-SVM models. (a) SEP depending on number of components used for EPO processing. (b) Value of σ (solid line) and γ (dashed line) for each model.

When using three components for EPO, LS-SVM performance seems to be slightly improved. Probably the most interesting effect of EPO is shown by the tuning parameter variation. The kernel width parameter, σ , is increased from 1.2 without EPO to 5 with three components correction. This increase of width parameter indicates that the model gets less non-linear. With a wider kernel more samples have a similarity degree, given by the RBF function, different than zero. The prediction of a new sample will then be based on more samples of the calibration database. The regularization parameter, γ , is decreased from 2000 to 120 as can be seen in Fig. 8. Typically, this result indicates that the regression coefficient becomes less complex and gain in stability. According to complexity and performance level, the LS-SVM_r model selected was the model based on EPO pre-processing with three components.

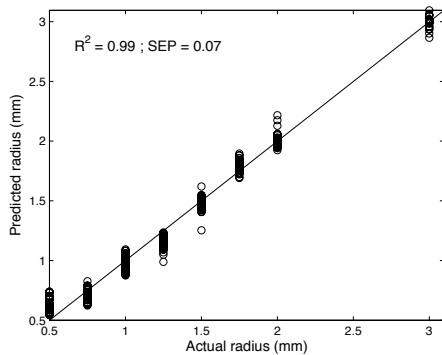


Fig. 9. Radius prediction using LS-SVM and EPO pre-processing.

Fig. 9 shows the results when using this model for predicting the radius of the test set. The performance is clearly better than for the PLS model. Even without reference value pre-processing, LS-SVM is better. Compared to the linear technique, the samples with small radius are more accurate predicted. SEP is reduced by a factor of two. This result demonstrates the ability of LS-SVM methods to deal with non-linear

problems. LS-SVM also appears to be less sensitive to external effects. With PLS, a residual effect can be noticed on the prediction plot where a reference value results in different predicted values. An interfering factor is the depth, which probably affects the spectra in a non-linear way. With LS-SVM this effect cannot be seen on the prediction plot. Since SVM is based on similarity between samples, the model can take into account non-linear external effects if a part of calibration sample variation is due to this effect.

Table 1 shows the results of LS-SVM_d models aiming at depth prediction. For each model the kernel parameter (σ) and regularization parameter (γ), Standard Error of Calibration (SEC), SECV and R^2 are given. SECV have been evaluated using 10 subsets, which each consists of 39 samples, rather than full cross validation, which is very time consuming with SVM. The first model based on raw spectra gives an over fitted model with a very good SEC and R^2 but a very high SECV. R^2 in cross validation is close to 0.4. Another important criterion is the very small kernel parameter (0.03) which induces a high non-linearity and therefore an increased sensitivity to over fitting. This model cannot be used for predicting the depth precisely (not shown). The EPO with 3 components pre-processing confer better stability and prediction ability to the model, with an increased kernel width parameter, a decreased regularization parameter and R^2 reduced to 0.87.

Table 1. LS-SVM models for depth prediction

Model	Sigma (σ)	Gamma (γ)	SEC (mm)	SECV (mm)	R^2
Unprocessed	0.03	200	0.17	2.49	1
+ EPO (3cp)	1.2	50	1.17	1.72	0.87
Processed+1 cp EPO	7.7	4000	1.06	1.47	0.89
Processed+2 cp EPO	2	120	0.22	0.90	0.99
Processed+3 cp EPO	2.5	50	0.37	0.88	0.99
Processed+4 cp EPO	2.8	100	0.43	1.04	0.98
Processed+5 cp EPO	2.6	120	0.46	1.14	0.98

The rest of the models presented in Table 1 include a processing of the spectra using the radius prediction and an EPO. Increasing the number of components used for EPO from 1 to 3, results in a global performance increase:

- (i) Regularization parameter fall from 4000 till 50, hence the regression coefficient gets less noisy
- (ii) Kernel width parameter is stabilized around a constant value 2.5
- (iii) R^2 increases towards 1
- (iv) SEC and SECV become more similar.

When 4 or 5 components are used for the EPO, the regularization parameter and SECV are unfavorably affected. This observation indicates that too much information is removed from the spectra which weaken the performance of the model. According to these considerations, the best selected LS-SVM_d model was based on radius processing and EPO with 3 components.

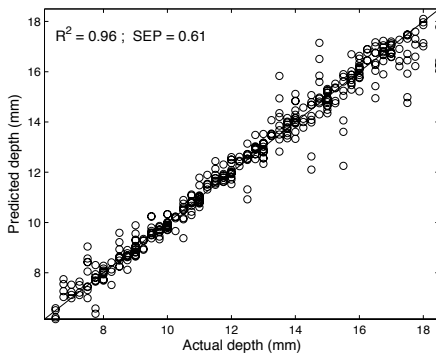


Fig. 10. Depth prediction performance on the test set with an LS-SVM model using EPO with 3 components and pre-processing of spectra using radius prediction.

In Fig. 10 the results of the depth prediction of the test set using this model are illustrated. As can be seen only a few samples are not well predicted. This can be seen as a consequence of inaccurate radius prediction that will then bring errors to the spectral correction. Main performance criteria are even better than the theoretically best PLS model using actual radius correction. In reality it was not possible to reach a good PLS model due to the non-linear behavior of the problem.

EPO seems an interesting approach for pre-processing spectra when applying SVM. Kernel methods such as LS-SVM calculate a similarity level between samples. For this reason, the influence of external parameters may impair the similarities between neighbor samples, which will damage LS-SVM performances. To cope with this issue, a PLS model can be used for pre-processing, PLS scores are then used as input into the LS-SVM model [18]. In this case, the prior projection into a linear space (PLS pre-processing) before a non-linear modeling might limit model performances. In comparison, EPO simply removes the interfering subspaces; the clean subspace still contains the non-linear relationships with the reference values. Thus, LS-SVM modeling will be more efficient with this type of pre-processing.

LS-SVM appears to be the most interesting modeling approach for predicting both radius and depth using fluorescence techniques. This study was performed on a simulated fluorescence data set based on some simplifications. In tissue the inclusion most probably would have an arbitrary shape, although the simplification of a sphere may hold for many cases. The choice of fluorescence contrasts in the data set was also arbitrarily selected. Future work includes experimental studies on tissue phantoms to verify how well the models work with experimental data and find the limitations. The concept of using multispectral data as input to LS-SVM models could provide useful information in finding the location of a fluorescent inclusion for applications like tumor diagnostics or give additional information for treatment progression in longitudinal animal studies [4]. The intended use of the algorithms presented here is to define the region of interest in a tissue volume [26]. Given this region the robustness of the quantitative analysis, i.e. concentration reconstruction, is enhanced.

5. Conclusion

Radius and depth prediction of an inclusion inside tissue using fluorescence is a difficult topic, mainly due to the non-linear relationships between various parameters. It has been possible to obtain a satisfactory PLS model for radius prediction using a convenient reference value processing. However, the depth of the inclusion cannot be predicted using PLS. Introducing pre-processing based on physical analysis result in poor PLS models. In contrast to PLS, LS-SVM gives a good level of performance for both depth and radius prediction. EPO was successfully used for improving the model further. For depth prediction EPO pre-processing is mandatory for reaching good performance. This clearly indicates the application of this method as a spectral pre-processing tool for non-linear models. The presented study demonstrates the non-linear relation of the depth and radius to the fluorescence signal. A further investigation of the best modeling method could be to compare the SVM performance with kernel-PLS [27] and neural networks.

Acknowledgement

This work was supported by the EU Integrated Project "Molecular Imaging" LSHG-CT-2003-503259.

References

- [1] N. Ramanujam, Fluorescence spectroscopy of neoplastic and non-neoplastic tissues, *Neoplasia* 2 (1-2) (2000) 89-117.
- [2] V. Ntziachristos, C. Bremer, R. Weissleder, Fluorescence imaging with near-infrared light: new technological advances that enable in vivo molecular imaging, *Eur. Radiol.* 13 (1) (2002) 195-208.
- [3] V. Ntziachristos, J. Ripoll, L. V. Wang, R. Weissleder, Looking and listening to light: the evolution of whole-body photonic imaging, *Nature Biotechnology*. 23 (3) (2005) 313-320.
- [4] V. Ntziachristos, Fluorescence molecular imaging, *Annual Review of Biomedical Engineering* 8 (2006) 1-33.
- [5] C. Bremer, V. Ntziachristos, R. Weissleder, Optical-based molecular imaging: contrast agents and potential medical applications, *Eur. Radiol.* 13 (2003) 231-243.
- [6] M. G. Muller, I. Georgakoudi, Q. Zhang, J. Wu, M. S. Feld, Intrinsic fluorescence spectroscopy in turbid media: disentangling effects of scattering and absorption, *Appl. Opt.* 40 (25) (2001) 4633-4646.
- [7] N. Ramanujam in R.A. Meyers (Ed), *Encyclopedia of analytical chemistry, Fluorescence spectroscopy in vivo*, John Wiley & sons ltd, Chichester, 2000 pp. 1-37.
- [8] S. Avrillier, E. Tinet, D. Ettore, J.-M. Tualle, B. Gélébart, Influence of the emission-reception geometry in laser-induced fluorescence spectra from turbid media, *Appl. Opt.* 37 (13) (1998) 2781-2787.
- [9] J. Svensson, S. Andersson-Engels, Modeling of spectral changes for depth localization of fluorescent inclusion, *Opt. Express*. 13 (11) (2005) 4263-4274.
- [10] J. Swartling, J. Svensson, D Bengtsson, K Terike, S. Andersson-Engels, Fluorescence spectra provide

- information on the depth of fluorescent lesions in tissue, *Appl. Opt.* 44 (10) (2005) 1934-1941.
- [11] R. J. Barnes, M. S. Dhanoa, S. J. Lister, Standard Normal Variate Transformation and De-trending of Near-infrared Diffuse Reflectance Spectra, *Appl. Spectrosc.* 43 (5) (1989) 772-777.
- [12] P. Geladi, D. MacDougall, H. Martens, Linearization and Scatter Correction for Near-infrared Reflectance Spectra of Meat, *Appl. Spectrosc.* 39 (3) (1985) 491-500.
- [13] A. Savitzky, M. J. E. Golay, Smoothing and differentiation of data by simplified least squares procedures, *Anal. Chem.* 36 (8) (1964) 1627-1639.
- [14] X. D. Li, M. A. O'Leary, D. A. Boas, B. Chance, A. G. Yodh, Fluorescent diffuse photon: density waves in homogeneous and heterogeneous turbid media: analytic solutions and applications, *Appl Opt.* 35 (19) (1996) 3746-3758.
- [15] S. Wold, H. Antti, F. Lindgren, J. Ohman, Orthogonal Signal Correction of Near-Infrared Spectra, *Chemom. Intell. Lab. Syst.* 44 (1-2) (1998) 175-185.
- [16] J. M. Roger, F. Chauchard, V. Bellon-Maurel, EPO-PLS external parameter orthogonalisation of PLS application to temperature-independent measurement of sugar content of intact fruits, *Chemom. Intell. Lab. Syst.* 66 (2) (2003) 191-204.
- [17] M. Zeaiter, J. M. Roger, V. Bellon-Maurel, Dynamic orthogonal projection. A new method to maintain the on-line robustness of multivariate calibrations. Application to NIR-based monitoring of wine fermentation, *Chemom. Intell. Lab. Syst.* 80 (2) (2006) 227-235.
- [18] F. Chauchard, R. Cogdill, S. Roussel, J. M. Roger, V. Bellon-Maurel, Application of LS-SVM to non-linear phenomena in NIR spectroscopy: Development of a robust and portable sensor for acidity prediction in grapes, *Chemom. Intell. Lab. Syst.* 71 (2) (2004) 141-150.
- [19] R. P. Cogdill, L. R. Schimleck, P. D. Jones, G. F. Peter, R. F. Daniels, A. Clark, Estimation of the physical wood properties of *Pinus taeda* L. radial strips using least squares support vector machines, *Journal of Near Infrared Spectroscopy.* 12 (4) (2004) 263-269.
- [20] J. A. Pierna Fernández, V. Baeten, A. M. Renier, R. P. Cogdill, P. Dardenne, Combination of support vector machines (SVM) and near-infrared (NIR) imaging spectroscopy for the detection of meat and bone meal (MBM) in compound feeds, *J. Chemom.* 18 (7-8) (2004) 341-349.
- [21] G. M. Palmer, C. Zhu, T. M. Breslin, F. Xu, K. W. Gilchrist, N. Ramanujam, Comparison of multiexcitation fluorescence and diffuse reflectance spectroscopy for the diagnosis of breast cancer (march 2003), *IEEE Trans Biomed Eng.* 50 (11) (2003) 1233-1242.
- [22] H. Martens, T. Naes, *Multivariate Calibration*, Wiley & Sons Ltd, New York, (1991).
- [23] J.A.K. Suykens, J. Vandewalle (Eds.), *Nonlinear modelling: advanced black-box techniques*, Kluwer Academic Publishing, Boston, (1998), pp.1-274.
- [24] G. Alexandrakis, F. R. Rannou, A. F. Chatziioannou, Tomographic bioluminescence imaging by use of a combined optical-PET (OPET) system: a computer simulation feasibility study, *Phys. Med. Biol.* 50 (2005) 4225-4241.
- [25] S. A. Prahl. Optical Absorption of Hemoglobin. <http://omlc.ogi.edu/spectra/hemoglobin/index.html> (2004).
- [26] H Xu, R. Springett, H. Dehghani, B. W. Pogue, K. D. Paulsen, J. F. Dunn, Magnetic-resonance-imaging-coupled broadband near-infrared tomography system for small animal brain studies, *Appl. Opt.* 44 (11) (2005) 2177-2188.
- [27] T Czekaj, W Wu, B. Walczak, About kernel latent variable approaches and SVM, *J. Chemom.* 19 (5-7) (2005) 341-354.

Fluorescence and absorption assessment of a lipid mTHPC formulation following topical application in a non-melanotic skin tumor model

Ann Johansson^{*1}, Jenny Svensson¹, Niels Bendsoe², Katarina Svanberg³, Eleni Alexandratou⁴, Maria Kyriazi⁴, Dido Yova⁴, Susanna Gräfe⁵, Tilmann Trebst⁶, Stefan Andersson-Engels¹

¹Department of Physics, Lund University, PO Box 118, SE-221 00 Lund, Sweden

²Department of Dermatology and Venereology, Lund University Hospital, SE-221 85 Lund, Sweden

³Department of Oncology, Lund University Hospital, SE-221 85 Lund, Sweden

⁴Department of Electrical Engineering and Computing, Biomedical Optics and Applied Biophysics Laboratory, National Technical University of Athens, G-15780 Athens, Greece

⁵Research & Development, biolitec AG, D-07745 Jena, Germany

⁶CeramOptec GmbH, D-53121 Bonn, Germany

* Phone: +46 462223120, Fax: +46 462224250, ann.johansson@fysik.lth.se

ABSTRACT

Although the benefits of topical sensitizer administration have been confirmed for photodynamic therapy (PDT), ALA-induced protoporphyrin IX is the only sensitizer clinically used with this administration route. Unfortunately, ALA-PDT results in poor treatment response for thicker lesions. Here, selectivity and depth distribution of the highly potent sensitizer *meso*-tetra(hydroxyphenyl)chlorin (mTHPC), supplied in a novel liposome formulation was investigated following topical administration for 4 and 6 hours in a murine skin tumor model. Extraction data indicated an average (\pm SD) mTHPC concentration within lesions of 6.0 (\pm 3.1) ng/mg tissue with no significant difference ($P < 0.05$) between 4 and 6 hour application times and undetectable levels of generalized photosensitivity. Absorption spectroscopy and chemical extraction both indicated a significant selectivity between lesion and normal surrounding skin at 4 and 6 hours, whereas the more sensitive fluorescence imaging setup revealed significant selectivity only for the 4 hour application time. Absorption data showed a significant correlation with extraction, whereas the results from the fluorescence imaging setup did not correlate with the other methods. Our results indicate that this sensitizer formulation and administration path could be interesting for topical mTHPC-PDT, decreasing the effects of extended skin photosensitivity associated with systemic mTHPC administration.

Keywords: pharmacokinetics, fluorescence imaging, absorption spectroscopy, photodynamic therapy, mTHPC

1 INTRODUCTION

Photodynamic therapy (PDT) as a cancer treatment modality has shown promising results both in terms of efficacy and selectivity.¹ The PDT effect is caused by a combination of treatment induced apoptosis and direct necrosis,² vascular damage³ and possibly an elicited immune response,⁴ where the extent of tissue damage depends on the total light dose, the tissue oxygenation and the sensitizer concentration.⁵ The most common administration route is intravenous injection, leading to an extended photosensitivity following treatment for some sensitizers.⁶

In the case of easily accessible and thin lesions, e.g. superficial skin malignancies, topical sensitizer application is highly desirable from a clinical point of view. ALA-induced protoporphyrin IX is a photosensitizer that has been used with this administration route for the treatment of various skin tumors.⁷ To overcome the poor skin permeability caused by the hydrophilic character of the ALA-molecule, several groups have investigated the selectivity and penetration depths of some of its esters. Utilizing the less hydrophilic methyl esterified ALA-Me, good tumor selectivity has been observed both in animal skin tumor models and in human basal cell carcinomas (BCCs).^{8,9} However, the limited light penetration of the activating light,¹⁰ the localization of the protoporphyrin IX molecule within biological tissue¹¹, and the

relatively low extinction coefficient of this sensitizer¹² are additional factors that might limit the treatment efficacy.^{7,13}

In contrast to protoporphyrin IX, *meso*-tetra(hydroxyphenyl)chlorin (mTHPC) has been reported as one of the most efficient sensitizers, as relatively small drug and light doses are required in order to achieve treatment response.¹⁴ Though, the hydrophobic mTHPC molecules form aggregates in aqueous surroundings, leading to limited transportation of the sensitizer within biological media, tumor selectivity and PDT efficacy.¹⁵⁻¹⁷ Gupta *et al.* have reported on PDT following topical mTHPC administration for treatment of Bowen's disease and BCCs.¹⁸ In this study, the overall pathological tumor clearance was limited to 32% at the 2-month follow-up. The authors suggest the method of topical sensitizer application and mTHPC formulation were the primary limiting factors. In an effort to improve efficiency of topically administered drugs, the use of liposomes as drug delivery vehicles has been reported to increase skin penetration for some active substances.¹⁹ For example, ALA has been encapsulated into liposomes, leading to an improved retention within the epidermis and dermis in an *in vitro* skin model.²⁰ By incorporating the hydrophobic PDT-agent bacteriochlorin a into liposomes, an increased oxygen consumption and decreased cell survival during PDT in cell cultures was observed as compared to the raw formulation.²¹ Furthermore, the use of liposomes as carrier of benzoporphyrin derivative monoacid ring A resulted in better PDT efficiency in a mouse tumor model.²² These effects have been explained by monomerization of the sensitizer,²¹ a different micro-localization within the cells and an increased association with low density lipoproteins when incorporating the sensitizers into liposomes.^{21,22}

In the present study, the sensitizer distribution following topical application of a novel gel formulation containing liposome-encapsulated mTHPC, referred to as mTHPC-gel, is investigated in an animal skin tumor model. The drug-accumulation interval in this study is restricted to 4 and 6 hours, as clinically relevant for topically applied PDT photosensitizers.²³ In addition, the application of this new mTHPC formulation for several hours is possible as the compound is supplied in a heat-setting gel. Chemical extraction and non-invasive optical methods are utilized for investigating the selectivity between lesion and normal skin. In addition, the mTHPC concentration within the internal organs is monitored to assess the level of generalized photosensitivity.

A further incentive of the present study is the comparison of fluorescence and absorption spectroscopy to chemical extraction as methods for quantifying sensitizer concentration. The combination of a strongly fluorescing and absorbing PDT agent and superficially located lesions makes fluorescence imaging and absorption spectroscopy attractive tools for non-invasive studies of sensitizer concentration. These methods have the additional advantage that they can provide information in realtime. On the other hand, as the fluorescence signal depends on tissue optical properties, it is difficult to utilize the absolute fluorescence level to quantify the sensitizer concentration, especially within heterogeneous media. For the absorption spectroscopy data, the effect of varying tissue absorption can be handled by studying the total absorption imprint of tissue and exogenous chromophore over a sufficiently broad spectral interval.

In the present work, imaging of the tissue and sensitizer fluorescence levels is performed utilizing a near-ultraviolet light source and detection at a few selected wavelengths. The absorption spectroscopy setup utilizes a fiber optical source-detector pair, where the source-detector separation has been chosen to make the method insensitive to variations in scattering parameters for the range of scattering values typically found in biological tissue.²⁴ The predicted sensitizer concentration is tested for correlation between the two optical methods and the chemical extraction and we comment on the accuracy of the optical methods for this tumor model and measurement geometry.

2 Materials and Methods

2.1 mTHPC-gel preparation

The compound is comprised of a liposomal formulation of mTHPC in a thermogel matrix (biolitec AG, Jena, Germany) with a sensitizer concentration of 0.5 mg mTHPC/ml gel. The liposome formulation (Foslip) is based on dipalmitoylphosphatidylcholine (DPPC), monosaccharide, water and polyoxyethylene polyoxypropylene block copolymers and encapsulates the mTHPC.²⁵ The mTHPC-gel is liquid at the

storage temperature of 4°C but forms a highly viscous gel when heated by the skin to temperatures above 26°C. The thermo-thickening thus aids in increasing the retention time of the applied gel and transfer of the sensitizer into the tissue. No penetration enhancers are added to the mTHPC-gel.

2.2 Animal procedures

Malignant skin tumors were induced in seven male albino hairless mice (SKH-HR1), 8-10 weeks old and weighing 30-35 g. For skin carcinoma induction a two stage model of carcinogenesis was utilized with DMBA (7,12-dimethylbenz(a)anthracene) as initiator and ultraviolet radiation as skin cancer promoter. Details on the procedure for induction of skin carcinogenesis have been published by Kyriazi *et al.*²⁶ Tumors first appear as benign papillomas, progressing towards more malignant states, and finally developing into basal (10%) and squamous (80%) cell carcinomas as determined after histopathological examination of representative specimens. In the remaining 10%, no malignant transformation appears. This progress is consistent with previously described studies in hairless mice.²⁷ Here, tumor diameters ranged between 0.2 and 1 cm, where mice with tumor diameter greater than 1 cm were euthanized for ethical reasons. The study was carried out according to the guidelines established by the European Parliament and Council Directive 2003/65/EC and the Greek Animal Ethics Committee.

Twenty µl of mTHPC-gel was applied topically on each of the areas investigated, i.e., tumor, normal skin and skin in the immediate vicinity of the tumor. The sensitizer concentration was studied at 4 or 6 hours after mTHPC-gel administration utilizing non-invasive optical techniques. Three animals with a total of 10 lesions and another three animals with 5 lesions were investigated at the 4 and 6 hour time points, respectively. All tissue regions were carefully cleaned prior to fluorescence and absorption measurements to remove any gel remaining on the skin surface. In addition, the optical measurements were performed on all animals prior to administration of the mTHPC-gel. For all animals, application of the sensitizer and optical measurements were performed under general anesthesia (*i.p.* injection of 20 µl of γ -hydroxybutyric lactone solution in 0.9% sodium chloride (50:50, v:v)). Following the optical measurements at 4 or 6 hours, animals were killed by cervical dislocation and the tissue regions previously treated with the mTHPC-gel were excised for extraction measurements. In addition, the mTHPC concentration in blood, liver, spleen, muscle and normal skin where no sensitizer had been applied was also investigated by means of extraction. *In vivo* optical measurements were also performed for two lesions in another animal at 1.5, 3 and 5 hours after sensitizer application in an attempt to follow the temporal mTHPC concentration profile within a single animal. Though, prior to the spectroscopic investigations at 1.5, 3 and 5 hours, the tissue regions had to be carefully cleaned to avoid measuring fluorescence from mTHPC within the gel remaining only on top of the skin surface. After the optical measurements at 1.5 and 3 hours, another 20 µl of the mTHPC-gel was administered to allow further sensitizer accumulation. This procedure was thus slightly different from that employed for the remaining animals as it resulted in the application of three 20 µl aliquots of the sensitizer gel. After sacrificing the animal at the 5 hour drug-light interval, the mTHPC fluorescence and absorption levels were also investigated throughout a vertical cut of the two excised tumors in order to study the depth distribution.

2.3 Fluorescence imaging

A 405-nm continuous-wave diode laser (Power Technology Inc., Little Rock, Arkansas) emitting 2.1 mW was used to induce fluorescence within a 27-mm diameter area. The tissue autofluorescence at 500 (±10 nm) and mTHPC fluorescence at 654 nm (±20 nm) were filtered out using bandpass filters (Oriel, Stratford, Connecticut) and imaged using a cooled, intensified CCD (iStar, Andor Technology, Belfast, Northern Ireland). Two cut-off filters, GG475 and GG455 (Schott, Mainz, Germany), were used to attenuate the reflected excitation light. All data was compensated for differences in spectral response using a NIST-traceable light source.

For each animal, the fluorescence intensities at 654 and 500 nm were averaged within each investigated tissue region. The mTHPC distribution was quantified by a dimensionless contrast function resulting from forming a spectral ratio between the two detection bands;

$$F = \frac{I(654 \text{ nm}) - I_{bkg}}{I(500 \text{ nm}) - I_{bkg}} \quad (1)$$

$I(654\text{ nm})$ and $I(500\text{ nm})$ denote the fluorescence intensity at the two wavelengths and I_{bkg} is a constant background level originating from the dark current of the detector.

For this setup, the mTHPC detection limit was below $0.005\text{ }\mu\text{M}$ in liquid phantoms containing ink (Pelikan Fount India Ink, Hannover, Germany) at volume concentrations of 0.35-1.05%, giving background absorption of $0.2\text{-}0.6\text{ cm}^{-1}$, and Intralipid (Fresenius Kabi, Uppsala, Sweden) at volume concentrations of 2.8-3.7%, resulting in a reduced scattering coefficient between 7 and 9 cm^{-1} .

2.4 Absorption spectroscopy

The optical absorption setup together with the accuracy and validity of the method have been described in greater detail elsewhere.^{24,28} Briefly, the output from a pulsed Xenon short-arc lamp was delivered by a $400\text{ }\mu\text{m}$ diameter optical fiber and, after interacting with the tissue, the transmitted light was collected by a $200\text{ }\mu\text{m}$ diameter fiber. The center-to-center distance between delivery and collection fibers measured 2.0 mm . An S2000 miniature spectrometer (Ocean Optics Inc., Dunedin, Florida) was used to disperse and detect the collected light. Wavelength dependent fluctuations in source output and detector response were accounted for by taking a reference measurement from a spectrally flat diffuse reflector based on Spectralon material (Lab Sphere Inc., Cranfield, UK) in connection to each measurement sequence.

For source-detector separations in the range 1.5 to 2.6 mm , the pathlength of the collected photons has been shown to be relatively insensitive to variations in tissue scattering.²⁴ Therefore, the Beer-Lambert's law can be used to assess changes in tissue absorption. The negative logarithm of the transmission signal measured after the addition of an absorber, $I_2(\lambda) = I(\Delta\mu_a + \mu_a^0)$, to that before, $I_1(\lambda) = I(\mu_a^0)$, is given by;²⁸

$$R(\lambda) = -\ln\left(\frac{I_2}{I_1}\right) = -\ln\left(\frac{I(\Delta\mu_a + \mu_a^0)}{I(\mu_a^0)}\right) = \Delta\mu_a L_{eff}(\Delta\mu_a + \mu_a^0) + B. \quad (2)$$

In Eqs. (2-6), the wavelength-dependence of the absorption coefficients and the transmission signals is omitted for purpose of clarity. Although the pathlength is insensitive to scattering variations, the amount of collected light might change between measurements and hence the appearance of the factor B . $L_{eff}(\Delta\mu_a + \mu_a^0)$ denotes the effective pathlength, which depends on the total absorption coefficient. To determine this dependence, a non-sequential ray tracing software package (ASAP 8.0.3, Breault Research Organization, Tucson, Arizona) was used to track the pathlengths of collected rays for a geometry matching the experimental setup. For these simulations, the source and detection fibers, having diameters as stated above and a numerical aperture of 0.22 , were separated by 2 mm . The scattering and anisotropy coefficients were kept constant at 10 cm^{-1} and 0.9 , respectively. 167 million rays were simulated in the absence of absorption and the optical pathlengths, L_i , for all detected rays were stored. The effect of tissue absorption on the optical pathlengths was added to the simulation results and the effective pathlength for different absorption coefficients was evaluated by Eq. (3):

$$L_{eff}(\mu_a) = -\frac{1}{\mu_a} \ln\left(\frac{\sum_{i=1}^N \exp(-\mu_a L_i/n)}{N}\right). \quad (3)$$

Here n denotes the refractive index and N equals the number of detected rays, in this case 1.4 and 1000 , respectively. The absorption coefficient, μ_a , was allowed to vary between 0.001 and 5 cm^{-1} in steps of 0.001 cm^{-1} . In contrast to the work by Mourant *et al.*²⁸, where a slightly smaller fiber separation was used, no single functional dependency could adequately fit the effective pathlength to the total absorption coefficient over the entire absorption range. Therefore, a nearest-neighbor spline interpolation was used to describe the dependence of the effective pathlength on the total absorption coefficient.

In earlier work, Eq. (2) was in fact evaluated from measurements before and after addition of an exogenous absorber.²⁸ Here, both I_1 and I_2 are evaluated from a single measurement. By assuming that tissue absorption at 900 nm is dominated by water at a constant concentration of 60% , I_1 can be expressed as;

$$I_1 = I(\mu_a^{60\% \text{ water}}) = I(900 \text{ nm}) \cdot \exp[-L_{\text{eff}}(\mu_a^{60\% \text{ water}})\mu_a^{60\% \text{ water}}] \dots \quad (4a)$$

$$\exp[-L_{\text{eff}}(\mu_a^{60\% \text{ water}}(900 \text{ nm}))\mu_a^{60\% \text{ water}}(900 \text{ nm})]^{-1},$$

where $I(900\text{nm})$ is the detected signal at 900 nm. Furthermore, I_2 is given by the detected signal and is described as before;

$$I_2 = I(\Delta\mu_a + \mu_a^0) = I(\Delta\mu_a + \mu_a^{60\% \text{ water}}). \quad (4b)$$

Since both transmission signals originate from a single measurement, the factor B is eliminated and Eq. (2) is modified to:

$$R(\lambda) = -\ln\left(\frac{I(\Delta\mu_a + \mu_a^{60\% \text{ water}})}{I(\mu_a^{60\% \text{ water}})}\right) = \Delta\mu_a L_{\text{eff}}(\Delta\mu_a + \mu_a^{60\% \text{ water}}). \quad (5)$$

The function “lsqnonlin” in Matlab (MathWorks, Natick, Massachusetts) was used to solve for $\Delta\mu_a$ from Eq. (5). The spectral fitting interval was 500 to 800 nm. A singular value decomposition (SVD) algorithm was used to fit the extinction coefficients of relevant tissue chromophores to the calculated change in absorption coefficient. The SVD algorithm provides the best fit of a linear combination of a certain number of basis spectra to a data set and has been used previously in order to analyze fluorescence²⁹ and broadbanded reflectance spectra.³⁰ The extinction coefficients included in the evaluation of the absorbance data were those of mTHPC, deoxy- (Hb) and oxyhemoglobin (HbO).³¹ In addition, the mTHPC fluorescence spectrum was included in the model since experimental work gave evidence that the shorter wavelengths within the light source did induce detectable sensitizer fluorescence also in the presence of strong tissue absorption. This fluorescence component partly overlaps the absorption peak at 652 nm, leading to an underestimated mTHPC concentration if fitting the sensitizer extinction coefficient to this peak only. $\Delta\mu_a$ could thus be expressed as:

$$\Delta\mu_a = \Delta c_{\text{mTHPC}} \epsilon_{\text{mTHPC}} + \Delta c_{\text{Hb}} \epsilon_{\text{Hb}} + \Delta c_{\text{HbO}} \epsilon_{\text{HbO}} + AM(\lambda) + \sum_{i=0}^2 \omega_i C_i \lambda^i, \quad (6)$$

where the Δc 's denote concentration changes and the ϵ 's are the corresponding extinction coefficients. $M(\lambda)$ and A are the sensitizer fluorescence spectrum and fluorescence amplitude, respectively. The last summation on the right hand side of Eq. (6) was included in order to account for tissue autofluorescence overlapping the absorption signals. The number of components within this summation was determined empirically by minimizing the residuals returned by the algorithm. The magnitude of $M(\lambda)$ and the weights ω_i were chosen to match the magnitudes of the chromophore extinction coefficients. For each absorption spectrum, the SVD algorithm returned the chromophore concentrations, i.e. the Δc 's, the mTHPC fluorescence amplitude, A , and the individual C_i 's. The Δc_{mTHPC} was used to predict the mTHPC concentration from each measurement. The sensitizer level was determined by the average Δc_{mTHPC} from 2-5 absorption spectra acquired for each animal, tissue type and investigation time point, i.e. at 0 and 4 or 6 hours. For the absorption spectroscopy data, the error of the fit was quantified as:

$$r = \left[\frac{1}{m-1} \sum_{\lambda} (y_{\text{measured},\lambda} - y_{\text{fit},\lambda})^2 \right]^{1/2}, \quad (7)$$

where the summation includes the spectral fitting interval 500-800 nm and m denotes the number of data points within this interval. In the case of negative sensitizer concentration prediction, the mTHPC concentration was set to zero and the error of the fit was re-evaluated by only including deoxy- and oxyhemoglobin in the SVD algorithm.

Fig. 1(a) illustrates the different basis spectra used for the SVD algorithm within the spectral fitting range. Fig. 1(b) shows *in vivo* data from a lesion 4 hours after sensitizer administration together with the fit and the corresponding residuals. For this measurement, the predicted concentrations were 1.3, 11.6 and 8.9 μM for mTHPC, deoxy- and oxyhemoglobin. The mTHPC fluorescence amplitude was $+1.7 \cdot 10^{-6}$ a.u. It should be emphasized that the analysis of the absorption spectra assumes homogeneous medium. For this situation, the accuracy of the setup and method of data analysis was confirmed in TiO-based liquid phantoms with scattering similar to those levels encountered in normal tissue ($\mu_s \sim 5\text{-}15 \text{ cm}^{-1}$) and sensitizer concentration between 2 and 20 μM . The lower mTHPC detection limit was approximately 0.5 μM within the same set of liquid phantoms as described in Section 2.3.

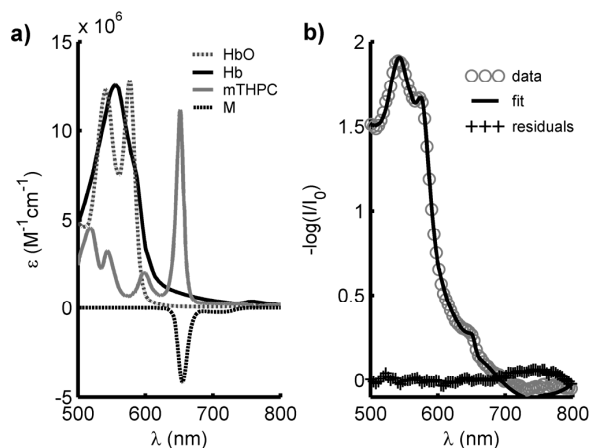


Fig. 1 (a) mTHPC fluorescence and extinction coefficients of mTHPC in ethanol, deoxy- (Hb) and oxyhemoglobin (HbO). The components constituting the background signal are not shown for purpose of clarity. Absorption and fluorescence data for mTHPC was kindly provided by biolitec AG. (b) Absorption data from animal 2. Also shown are the fit and the corresponding residuals. The error of the fit was 0.029.

2.5 Extraction

Tissue samples, weighing 100-200 mg, were homogenized in 3 ml of dimethyl sulfoxide (DMSO) at 24,000 rpm (T18 Basic Ultra Turrax, IKA, Staufen, Germany). The homogenate was centrifuged at 800g (3000 rpm) for 20 min (EconoSpin, Sorvall Instruments DuPont, Wilmington, Delaware). The supernatant was collected and following excitation at 420 nm, the fluorescence signal was recorded between 460 and 700 nm using a luminescence spectrometer (LS 45, Perkin Elmer, Buckinghamshire, UK). The detected fluorescence intensity at 652 nm was used to provide an absolute measure of sensitizer concentration after appropriate calibration. Blood samples were centrifuged at 360g (2,000 rpm) for 10 min in order to separate out the plasma. Fifty μ l of plasma were mixed with 2950 μ l DMSO for further analysis according to the same procedure as for the other organs. The lower detection limit for the extraction setup was 0.04 ng mTHPC/mg tissue, which corresponds to approximately 0.06 μ M assuming a tissue density of 1.06 g/ml.

2.6 Statistical analysis

To study agreement between two methods, the correlation of the data from each technique was calculated using Eq. (8):

$$R(x, y) = \frac{\text{cov}(x, y)}{[\text{cov}(x, x)\text{cov}(y, y)]^{1/2}}. \quad (8)$$

Here, $\text{cov}(x, y) = E[(x - m_x) \cdot (y - m_y)]$, where E denotes the mathematical expectation, x and y represent the mTHPC quantity as determined by each method and m_x and m_y are the corresponding averaged mTHPC quantities. For comparison of two means, a two-sided Student's t -test was used where $P \leq 0.05$ was considered significant.

3 RESULTS

The extraction results indicated preferential accumulation of mTHPC in lesions as compared to normal skin both at 4 and 6 hours after sensitizer application. The average mTHPC concentration in lesions was 6.0 ng/mg tissue with a standard deviation (SD) of 3.1 ng/mg. No significant difference could be identified between the two drug-light intervals. Sensitizer levels in liver, spleen, blood, muscle and normal skin where no mTHPC-gel had been applied were below the detection limit, indicating mTHPC concentrations below 0.04 ng/mg tissue.

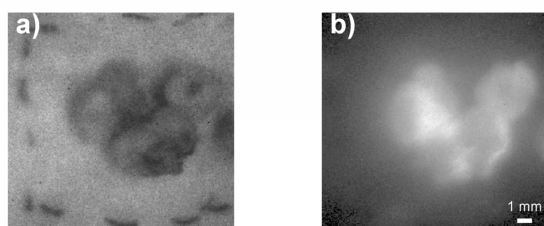


Fig. 2 (a) Room-light image showing lesions and surrounding skin for animal 3. (b) Fluorescence signal at 654 nm showing selective accumulation of mTHPC.

Fig. 2 shows room-light and 654-nm fluorescence images of three lesions 4 hours after application of the mTHPC-containing gel. The temporal profile of the mTHPC build-up assessed by the fluorescence imaging technique is shown in Fig. 3(a), where the averaged contrast function value is plotted as a function of mTHPC-gel application time for lesion (t), normal skin (n) and skin surrounding the visible lesion (m). The data indicated significant sensitizer selectivity within lesions for 4 but not 6 hours drug-light interval. Only normal skin (n) indicated a significant difference between 4 and 6 hour application times.

As for the extraction data but in contrast to the fluorescence results, the absorption spectroscopy data revealed a selective sensitizer accumulation within lesions for both drug-light intervals. The temporal profile of the calculated mTHPC concentration within lesions is shown in Fig. 3(b). For this tissue type, no significant differences in sensitizer build-up could be identified for the two different mTHPC accumulation times. Resulting mTHPC levels for normal skin and intact skin in close proximity to the lesion were below the detection limit of the setup and are therefore not shown. The model for the SVD algorithm, including mTHPC, deoxy- and oxyhemoglobin extinction coefficients and mTHPC fluorescence, resulted in good agreement with measurement data. The average fitting errors, evaluated according to Eq. (7), were 0.064 and 0.050 for lesion and intact skin in close proximity to the lesion, respectively. The fitting errors displayed no statistically significant differences with tissue type and drug-light interval.

Fig. 3(c) shows the extraction data for each individual lesion, illustrating large inter-tumor variations in sensitizer concentration. In general, lesions displayed a heterogeneous tissue structure sometimes also presenting necrotic areas. The high variability in mTHPC concentration was most likely influenced by the differences in tissue composition. Fig. 3(d) is a scatter plot illustrating the agreement between absorption and extraction data where each marker represents data from a specific lesion. The solid line shows the best fit in a linear-least square sense whereas the dashed line represents the ideal fit. The slope of the correlation curve was 1.2. The overestimation of the mTHPC concentration by the absorption data is mostly due to the outlier at $>30 \mu\text{M}$ as measured by the absorption technique. For tumor tissue, the absorption and extraction data showed a significant correlation ($P < 0.05$) with a correlation coefficient of 0.72. On the other hand, the fluorescence contrast ratio displayed no significant correlation to the other methods.

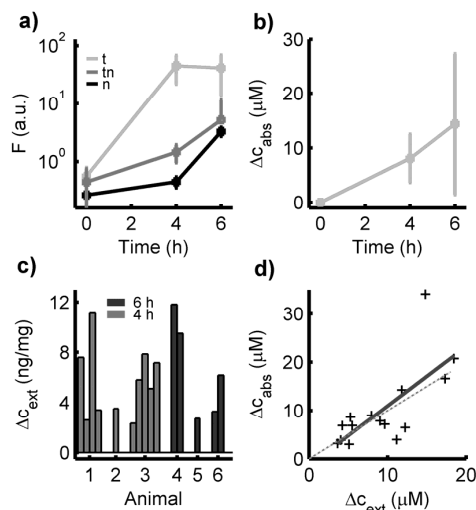


Fig. 3 (a) Contrast function value for normal tissue (*n*), tissue in close proximity to lesion (*tn*) and lesion (*t*). Each marker represents the averaged *F*-value and error bars denote ± 1 SD. (b) Temporal profile of the average mTHPC concentration within lesions as estimated by the absorption spectroscopy probe. (c) mTHPC concentration as determined by extraction for each lesion in six animals. (d) Scatter plot illustrating the covariance between absorption and extraction data for all lesions.

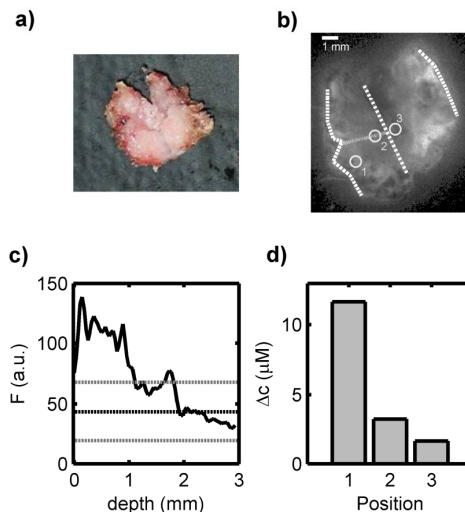


Fig. 4 (a) Digital photograph showing cross section of a vertical cut through a tumor. (b) Fluorescence contrast function image for the same tumor. The tumor surface and deepest tissue region are indicated by the bright dashed lines. (c) Fluorescence contrast function value along the thin dashed line in part b of the figure. The dashed lines indicate the average *F*-value ± 1 SD for all lesions. (d) mTHPC concentration as measured by the absorption spectroscopy probe. Measurement positions are marked in part b of the figure.

Fig. 4(a) is a photograph of one excised lesion, approximately 4 mm in depth, sliced parallel to its depth axis. The fluorescence contrast function image of the same lesion is presented in Fig. 4(b), illustrating the heterogeneous structure of the mTHPC content. Fig. 4(c) shows the fluorescence contrast value (*F*-value) along the depth profile marked by the thin dashed line in Fig. 4(b). As a comparison, the average (± 1 SD) *F*-value for all lesions *in vivo* is also included in the graph. The mTHPC concentration assessed by the absorption technique is plotted in Fig. 4(d) for three measurement positions, also showing the decrease in sensitizer concentration with depth. Possibly due to the administration of a total of three 20- μ l aliquots of the mTHPC-gel, *in vivo* absorption measurements on this lesion via the surface of the intact tumor indicated sensitizer levels slightly higher than for the remaining animals as tested by a one-sided Student's *t*-test ($P \leq 0.05$). The second lesion used for investigating the sensitizer depth penetration did not display significantly higher mTHPC concentration as compared to the other lesions. Though, some caution should be exercised when interpreting the sensitizer depth distribution from Fig. 4.

4 DISCUSSION

Topical application of ALA has been successfully used in combination with superficial PDT of skin malignancies.⁷ By employing methyl esterified ALA-Me, an improved tumor selectivity⁸ as well as homogeneous protoporphyrin distribution down to 2 mm in human BCCs⁹ have been achieved. Though, protoporphyrin IX still remains a PDT agent resulting in relatively limited treatment efficacies.^{7,13} This work reports on the first use of a topically applied liposomal mTHPC-formulation in a non-melanoma skin carcinoma model. This mTHPC-gel was investigated as a possible alternative to ALA-PDT and systemic administration of mTHPC, suffering from poor treatment outcome for thicker lesions and

prolonged photosensitivity, respectively. In the present study, significant sensitizer selectivity in lesions as compared to skin with intact stratum corneum was observed from extraction and optical absorption data for both 4 and 6 hour drug-light intervals. In fact, the mTHPC concentration within tissue characterized by an undamaged upper skin layer was below the detection limits of these setups. The extraction results from internal organs and normal skin where no mTHPC-gel had been applied showed no trace of the sensitizer, indicating undetectable levels of generalized photosensitivity. Data from the fluorescence imaging setup also indicated no significant variation in sensitizer concentration within lesions for the two application times. Though, increased mTHPC fluorescence was observed between the 4 and 6 hour application times for gel-treated normal skin with an intact stratum corneum, possibly due to the higher sensitivity of this setup. For the fluorescence spectroscopy data set, the selectivity between lesion and normal skin was thus only significant for the shorter drug-light interval, indicating an optimal drug-light interval of 4 hours for the present skin tumor model.

The observed sensitizer distribution is likely due to differences in the ability of mTHPC and liposomes to penetrate the tissue layers. The absence of stratum corneum over the lesion seems to facilitate the sensitizer penetration, whereas intact skin prevents the lower tissue layers from accumulating any substantial amount of mTHPC. Supporting the present observations, Schmid *et al.* state that intact liposomes penetrate only very superficial parts of the normal epidermis, whereas damaged skin constitutes a less efficient barrier.³² The diffusion of liposome-encapsulated ALA through healthy mouse skin has been shown to require tens of hours,²⁰ and this slow process could be explained by the way liposomes are believed to interact with intact skin, first adhering to and then disrupting the upper tissue membranes. The liposomes hence act as penetration enhancers.¹⁹ These previously published results are in agreement with the increasing, although still low, mTHPC levels found in normal mouse skin for the 6 hour administration time.

For tumor tissue, the large variations in mTHPC concentration and the lack of significant differences between 4 and 6 hour drug-light intervals could be due to a sensitizer build-up within lesions mostly determined by the tissue composition and the status of the uppermost layers. For example, it was noted that necrotic regions displayed overall lower sensitizer levels. It is also reasonable to suspect the depth penetration of the sensitizer to depend on the status of the upper skin layers. Within the lesions for which the sensitizer depth penetration was investigated, the mTHPC concentration was in the range of μM down to depths of 3-4 millimeters. Similar results have been reported by Peng *et al.*, where good selectivity and homogenous sensitizer distribution down to 2 mm in human BCCs were observed following topical application of ALA-Me.⁹ Since the liposomal mTHPC-formulation was not compared to its pure analog, it is difficult to determine the effect the use of liposomes had on the sensitizer distribution and depth penetration within the present study.

The mTHPC levels observed within lesions in the present study are in the range shown to induce significant PDT effects once irradiated at an appropriate wavelength.³³ Though, another factor important to the PDT outcome is the localization of the sensitizer molecule within the tissue and the cell. In the case of systemic mTHPC administration, short drug-light intervals result in vascularly targeted PDT,³³ whereas longer time periods allow the sensitizer to localize within the cells, targeting for example mitochondria.³⁴ In the case of topical mTHPC administration, the mTHPC levels found in blood were low for all time points investigated. We thus anticipate the PDT effect to more strongly correlate with maximum sensitizer concentration within the lesion and display less pronounced vascular effects.

In parallel to the extraction study, fluorescence imaging and absorption spectroscopy were evaluated as non-invasive methods for assessing sensitizer content *in vivo*. The fluorescence imaging setup has the advantage of being a more sensitive tool than the absorption spectroscopy probe. Furthermore, the ability to image larger areas quickly provides valuable information on the spatial sensitizer distribution. Though, for the range of optical properties found in biological tissue, the effective penetration depth of the near-ultra violet light used for exciting the mTHPC fluorescence is on the order of a couple of hundred micrometers, making the fluorescence imaging method applicable only when studying very superficial tissue regions. In addition, the fluorescence signal is highly dependent on tissue optical properties, making it difficult to use the absolute fluorescence level as a reliable concentration estimate. Within this study, the surface of the lesions displayed a heterogeneous structure, sometimes including superficial areas of dark necrotic regions.

The shallow investigation volume in combination with sensitivity to the optically heterogeneous tissue could thus explain the lack of significant correlation between extraction and fluorescence data.

In contrast to the fluorescence signal, the absorption spectroscopy data correlated rather well with the extraction results. One reason for the better agreement could be the higher overlap of probing volume of the two methods. A previous publication has reported on approximate probing depth of 1-2 mm for the absorption probe,²⁸ matching the depth of skin tumors likely to be treated by PDT using topical irradiation. In addition, since the analysis of the absorption spectrum takes into account the average tissue chromophore content, these results are not as easily corrupted by variations in tissue optical properties as is the fluorescence data. Though, the relatively high detection limit for the absorption spectroscopy probe is a major drawback. It is therefore highly desirable to combine the sensitivity of the fluorescence level with the ability of the absorption signal to account for varying tissue absorption. Finlay *et al.* have demonstrated a probe combining white-light absorption with fluorescence spectroscopy to recover the intrinsic tissue autofluorescence, i.e. the fluorescence spectra corrected for tissue absorption and scattering.³⁵ By utilizing the absorption spectrum to assess the tissue optical properties, the corrected fluorescence signal would constitute a more reliable fluorophore concentration estimate. A further drawback of the absorption spectroscopy probe is the inherent sensitivity to measurement site within the spatially heterogeneous structure of the lesions. The latter effect most likely explains part of the scattered appearance of the absorption data in relation to the ideal fit in Fig. 3(d). Furthermore, the outlier at $>30 \mu\text{M}$ as measured by the absorption spectroscopy setup could possibly be due to a small amount of mTHPC-gel remaining on the skin surface due to its inherent roughness. This effect highlights the importance of careful cleansing of the tissue surface prior to optical measurements in order to detect the true sensitizer distribution, i.e. the amount of mTHPC that has penetrated into the tissue.

In connection to this discussion, we emphasize the importance of including the mTHPC fluorescence as one of the components of the SVD algorithm. The shorter wavelengths present in the output from the Xenon arc lamp induce sensitizer fluorescence overlapping the absorption peak at 652 nm. In contrast to the effective pathlength, the fluorescence level is dependent on the sample scattering for this source-detector separation. Although this was not taken into account in the analysis process as it was outlined in Section 2.4, including the fluorescence component significantly improved the accuracy of the setup. By simply excluding the sensitizer fluorescence component from the analysis resulted in underestimation of the sensitizer concentration by a factor of 1.5 for the investigated lesions. Furthermore, if also limiting the spectral fitting range to 630-750 nm in order to avoid the strong hemoglobin absorption bands, the mTHPC concentration was underestimated by a factor 2. We conclude that sensitizer fluorescence should be taken into account when utilizing the tissue absorption imprint for absolute concentration estimates. A significant underestimation has also been reported by Patterson *et al.* when utilizing a reflectance spectroscopy probe with multiple source-detector fibers for determining AlPcS₄ concentration in *in vivo* rabbit skin.³⁶ The underestimation of the sensitizer concentration by a factor of 3 was attributed the layered skin structure and non-uniform AlPcS₄ distribution. Within our work, the investigated tissue was highly heterogeneous also presenting a depth-dependent sensitizer concentration. Therefore, these effects constitute another source of error as they were not considered in the present evaluation of the optical absorption signal, which assumes homogeneous medium.

In conclusion, we have reported on the use of a topically administered mTHPC-formulation in a murine skin tumor model. In this sensitizer formulation, the hydrophobic mTHPC molecule was incorporated into conventional liposomes, rendering the sensitizer preparation water soluble. By administering the compound via a heat-setting gel, the retention time of the applied gel could be increased. Fluorescence and absorption spectroscopy as well as extraction data indicated significant mTHPC accumulation within lesions but no difference in tumor sensitizer concentration between the 4 and 6 hour application times. The more sensitive fluorescence setup indicated optimal tumor selectivity for the 4 hour drug-light interval. Furthermore, the topical administration route led to low levels of systemic photosensitization. Based on these results, this sensitizer formulation and administration path would be interesting to pursue for topical mTHPC-PDT. Presently, a Phase I clinical trial has been initiated in order to study the feasibility of using the mTHPC-gel for treatment of skin tumors.

ACKNOWLEDGEMENTS

This work was funded by the EC integrated project BRIGHT IST-511-722-2003 and NIH Prime Cooperative Agreement# 1 U54 CA 104677. The authors gratefully acknowledge Irving Bigio at Boston University for providing instrumentation and technical support for the optical absorption spectroscopy setup.

REFERENCES

1. T. J. Dougherty, C. J. Gomer, B. W. Henderson, G. Jori, D. Kessel, M. Korbek, J. Moan, and Q. Peng, "Photodynamic therapy," *J. Natl. Cancer Inst.* **90**(12), 889-905 (1998).
2. R. D. Almeida, B. J. Manadas, A. P. Carvalho, and C. B. Duarte, "Intracellular signaling mechanisms in photodynamic therapy," *Biochim. Biophys. Acta* **1704**(2), 59-86 (2004).
3. M. Triesscheijn, M. Ruevekamp, M. Aalders, P. Baas, and F. A. Stewart, "Outcome of mTHPC mediated photodynamic therapy is primarily determined by the vascular response," *Photochem. Photobiol.* **81**(5), 1161-1167 (2005).
4. F. H. van Duijnhoven, R. I. J. M. Aalbers, J. P. Rovers, O. T. Terpstra, and P. J. K. Kuppen, "Immunological aspects of photodynamic therapy of liver tumors in a rat model for colorectal cancer," *Photochem. Photobiol.* **78**(3), 235-240 (2003).
5. J. S. Dysart, G. Singh, and M. S. Patterson, "Calculation of singlet oxygen dose from photosensitizer fluorescence and photobleaching during mTHPC photodynamic therapy of MLL cells," *Photochem. Photobiol.* **81**(1), 196-205 (2005).
6. C. Hopper, A. Kubler, H. Lewis, I. BingTan, and G. Putnam, "mTHPC-mediated photodynamic therapy for early oral squamous cell carcinoma," *Int. J. Cancer* **111**(1), 138-146 (2004).
7. Q. Peng, T. Warloe, K. Berg, J. Moan, M. Kongshaug, K.-E. Giercksky, and J. M. Nesland, "5-aminolevulinic acid-based photodynamic therapy: Clinical research and future challenges," *Cancer* **79**, 2282-2308 (1997).
8. P. Juzenas, S. Sharfaei, J. Moan, and R. Bissonnette, "Protoporphyrin IX fluorescence kinetics in UV-induced tumours and normal skin of hairless mice after topical application of 5-aminolevulinic acid methyl ester," *J. Photochem. Photobiol., B.* **67**(1), 11-17 (2002).
9. Q. Peng, A. M. Soler, T. Warloe, J. M. Nesland, and K. E. Giercksky, "Selective distribution of porphyrins in skin thick basal cell carcinoma after topical application of methyl 5-aminolevulinic acid," *J. Photochem. Photobiol., B.* **62**(3), 140-145 (2001).
10. S. Mitra and T. H. Foster, "Carbogen breathing significantly enhances the penetration of red light in murine tumours *in vivo*," *Phys. Med. Biol.* **49**(10), 1891-1904 (2004).
11. Q. G. Ren, S. M. Wu, Q. Peng, and Y. J. Chen, "Comparison of 5-aminolevulinic acid and its hexylester mediated photodynamic action on human hepatoma cells," *Acta Biochimica et Biophysica Sinica* **34**(5), 650-654 (2002).
12. E. Balasubramaniam and P. Natarajan, "Photophysical properties of protoporphyrin IX and thionine covalently attached to macromolecules," *J. Photochem. Photobiol., A.* **103**(3), 201-211 (1997).
13. P. Schleier, A. Berndt, S. Kolossa, and M. Wood, "Comparison between mALA- and ALA-PDT in the treatment of basal cell carcinomas," *Oral Onc. Suppl.* **1**(1), 67-68 (2005).
14. S. Mitra and T. H. Foster, "Photophysical parameters, photosensitizer retention and tissue optical properties completely account for the higher photodynamic efficacy of meso-tetra-hydroxyphenyl-chlorin vs Photofrin," *Photochem. Photobiol.* **81**(4), 849-859 (2005).
15. S. Sasnouski, V. Zorin, I. Khludeyev, M. A. D'Hallewin, F. Guillemin, and L. Bezdtnaya, "Investigation of Foscan interactions with plasma proteins," *Biochim. Biophys. Acta* **1725**(3), 394-402 (2005).
16. P. Westerman, T. Glanzmann, S. Andrejevic, D. R. Braichotte, M. Forrer, G. A. Wagnieres, P. Monnier, H. van den Bergh, J. P. Mach, and S. Folli, "Long circulating half-life and high tumor selectivity of the photosensitizer meta-tetrahydroxyphenylchlorin conjugated to polyethylene glycol in nude mice grafted with a human colon carcinoma," *Int. J. Cancer* **76**(6), 842-850 (1998).
17. J. P. Keene, D. Kessel, E. J. Land, R. W. Redmond, and T. G. Truscott, "Direct detection of singlet oxygen sensitized by haematoporphyrin and related compounds," *Photochem. Photobiol.* **43**(2), 117-120 (1986).
18. G. Gupta, C. A. Morton, C. Whitehurst, J. V. Moore, and R. M. Mackie, "Photodynamic therapy with

- meso-tetra(hydroxyphenyl) chlorin in the topical treatment of Bowen's disease and basal cell carcinoma," *Br. J. Dermatol.* **141**(2), 385-386 (1999).
19. M. J. Choi and H. I. Maibach, "Liposomes and niosomes as topical drug delivery systems," *Skin Pharmacol. Physiol.* **18**(5), 209-219 (2005).
20. M. B. Pierre, A. C. Tedesco, J. M. Marchetti, and M. V. Bentley, "Stratum corneum lipids liposomes for the topical delivery of 5-aminolevulinic acid in photodynamic therapy of skin cancer: preparation and in vitro permeation study," *BMC Dermatol.* **1**(1), 5 (2001).
21. X. Damoiseau, H. J. Schuitmaker, J. W. M. Lagerberg, and M. Hoebeke, "Increase of the photosensitizing efficiency of the Bacteriochlorin a by liposome-incorporation," *J. Photochem. Photobiol., B.* **60**(1), 50-60 (2001).
22. A. M. Richter, "Liposomal delivery of a photosensitizer, benzoporphyrin derivative monoacid ring A (BPD), to tumor tissue in a mouse tumor model," *Photochem. Photobiol.* **57**, 1000-1006 (1993).
23. C. af Klinteberg, A. M. K. Enejder, I. Wang, S. Andersson-Engels, S. Svanberg, and K. Svanberg, "Kinetic fluorescence studies of 5-aminolaevulinic acid-induced protoporphyrin IX accumulation in basal cell carcinomas," *J. Photochem. Photobiol., B.* **49**(2-3), 120-128 (1999).
24. J. R. Mourant, I. J. Bigio, D. A. Jack, T. M. Johnson, and H. D. Miller, "Measuring absorption coefficients in small volumes of highly scattering media: source-detector separations for which path lengths do not depend on scattering properties," *Appl. Opt.* **36**(22), 5655-5661 (1997).
25. B. Pegaz, E. Debeve, J. P. Ballini, G. Wagnieres, S. Spaniol, V. Albrecht, D. V. Scheglmann, N. E. Nifantiev, H. van den Bergh, and Y. N. Konan-Kouakou, "Photothrombic activity of m-THPC-loaded liposomal formulations: Pre-clinical assessment on chick chorioallantoic membrane model," *Eur. J. Pharm. Sci.* **28**, 134-140 (2006).
26. M. Kyriazi, D. Yova, M. Rallis, and A. Lima, "Cancer chemopreventive effects of Pinus Maritima bark extract on ultraviolet radiation and ultraviolet radiation-7,12,dimethylbenz(a)anthracene induced skin carcinogenesis of hairless mice," *Cancer Lett.* **237**(2), 234-241 (2006).
27. C. H. Gallagher, P. J. Canfield, G. E. Greenoak, and V. E. Reeve, "Characterization and histogenesis of tumors in the hairless mouse produced by low-dosage incremental ultraviolet radiation," *J. Invest. Dermatol.* **83**(3), 169-174 (1984).
28. J. R. Mourant, T. M. Johnson, G. Los, and I. J. Bigio, "Non-invasive measurement of chemotherapy drug concentrations in tissue: preliminary demonstrations of in vivo measurements," *Phys. Med. Biol.* **44**(5), 1397-1417 (1999).
29. W. J. Cottrell, A. R. Oseroff, and T. H. Foster, "Portable instrument that integrates irradiation with fluorescence and reflectance spectroscopies during clinical photodynamic therapy of cutaneous disease," *Rev. Sci. Instrum.* **77**(6), 064302 (2006).
30. E. L. Hull, M. G. Nichols, and T. H. Foster, "Quantitative broadband near-infrared spectroscopy of tissue-simulating phantoms containing erythrocytes," *Phys. Med. Biol.* **43**(11), 3381-3404 (1998).
31. Prah, S. A. "Tabulated molar extinction coefficient for hemoglobin in water," <http://omlc.org/spectra/hemoglobin/summary.html> (1999).
32. M. H. Schmid and H. C. Korting, "Therapeutic progress with topical liposome drugs for skin disease," *Adv. Drug Del. Rev.* **18**(3), 335-342 (1996).
33. P. Cramers, M. Ruevekamp, H. Oppelaar, O. Dalesio, P. Baas, and F. A. Stewart, "Foscan[®] uptake and tissue distribution in relation to photodynamic efficacy," *Br. J. Cancer* **88**(2), 283-290 (2003).
34. C. M. N. Yow, J. Y. Chen, N. K. Mak, N. H. Cheung, and A. W. N. Leung, "Cellular uptake, subcellular localization and photodamaging effect of Temoporfin (mTHPC) in nasopharyngeal carcinoma cells: comparison with hematoporphyrin derivative," *Cancer Lett.* **157**(2), 123-131 (2000).
35. J. C. Finlay and T. H. Foster, "Recovery of hemoglobin oxygen saturation and intrinsic fluorescence with a forward-adjoint model," *Appl. Opt.* **44**(10), 1917-1933 (2005).
36. R. A. Weersink, J. E. Hayward, K. R. Diamond, and M. S. Patterson, "Accuracy of noninvasive *in vivo* measurements of photosensitizer uptake based on a diffusion model of reflectance spectroscopy," *Photochem. Photobiol.* **66**(3), 326-335 (1997).

Tumor Selectivity at Short Times Following Systemic Administration of a Liposomal Temoporfin Formulation in a Murine Tumor Model

Jenny Svensson^{*1}, Ann Johansson¹, Susanna Gräfe², Burkhard Gitter², Tilmann Trebst³, Niels Bendsoe⁴, Stefan Andersson-Engels¹ and Katarina Svanberg⁵

¹ Department of Physics, Lund University, Lund, Sweden

² Research & Development, Biolitec AG, Jena, Germany

³ CeramOptec GmbH, Bonn, Germany

⁴ Department of Dermatology, Lund University Hospital, Lund, Sweden

⁵ Department of Oncology, Lund University Hospital, Lund, Sweden

*Corresponding author: Jenny Svensson, Department of Physics, Lund University, Professorsgatan 1, SE-223 62 Lund, Sweden, Phone: +46 46 222 31 19, Fax: +46 46 222 42 50, E-mail: jenny.svensson@fysik.lth.se

Abbreviations: AMD, age-related macular degeneration; CCD, charge-coupled device; DMSO, Dimethyl sulfoxide; DPPC, dipalmitoylphosphatidylcholine; HPLC, high performance liquid chromatography; LCTF, liquid crystal tunable filter; mTHPC, *meso*-tetra(hydroxyphenyl)chlorin; PDT, photodynamic therapy; PEG, poly(ethylene glycol); ROI, region of interest; SVD, singular value decomposition.

ABSTRACT

Meso-tetra(hydroxyphenyl)chlorin (mTHPC) (INN: Temoporfin) is one of the most potent photodynamically active substances in clinical use. Treatment protocols for Temoporfin-mediated photodynamic therapy often rely on drug-light intervals of several days in order for the photosensitizer to accumulate within the target tissue, though tumor selectivity is limited. Here, the mTHPC localization was studied at 2-8 hours following systemic administration of a liposomal Temoporfin formulation (0.15 mg/kg b.w.) in HT29 human colon adenocarcinoma in NMRI nu/nu mice. Photosensitizer distribution within tumor and internal organs was investigated by means of HPLC following chemical extraction, as well as *in situ* fluorescence imaging and point-monitoring fluorescence spectroscopy. For tumor tissue, the Temoporfin concentrations at 4 (0.16±0.024 ng/mg) and 8 (0.18±0.064 ng/mg) hours were significantly higher than at 2 (0.08±0.026 ng/mg) hours. The average tumor-to-muscle and the tumor-to-skin selectivity were 6.6 and 2, respectively, and did not vary significantly with time after photosensitizer injection. In plasma, the Temoporfin concentration was low (0.07±0.07 ng/mg) and showed no significant variation with time. Our results indicate a rapid biodistribution and clearance from the blood stream. Within the same type of organ, data from both fluorescence methods generally exhibited a significant correlation with the extraction results.

INTRODUCTION

Photodynamic therapy (PDT) is an investigational clinical method for local treatment of certain types of malignancies in various organs. The modality exhibits interesting advantages such as the possibility of repeated treatment and restriction of the treatment-induced tissue damage to irradiated sites. In PDT, a photosensitizer is excited by absorption of light at an appropriate wavelength followed by energy transfer to oxygen molecules or other tissue constituents. The toxic radicals thus formed, of which singlet oxygen is believed to be the most important, cause tissue destruction by means of direct cell kill, vascular damage and activation of the anti-tumor immune system components (1).

Meso-tetra(hydroxyphenyl)chlorin (mTHPC) (INN: Temoporfin) is one of the most potent photosensitizers for PDT in present use (2) and it has been successfully applied in the treatment of various indications, for example head and neck (3), prostate (4) and pancreatic (5) cancer. Strong response to Temoporfin-mediated PDT has been observed for short drug-light intervals, when the treatment outcome is mostly influenced by vascular response as the photosensitizer is located within blood vessels, vascular endothelial cells and tissue close to blood vessels (6-8). On the other hand, longer drug-light intervals, i.e. exceeding two days, allow the photosensitizer to diffuse further away from blood vessels and into tumor cells (8) possibly leading to a selective uptake in tumors (9,10). Clinical Temoporfin-PDT therefore often relies on drug-light intervals in the order of several days during which patients are restricted to limited light exposures (3-5). This prolonged skin photosensitivity is one of the

disadvantages when using Temoporfin. Due to the high affinity of the drug to bind to lipid structures, which is of importance for its relatively high PDT efficiency, the drug diffuses rapidly from the blood stream into surrounding tissues, an effect that has been observed to cause problems at the injection site (5,7). Furthermore, the hydrophobic character of the molecule leads to poor water solubility and formation of aggregates within aqueous media (11), altering the spectroscopic and photosensitizing characteristics of the compound (12).

In order to prevent formation of aggregates, prolong photosensitizer circulating lifetimes and to improve water solubility, tumor selectivity and PDT response, several research groups have tried different delivery vehicles such as liposomes, nano-particles and conjugation to antibodies (13,14). The potential importance of avoiding aggregation was observed within a cell culture medium, where encapsulation of the hydrophobic photosensitizer bacteriochlorin a in liposomes, thereby promoting monomerization, was shown to increase oxygen consumption during PDT and decrease cell survival as compared to its partly aggregated original formulation (15). Possible evidence of mTHPC aggregation *in vivo* has been observed by Hopkinson *et al.* (16). Richter *et al.* have studied the use of liposomes as carrier of the hydrophobic benzoporphyrin derivative monoacid ring A (BPD-MA), reporting on higher absolute photosensitizer concentration within tumor and more pronounced PDT effect as compared to the original formulation (17). These findings were attributed to a different micro-localization within the cells and an increased association with low density lipoproteins (LDLs) when incorporated into liposomes. Pegaz *et al.* have recently compared two different liposomal Temoporfin formulations (Foslip, containing conventional liposomes based on dipalmitoylphosphatidylcholine (DPPC), and Fospeg, based on poly(ethylene glycol) (PEG)-modified liposomes) in terms of plasma circulation half-life times and PDT-induced photothrombic activity (18). The Temoporfin levels within the vasculature were studied up to 1200 s after photosensitizer injection, which is relevant for the treatment of age-related macular degeneration (AMD) by means of PDT. For the two formulations investigated, similar fluorescence pharmacokinetic profiles were observed, whereas the Temoporfin within the PEGylated liposome carrier proved more efficient for vascularly targeted PDT. In addition, the observation of plasma half lives exceeding that of Visudyne[®], a photosensitizer commonly used in the treatment of AMD, was ascribed to the more stable composition of the liposomes incorporating the mTHPC molecules. Fospeg has also been compared to an ethanol formulation of Temoporfin in PDT of feline skin tumors (19). In that study, the use of Fospeg demonstrated PDT response in all subjects, higher bioavailability, faster distribution and a slightly improved tumor selective uptake as compared to an ethanol formulation of Temoporfin.

An important issue in improving the understanding of various transportation vehicles for PDT photosensitizers is to be able to non-invasively measure the photosensitizer concentration. Optical methods are promising tools for tissue diagnostics and measurement of photosensitizer tissue levels in clinical environments. Fluorescence spectroscopy can provide signals related to the photosensitizer concentration and has the advantage of being a non-invasive technique that reveals results in real time (20). Fluorescence can either be studied in a point-monitoring mode (21), often using an optical fiber or a thin fiber probe for light delivery and collection, or in an imaging mode (22), where larger areas can be examined in a non-contact configuration. An imaging approach provides additional information on heterogeneities that are difficult to obtain with a point-monitoring detection technique. As Temoporfin is characterized by a relatively strong fluorescence yield, where excitation within the near-ultraviolet wavelength region results in distinctive fluorescence around 652 nm, fluorescence spectroscopy is a valuable tool in estimating photosensitizer concentration *in situ* within various tissue types.

In this work we present *ex vivo* pharmacokinetic studies following systemic administration of Temoporfin incorporated into conventional liposomes based on DPPC. The use of these liposomes provides a good biocompatibility. High performance liquid chromatography (HPLC), in this work considered as the 'gold standard', and fluorescence spectroscopy, both in point-monitoring and imaging mode, are used to assess Temoporfin levels in a subcutaneously implanted HT29 human colon adenocarcinoma model as well as in internal organs in a murine model. By employing these three methods, issues such as possible selectivity at short times following drug administration (2-8 hours) and heterogeneity of the photosensitizer accumulation are addressed. This study adds to the previous work by Pegaz *et al.* (18) the use of longer time intervals after administration and to that by Buchholz *et al.* (19) the monitoring of Temoporfin concentration within internal organs. Furthermore, the possibilities of using non-invasive fluorescence spectroscopy to quantify Temoporfin concentration in exposed tissues are explored. The resulting photosensitizer concentrations are tested for correlation between the three methods employed and we speculate on how to improve the accuracy in absolute fluorescence level as a photosensitizer concentration estimate.

MATERIALS AND METHODS

Photosensitizer. Temoporfin is a dark purple, non-hygroscopic, non-solvated crystalline powder, which is soluble in alcohol/acetone/ethyl acetate and practically insoluble in all aqueous media. The single component is of 98 % purity with a molecular weight of 680.24 and a fluorescence emission peak at 652 nm. In the novel formulation used, Foslip (Biolitec Pharma Ltd, Dublin, Ireland), the hydrophobic mTHPC is bound to the membrane compartment of a phospholipid bilayer. The liposome formulation is based on DPPC, monosaccharide, water and polyoxyethylene polyoxypropylene block copolymers (18). The liposomes were reconstituted and dissolved in 3 ml of sterile water to give a photosensitizer concentration of 1.5 mg/ml. Further dilution in 5 % aqueous glucose solution provided a photosensitizer concentration of 0.075 mg/ml Foslip. All compounds were stored at 4°C in the dark.

Animal model. The study was performed on adult female athymic NMRI nu/nu mice (Harlan Winkelmann GmbH, Borchen, Germany). All animal experiments were carried out in compliance with the German Animal Protection Act. Six to eight-week old mice, weighing 22-24 g, were inoculated subcutaneously in the left and right hind thigh with a suspension of HT29 human colorectal carcinoma cells (0.1 ml of 8×10^7 cells/ml in 5 % glucose). Experiments were performed 11 days later, when the tumors had reached a surface diameter of 5-8 mm, and a thickness of 2-4 mm. Mice were injected with 50 μ L of Foslip, corresponding to 0.15 mg Temoporfin/kg b.w., into the lateral tail vein. A dose of 50 mg/kg b.w. sodium pentobarbital injected i.p. was used for anaesthesia. Animals were sacrificed at four different time-intervals after injection of Foslip (2, 4, 6 or 8 hours) and samples of plasma, spleen, liver, lung, heart, kidney, skin, muscle and the two tumors were excised for HPLC analysis. Furthermore, spleen, liver, skin, muscle and tumors were also investigated by imaging and point-monitoring fluorescence spectroscopy immediately after animal sacrifice. Both muscle and skin tissues studied were excised from regions just at the tumor periphery. All excised tissue samples were stored in darkness at -80°C until the HPLC analysis. Three animals without Foslip injection were used as controls. The number of samples investigated for each organ, time following photosensitizer administration and method of photosensitizer quantification are listed in Table 1.

Table 1. The number of samples for the time points 2, 4, 6 and 8 hours, respectively.

Organ/Fluid	HPLC	Fluorescence point	Fluorescence imaging
Plasma	[6 3 3 3]	-	-
Spleen	[5 [†] 3 3 3]	[5 3 3 3]	[6 3 3 3]
Liver	[6 3 3 3]	[5 3 3 3]	[6 3 3 3]
Lung	[6 3 3 3]	-	-
Heart	[6 3 3 3]	-	-
Kidney	[6 3 3 3]	-	-
Skin	[6 3 3 3]	[5 3 3 3]	[6 3 3 3]
Tumor	[11 6 6 3]	[11 6 5 [†] 6]	[6 3 3 3]
Muscle	[6 3 3 2 [†]]	[5 3 3 3]	[6 3 3 3]

†: 1 sample identified as outlier

HPLC analysis. All tissue samples were minced by cutting with a scalpel, weighed and freeze dried (freeze drying system Alpha 1-4 LSC, Martin Christ Gefriertrocknungsanlagen GmbH, Osterode, Germany). The resulting powdered tissue was weighed and 10-20 mg was transferred to a 2.0 ml reaction tube after which 1.5 ml of methanol:DMSO (3:5, v:v) was added. The samples were immediately mixed for 3 to 5 s periods using a vortex mixer operating at 2,400 rpm and then incubated at 60°C under continuous shaking for at least 12 hours. All samples were spun at 16,000 g in a centrifuge for five minutes. One ml of the supernatant was transferred to a HPLC vial for subsequent HPLC analysis. The HPLC device had the following specifications; Pump: "System Gold, 126 Solvent Module" (Beckman Coulter Inc., Fullerton, CA, USA), Autosampler: "Triathlon", Diode Array Detector: "System Gold, Module 168" (Beckman Coulter Inc., Fullerton, CA, USA) and a Fluorescence detector: "RF-10A XL" with interface SS420x (Shimadzu Europa GmbH, Duisburg, Germany). The fluorescence was excited at 410 nm and detected at 653 nm. The separation was carried out on a "LiChroCART 250-4" column (Merck KGaA, Darmstadt, Germany) with Purospher STAR RP-18 endcapped; 5 μ m Guard column:

"LiChroCART 4-4" with Purospher STAR RP-18e; 5 μm (Merck KGaA, Darmstadt, Germany) Temperature: 30°C. The mobile phase consisted of acetonitrile: H₂O + 0.1 % trifluoroacetic acid (TFA) = 57.5 %: 42.5 % with a flow rate of 1 ml/min. The tissue concentration of Temoporfin, given in ng/mg wet weight, was calculated from a calibration curve constructed by plotting the peak height values of Temoporfin standard solutions versus their concentrations.

Fluorescence imaging system. Fluorescence *ex vivo* measurements using both imaging and point detection were performed on the two tumors, skin, muscle, liver and spleen. For the imaging setup, the light source for fluorescence induction consisted of 12 light emitting CW diodes with peak emission at 405 nm. The beam radius of the spot focused onto the organs was 2.5 cm and the irradiance was approximately 30 $\mu\text{W}/\text{cm}^2$. Fluorescence emitted by the tissue was recorded by a detection unit consisting of a CCD-camera (C4742-80-12AG, Hamamatsu Photonics, Hamamatsu, Japan), a liquid crystal tunable filter having a full-width-half-maximum (FWHM) of 20 nm (LCTF VIS 20-35, Varispec, CRI, Inc., Woburn, CA, USA) and a zoom objective lens (50 mm focal length and $f/1.8$, Nikon, Tokyo, Japan). The object distance was 23 cm and the field of view of the detection system was 3.2 x 4.2 cm. Room light images at 550 nm and fluorescence images at 500 and 653 nm, corresponding to wavelengths within the tissue autofluorescence and Temoporfin fluorescence bands, respectively, were collected. The exposure time was set to 3 s for each wavelength. All fluorescence images were recorded with dimmed room light to avoid any influence from background light. Background images in the absence of excitation light were also acquired using the same wavelengths and exposure times.

For each fluorescence image, the background was subtracted pixel by pixel and the data were normalized with respect to the exposure time. Each fluorescence image was divided by a fluorescence image at 653 nm from a fluorescence standard (USFS 336020, LabSphere, North Sutton, NH, USA) to account for the non-uniform distribution of the excitation light. In connection to the measurements, the output from a calibrated white-light source was recorded at 500 and 653 nm and all fluorescence images were corrected for the difference in relative detection efficiency between these two fluorescence wavelengths. For each animal and organ, mean and standard deviations of the fluorescence intensity at 500 and 653 nm were calculated within a region of interest (ROI) corresponding to the entire organ as outlined from the room-light images. The Temoporfin concentration within each organ was estimated by calculating a fluorescence contrast ratio, R (23);

$$R = \frac{I_a(653) - k \cdot I_c(653)}{I_a(500)} \quad (1)$$

where $I_a(653)$ and $I_a(500)$ represent the mean value of the intensities within the ROI at 653 and 500 nm, respectively, for each Temoporfin-injected animal. $I_c(653)$ and $I_c(500)$ refer to tissue autofluorescence at 653 and 500 nm in the absence of mTHPC, assessed as the average fluorescence signals from the control animals. $k = I_a(500) / I_c(500)$, constituting a scaling factor between data from each Temoporfin-injected animal and the mean of the three control animals.

Point-monitoring fluorescence. The Temoporfin concentration was also measured by point-monitoring fluorescence spectroscopy using an instrument described in detail in Ref (24). Briefly, approximately 1 mW at 375 nm was delivered through a 400 μm quartz fiber with a clear cut distal end in contact with the tissue. The induced fluorescence was collected using the same optical fiber and reflected laser light was removed by a dichroic beamsplitter (LWP-45-RS396-TU450-700PW1012UV, CVI Technical Optics LTD, Onchan, UK) and a long pass filter (RG395, Schott AG, Mainz, Germany). The fluorescence signal, $F(\lambda)$, was detected by a spectrometer (USB4000, Ocean Optics, Dunedin, FL, USA) and normalized at 500 nm.

A singular value decomposition (SVD) algorithm was used to fit a set of normalized basis spectra to the data (25), where these basis spectra consisted of the Temoporfin fluorescence signal (26), a fluorescence signal peaking in the blue-green spectral region representing the combined tissue and fiber autofluorescence and assessed as an average of the detected fluorescence signal in each organ of the control animals, and a constant offset representing background in the detection unit. The algorithm was implemented in the software program MATLAB (The MathWorks Inc., Natick, MA, USA). In addition, a 15-term Fourier series was included in the fit to account for the influence of varying blood content on the autofluorescence spectra (25);

$$F(\lambda) = A_{mTHPC} f_{mTHPC}(\lambda) + A_{auto} f_{auto}(\lambda) + A_{offset} + \dots$$

$$\left[\omega \sum_{i=1}^{15} \left(B_i \cos\left(\frac{\pi i(\lambda - \lambda_{start})}{\lambda_{end} - \lambda_{start}}\right) + C_i \sin\left(\frac{\pi i(\lambda - \lambda_{start})}{\lambda_{end} - \lambda_{start}}\right) \right) \right], \quad (2)$$

where the A 's, B 's and C 's are the spectral amplitudes resulting from the fit and the $f(\lambda)$'s denote the normalized basis spectra. The spectral fitting range was 500-700 nm but the terms within the square brackets were included only between 500 (λ_{start}) and 640 nm (λ_{end}). The number of components included in the Fourier series was determined by minimizing the error of the fit;

$$E = \left(\sum_i \frac{(y_{measured,i} - y_{fit,i})^2}{(n-1)} \right)^{1/2}, \quad (3)$$

where the summation is taken within the fitting range and n denotes the number of data points in this spectral interval. The factor ω , representing the weighting of the Fourier components in relation to the other factors, was not critical for the performance of the algorithm and was arbitrarily set to 1. The SVD algorithm was used to evaluate each of the fluorescence spectra acquired at 1-3 sites in each organ and the Temoporfin concentration was quantified by averaging the resulting A_{mTHPC} .

Statistical analysis: For each organ, the Temoporfin concentration estimate of every sample was compared with the mean value from the 15 animals. If the difference was greater than three standard deviations, the data point was considered to be an outlier and removed from the following analysis. Identified outliers are indicated in Table 1. With an ANOVA-test the null hypothesis, stating that the four time points do not result in different Temoporfin concentrations, was tested for each individual organ. The agreement between the three methods used for assessing the Temoporfin concentration was quantified by studying the correlation of the HPLC data, the fluorescence contrast ratio and the Temoporfin fluorescence spectral amplitude. The hypothesis of no correlation for each organ was tested. For all tests, $P < 0.01$ was considered significant.

RESULTS

HPLC results

The Temoporfin concentration as a function of time after injection is shown in Fig. 1. For all organs except the tumors, the error bars indicate the standard deviations arising due to inter-animal variations, whereas for tumor tissue, the error bars also partly reflect intra-animal differences as each animal had two inoculated tumors. For tumor tissue, the Temoporfin levels at 4 (0.16 ± 0.024 ng/mg) and 8 (0.18 ± 0.064 ng/mg) hours were significantly higher than at 2 (0.08 ± 0.026 ng/mg) hours. Within the entire time interval, the average Temoporfin concentration was 0.12 ng/mg, ranging between 0.04-0.25 ng/mg. No difference in photosensitizer concentration was found between left and right tumors. Also, no trace of Temoporfin was found in any of the control animals. According to the ANOVA-test, only within tumor tissue did the photosensitizer concentration display any significant variation with time after injection. In Table 2, the average selectivity of Temoporfin in tumor compared to other organs investigated is listed for the time points investigated. The tumor-to-muscle ratio averaged for each time point is between 5.5 and 8.1 in the time interval of 2-8 hours, with the highest selectivity achieved at 2 hours. The tumor-to-muscle ratio did not change significantly with time and displayed a total average of 6.6. The large variation of tumor-to-muscle selectivity at 8 hours is partly due to the small number of samples. At 2 hours the tumor-to-muscle ratio ranges between 2.8 and 26.5, mostly reflecting a large biological variation at this short time point. A tumor-to-skin selectivity in the order of 2 was observed, which did not vary significantly with time. The Temoporfin selectivity in tumor tissue as compared to the internal organs is low, and exhibits a slight increase for the later time points.

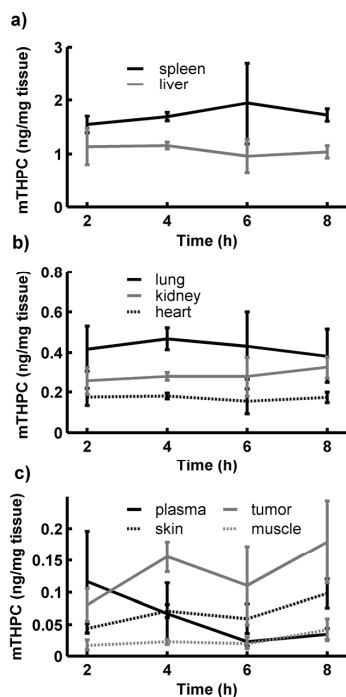


Figure 1. a) - c) Temoporfin concentration as a function of time following injection within organs investigated by HPLC. Error bars represent ± 1 standard deviation (SD).

Table 2. Selectivity of Temoporfin analyzed from HPLC data. The average value and standard deviation are given for each time point and organ investigated. A P-value less than 0.01 rejects the hypothesis of time-independent selectivity.

	Tumor/ Spleen	Tumor/ Liver	Tumor/ Lung	Tumor/ Heart	Tumor/ Kidney	Tumor/ Skin	Tumor/ Muscle
2 hour	0.049 \pm 0.016	0.072 \pm 0.017	0.19 \pm 0.054	0.47 \pm 0.10	0.31 \pm 0.058	1.8 \pm 0.47	8.1 \pm 8.1
4 hour	0.092 \pm 0.012	0.13 \pm 0.016	0.33 \pm 0.043	0.86 \pm 0.099	0.56 \pm 0.068	2.2 \pm 0.45	6.6 \pm 0.99
6 hour	0.056 \pm 0.018	0.11 \pm 0.037	0.24 \pm 0.047	0.69 \pm 0.13	0.38 \pm 0.088	1.8 \pm 0.43	5.5 \pm 1.3
8 hour	0.11 \pm 0.048	0.17 \pm 0.036	0.52 \pm 0.21	1.0 \pm 0.34	0.55 \pm 0.090	1.8 \pm 0.28	6.2 \pm 5.4
P-value	<0.01	<0.01	<0.01	<0.01	<0.01	0.24	0.83

Fluorescence measurements

A typical fluorescence spectrum from skin overlying the tumor 8 hours after Foslip injection is shown in Fig. 2a. The tissue autofluorescence, the Temoporfin fluorescence and the total fit including the Fourier components are also shown. For the purposes of clarity, the autofluorescence component is displayed at 50 % of its true value. The fluorescence peak at 635 nm, present only in skin samples, is believed to originate from endogenous porphyrins in

the mouse skin. Fig. 2b shows the corresponding fluorescence signal and the fitted fluorescence components from tumor tissue. Figs. 2c and d illustrate the corresponding residuals, ε , calculated as the difference between measured and modeled data, and the error of the fit, calculated according to Eq. (3).

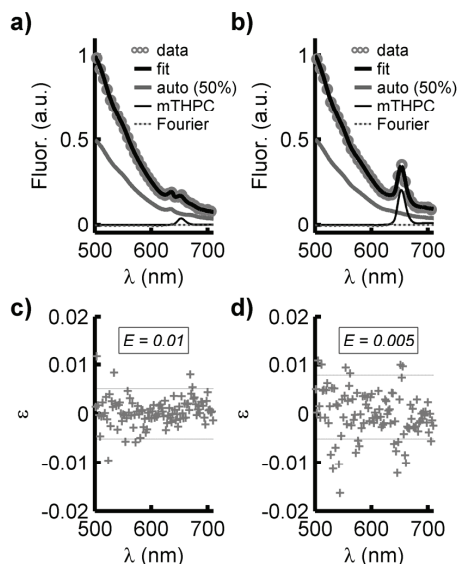


Figure 2. Ex vivo a) skin and b) tumor fluorescence spectra, the fit components representing autofluorescence and Temoporfin fluorescence, and the total fit, which also includes the Fourier terms. The autofluorescence component is displayed at 50 % of the true value and only every 30 data points are shown for purposes of clarity. c) and d) illustrate the residuals, ε , corresponding to a and b, respectively. The dashed lines indicate ± 2 SD of the residuals and E denotes the fitting error according to Eq. (3). For the residuals, only every ten data points are plotted for purpose of clarity.

The fluorescence contrast ratio, R , as a function of time after injection is shown in Fig. 3a. For the control animals, the contrast ratio was not significantly different from zero. The heterogeneity in evaluated Temoporfin concentration within an organ was characterized by the relative standard deviation arising when averaging the fluorescence contrast function within each ROI. Data from liver and spleen resulted in relative standard deviations approximately 4 times higher compared to the other organs. The Temoporfin fluorescence amplitude, A_{mTHPC} , resulting from the point-monitoring measurements, as a function of time after injection is shown in Fig. 3b. No peak at 653 nm was present in the spectra from any of the control animals. The average fitting errors, \hat{E} , for each organ are also shown. For all tissue types, the fitting errors were small compared to the fluorescence signal amplitude, indicating a good fit. The influence of the Fourier terms on the total fit was typically less than 10 % of the autofluorescence component and their appearance mostly reflected the heterogeneous blood distribution within the tissue. Furthermore, the magnitudes of Fourier components 11-15 were less than 5 % of the maximum Fourier component, reflecting the smaller importance of the higher order terms in Eq. (2).

The results from the fluorescence methods demonstrate similar time dependence in tumor tissue as the HPLC data, with a significantly lower value of Temoporfin at 2 hours compared to 4 and 8 hours after injection. The order of the magnitudes of the estimated Temoporfin levels in investigated organs is overall similar for the three analysis methods. The average tumor-to-muscle ratios were 3.3 ± 0.92 , 3.9 ± 0.93 , 3.1 ± 1.1 and 4.0 ± 1.5 for the four time intervals investigated with the fluorescence imaging method and corresponding average tumor-to-skin ratios were 5.4 ± 1.8 , 7.5 ± 6.4 , 2.9 ± 1.6 and 2.8 ± 0.36 . For the point-monitoring method average tumor-to-muscle ratios were 6.1 ± 2.9 , 9.5 ± 8.9 , 6.4 ± 3.6 and 8.4 ± 5.4 and average tumor-to-skin ratios were 6.3 ± 2.9 , 10 ± 5.1 , 4.9 ± 3.2 and 6.7 ± 2.1 . For both fluorescence methods, the Temoporfin tumor selectivity displayed no time-dependence. The

different values of the selectivity are obtained with the fluorescence methods as compared to HPLC. This can be explained by the sensitivity of the optical methods to differences in tissue optical properties. The influence of optical properties in the fluorescence measurements are discussed in a later section.

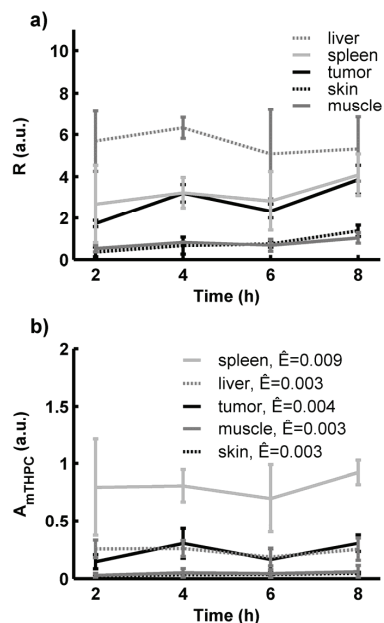


Figure 3. a) The fluorescence contrast ratio, R , as a function of time after injection. b) Point-monitoring Temoporfin fluorescence amplitude, A_{mTHPC} , as a function of time following injection. Also shown are the average fitting errors. Error bars represent ± 1 standard deviation.

Correlation of HPLC and fluorescence data

The possibility of using the fluorescence image contrast ratio or the point-monitoring Temoporfin fluorescence amplitude as absolute photosensitizer measures was investigated by studying the correlation between the Temoporfin quantities predicted by each method and the HPLC data, in this study considered 'gold standard'. Table 3 lists the correlation between data from the three methods for the individual organs as well as the P-value for testing the hypothesis of no significant correlation. The obtained correlation values and the magnitudes of the P-values indicate a significant agreement between the three methods for all organs with a few exceptions; poor correlation was noted between optical methods and HPLC for spleen as well as between point-monitoring fluorescence and HPLC for skin. Also, for all organs except spleen and skin, the 95% confidence intervals of the predicted correlation coefficients greatly overlap, indicating no significant difference of the degree of correlation of data from different organs.

Table 3. Correlation between data sets from the three methods used for assessing Temoporfin concentration within five organs. The P-values for testing the hypothesis of no correlation are also given.

	Spleen	Liver	Skin	Tumor	Muscle
HPLC vs fluo. point	0.43 ($P=0.15$)	0.74 ($P<0.01$)	0.56 ($P=0.04$)	0.76 ($P<0.01$)	0.88 ($P<0.01$)
HPLC vs fluo. imag	0.53 ($P=0.05$)	0.85 ($P<0.01$)	0.70 ($P<0.01$)	0.87 ($P<0.01$)	0.78 ($P<0.01$)
Fluo. imag vs fluo. point	0.67 ($P<0.01$)	0.78 ($P<0.01$)	0.75 ($P<0.01$)	0.63 ($P<0.01$)	0.70 ($P<0.01$)

The co-variation between HPLC and fluorescence data for each of the organs investigated by HPLC and both fluorescence spectroscopy methods is illustrated in Figs. 4a-d. The correlation between HPLC and fluorescence data illustrated in Table 3 is also clearly visualized in Figs. 4a-d, while the disjoint data sets underline the necessity of multiple correlation curves to adequately describe the connection between the fluorescence contrast ratio or the fluorescence amplitude and the HPLC data for all organs combined. The varying slope of the correlation curves, shown by the solid lines in Figs. 4a-d, could be partly explained by differences in tissue optical properties. For example, the high blood content in liver and spleen causes a higher overall light absorption and thus a comparatively smaller fluorescence signal. Other factors that influence the slope of the correlation curve, especially for the high Temoporfin concentrations encountered within liver and spleen, include saturation and re-absorption of the Temoporfin fluorescence and the possibly formation of less fluorescent mTHPC aggregates (11). The optically more transparent character of the remaining organs leads to a much steeper slope of the correlation curve in Figs. 4a-d. The co-variation between the two fluorescence methods is shown in Fig. 4e and f. In contrast to Figs. 4a and c, the slopes of the correlation curves in Fig. 4e vary less for the different organs. As the tissue volumes probed by the optical methods show a better overlap than that of HPLC and the fluorescence data are influenced by the tissue optical properties whereas the HPLC result is not, the slope should ideally be identical for all organs. Though, the differences in excitation wavelength and detection geometry lead to slightly different tissue volumes probed by the two fluorescence methods, a fact that might limit the agreement between the optical data sets.

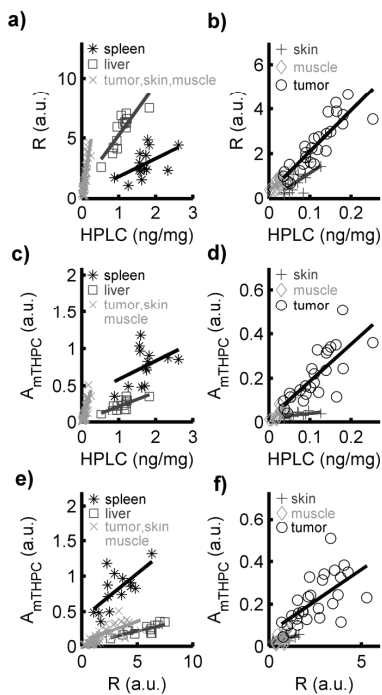


Figure 4. Scatter plots showing the correlation between a) and b) Temoporfin concentrations acquired from HPLC and the fluorescence imaging contrast ratio, R , calculated from Eq. (1). c) and d) illustrate the co-variation between Temoporfin concentrations acquired from HPLC and the Temoporfin fluorescence amplitude, A_{mTHPC} , obtained from point-monitoring fluorescence data. Correspondingly, e) and f) show the covariance of the fluorescence contrast ratio, R , and the Temoporfin fluorescence amplitude, A_{mTHPC} . In all subplots, the markers represent data points from individual animals and the solid lines illustrate correlation curves.

DISCUSSION

By incorporating hydrophobic photosensitizers into liposomes, improved selectivity and more pronounced PDT effect have been observed for PDT agents such as benzoporphyrin derivative monoacid ring A (BPD-MA) (17) and bacteriochlorin a (15) as compared to the original formulation. The compound Temoporfin, also a hydrophobic photosensitizer, is one of the most potent sensitizers (2) in present use. This photosensitizer possesses interesting photophysical properties, e.g. a strong absorption band in the red wavelength region and a high fluorescence yield, making it desirable to use optical methods in order to study photosensitizer pharmacokinetics and distribution. The ethanol formulation of Temoporfin is associated with prolonged general photosensitivity, limited tumor selective uptake, and aggregation within aqueous media.

Here, we investigated photosensitizer distribution for short times following systemic administration of a liposomal Temoporfin formulation utilizing chemical extraction as well as fluorescence spectroscopy. In the animal tumor model used, athymic NMRI nu/nu mice with implanted HT29 human colon adenocarcinoma, both HPLC and optical methods demonstrated selectivity in Temoporfin accumulation between tumor and muscle and tumor and skin for time intervals of 2 to 8 hours after drug administration.

The tumor-to-muscle and tumor-to-skin selectivity displayed no significant time-dependence. The average tumor-to-muscle ratio observed in the present study indicates an early Temoporfin selectivity that is slightly higher than found following administration of mTHPC dissolved in ethanol, polyethylene glycol (PEG) and water. For example, Westermann *et al.* reported on a selectivity around 3-4 at 2-8 hours after administration of mTHPC dissolved in an ethanol-PEG-water solution in nude mice with a human colon carcinoma model (LS174T) (27). For that study, the selectivity increased slightly for drug-light intervals exceeding 8 hours. Further comparison of our results to those of Westermann *et al.* shows that the average tumor-to-skin selectivity displays slight improvement over the original formulation. Pharmacokinetic studies of liposome-encapsulated BPD-MA (M1 tumors in DBA/2 mice) (17) and SIM01 (28) have also reported on an improved tumor-to-muscle selectivity as compared to administration of the original formulation of the photosensitizer. In agreement with our results, neither of these PDT-agents showed improved tumor-to-skin selectivity when incorporated into liposomes. In contrast to the results published by Westermann *et al.*, no selectivity has been observed between human mesothelioma xenograft and muscle in nude BALB/c mice (29) or only little selectivity within a mammary carcinoma model in C₃D₂/F₁ mice (9) for similar short times after administration of Temoporfin in an ethanol-PEG-water solution. Our results thus indicate an early Temoporfin selectivity that is higher than observed for its original ethanol formulation.

Selective accumulation of liposome-encapsulated photosensitizers has previously been explained by the fact that the liposomes serve as donors of photosensitizer molecules to lipoproteins (13,14). Since proliferating cells show an increased number of low-density lipoprotein (LDL) receptors, the association of the photosensitizer to these proteins has been shown to promote selective accumulation and increased treatment efficiency (14,30,31). Conventional liposomes, such as DPPC used in the present study, are quickly opsonized by plasma proteins. Following this, the liposomes are taken up by phagocytosis and transported to organs with a rich mononuclear phagocyte system, such as liver and spleen (13). This process also affects the bioavailability of the mTHPC molecules, supporting our observation of high Temoporfin concentration within liver, spleen and lung. The association to the mononuclear phagocyte system could perhaps also contribute to the selectivity of Temoporfin in the tumor, as a higher degree of inflammatory cells, such as macrophages, phagocytes and leucocytes, are present in close proximity of the tumor periphery.

The photosensitizer concentration within tumor was significantly higher at 4 and 8 hours than at 2 hours. For the entire time interval, the average Temoporfin level in tumor tissue was 0.12 ng/mg. This can be compared to an observed photosensitizer concentration below approximately 0.04 ng/mg in tumor tissue between 5 min and 6 hours after administration of the original ethanol formulation of Temoporfin at the double photosensitizer dose (29). Our data for tumor tissue are also slightly higher than reported by Westermann *et al.* for similar time points after administration of mTHPC in ethanol, polyethylene glycol and water (27). The Temoporfin levels detected in plasma were relatively low for all time points investigated, resulting in an average concentration of 0.07 ng/mg. Cramers *et al.* reported on Temoporfin levels in plasma ranging between 0.3 and 2 ng/mg for similar time periods following systemic administration of mTHPC in an ethanol-PEG-water solution (29). Within muscle, skin, liver,

lung, kidney and heart the Temoporfin levels were in the range previously published (9,27,29). Despite the use of conventional liposomes, which are known to accumulate within organs rich in mononuclear phagocytic cells, the photosensitizer concentration within liver, spleen and lung in the present study was not higher than previously published.

In agreement with our results, a higher bioavailability has previously been noted for other hydrophobic PDT substances incorporated into liposomes (15,17,32). Maximum photosensitizer concentrations within tumor tissue, using photosensitizers incorporated with liposomes, have been shown to peak either at earlier (17), similar (28) or at later (32) time points after administration as compared to the original formulation of the photosensitizer. These differences might be due to the specific liposome and/or photosensitizer used as well as the tumor and animal model. The pharmacokinetic profile of liposome-encapsulated Temoporfin observed in the present study for short times after injection might mostly reflect the fate of the liposomes. Opsonization and association with lipoproteins or phagocytosis of conventional liposomes, such as used in the present study, are rapid processes that lead to a fast transfer of the sensitizer from the vascular compartment. These effects can explain the low photosensitizer levels in plasma and the almost flat pharmacokinetic profiles within the internal organs. Further improvements of tumor selectivity and bioavailability might be possible by prolonging the circulation time of the liposomes, for example by utilizing a pegylated liposomal formulation, also referred to as a stealth liposome (19). Another reason for the delayed concentration maximum within tumor tissue when using ethanol formulations of Temoporfin as compared to liposome-encapsulated Temoporfin could be the formation of photosensitizer aggregates in blood when administering an ethanol photosensitizer formulation. These aggregates need to be disassociated before the photosensitizer molecules can bind to plasma proteins (11,16).

The present study is limited in that photosensitizer distribution and the generalized photosensitivity were only studied up to 8 hours. Within a different animal group, the photosensitizer levels displayed a decrease within the internal organs at 24 hours (unpublished data). These data, which were not merged with the present study due to slightly different experimental procedures, also indicated that the Temoporfin concentration within skin, muscle and tumor did in fact not increase for this later time point. More extensive studies are needed in order to understand the pharmacokinetics of Temoporfin at later time points following systemic administration of this novel liposomal formulation.

In this study, HPLC was considered the 'gold standard' to which the optical methods were compared and the data correlated. As seen in Figs. 4a-d, the extraction and fluorescence data showed a relatively good agreement within individual organs but one could also see that no single correlation curve could adequately fit the HPLC and fluorescence data for all organs. One factor that dramatically influences the overall correlation between the HPLC and fluorescence results is varying optical properties of the tissue under investigation. Optically opaque tissues, such as liver and spleen, result in comparatively lower fluorescence signals than in for example muscle, characterized by a higher albedo. Clearly, this indicates the importance of taking into account the influence of scattering and absorption on the detected fluorescence signal. Several authors have utilized white-light reflectance signal probing the same tissue volume as the fluorescence, to assess the tissue absorption and scattering levels. Based on this information, empirical and theoretical models have been used to solve for the intrinsic tissue fluorescence (33,34). White-light reflectance measurements could thus yield information on how to "unmask" the fluorescence amplitude and possibly improve agreement between extraction and Temoporfin fluorescence level.

Another reason is that the extraction data represent the average Temoporfin concentration within the entire organ, whereas the fluorescence methods probe only the most superficial tissue regions. Furthermore, the differences in excitation wavelength and measurement geometry cause slightly different probing depths for the two optical methods. Any variation in Temoporfin concentration with depth from the exposed tissue surface in combination with varying, tissue-specific optical properties would negatively influence the agreement between the three methods both within and between individual organs. Finally, within aqueous media, the hydrophobic mTHPC molecules are known to form non-fluorescent oligomers. Despite being in monomeric form when incorporated into liposomes, it is possible that the photosensitizer molecules aggregate upon distribution within cells, especially in the case of high concentrations (35). The HPLC results are independent of such aggregation, whereas the fluorescence measurements are not, possibly resulting in the lower slope observed for liver and spleen in Figs. 4a and c.

The liver and spleen are surrounded by a capsule rich in collagen and elastin. For liver, its capsule was cut open and measurements were performed directly on the liver parenchyma, whereas the capsule of the spleen was kept intact during the optical measurements. The combination of differences in photosensitizer concentration between

capsule and parenchymal tissue and the shallow probing depth of the fluorescence signals could explain the lack of significant agreement between HPLC and fluorescence data for the spleen. The poor correlation between point-monitoring and extraction data for skin may be explained by the difference in probing depth in combination with the layered skin structure. The measurement geometry (36) and the strong scattering within the epidermis, that mostly consists of dead cells with a low uptake of Temoporfin and high collagen content, limit the probing depth of the 375-nm light used for the point-monitoring fluorescence spectroscopy.

The two fluorescence methods showed similar agreement with the extraction data despite being based on different methods of analysis. Each method has its individual advantages. The fluorescence imaging method performs better within heterogeneous organs as it allows e.g. for spatial averaging of specific areas. The point-monitoring setup yields more detailed spectroscopic information making it possible to separately monitor individual tissue fluorophores, such as tissue autofluorescence and skin porphyrin content. The ultimate system would provide full spectroscopic data in each spatial point of an image plane possibly allowing a precise delineation of tissue types. Future use of more detection bands of the LCTF would develop into such a system.

In conclusion, we have reported on significant photosensitizer selectivity between tumor and muscle tissue at 2 to 8 hours following systemic administration of Temoporfin incorporated into conventional liposomes. The average tumor-to-muscle selectivity was slightly higher than observed for mTHPC dissolved in ethanol, polyethylene glycol and water (27) and other hydrophobic PDT agents incorporated into liposomes (17) upon investigation at similar times after injection. The tumor-to-muscle selectivity was not significantly dependent on time, whereas the ratio of photosensitizer concentration in tumor to internal organs increased for the later time points. These observations in combination with the overall low photosensitizer concentration within plasma, indicates a rapid photosensitizer distribution process. The biocompatibility of the liposomes, the rapid pharmacokinetics and the early selectivity observed for the liposome-encapsulated Temoporfin are interesting features in trying to limit the drug-light interval used clinically and need further investigation. Furthermore, we have observed that within individual homogeneous organs the Temoporfin fluorescence level, both in imaging and point-monitoring mode, can be used as a reasonable substance concentration estimate. Though, when studying numerous and optically different tissues one needs to take into account the influence of background optical properties on the resulting fluorescence signal.

Acknowledgments-- This work was partly funded by the EC integrated projects BRIGHT.EU FP6- IST-2003-511722 and Molecular Imaging LSHG-CT-2003-503259.

REFERENCES

1. Pass, H. I. (1993) Photodynamic therapy in oncology: mechanisms and clinical use [review]. *J. Natl. Cancer Inst.* **85**, 443-456.
2. Mitra, S. and T. H. Foster (2005) Photophysical parameters, photosensitizer retention and tissue optical properties completely account for the higher photodynamic efficacy of meso-tetra-hydroxyphenyl-chlorin vs Photofrin. *Photochem. Photobiol.* **81**, 849-859.
3. D'Cruz, A. K., M. H. Robinson, and M. A. Biel (2004) mTHPC-mediated photodynamic therapy in patients with advanced, incurable head and neck cancer: a multicenter study of 128 patients. *Head Neck* **26**, 232-240.
4. Moore, C. M., T. R. Nathan, W. R. Lees, A. Freeman, C. A. Mosse, M. Emberton, and S. G. Bown (2004) Photodynamic therapy for primary prostate cancer - A pilot study using MTHPC. *Br. J. Cancer* **91**, S35.
5. Bown, S. G., A. Z. Rogowska, D. E. Whitelaw, W. R. Lees, L. B. Lovat, P. Ripley, L. Jones, P. Wyld, A. Gillams, and A. W. Hatfield (2002) Photodynamic therapy for cancer of the pancreas. *Gut* **50**, 549-557.
6. Triesscheijn, M., M. Ruevekamp, M. Aalders, P. Baas, and F. A. Stewart (2005) Outcome of mTHPC mediated photodynamic therapy is primarily determined by the vascular response. *Photochem. Photobiol.* **81**, 1161-1167.
7. Triesscheijn, M., M. Ruevekamp, N. Antonini, H. Neering, F. A. Stewart, and P. Baas (2006) Optimizing Meso-tetra-hydroxyphenyl-chlorin Mediated Photodynamic Therapy for Basal Cell Carcinoma. *Photochem. Photobiol.* **82**, 1686-1690.
8. Mitra, S., E. Maugain, L. Bolotine, F. Guillemain, and T. H. Foster (2005) Temporally and spatially heterogeneous distribution of mTHPC in a murine tumor observed by two-color confocal fluorescence imaging and spectroscopy in a whole-mount model. *Photochem. Photobiol.* **81**, 1123-1130.
9. Peng, Q., J. Moan, L. W. Ma, and J. M. Nesland (1995) Uptake, localization, and photodynamic effect of meso-tetra(hydroxyphenyl)porphine and its corresponding chlorin in normal and tumor tissues of mice bearing

- mammary carcinoma. *Cancer Res.* **55**, 2620-2626.
10. Alian, W., S. Andersson-Engels, K. Svanberg, and S. Svanberg (1994) Laser-induced fluorescence studies of meso-tetra(hydroxyphenyl)chlorin in malignant and normal tissues in rat. *Br. J. Cancer* **70**, 880-885.
 11. Sasnouski, S., V. Zorin, I. Khludeyev, M. A. D'Hallewin, F. Guillemin, and L. Bezdetnaya (2005) Investigation of Foscan interactions with plasma proteins. *Biochim. Biophys. Acta* **1725**, 394-402.
 12. Bonnett, R., B. D. Djelal, and A. Nguyen (2001) Physical and chemical studies related to the development of m-THPC (FOSCAN[®]) for the photodynamic therapy (PDT) of tumours. *J. Porphyrins Phthalocyanines* **5**, 652-661.
 13. Derycke, A. S. L. and P. A. M. de Witte (2004) Liposomes for photodynamic therapy. *Adv. Drug. Deliv. Rev.* **56**, 17-30.
 14. Konan, Y. N., R. Gurny, and E. Allemann (2002) State of the art in the delivery of photosensitizers for photodynamic therapy. *J. Photochem. Photobiol. B* **66**, 89-106.
 15. Damoiseau, X., H. J. Schuitmaker, J. W. M. Lagerberg, and M. Hoebeke (2001) Increase of the photosensitizing efficiency of the Bacteriochlorin a by liposome-incorporation. *J. Photochem. Photobiol. B* **60**, 50-60.
 16. Hopkinson, H. J., D. I. Vernon, and S. B. Brown (1999) Identification and partial characterization of an unusual distribution of the photosensitizer meta-tetrahydroxyphenyl chlorin (temoporfin) in human plasma. *Photochem. Photobiol.* **69**, 482-488.
 17. Richter, A. M. (1993) Liposomal delivery of a photosensitizer, benzoporphyrin derivative monoacid ring A (BPD), to tumor tissue in a mouse tumor model. *Photochem. Photobiol.* **57**, 1000-1006.
 18. Pegaz, B., E. Debefve, J. P. Ballini, G. Wagnieres, S. Spaniol, V. Albrecht, D. V. Scheglmann, N. E. Nifantiev, H. van den Bergh, and Y. N. Konan-Kouakou (2006) Photothrombic activity of m-THPC-loaded liposomal formulations: Pre-clinical assessment on chick chorioallantoic membrane model. *Eur. J. Pharm. Sci.* **28**, 134-140.
 19. Buchholz, J., B. Kaser-Hotz, T. Khan, C. R. Bleyl, K. Melzer, R. A. Schwendener, M. Roos, and H. Walt (2005) Optimizing photodynamic therapy: In vivo pharmacokinetics of liposomal meta-(tetrahydroxyphenyl)chlorin in feline squamous cell carcinoma. *Clin. Cancer Res.* **11**, 7538-7544.
 20. Ramanujam, N. (2000) Fluorescence spectroscopy of neoplastic and non-neoplastic tissues. *Neoplasia* **2**, 89-117.
 21. af Klinteberg, C., M. Andreasson, O. Sandström, S. Andersson-Engels, and S. Svanberg (2005) Compact medical fluorosensor for minimally invasive tissue characterisation. *Rev. Sci. Instrum.* **76**, 034303-034306.
 22. Andersson-Engels, S., J. Johansson, and S. Svanberg (1994) Medical diagnostic system based on simultaneous multispectral fluorescence imaging. *Appl. Opt.* **33**, 8022-8029.
 23. Andersson-Engels, S., J. Ankerst, S. Montán, K. Svanberg, and S. Svanberg (1988) Aspects of tumour demarcation in rats by means of laser-induced fluorescence and hematoporphyrin derivatives. *Lasers Med. Sci.* **3**, 239-248.
 24. Gustafsson, U., S. Pålsson, and S. Svanberg (2000) Compact fibre-optic fluorosensor using a continuous wave violet diode laser and an integrated spectrometer. *Rev. Sci. Instrum.* **71**, 3004-3006.
 25. Finlay, J. C., S. Mitra, and T. H. Foster (2002) In vivo mTHPC photobleaching in normal rat skin exhibits unique irradiance-dependent features. *Photochem. Photobiol.* **75**, 282-288.
 26. Angotti, M. (2001) Etude par spectrometrie de masse des photoreactions laser de sensibilisants colores utilises en therapie photodynamique (PDT). Thesis. University Paul Verlaine, Metz, France.
 27. Westerman, P., T. Glanzmann, S. Andrejevic, D. R. Braichotte, M. Forrer, G. A. Wagnieres, P. Monnier, B. H. van den, J. P. Mach, and S. Folli (1998) Long circulating half-life and high tumor selectivity of the photosensitizer meta-tetrahydroxyphenylchlorin conjugated to polyethylene glycol in nude mice grafted with a human colon carcinoma. *Int. J. Cancer* **76**, 842-850.
 28. Bourre, L., S. Thibaut, M. Fimiani, Y. Ferrand, G. Simonneaux, and T. Patrice (2003) In vivo photosensitizing efficiency of a diphenylchlorin sensitizer: interest of a DMPC liposome formulation. *Pharmacol. Res.* **47**, 253-261.
 29. Cramers, P., M. Ruevekamp, H. Oppelaar, O. Dalesio, P. Baas, and F. A. Stewart (2003) Foscan[®] uptake and tissue distribution in relation to photodynamic efficacy. *Br. J. Cancer* **88**, 283-290.
 30. Allison, B. A., E. Waterfield, A. M. Richter, and J. G. Levy (1991) The effects of plasma lipoproteins on *in vitro* tumor cell killing and *in vivo* tumor photosensitization with benzoporphyrin derivative. *Photochem. Photobiol.* **54**, 709-715.
 31. Jori, G. and E. Reddi (1993) The role of lipoproteins in the delivery of tumour-targeting photosensitisers. *Int.*

J. Biochem. **25**, 1369-1375.

32. Wang, Z. J., Y. Y. He, C. G. Huang, J. S. Huang, Y. C. Huang, J. Y. An, Y. Gu, and L. J. Jiang (1999) Pharmacokinetics, tissue distribution and photodynamic therapy efficacy of liposomal-delivered hypocrellin A, a potential photosensitizer for tumor therapy. *Photochem. Photobiol.* **70**, 773-780.
33. Finlay, J. C. and T. H. Foster (2005) Recovery of hemoglobin oxygen saturation and intrinsic fluorescence with a forward-adjoint model. *Appl. Opt.* **44**, 1917-1933.
34. Muller, M. G., I. Georgakoudi, Q. Zhang, J. Wu, and M. S. Feld (2001) Intrinsic fluorescence spectroscopy in turbid media: disentangling effects of scattering and absorption. *Appl. Opt.* **40**, 4633-4646.
35. Sasnouski, S. (2006) Aggregation state and phototoxicity of Foscan in MCF-7 cells. Thesis. University Henri Poincaré, Nancy, France.
36. Pfefer, T. J., L. S. Matchette, and R. Drezek (2004) Influence of illumination-collection geometry on fluorescence spectroscopy in multilayer tissue. *Med. Biol. Eng. Comput.* **42**, 669-673.

VIII

Fluorescence monitoring of a topically applied liposomal Temoporfin formulation and photodynamic therapy of non-pigmented skin malignancies

Niels Bendsoe¹, Linda Persson², Ann Johansson², Johan Axelsson², Jenny Svensson², Susanna Gräfe³, Tilmann Trebst³, Stefan Andersson-Engels², Sune Svanberg² and Katarina Svanberg⁴

¹Department of Dermatology, Lund University Hospital, Lund, Sweden

²Department of Physics, Lund University, Lund, Sweden

³Research & Development, Biolitec AG, Jena, Germany

⁴Department of Oncology, Lund University Hospital, Lund, Sweden

Department of Oncology, Lund University Hospital,
SE-221 85 Lund, Sweden

Phone: +46 (0)46 222 40 48

Fax: +46 (0)46 222 42 50

E-mail: Katarina.Svanberg@onk.lu.se

ABSTRACT

Meso-tetra(hydroxyphenyl)chlorin (mTHPC) (INN: Temoporfin) is a potent photodynamically active substance in clinical use today. Usually the substance is given systemically and a known drawback with this administration route is a prolonged skin light sensitization. For the first time to our knowledge, a liposomal Temoporfin gel formulation for topical application was studied in connection with photodynamic therapy (PDT) of non-pigmented skin malignancies in humans. Intervals of 4 hours between drug administration and light irradiation were used. Sensitizer distribution within tumor and surrounding normal skin was investigated by means of point-monitoring and imaging fluorescence spectroscopy before, during and after PDT, showing high tumor selectivity. Furthermore, the bleaching of Temoporfin was studied during the PDT procedure by monitoring the fluorescence following excitation by using the therapeutic light. A 30-35% light-induced photo-metabolization was shown. No pain occurred during or after treatment. It was also observed that the treated area did not show any swollen tissue or reddening as is often seen in PDT using topical δ -amino-levulinic acid. On controlling the patients one week after treatment, healing progress was observed in several patients and no complications were registered.

Abbreviations: ALA, δ -aminolevulinic acid; BCC, basal cell carcinoma; CCD, charge-coupled device; DPPC, dipalmitoylphosphatidylcholine; LCTF, liquid crystal tunable filter; mTHPC, *meso*-tetra(hydroxyphenyl)chlorin; PDT, photodynamic therapy; SD, standard deviation;

Running: A topical Temoporfin formulation for PDT

Keywords: mTHPC, PDT, basal cell carcinoma, fluorescence, bleaching, spectroscopic monitoring, Temoporfin topically

1. Introduction

This paper presents, to our knowledge, the first use of a new photosensitizer, a liposomal Temoporfin gel formulation, for topical application in humans. Photodynamic therapy (PDT) is a modality for local treatment of cancer and relies on a photosensitizing agent being activated by light at an appropriate wavelength, usually within the red wavelength region to optimize light penetration within tissue¹. Many of the sensitizers are selectively located in malignant cells due to a variety of biological reasons² and therefore selectivity in the therapy is achieved. Provided the simultaneous presence of sensitizer and oxygen, a cytotoxic reaction can be photochemically induced, causing selective cell destruction. The PDT outcome is

governed by a combination of the effect of direct cell kill and induction of apoptosis³, vascular damage⁴ and an elicited immune response⁵.

The majority of photosensitizers are administered systemically, which causes an unwanted side effect of skin sensitization. In PDT of certain types of skin abnormalities topical application of a sensitizer is preferable in order not to cause general skin sensitization. Topical administration of δ -aminolevulinic acid (ALA) in combination with illumination from a laser or a light emitting diode with light doses in the range of 35 and 200 J/cm^{2,6} has been successfully used for treatment of non-melanoma skin malignancies over the past decades^{6,7}. ALA is often supplied in a cream at a concentration of 20% and application times range between 3 and 6 hours⁸. During this time period, the ALA molecules diffuse into the tissue followed by the synthesis of protoporphyrin IX (PpIX), which is the photodynamically active metabolite². Due to an increased permeability of the ALA molecules through the damaged epidermis of many cutaneous tumors and differences in the enzymatic activity, the accumulation of PpIX often displays a significant selectivity between normal and malignant tissue for shorter application times up to about 3-6 hours². The sensitizer distribution can easily be monitored via the characteristic PpIX fluorescence within the red wavelength region, thus making optical methods highly desirable as non-invasive tools for sensitizer monitoring.

For superficial basal cell carcinomas (sBCC), PDT following topical application of ALA has led to cure rates (CR's) of 79-100%⁶. Though, for nodular lesions, the reported CR's are often about 50-70%⁷, a fact that has been partly explained by the limited penetration (1-3mm) of the hydrophilic ALA molecules. A further drawback of ALA-mediated PDT is skin sensation, such as itching and sometimes pain reported in many trials^{9,10}. ALA-PDT also induces immediate post therapy tissue reactions with swollen, reddening and oozing skin.

Due to the lipophilic character of ALA esters, these derivatives are expected to show better biological availability and tissue penetration than ALA. Peng *et al.* reported on a highly selective and homogeneous sensitizer distribution following topical administration of methyl δ -aminolaevulinate, Metvix^{®11}. A high tumor selectivity was observed by means of PpIX fluorescence both in animal skin tumor models and in human basal cell carcinomas (BCC's)^{12,13}. On the other hand, as the PpIX molecule is activated at slightly shorter wavelengths than many other PDT agents, the light absorption of hemoglobin limits the light penetration and treatment depth to approximately a few millimeters¹⁴. Furthermore, the PpIX molecule itself presents some shortcomings in terms of the localization of the substance within the tissue¹⁵, and the relatively low extinction coefficient of this sensitizer¹⁶. These factors might limit the treatment outcome irrespective of which kind of ALA is used^{6,17}.

Meso-tetra(hydroxyphenyl)chlorin (mTHPC) (INN: Temoporfin) has been reported as one of the most efficient sensitizers, as relatively small drug and light doses are required in order to achieve treatment response¹⁸. Another advantage with Temoporfin is the wavelength of the absorption maximum at 652 nm as compared to 635 nm for ALA, resulting in an enhanced light penetration. Systemically administered Temoporfin in ethanolic formulation, Foscan[®], has been successfully used for PDT of head- and neck malignancies¹⁹, prostate²⁰ and for BCCs²¹. A major drawback utilizing systemic administration of Temoporfin is the prolonged photosensitivity, subjecting patients to subdued light conditions for several weeks following sensitizer administration. In addition, due to the hydrophobic character of the mTHPC molecules, it is practically insoluble in aqueous media. Following systemic administration of the ethanolic formulation, the sensitizer therefore forms aggregates, leading to limited transportation of the sensitizer within biological media as well as poor tumor selectivity and PDT efficacy²²⁻²⁴. The above factors can also lead to an intense inflammation at the injection site²¹.

To overcome the problem of the extended photosensitization associated with systemic administration of Temoporfin, Gupta *et al.* have reported on PDT combined with topical mTHPC administration for treatment of Bowen's disease and BCCs²⁵. In this study, the CR was 32% at the 2-month follow-up. The authors suggested that the formulation of Temoporfin they used was a limiting factor for the treatment outcome.

Previously, our group has reported on sensitizer distribution studies following topical administration of a novel liposomal formulation of Temoporfin in a murine skin tumor model²⁶. For Temoporfin gel

application times of 4 and 6 hours the chemical extraction from different organs revealed a selective accumulation of the substance within tumor tissue. The average sensitizer concentration within lesions was 6.0 ng/mg, whereas no detectable levels of generalized photosensitivity were shown. Within the study, the strongly fluorescing and absorbing characteristics of Temoporfin were also used for monitoring the drug distribution by fluorescence imaging and absorption spectroscopy. These non-invasive methods confirmed the selective sensitizer distribution and indicated sensitizer penetration depths of 3-4 mm within the investigated tumors.

Following these initial promising results on the animal skin tumor model, the same liposomal Temoporfin formulation is introduced for non-pigmented skin malignancies in patients. In this study, we include spectroscopic measurements to monitor the uptake of the liposomal Temoporfin formulation in connection with PDT using laser light at 652 nm. By incorporating Temoporfin in a liposomal formulation, the substance is made more suitable and transport within biological media is facilitated. The liposome encapsulated Temoporfin is supplied in a water-based heat-setting gel, rendering application times of several hours possible. Fluorescence spectroscopy data are presented as a tool to study sensitizer distribution and treatment-induced photobleaching. Clinical parameters, such as skin sensations during the treatment and other local skin reactions during the first week after treatment, are monitored.

2. Material and Methods

Sensitizer: The sensitizer compound is comprised of a liposomal formulation of mTHPC (Temoporfin) in a thermo gel matrix with a sensitizer concentration of 0.5 mg mTHPC/ml gel (Biolitec AG, Jena, Germany). The liposome formulation is based on dipalmitoylphosphatidylcholine (DPPC), monosaccharide, water and polyoxyethylene polyoxypropylene block copolymers encapsulating mTHPC²⁷. The mTHPC gel is in a liquid phase at the storage temperature of 4°C but forms a highly viscous gel when heated by the skin to temperatures above 26°C. The thermo-thickening thus aids in increasing the retention time of the applied gel and transfer of the sensitizer into the tissue. No penetration enhancers are added to the Temoporfin gel.

Patients: The Temoporfin gel was used for topical PDT of 35 lesions in 10 consecutive patients in the ambulatory out patient ward. The histopathology showed basal cell carcinoma for 29 and squamous cell carcinoma for the remaining 6 lesions. The gel was applied on the visible lesion and an additional margin of about 10 millimeters on the surrounding skin. Tegaderm[®] was used to cover the area (Fig. 1a). Four hours later, the gel was removed and the site was carefully cleaned with alcohol. PDT was performed by irradiating lesions with diode laser light at 652 nm (Ceralas, Bonn, Germany) at a light dose of 20 J/cm². Two tumors in one patient were treated with a different light dose; one with 40 J/cm² and one with 60 J/cm². The optical fiber used for light delivery was equipped with a microlens giving a uniform irradiance adjusted to 100 mW/cm².

Optical measurements: Point-monitoring fluorescence spectroscopy measurements were performed prior to and post PDT to study both the Temoporfin-related signal and tissue autofluorescence. Several sites within and in close proximity to the lesions were studied. The point-monitoring fluorosensor utilizes a nitrogen laser pumping a dye laser emitting pulsed excitation light at 405 nm. The light is guided to the tissue through an optical fiber with a core diameter of 600 µm. The induced fluorescence light is transmitted through the same fiber back to a detection unit. This unit incorporates an RG435 cut-off filter, a spectrometer and a cooled intensified CCD recording fluorescence spectra in the range from 450 to 800 nm²⁸.

In addition, a fluorescence imaging system was used to monitor the whole treatment site including the surrounding normal skin margin prior to, during and post PDT. Fluorescence images were collected by a CCD camera (C4742-80-12AG, Hamamatsu) equipped with a liquid crystal tunable filter (LCTF VIS 20-35, Varispec) and a zoom objective lens (50 millimeters focal length and f/1.8, Nikon). For the measurements performed prior to and post PDT, the excitation light source consisted of 12 light emitting diodes with optical output centered at 405 nm, and the fluorescence was imaged at 652 nm.

Measurements performed in order to study the sensitizer photobleaching during PDT utilized the treatment light at 652 nm to induce Temoporfin fluorescence, which was detected at 720 nm. In each treatment

session, a total of 60 fluorescence images were collected at 3 s intervals in order to follow the photobleaching of the sensitizer. For evaluation of the Temoporfin bleaching kinetics, a subset of 12 images, separated by approximately 16 s, were extracted from the data set. In each image, 4 regions with an area of about 0.2 mm² were selected and the mean of the intensity within these regions was calculated. This procedure was performed for the same 4 regions in the consecutive images. By normalizing the mean intensity for each image to the mean intensity at the start of the irradiation, a normalized temporal profile of the fluorescence intensity was calculated.

3. Results and Discussion

The use and handling of the novel liposomal Temoporfin gel was very convenient as the gel was fluid only at the low storage temperature in the refrigerator. As soon as the gel was applied on the skin of the patients it became more viscous and was not as easily smeared off the surface. Despite this, a covering film was placed over the area in order to keep the gel in place during the 4 hours before PDT illumination (Fig. 1a). In contrast to the use of the PpIX-precursor ALA, this liposomal Temoporfin formulation is not dependent on an enzymatic transformation. The application time is only for the purpose of letting the substance diffuse into the tumor tissue. The use of a 4 hour drug-light interval was motivated by the results from a previous study in a murine skin tumor model²⁶. Unlike ALA, mTHPC is a strongly fluorescing substance. Any Temoporfin gel remaining on the skin surface will thus cause a false non-tissue-uptake related fluorescence signal. Within this study, a careful cleansing of the skin was of importance to avoid influence by superficially located Temoporfin gel.



Fig. 1. a) A picture of a Temoporfin vial together with Tegaderm® dressing and a light protecting cover. b) and c) Digital images from a tumor prior to the PDT procedure and 1 week after, respectively. Remaining scar structures are due to previous non-PDT treatments.

Further comparison with ALA and its esters shows an advantage for Temoporfin-PDT in that it did not cause any discomfort to the patients. Previous work has reported on a majority of the patients experience painful sensation in the skin during ALA-PDT⁹. Our own clinical experience includes rare cases of patients feeling inclined to interrupt the ALA-PDT and not accepting another PDT treatment using the same type of sensitizer. Different methods, such as spraying water or using a fan on the area treated, have been reported to relieve the ALA-PDT-related pain. However, other studies show less discomfort where only 25% of the patients experienced some kind of skin sensation and very few patients felt any pain¹⁰. In the present Temoporfin study, none of the treated patients spontaneously complained about any pain. Also, upon interviewing all 10 patients concerning their sensations during the treatment, no one reported on any pain, itching or stinging and all patients could finish the treatments without any complaints. As mentioned above, the PDT light dose was generally 20 J/cm² delivered at 100 mW/cm². This rendered the treatment time acceptably short (approximately 200 s), an attractive feature especially for elderly patients. This light dose resulted in only a partial bleaching of the Temoporfin as monitored by the fluorescence levels. Due to this fact, we increased the light dosage up to 40-60 J/cm² for a few treatment procedures as mentioned above. This increased light dose also did not result in any inconvenience for the patient. All the patients, treated with the novel Temoporfin formulation and PDT, were reviewed in order to record immediate post-PDT reactions (Fig. 1b and c). In the case of ALA-PDT it is normal to see swollen tissue and some reddening, oozing and formation of small pustules in the area where ALA is applied. No such reactions were seen in the patients, who had undergone Temoporfin-PDT. It was also noted that tumor sites oozing or bleeding before the Temoporfin-PDT seemed to dry out during the first week

following the treatment. Therefore, no post treatment dressings or other medical procedures were necessary.

Fluorescence spectroscopy, both in point-monitoring and imaging mode, was used to study Temoporfin distribution within the PDT target area. Point-monitoring fluorescence spectra recorded in a scan over a tumor, tumor border and surrounding normal skin margin out to 10 mm before and after PDT are shown in Fig. 2 together with a digital photo of the tumor. In the region outside the tumor, the spectra shown are the average of data recorded at 2, 5, and 10 mm outside the visible boundary of the tumor. For the center of the tumor, the spectra displayed are the average of three recorded spectra, whereas fluorescence spectra for the tumor border represent single acquisitions. The Temoporfin fluorescence emission is clearly seen in the red part of the wavelength region peaking at about 653 nm and also a second broader peak at approximately 720 nm. Beside the drug-related fluorescence, the autofluorescence from the tissue itself, characterized by broad emission in the blue/green part of the wavelength region, is also seen. As known from earlier studies, the autofluorescence shows very low intensity within the tumor area as well as in the tumor border zones⁸. It can be noted that in one of the areas outside the visible border of the tumor the autofluorescence is very low and the Temoporfin signal high (the rightmost spectrum), which may well represent an outstretching part of the tumor. Even if it is not histopathologically proven it is a clear indication to include also this part in the PDT irradiated field to enhance the radicality of the treatment. After PDT, the substance-related emission is shown with a decreased intensity, which is a sign of photobleaching of the drug during the PDT procedure.

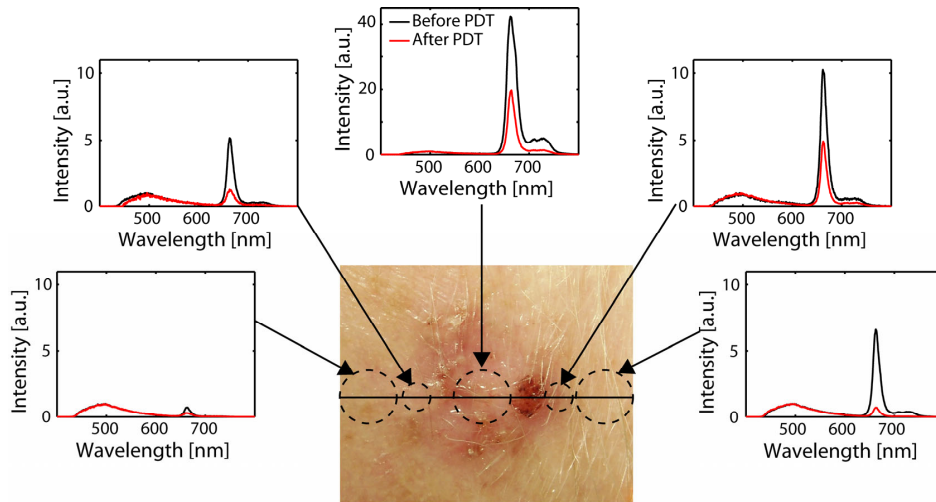


Fig. 2. Fluorescence spectra induced by 405 nm excitation recorded from outside the lesion, border of the lesion and center of the lesion before and after the PDT procedure.

By using both the Temoporfin-related signal and the tissue autofluorescence, a diagnosis-related contrast function, C_{diag} can be calculated (Fig. 3a);

$$C_{diag} = \frac{mTHPC_{\lambda[640-690]} - Auto_{\lambda[640-690]}}{Auto_{\lambda[470-520]}}$$

The function results in higher values in tumor, since the Temoporfin intensity is high and the autofluorescence is low compared to normal tissue (Fig. 2). This contrast function is slightly different from a contrast based only on the Temoporfin fluorescence amplitude without taking into account the tissue autofluorescence at this wavelength. Although the latter is perhaps more related to the sensitizer concentration and the PDT effect, C_{diag} was employed in the present work. The values of this contrast

function obtained before and after PDT for the tissue region in Fig. 2, are plotted in Fig. 3b. As can be seen, the contrast between tumor and manifest normal skin (the outermost left point) is very high. It can also be noted that the effect of bleaching due to PDT is substantial (about a factor of 2).

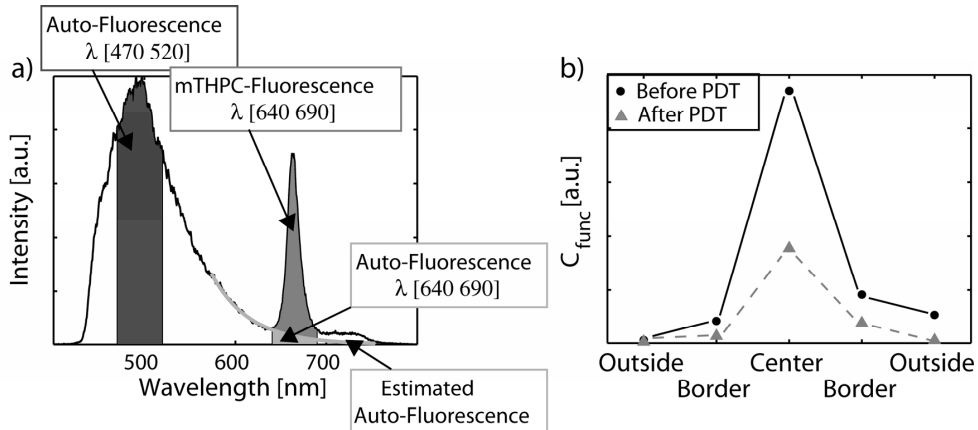


Fig. 3. a) Indications of the different areas used in the contrast function, C_{diag} b) The contrast function, C_{diag} , applied on spectra in Fig. 2 before and after PDT procedure. The data points are connected by lines for the guidance of the eye.

Typical fluorescence images of a tumor and surrounding skin following excitation at 405 nm with detection at 652 nm are shown in Fig. 4a. The images are monitored before and after the PDT procedure. The presented images are background subtracted, where the background was acquired without excitation light. For comparison both images are normalized using the maximum intensity in the first image. It can be observed that the sensitizer distribution is heterogeneous within the tumor, an effect that was observed in most of the tumors studied. Similar results were observed in the murine skin tumor model following administration of this liposome encapsulated Temoporfin gel²⁶. In that study, the increased penetration within lesions was ascribed the absence of the stratum corneum, whereas an intact epidermis prevented normal skin from accumulating any detectable levels of the photosensitizer. Thus, the heterogeneous fluorescence signals observed within this study may reflect the status of the uppermost skin layers. A further explanation to the heterogeneous Temoporfin distribution might be the tumor growth pattern, as it is well known that BCCs grow in spots or patches with normal tissue intermixed within the tumor site as illustrated in the photo in Fig. 2.

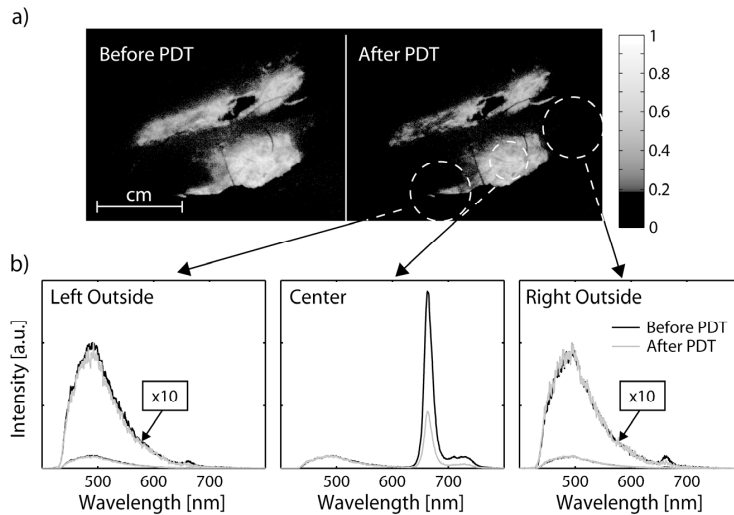


Fig. 4. a) Images of a tumor showing the fluorescence intensity at 652 nm for excitation at 405 nm before and after the PDT procedure, respectively. b) The fluorescence spectra obtained in point monitoring for excitation at 405 nm from three different locations marked by circles; outside to the left and to the right of the visible tumor location, and inside the tumor area.

Fluorescence spectra acquired with the point-monitoring setup are also presented before and after PDT (Fig. 4b). The spectra are normalized to the maximum of the autofluorescence from surrounding skin between 470-520 nm. As the Temoporfin signal shows a very low intensity in surrounding normal skin the spectra are shown also with a ten-fold magnification. A tumor demarcation based on the diagnosis-related contrast function, C_{diag} , of approximately 10:1 can be seen when comparing the tumor center spectrum with the two spectra from normal tissue outside the tumor. This is comparable to the contrast obtained for the majority of the tumors included in the study. Post PDT, a decrease of the Temoporfin fluorescence in the center of the tumor as well as in the surrounding tissue can clearly be seen.

The laser light at 652 nm used for treatment also excites mTHPC fluorescence at 720 nm. Fig. 5a shows the mean relative fluorescence intensity over time for ten representative tumors following excitation by the therapeutic laser light. The photodegradation of Temoporfin as monitored at 720 nm can clearly be seen. A photobleaching of about 30-35% is recorded after 200 s of therapeutic irradiation (20 J/cm^2), which concurs well with previously reported results for the photobleaching in mTHPC-sensitized spheroids²⁹. Fluorescence images of a tumor are shown at three different time intervals during the PDT procedure (Fig. 5b); before, in the middle and at the end of the session. These fluorescence images, detected at 720 nm following excitation by the therapeutic light at 652 nm, also illustrate the treatment-induced photobleaching. An apparent lower overall photobleaching can be observed following fluorescence excitation at 652 nm as compared to 405 nm excitation, see for example Figs. 4b and 5a. This effect might be explained by the different effective penetration depths of the two excitation wavelengths. I.e., violet light probes the superficial tissue regions where the therapeutic irradiation has efficiently bleached away most of the photosensitizer, whereas the red excitation wavelength also probes deeper into the tissue volume where less bleaching has occurred due to the lower irradiance during treatment. These observations might suggest that sensitizer photobleaching as a parameter related to PDT outcome should be monitored utilizing the same excitation wavelength as for PDT induction whenever possible. Then a more representative tissue volume is probed.

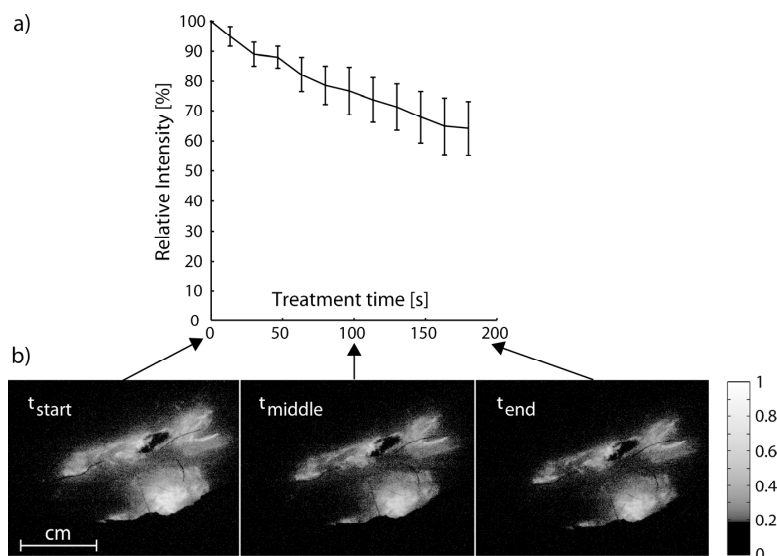


Fig. 5. a) Decrease of the normalized fluorescence intensity at 720 nm detected over time for ten tumors following excitation by the therapeutic radiation at 652 nm. Error bars represent ± 1 SD. b) Fluorescence images at 720 nm showing one of the tumors included in the data analysis after 0, 100 and 200 s of therapeutic irradiation, corresponding to 0, 10 and 20 J/cm².

4. Conclusions

In conclusion, we have reported a significant selectivity between tumor and surrounding skin at 4 hours following administration of liposome-encapsulated Temoporfin embedded into a thermo-setting gel, constituting a novel Temoporfin formulation for topical use. The uptake of the substance was monitored by point-monitoring as well as imaging fluorescence spectroscopy. Fluorescence was induced either at 405 nm or by the treatment light at 652 nm. The bleaching of the sensitizer was estimated from the fluorescence levels by comparing the fluorescence images before, during and after PDT. Furthermore, our initial results show that this new formulation is easy applicable due to its temperature dependent viscosity, rendering the gel to firm after application onto the lesions. The light illumination is not connected with any treatment related pain or other adverse reactions. As compared to ALA-PDT no swollen tissue or oozing were noticed at the weekly follow-up. In cases where the tumor area was associated with a wound with or without bleeding it was noted that these lesions seemed to dry up after few days. After these promising initial results further studies are needed in order to understand the penetration of the Temoporfin in skin following topical administration. Furthermore, studies for following long term tumor response are being planned.

Acknowledgment

The economical support from the Swedish Research Council and the Knut and Alice Wallenberg Foundation is highly appreciated as well as the valuable support from Stefan Spaniol at Biolitec, Bonn. The work was performed within the frameworks of the EU-BRIGHT project IST-511-722-2003 and the EU project "Molecular imaging" LSHG-CT-2003-503259.

Reference List

- (1) Dougherty TJ, Gomer CJ, Henderson BW, Jori G, Kessel D, Korbek M et al. Photodynamic therapy. *J Natl Cancer Inst* 1998; 90(12):889-905.
- (2) Peng Q, Berg K, Moan J, Kongshaug M, Nesland JM. 5-aminolevulinic acid-based photodynamic therapy: Principles and experimental research. *Photochem Photobiol* 1997; 65(2):235-251.
- (3) Almeida RD, Manadas BJ, Carvalho AP, Duarte CB. Intracellular signaling mechanisms in photodynamic therapy. *Biochim Biophys Acta* 2004; 1704(2):59-86.
- (4) Triesscheijn M, Ruevekamp M, Aalders M, Baas P, Stewart FA. Outcome of mTHPC mediated photodynamic therapy is primarily determined by the vascular response. *Photochem Photobiol* 2005; 81(5):1161-1167.
- (5) van Duijnhoven FH, Aalbers RIJM, Rovers JP, Terpstra OT, Kuppen PJK. Immunological aspects of photodynamic therapy of liver tumors in a rat model for colorectal cancer. *Photochem Photobiol* 2003; 78(3):235-240.
- (6) Peng Q, Warloe T, Berg K, Moan J, Kongshaug M, Giercksky K-E et al. 5-aminolevulinic acid-based photodynamic therapy: Clinical research and future challenges. *Cancer* 1997; 79:2282-2308.
- (7) Svanberg K, Andersson T, Killander D, Wang I, Stenram U, Andersson-Engels S et al. Photodynamic therapy of non-melanoma malignant tumours of the skin using topical δ -aminolevulinic acid sensitization and laser irradiation. *Br J Dermatol* 1994; 130:743-751.
- (8) af Klinteberg C, Enejder AMK, Wang I, Andersson-Engels S, Svanberg S, Svanberg K. Kinetic fluorescence studies of 5-aminolaevulinic acid-induced protoporphyrin IX accumulation in basal cell carcinomas. *J Photochem Photobiol B* 1999; 49(2-3):120-128.
- (9) Holmes MV, Dawe RS, Ferguson J, Ibbotson SH. A randomized, double-blind, placebo-controlled study of the efficacy of tetracaine gel (Ametop((R))) for pain relief during topical photodynamic therapy. *Br J Dermatol* 2004; 150(2):337-340.
- (10) Wang I, Bendsoe N, af Klinteberg C, Enejder AMK, Andersson-Engels S, Svanberg S et al. Photodynamic therapy versus cryosurgery of basal cell carcinomas; results of a phase III randomized clinical trial. *Br J Dermatol* 2001; 144(4):832-840.
- (11) Peng Q, Soler AM, Warloe T, Nesland JM, Giercksky KE. Selective distribution of porphyrins in skin thick basal cell carcinoma after topical application of methyl 5-aminolevulinic acid. *J Photochem Photobiol B* 2001; 62(3):140-145.
- (12) Moan J, Ma LW, Iani V. On the pharmacokinetics of topically applied 5-aminolevulinic acid and two of its esters. *Int J Cancer* 2001; 92(1):139-143.
- (13) Juzenas P, Sharfaei S, Moan J, Bissonnette R. Protoporphyrin IX fluorescence kinetics in UV-induced tumours and normal skin of hairless mice after topical application of 5-aminolevulinic acid methyl ester. *J Photochem Photobiol B* 2002; 67(1):11-17.
- (14) Mitra S, Foster TH. Carbogen breathing significantly enhances the penetration of red light in murine tumours in vivo. *Phys Med Biol* 2004; 49(10):1891-1904.
- (15) Ren QG, Wu SM, Peng Q, Chen YJ. Comparison of 5-aminolevulinic acid and its hexylester mediated photodynamic action on human hepatoma cells. *Acta Biochimica et Biophysica Sinica* 2002; 34(5):650-654.

- (16) Balasubramaniam E, Natarajan P. Photophysical properties of protoporphyrin IX and thionine covalently attached to macromolecules. *J Photochem Photobiol A* 1997; 103(3):201-211.
- (17) Schleier P, Berndt A, Kolossa S, Wood M. Comparison between mALA- and ALA-PDT in the treatment of basal cell carcinomas. 50 Apr; 10th International Congress on Oral Cancer: Oral Onc Suppl 2005; 1(1):67-68.
- (18) Mitra S, Foster TH. Photophysical parameters, photosensitizer retention and tissue optical properties completely account for the higher photodynamic efficacy of meso-tetra-hydroxyphenyl-chlorin vs Photofrin. *Photochem Photobiol* 2005; 81(4):849-859.
- (19) Lou PJ, Jager HR, Jones L, Theodossy T, Bown SG, Hopper C. Interstitial photodynamic therapy as salvage treatment for recurrent head and neck cancer. *Br J Cancer* 2004; 91(3):441-446.
- (20) Moore CM, Nathan TR, Lees WR, Mosse CA, Freeman A, Emberton M et al. Photodynamic therapy using meso tetra hydroxy phenyl chlorin (mTHPC) in early prostate cancer. *Lasers Surg Med* 2006; 38(5):356-63.
- (21) Triesscheijn M, Ruevekamp M, Antonini N, Neering H, Stewart FA, Baas P. Optimizing Meso-tetra-hydroxyphenyl-chlorin Mediated Photodynamic Therapy for Basal Cell Carcinoma. To appear in *Photochem Photobiol* 2006.
- (22) Sasnouski S, Zorin V, Khludeyev I, D'Hallewin MA, Guillemin F, Bezdetnaya L. Investigation of Foscan interactions with plasma proteins. *Biochim Biophys Acta* 2005; 1725(3):394-402.
- (23) Westerman P, Glanzmann T, Andrejevic S, Braichotte DR, Forrer M, Wagnieres GA et al. Long circulating half-life and high tumor selectivity of the photosensitizer meta-tetrahydroxyphenylchlorin conjugated to polyethylene glycol in nude mice grafted with a human colon carcinoma. *Int J Cancer* 1998; 76(6):842-850.
- (24) Keene JP, Kessel D, Land EJ, Redmond RW, Truscott TG. Direct detection of singlet oxygen sensitized by haematoporphyrin and related compounds. *Photochem Photobiol* 1986; 43(2):117-120.
- (25) Gupta G, Morton CA, Whitehurst C, Moore JV, Mackie RM. Photodynamic therapy with meso-tetra(hydroxyphenyl) chlorin in the topical treatment of Bowen's disease and basal cell carcinoma. *Br J Dermatol* 1999; 141(2):385-386.
- (26) Johansson A, Svensson J, Andersson-Engels S, Svanberg K, Bendsoe N, Alexandratou E et al. Fluorescence and absorption assessment of a lipid mTHPC formulation following topical application in a skin tumor model. Manuscript for *J Biomed Opt* 2006.
- (27) Pegaz B, Debeve E, Ballini JP, Wagnieres G, Spaniol S, Albrecht V et al. Photothrombic activity of m-THPC-loaded liposomal formulations: Pre-clinical assessment on chick chorioallantoic membrane model. *Eur J Pharm Sci* 2006; 28:134-140.
- (28) af Klinteberg C, Andreasson M, Sandström O, Andersson-Engels S, Svanberg S. Compact medical fluorosensor for minimally invasive tissue characterisation. *Rev Sci Instrum* 2005; 76(3):034303-034306.
- (29) Coutier S, Mitra S, Bezdetnaya LN, Parache RM, Georgakoudi I, Foster TH et al. Effects of fluence rate on cell survival and photobleaching in meta-tetra-(hydroxyphenyl)chlorin-photosensitized colo 26 multicell tumor spheroids. *Photochem Photobiol* 2001; 73(3):297-303.

Tissue temperature monitoring during Interstitial Photodynamic Therapy

Jenny Svensson, Ann Johansson, Katarina Svanberg^a, Stefan Andersson-Engels

Lund University Medical Laser Centre, Department of Physics, Lund Institute of Technology,
P.O. Box 118, SE-221 00 Lund, Sweden. Tel. +46 46 222 31 19

^aLund University Medical Laser Centre, Department of Oncology, Lund University Hospital,
SE-221 85 Lund, Sweden. Tel. +46 46 222 40 48.

ABSTRACT

During δ -aminolevulinic acid (ALA) based Interstitial Photodynamic Therapy (IPDT) a high light fluence rate is present close to the source fibers. This might induce an unintentional tissue temperature increase of importance for the treatment outcome. In a previous study, we have observed, that the absorption in the tissue increases during the treatment. A system to measure the local tissue temperature at the source fibers during IPDT on tissue phantoms is presented. The temperature was measured by acquiring the fluorescence from small Cr^{3+} -doped crystals attached to the tip of the illumination fiber used in an IPDT-system. The fluorescence of the Alexandrite crystal used is temperature dependent. A ratio of the intensity of the fluorescence was formed between two different wavelength bands in the red region. The system was calibrated by immersing the fibers in an Intralipid solution placed in a temperature controlled oven. Measurements were then performed by placing the fibers interstitially in a pork chop as a tissue phantom. Measurements were also performed superficially on skin on a volunteer. A treatment was conducted for 10 minutes, and the fluorescence was measured each minute during the illumination. The fluorescence yielded the temperature at the fiber tip through the calibration curve. The measurements indicate a temperature increase of a few degrees during the simulated treatment.

Keywords: interstitial photodynamic therapy, temperature-dependent fluorescence, Cr^{3+} -ions

1. INTRODUCTION

The aim of this study is to present results of an optical method to monitor tissue temperature behaviour during simulated Photodynamic Therapy (PDT) treatments superficially on skin, but also interstitial PDT illumination in a piece of meat.

1.1 Interstitial Photodynamic Therapy (IPDT)

Photodynamic therapy, PDT, is a method for treating locally situated tumours.¹ The patient is given a photosensitising drug a certain time period before the treatment. The photosensitiser can be administered in different ways. After some time the photosensitiser has selectively accumulated in the tumour and the treatment is initiated. By illuminating the tumour, with light of a wavelength matching an absorption peak of the photosensitiser, the photosensitiser is excited. The photosensitiser can interact with other molecules and an energy transfer is therefore possible. If the energy is transferred to an oxygen molecule, this molecule can be excited from a triplet ground state to a first singlet excited state. This singlet state is very reactive and can oxidise proteins and cell constituents, which can lead to cell necrosis or apoptosis in the tumour.

The main advantages of PDT are that the treatment is selective, can be repeated and that the treated areas heal fast. A major disadvantage is that only superficial tumours can be treated and with tumour thickness only up to a few millimetres. A possible solution to this problem is to use interstitial photodynamic therapy, IPDT, where optical fibers are inserted into the tumour mass. This will give the advantage to enable treatment of more solid tumours, either primary tumours or e.g. liver metastases.²

1.2 Why is it important to monitor the temperature locally?

During an IPDT treatment procedure a high light fluence rate is present close to the source fibers, especially when using bare end cut fibers.³ This might induce an unintentional tissue temperature increase of importance for the treatment outcome. In addition, an increase in the measured absorption coefficient has been seen during IPDT treatments, in a recent study.³ The increase in the absorption coefficient could be an effect of tissue deoxygenation, changes in blood flow, local bleeding or temperature increase close to the fiber tips.

The goal of an IPDT treatment is not to have a hyperthermal, but a photochemical effect, on the lesion. If a small bleeding occurs at the fiber tip, the absorption coefficient will increase drastically and this could lead to an abrupt temperature increase. Such bleeding would reduce the efficacy of the treatment, since most of the light would be absorbed in the blood right at the fiber tip.

In an earlier published study, the blood perfusion and the temperature were measured during superficial PDT, both on patients with lesions and on skin on volunteers⁴. The temperature was studied with an infrared camera and an increase in temperature 1-4 °C could be seen during the treatment. This small temperature increase shows that there is no hypothothermal effect during the treatment when an initial temperature was about 35 °C. The infrared camera only monitor the really superficial layer of the skin and in deeper lying tissue the temperature could actually be higher. With a thermometer based on an optical technique, the temperature could actually be measured at other deeper locations.

2. MEASUREMENT PRINCIPLES

One way to measure the temperature with an optical technique is to use crystals, which fluorescence is temperature dependent. To be able to measure the temperature locally in the tissue where the treatment fibers are located, a small crystal can be attached to the fiber tip. In this study a crystal doped with Cr³⁺-ions was used. Cr³⁺-ions in ionic crystals interact strongly with the crystal field and the lattice vibrations. The crystal field arises because of the influence on the Cr³⁺-ion from the neighbouring ions. The interaction between the Cr³⁺-ions and the crystal field arises due to the fact that there are no outer shells to shield the three valence electrons. As a result Cr³⁺-activated materials are characterised by a wide absorption spectrum, from UV to infrared. This has two advantages, the possibility to choose excitation source and that a small drift in the excitation source will not cause a significant change in the fluorescence intensity. Because of the strong crystal field interaction, the energy gaps of the electronic levels of Cr³⁺ can vary from one host crystal to another. The temperature dependence of the fluorescence lifetime varies with the energy gap and will thus differ for different Cr³⁺-doped materials. Different Cr³⁺-doped crystals show different temperature dependence in the fluorescence signal. Among the different crystals, Alexandrite seems to show good temperature sensitivity in the interesting temperature range (15 – 100 °C) in this case.⁵

A Jablonsky diagram of Alexandrite is shown in Figure 1. The ground state in Cr³⁺ is always ⁴A₂, independent of the strength of the crystal field. Two excited energy levels are involved, following excitation at 635 nm: ⁴T₂ and ²E. The energy splitting between these two low-lying states is denoted $\Delta E = E(^4T_2) - E(^2E)$. ΔE varies strongly with the strength of the crystal field and can be both negative and positive. The emission spectrum of Cr³⁺ consists of two different features, a broad spectral band and two sharp peaks, so called R-lines. The broad band originates from the vibrational transitions, ⁴T₂ → ⁴A₂, where ions in the ⁴T₂ state decay to the empty vibrational levels of the ⁴A₂ state. The R-lines appear because of a further split of the ²E state into two levels, E and 2 \bar{A} , separated by a small energy gap. The R₁-line is the transition E → ⁴A₂ and the R₂-line comes from the transition 2 \bar{A} → ⁴A₂.⁵ Lattice vibrations in the crystal interact with the electronic levels of the Cr³⁺-ion. The effects of this are the initiation of vibrational transitions, radiationless transitions and phonon scattering. The first of these effects produces broad bands in the spectra, the second effect leads to a temperature dependent decrease of the fluorescence lifetimes of the R-lines and both the second and third effect can cause a thermal broadening of the R-lines.⁶

In Alexandrite, the lowest excited state of the Cr³⁺-ions is the ²E state (Figure 1). At low temperatures the emission is dominated by the transition ²E → ⁴A₂ (the R-lines), yielding an effective long fluorescence lifetime, since the transition is parity and spin forbidden. The ⁴T₂ state has a much shorter lifetime than the ²E state. When the temperature increases, a higher percentage of the Cr³⁺-ions will populate the ⁴T₂ state according to the Boltzmann distribution. Consequently more ions will decay through the ⁴T₂ → ⁴A₂ path, resulting in a decrease of the fluorescence lifetime. Thus, at low temperatures the thermally activated populations of the ²E and ⁴T₂ states determine the fluorescence properties.⁵

This phenomenon can also be seen in the intensity of the fluorescence. The fluorescence, corresponding to the R-lines, will decrease when less ions will follow the path ${}^2E \rightarrow {}^4A_2$. This can be used as a measure of the temperature by forming a dimensionless ratio for the intensities from the R-lines divided by the intensity at longer wavelengths.

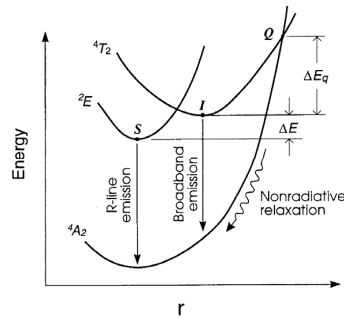


Figure 1. The energy levels as a function of nearest neighbour distance for a crystal with a high crystal field strength (See Ref 5).

An evaluation of the method measuring the temperature with fluorescence from crystals has been reported earlier.⁷ In that study fluorescence lifetime measurements were performed. In this study we go one step further and use an integrated system developed for IPDT to measure the fluorescence and calculate an intensity ratio of the fluorescence to give a value of the actual temperature. There are commercially available fiber based thermometers using optical techniques to measure temperature dependent fluorescence, which can be used for temperature monitoring.⁸ The concept we use in this study is that the crystal is located on the fiber tip of the fiber delivering the treatment light during a real IPDT treatment.

3. MATERIAL AND METHODS

3.1 Material

In this section the Interstitial Photodynamic Therapy system used will be described and also a short description of how the crystal was attached to a bare end fiber tip will be given.

3.1.1 IPDT system

An instrument for interstitial photodynamic therapy has been developed by the company SpectraCure AB (Ideon Research Park, Lund, Sweden). A general schematic drawing of the instrument is shown in Figure 2. The instrument uses a maximum of six bare end optical fibers that are used to deliver the therapeutic light into the tumour mass. The same fibers can also be used in order to perform diagnostic measurements during the treatment session.³ The therapeutic light unit consists of six diode lasers emitting at 635 nm with an individual maximum output power of 200 mW. While in treatment mode, light from the therapeutic light unit is guided into the light distribution module and further coupled into the six 400 μm diameter fibers, which are inserted in the tumor.

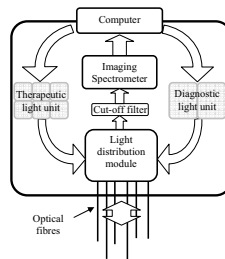


Figure 2. A schematic description of the interstitial photodynamic therapy system used for the experiments (See Ref 3).

In the measurement mode, light from the diagnostic light unit is coupled into one of the “patient fibers” via the light distribution module. After interacting with the sample the fluorescence light is collected by the other fibers and coupled into an imaging spectrometer covering the spectral range between 620 and 810 nm. A cut-off filter (Schott RG665) is used to attenuate the intense laser light at 635 nm from the laser light source. Wavelength calibration of the spectrometer is carried out using an HgAr lamp to determine the relation between wavelength and pixel number in the horizontal direction of the CCD chip.³

3.1.2 Attachment of crystal to fiber tip

For the measurements, an end cut fiber with a core diameter of 400 μm (Fiberguide Industries, USA), was used. A small Alexandrite crystal was glued to the clear cut fiber tip, using the glue (Nordland Optical Adhesive 68, Norland Products) which needed to cure in UV-light for 30 minutes.

3.2 Calibration of fiber

The set-up used for temperature calibration is shown in Figure 3. The calibration was performed in the temperature interval 15 – 50 °C. Two fibers were immersed in an Intralipid solution of 1.28 % in a vessel. The distance between the fibers was approximately 12 mm. Initial tests were performed to investigate the influence of different scattering coefficients, by changing the Intralipid concentration. Different distances were also tested to study the effect of the distance between the two fibers. One fiber was used only for delivering the excitation light and the other one, with an attached piece of crystal, was used for detection of induced fluorescence light. The vessel and the fibers were placed inside a temperature controlled oven (FN300 Nüve Microprocessor). To monitor the actual temperature in the Intralipid, two thermistors were also placed in the vessel, close to the fibers. After approximately 45 minutes the temperature had stabilized in the solution, the laser in the IPDT system was turned on and was illuminating through fiber 1. The induced fluorescence light from the crystal was detected through fiber 2 in Figure 3, and an image was acquired with the detection unit. For each temperature, two different powers (90 mW and 130 mW) of the laser light were tested, in order to monitor the influences of the power in the fluorescence light. Then the temperature of the oven was increased and the procedure was repeated.

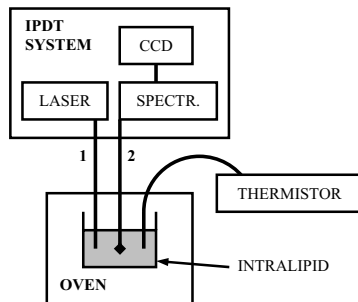


Figure 3. The set-up used for calibration. The fiber used for illumination of the laser light (denoted 1) and the fiber with a piece of crystal (marked 2) are shown.

3.3 Evaluation of a fluorescence spectrum

The evaluation of the temperature was performed by using the concept of forming a dimensionless ratio. A summation was made for the intensities in two different wavelength bands, marked with Area 1 and Area 2 in Figure 4. A ratio was then formed between the two values from Area 1 and Area 2 for each measured temperature.

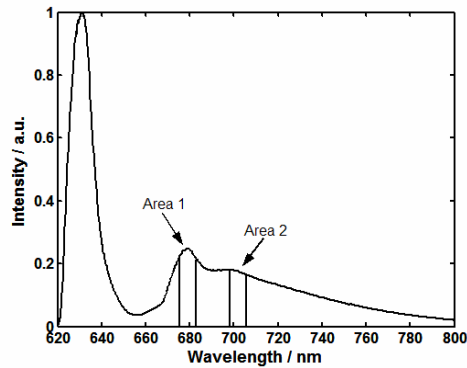


Figure 4. A fluorescence spectrum from alexandrite showing the wavelength bands used for forming a ratio.

3.4 Experiment

For the experiments performed in this study, two different arrangements of the two fibers were used. In arrangement A, see Figure 5a, the end cut fiber, denoted with 1 in the figure, was used for illumination during the simulated treatment. The other fiber (denoted 2), with a crystal attached to the fiber tip, was used to monitor the temperature. The treatment light was used to induce fluorescence in the crystal. The fluorescence light was guided through the fiber into the detection unit in the IPDT system. With this arrangement the temperature was monitored in the spot where the doped fiber was placed, which means a small distance from the treatment fiber.

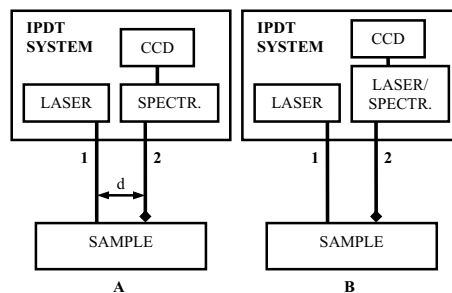


Figure 5. Two different arrangements of the fibers are shown. In A, the illumination fiber is denoted 1 and the detection fiber with the crystal is marked 2. In the arrangement in B, the illumination fiber is the doped fiber, (2), measuring the temperature in the same spot where the treatment takes place. The fiber, denoted 1, in B, is only used for inducing fluorescence in the crystal when a temperature measurement is performed.

In fiber arrangement B, see Figure 5b, the fiber with a piece of crystal attached to the tip (denoted 2), was used for illumination during the treatment. This fiber was illuminating the whole time except during the temperature measurements, when it was used for detection of fluorescence light. The other fiber, denoted 1 in Figure 5b, was placed approximately 2 mm apart from the first fiber. Fiber 1 was only illuminating during the temperature measurements to induce the fluorescence in the crystal at the other fiber tip. With this set-up the temperature is monitored where the illumination fiber is located and not at a small distance as in arrangement A.

3.4.1 Simulation of a superficial treatment on skin

Both the fiber arrangements were used for the investigation on skin. With arrangement A, (Figure 5a), the two fibers were placed in close contact with the skin on the arm of a healthy volunteer. In the first measurement, a power of 130

mW through the illumination fiber was used, and detection of fluorescence light, with the doped fiber, was performed each 10 seconds during 2 minutes. This was done to see how the temperature increases in the beginning of the illumination period. In the following three measurements the distance between the two fibers was changed (see distance d in Figure 5a) with the values of 1 and 3 mm. The power from the illumination fiber was measured to 130 mW and the illumination was continued during 10 minutes. A fluorescence measurement was acquired each minute. The temperature of a larger area of the skin was monitored using an infrared camera (uncooled, AGEMA 570 Elite, Flir Systems Inc), which was saving a temperature image every minute.

In the experiment using fiber arrangement B, two different powers, 75 mW and 110 mW, were used for illumination in order to monitor how the temperature changed as a result of different treatment power. One temperature measurement was performed before the treatment, to get information about the initial temperature. The treatment started by illuminating with the doped fiber (denoted 2 in Figure 5b). After 1 minute the other fiber (denoted 1 in Figure 5b) started to illuminate. Detection of induced fluorescence light from the crystal was performed through fiber 2. The illumination was continued as before and a temperature measurement was recorded each minute during the treatment. After 10 minutes the treatment was interrupted, but the measurements continued for a few minutes to study the temperature change without any illumination.

3.4.2 Simulation of an interstitial treatment in meat

In the final experiments, regarding interstitial treatment, measurements were performed using a pork-chop as a tissue phantom. The two fibers were placed next to each other inside the meat. By using fiber arrangement A, a 10 minutes treatment was performed. In this case an output power from the illumination fiber was 130 mW and the depth of the fibers in the meat was approximately 12 mm. Two experiments were also conducted with arrangement B. In the first experiment the depth of the fibers was 18 mm and a power of 110 mW. The treatment continued during 20 minutes. In the last experiment the fibers were placed at a depth of 10 mm and a power of 110 mW, but only for 10 minutes. A temperature measurement was performed each minute.

4. RESULTS AND DISCUSSION

4.1 Calibration curve for fiber with attached crystal

A calibration curve is shown in Figure 6, with the dimensionless ratio as a function of the corresponding temperature. For the calibration curve different fluorescence excitation powers were used. It can be seen in the figure that the influence of the power is very weak. The reason for that might be the formation of a dimensionless ratio, with the main advantage of cancelling out environmental effects. Tests were also performed when changing the distance between the fibers and different scattering in the Intralipid. The results, not presented here, show that the distance, between the illumination and detection fiber, does not affect too much, more when the distance is too big so the detected fluorescence signal becomes too weak, and noise disturbs the measurements. A different scattering power of the Intralipid phantom does not affect the ratio either. A quadratic polynomial was fitted to the acquired data points. This curve was later used as a calibration curve for determining the temperature measured during the tissue measurements.

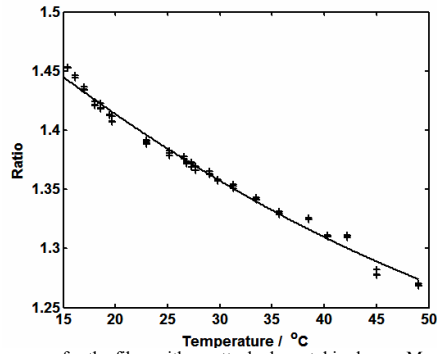


Figure 6. A calibration curve for the fiber with an attached crystal is shown. Measured values (crosses) and the fitted calibration curve (solid line) to these values are shown.

4.2 Superficial measurements on skin

The absolute temperature as a function of time can be seen at a small distance from the illumination fiber during a two minute long session on skin (Figure 7). A quadratic polynomial has been fitted to the measured values. As can be seen the temperature is increasing during the first two minutes and it is stabilizing at later times.

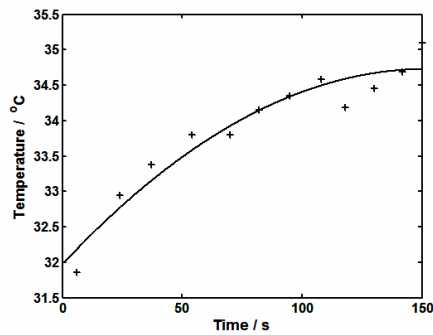


Figure 7. The temperature increase during the first two minutes of superficial illumination on skin is shown. Measured temperatures (crosses) and a fitted line to the measured values are shown.

The temperature increase can be seen as a function of time when changing the distance between the illumination and the doped detection fiber (denoted d in Figure 5A) for two different simulated treatment sessions, in Figure 8. When changing the distance between the two fibers, the temperature in different spots from the illumination spot will be monitored. As can be seen the temperature is increasing the closer to the illumination fiber the detection fiber is located.

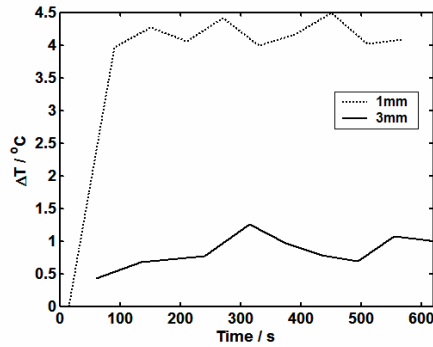


Figure 8. The measured temperature increase at two different fiber separations.

An infrared image is shown after 5 minutes of a superficial treatment on skin (Figure 9). The same figure presents a graph of the temperature increase as a function of distance in the infrared image. As can be seen the increase is about 4 °C close to the middle, which can be related to the same increase seen in Figure 8 for the distance 1 mm. Further out the increase is not of that high value. This shows how important it is to monitor the temperature in the right spot where the illumination is.

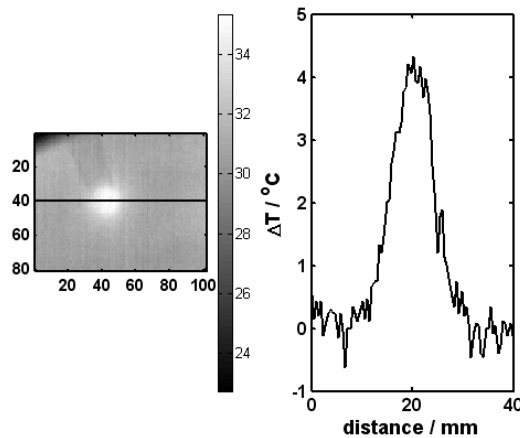


Figure 9. An infrared image is shown 5 minutes after the start of a superficial treatment on skin (left). The temperature increase is shown as a function of distance (right). The solid line in the left image corresponds to the cross section showed in the right graph.

It is interesting to see the temperature increase when using two different powers, as shown in Figure 10. In this figure the illumination fiber is the same as the doped fiber, (see fiber arrangement in Figure 5b), which means that it is the local temperature where the illumination fiber is located that is monitored. As can be seen, the temperature increase is larger when using the power of 110 mW compared to a power of 75 mW. This is not an unexpected behaviour when more energy is delivered to the tissue with a higher power. Another interesting feature is that the temperature increase is stabilized after 3 minutes for the power of 75 mW and after 4 minutes with the power of 110 mW, and for the rest of the treatment the temperature is rather constant. This can be explained by a balance between energy deposition due to light absorption and energy dissipation due to the blood flow where the illumination fiber is located. If the increase, as can be seen in the graph, is about 2-4 °C, the blood perfusion will increase to the area of the fiber to remove some of the extra heat. This might take about 3-4 minutes. The laser illumination was stopped after 10 minutes, but a few extra

temperature measurements were performed to see how the temperature was decreasing. It seems like the temperature decreased even below the initial temperature. An explanation to this can be the increased blood perfusion in the area stimulated by the procedure. Only a few minutes after the treatment was interrupted, it seems like the temperature is stabilized again and probably will reach the initial temperature after a short while. A change in the blood perfusion to the initial perfusion will probably take a few minutes.

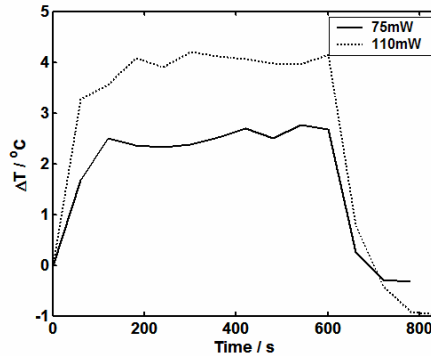


Figure 10. The temperature increase as a function of time conducted at two different powers, 75 and 110 mW.

The reason that the temperature increase is shown instead of an absolute temperature is that there is a difference in the initial temperatures on different locations of the skin.

4.3 Interstitial measurements in meat

The temperature increase during an interstitial treatment in a piece of meat is shown in Figure 11. Three different curves are shown, corresponding to three different treatment sessions. Two of the treatments were conducted for 10 minutes and one for 20 minutes. As can be seen in the graph, the temperature is increasing during the whole session. This can be compared to the superficial measurements on skin where the temperature increase is stabilized after a while as the blood perfusion most probably removes the heat. In interstitial treatment in meat there is no convection or blood perfusion which can stabilize the temperature, instead there will be an increase during the whole treatment. The measurements on meat symbolise thus no entirely realistic scenario because of the lack of tissue perfusion.

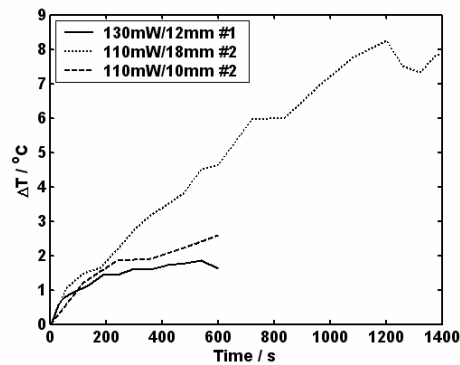


Figure 11. The temperature increase for 3 different interstitial treatments performed in a piece of meat. The power/depth and the arrangement used are shown in the legend.

5. CONCLUSIONS

In this study we have shown that tissue temperature can be measured with an optical technique based on the detection of temperature dependent fluorescence light from the Alexandrite crystal. Simulations of superficial treatments on skin, using a bare cut fiber delivering 110 mW light power at 635 nm, showed that the temperature increase is about 2-4 °C for a treatment of 10 minutes. After 3-4 minutes the temperature remains almost constant most likely due to an increased blood perfusion to the area where the illumination fiber is located.

Simulations of interstitial treatment in meat were also conducted, showing the similar temperature increase, but continuing through the entire treatment. In these cases an increase was shown for the whole treatment as no blood flow is existent in the meat.

In the study we worked with two different fiber arrangements used for treatment. In the first arrangement the illumination fiber was not the same as the doped fiber. With this arrangement the temperature is not measured right at the illumination fiber where the light fluence rate is high. With the second arrangement, where the illumination fiber is also the crystal doped fiber, the temperature will be monitored exactly at the fiber tip where a high fluence rate is located. A big temperature increase will only occur in a distance of a few hundred micrometers from the tip of the illumination fiber.⁹ This means that the fiber arrangement B (see Figure 5B) is the best for monitoring the local temperature at the fiber tip.

Future work in the project involves more temperature measurements on simulated superficial treatments on volunteers to get a better statistics. Also more interstitial measurements in meat will be conducted. The robustness of the attachment of the crystal to the fiber tip is also an urgent question to be solved. So far, we have seen that only using glue to attach the crystal is not enough. The fiber tip becomes very fragile.

ACKNOWLEDGEMENTS

The authors would like to thank Nina Reistad, for supplying an infrared camera, and Lars Wallman, for supplying us with an oven used for calibration of fiber. The financial support by the company SpectraCure AB and the Swedish Strategic Research Foundation (SSF) are gratefully acknowledged.

REFERENCES

1. T. J. Dougherty, C. J. Gomer, B. W. Henderson, G. Jori, D. Kessel, M. Korbelik, J. Moan, and Q. Peng, "Photodynamic therapy," *J. Natl. Cancer Inst.* **90**(12), 889-905 (1998)
2. T. J. Vogl, K. Eichler, M. G. Mack, S. Zangos, C. Herzog, A. Thalhammer, and K. Engelmann, "Interstitial photodynamic laser therapy in interventional oncology," *Eur. Radiol.* **14**(6), 1063-1073 (2004)
3. M. Soto Thompson, A. Johansson, T. Johansson, S. Andersson-Engels, N. Bendsoe, K. Svanberg, and S. Svanberg, "Clinical system for interstitial photodynamic therapy with combined on-line dosimetry measurements", 2004, Submitted 2004
4. S. Pålsson, L. Gustafsson, N. Bendsoe, M. Soto Thompson, S. Andersson-Engels, and K. Svanberg, "Kinetics of the superficial perfusion and temperature in connection with photodynamic therapy of basal cell carcinomas using esterified and non-esterified 5-aminolevulinic acid," *Br. J. Dermatol.* **148**(6), 1179-1188 (2003)
5. K. T. V. Grattan and Z. Y. Zhang, *Fiber optic fluorescence thermometry*, Chapman & Hall, London, 1995
6. R. C. Powell, L. Xi, X. Gang, G. J. Quarles, and J. C. Walling, "Spectroscopic properties of alexandrite crystals," *Physical Review B* **32**(5), 2788-2797 (1985)
7. J. Svensson, A. Ralsgård, T. Johansson, and S. Andersson-Engels, "Tissue temperature measurements during interstitial laser therapy using Cr³⁺-doped crystals at the fiber tip", *Therapeutic laser applications and laser-tissue interactions*, R.W. Steiner, 5142, (30-41), Proc SPIE, Munich, 2003.
8. J. Wren, "Evaluation of three temperature measurement methods used during microwave thermotherapy of prostatic enlargement," *Int. J. Hyperthermia* **20**(3), 300-316 (2004)
9. L. Lilje, Private communication, 2004

